



# Functional Optoacoustic Neuro- Tomography for Large Scale Electrophysiology in Optically Scattering Tissues

**Benedict Edward Mc Larney**

Vollständiger Abdruck der von der Fakultät für Medizin der Technischen Universität München zur Erlangung des akademischen Grades eines **Doktors der Naturwissenschaften (Dr. rer. nat.)** genehmigten Dissertation.

**Vorsitzender:** Prof. Dr. Wolfgang Weber

**Prüfer der Dissertation:** 1. Prof. Dr. Vasilis Ntziachristos

2. Prof. Dr. Bernd Reif

Die Dissertation wurde am 12.05.2020 bei der Technischen Universität München eingereicht und durch die Fakultät für Medizin am 29.12.2020 angenommen.



## Acknowledgements

Firstly, I would like to thank Prof. Daniel Razansky for his guidance throughout this dissertation work. Before joining his lab, I had no experience in optoacoustic imaging and have since become a proficient user with a wealth of experience. His approach to science, open door policy and the environment he has established have been key components for that. Secondly, I would like to thank everyone at Prof. Razansky's lab, who gave their invaluable insight into my work as well as incredible advice. A special thanks goes to Sven Gottschalk, Xosé Luis Dean-Ben, Oleksiy Degtyaruk, Magdalena Hutter, Johannes Rebling, Ivana Ivankovic, Michael Reiss, Sarah Glasl, Prof. Shy Shoham and everyone at his lab in NYU and Prof. Robert Campbell and his lab at the University of Alberta. I would also like to thank everyone at IBMI, in particular Prof. Vasilis Ntziachristos and the work ethic there, which has led to many publications. A big thanks goes out to my Mam (Liz), Dad (Ben Snr) and sister (Kate) who have always been there to listen to me and help me in any way they could. My parents encouraged me to pursue science at a young age and it's been great advice ever since. A special thanks goes to John Nealon for his proof reading, support, and lively scientific discussions. Lastly, I would like to thank my (now) wife Nora Mc Larney for all her care, support and help throughout the last 4 years, not to mention her patient proof-reading skills.

## Abstract

Electrophysiology is an integral component of understanding brain function, giving real time information on neuronal signaling using strategically placed needle electrodes or patches. Imaging electrophysiology in small animal research is achieved via direct (genetically encoded calcium and voltage sensitive indicators, GECIs and GEVIs) as well as indirect (hemodynamics) methods with functional magnetic resonance imaging (fMRI), functional ultrasound (fUS) and optical imaging (fluorescence). For murine imaging, current methods suffer from one or many of the following: poor spatiotemporal resolution, small field of view (FOV) and shallow penetration depths. Recently, optoacoustic tomography (OAT) in the form of functional optoacoustic neurotomography (FONT) has emerged as a method of indirect imaging of neuronal activity via hemodynamics capable of imaging the entire mouse brain at high spatiotemporal resolution. This dissertation focuses on the improvement and application of a novel FONT system to achieve direct imaging of electrophysiological activity in scattering tissues i.e., the brain via GECIs. In the scope of this thesis, a system was developed capable of imaging isolated *ex vivo* mouse brains & hearts in their entirety with a single laser pulse and provided high resolution anatomical detail. The lack of inherent motion in brain imaging and wide availability of transgenic GECI expressing mouse lines organisms were most suitable for FONT. Prior to GECI imaging the FONT system was employed to detect, and map electrical paw stimulated hemodynamic activity in the somatosensory cortex *in vivo*. FONT allowed the detection of all hemodynamic components (HbO, HbR and HbT) showing elevated contralateral responses and the presence of an initial dip in the HbO component. Following this sparsely labelled GCaMP6s/f detection was achieved despite strong background absorption of hemoglobin. Finally, the project looked to novel electrophysiological proteins for FONT detection of voltage responses via a FRET based GEVI (Butterfly 1.2) and to overcome inherent visible light absorption & scattering with a NIR GECI (NIR-GECO1). The proteins were tested for their suitability for FONT in combination with fluorescence for validation and while both proved successful for fluorescence imaging, neither are currently suitable for FONT. However, strategies and steps for development of FONT and these proteins are outlined to realize this. The work described here has established a platform for the non-invasive testing of electrophysiological proteins and improves current FONT techniques and practices with broad implications for neuroimaging.

# Zusammenfassung

Die Elektrophysiologie ist ein integraler Bestandteil des Verständnisses der Hirnfunktion und liefert mit Hilfe von strategisch platzierten Nadelelektroden oder Pflastern Informationen über die neuronale Signalübertragung in Echtzeit. Die Abbildung der Elektrophysiologie in der Kleintierforschung erfolgt sowohl über direkte (genetisch kodierte Calcium- und spannungssensitive Indikatoren, GECIs und GEVIs) als auch indirekte (hämodynamische) Methoden mit funktioneller Magnetresonanztomographie (fMRI), funktionellem Ultraschall (fUS) und optischer Bildgebung (Fluoreszenz). Für die Bildgebung bei Mäusen leiden die aktuellen Methoden unter einer oder mehreren der folgenden Eigenschaften: schlechte räumlich-zeitliche Auflösung, kleines Sichtfeld (FOV) und geringe Eindringtiefe. In jüngster Zeit hat sich die optoakustische Tomographie (OAT) in Form der funktionellen optoakustischen Neurotomographie (FONT) als eine Methode zur indirekten Darstellung neuronaler Aktivität über die Hämodynamik herauskristallisiert, die in der Lage ist, das gesamte Maushirn mit hoher räumlicher und zeitlicher Auflösung abzubilden. Diese Dissertation befasst sich mit der Verbesserung und Anwendung eines neuartigen FONT-Systems zur direkten Abbildung elektrophysiologischer Aktivität in streuenden Geweben, z.B. dem Gehirn, mittels GECIs. Im Rahmen dieser Arbeit wurde ein System entwickelt, das in der Lage ist, isolierte ex vivo Mäusegehirne und -herzen in ihrer Gesamtheit mit einem einzigen Laserpuls abzubilden und hochauflösende anatomische Details zu liefern. Das Fehlen inhärenter Bewegungen bei der Bildgebung von Gehirnen und die breite Verfügbarkeit von transgenen GECI exprimierenden Mauslinien waren für FONT am besten geeignete Organismen. Vor der GECI-Bildgebung wurde das FONT-System zur Detektion und Kartierung elektrischer, durch die Pfote stimulierter hämodynamischer Aktivität im somatosensorischen Kortex in vivo eingesetzt. FONT ermöglichte die Detektion aller hämodynamischen Komponenten (HbO, HbR und HbT), die erhöhte kontralaterale Antworten und das Vorhandensein eines anfänglichen Einbruchs in der HbO-Komponente zeigten. Anschließend wurde trotz starker Hintergrundabsorption des Hämoglobins eine spärliche GCaMP6s/f-Detektion erreicht. Schließlich wurden neuartige elektrophysiologische Proteine für die FONT-Detektion von Spannungsantworten mittels eines FRET-basierten GEVI (Butterfly 1.2) und zur Überwindung der inhärenten Absorption & Streuung von sichtbarem Licht mit einem NIR-GECI (NIR-GECO1) untersucht. Die Proteine wurden zur Validierung auf ihre Eignung für FONT in Kombination mit Fluoreszenz getestet. Während sich beide für die Fluoreszenz-Bildgebung als erfolgreich erwiesen, sind beide derzeit nicht für FONT geeignet. Es werden jedoch Strategien und Schritte zur Entwicklung von FONT und dieser Proteine skizziert, um dies zu realisieren. Die hier beschriebene Arbeit hat eine Plattform für das nicht-invasive Testen von elektrophysiologischen Proteinen etabliert und verbessert aktuelle FONT-Techniken und -Praktiken mit weitreichenden Implikationen für das Neuroimaging.

# Contents

Acknowledgements .....	ii
Abstract .....	iii
Zusammenfassung .....	iv
Contents .....	v
List of Abbreviations .....	vi
Preface .....	xi
List of Publications .....	xiv
1. Introduction .....	1
1.1 Fluorescence imaging .....	1
References .....	6
1.2 Optoacoustic Tomography .....	10
References .....	18
1.3 Neuroimaging .....	23
References .....	30
2. Uniform light delivery in volumetric optoacoustic tomography .....	36
2.1 Summary and author contribution .....	36
3. Monitoring of stimulus evoked murine somatosensory cortex hemodynamic activity with volumetric multi-spectral optoacoustic tomography .....	53
3.1 Summary and author contribution .....	53
4. A genetically encoded near-infrared fluorescent calcium ion indicator .....	68
4.1 Summary and Author Contribution .....	68
5. Conclusion and Outlook .....	106
References .....	115
Permission letters from publishers .....	117

## List of Abbreviations

### #

2D	Two dimensional
3D	Three dimensional
5D	Five dimensional

### A

AAV	Adeno-associated virus
ACSF	Artificial cerebrospinal fluid
ANSI	American national standards institute

### B

BBB	Blood brain barrier
BNC	Bayonet Neill Conelman connector
BOLD	Blood oxygen level-dependent
BV	Biliverdin
BP	Back-projection
Butterfly 1.2	Butterfly 1.2, a genetically encoded voltage sensitive protein

### C

C57BL/6	Black inbred mice
Ca <sup>2+</sup>	Calcium
Ca <sup>-</sup>	Calcium free
CaCl <sub>2</sub>	Calcium chloride
CAD	Computer aided design
CAS9	CRISPR associated protein 9
CBV	Cerebral blood volume
CCD	Charge coupled device
CD-1	Albino outbred mice
CL	Contralateral
CMOS	Complementary metal oxide semiconductor
CMV	Cytomegalovirus
CNR	Contrast to noise ratio
CNS	Central nervous system

Cre-Lox	Cyclic recombinase with loxP site recognition
CRISPR	Clustered regularly interspaced short palindromic repeats
CT	Computed tomography
CW	Continuous wave
<b>D</b>	
D%	Dip percentage
DAPI	4',6-Diamidino-2-Phenylindole (double stranded DNA staining)
DAQ	Data acquisition card
DeT	Decay time
Dip %	Dip percentage change
DTTP	Dip time to peak
DOT	Diffuse optical tomography
<b>E</b>	
ECG	Electro cardiograph
EEG	Electroencephalogram
EGFP	Enhanced green fluorescence protein
EGTA	Ethylene glycol-bis( $\beta$ -aminoethyl ether)-N,N,N',N'-tetra acetic acid
EM	Electromagnetic
EMCCD	Electron multiplied charge coupled device
EYFP	Enhanced yellow fluorescence protein
<b>F</b>	
FDM	Fused deposition modelling
FFT	Fast Fourier transform
FL	Fluorescence
Fluo-3-AM	Fluorescent calcium indicator, Acetoxymethyl ester form
fMRI	Functional magnetic resonance imaging
FONT	Functional optoacoustic neurotomography
FOV	Field of view
FRET	Förster resonance energy transfer
fUS	Functional ultrasound
FWHM	Full width half maximum

## **G**

GABA	Gamma-aminobutyric acid
GFP	Green fluorescent protein
GECI	Genetically encoded calcium indicator
GEVI	Genetically encoded voltage indicator
GPU	Graphics processing unit

## **H**

HbO	Oxygenated hemoglobin
HbR	Reduced hemoglobin (deoxygenated)
HbT	Total hemoglobin
HP	Hind paw
Hz	Hertz

## **I**

IBMI	Institute of Biological and Medical Imaging
IL	Ipsilateral
IP	Intraperitoneal
IR	Infrared
IV	Intravenous

## **K**

KHz	Kilohertz
-----	-----------

## **L**

LED	Light emitting diode
LSI	Laser speckle imaging

## **M**

MB	Model based
MC	Motor cortex
miRFP	Monomeric infrared fluorescent protein
MIP	Maximum intensity projection
MIT	Massachusetts Institute of Technology
MHz	Megahertz
MRI	Magnetic resonance imaging

MSOT	Multispectral optoacoustic tomography
<b>N</b>	
NA	Numerical aperture
NDMA	N-methyl-D-aspartate
NIR	Near infrared
NIR-GECO1	Near infrared genetically encoded calcium opsin one
NYU	New York University
<b>O</b>	
OA	Optoacoustic
OAT	Optoacoustic tomography
OCT	Optical coherence tomography
OI	Optical imaging
OISI	Optical intrinsic signal imaging
OPO	Optical parametric oscillator
<b>P</b>	
P%	Peak percentage
PCR	Polymerase chain reaction
PFA	Paraformaldehyde
PBS	Phosphate buffer solution
PP	Polypropylene
PRF	Pulse repetition frequency
PTZ	Pentylentetrazol
PVB	Parvalbumin
PVC	Polyvinyl chloride
<b>R</b>	
RF	Radio frequency
RFP	Red fluorescence protein
ROI	Region of interest
RT	Room temperature
<b>S</b>	
SM	Somatomotor

SNR	Signal to noise ratio
SPIE	Society of Photographic Instrumentation Engineers
SPIM	Single plane illumination microscopy
SS	Somatosensory
SSS	Superior sagittal sinus
SST	Somatostatin
<b>T</b>	
TECS	Technology enhanced clad silica
TIGRE	Target gene inserted into a tightly regulated (genomic locus)
TTP	Time to peak
TUM	Technical University of Munich
<b>U</b>	
UK	United Kingdom
US	Ultrasound
USA	United states of America
<b>W</b>	
WT	Wild type
<b>V</b>	
VSFP	Voltage sensitive fluorescent protein
VSD	Voltage sensing domain
<b>Y</b>	
YFP	Yellow fluorescence protein
YR	Yellow red

## Preface

This chapter will provide a brief understanding of the content of the work in this thesis and how each of these chapters are linked. The work carried out here was multi-disciplinary and ranged from MATLAB coding to animal experiments and rapid prototyping. This research focused on the biological and engineering applications of OAT in the form of functional optoacoustic neurotomography (FONT) with the goal of imaging of electrophysiological signals in 3D, real-time and over the field-of-view (FOV) of an entire organ.

Electrophysiology is the recording of electrical potential across the cell membrane, from neighboring or groups of cells. It is a highly invasive method requiring the insertion of glass capillaries or needle electrodes attached to cell membranes or into the brain.[1] Electrophysiological signals from single or groups of cells can be recorded less invasively via fluorescent genetically encoded indicators.[2, 3] These are sensitive to either calcium (similar to electrophysiological activity) or voltage changes, modulating output fluorescent signals, which are detected with sensitive optical systems.[4] However, fluorescent imaging suffers from the optical aberrations (scattering and absorption) properties of tissues.[5] Thus, fluorescence imaging is often limited to superficial layers of the brain, slow acquisition times, small FOVs and is highly invasive e.g. optical window implantation, which involves scalp removal, skull thinning and optical window implantation. This can have adverse negative effects on the sample with implications for longitudinal imaging.[6] Only small areas of the brain can be recorded in 3D via confocal methods, but these often lack the required speed needed to detect whole brain electrophysiology in real time.

Optoacoustic tomography (OAT) in when applied to brain imaging is known as functional optoacoustic neurotomography (FONT). OAT uses nanosecond laser pulses ( $< 10$  ns) which are absorbed by tissue.[7] This absorption of optical light (optical contrast) is converted to heat causing rapid expansion and contraction of the tissue, generating ultrasound (US).[8] Detection is achieved via the emitted US, which undergoes minute absorption and scattering in tissue compared to optical methods. FONT has increased penetration depths compared to fluorescence imaging with optical contrast and can carry out all of this completely non-invasively (no removal of scalp or skull). Endogenous chromophores such hemoglobin or lipids present in the tissue differentially absorb light across the spectrum of light. For example, the peak of oxygenated hemoglobin is 575 nm whilst for lipids this is 1210 nm. FONT can further take advantage of this to spectrally unmix components within the tissue.[8] A vast array of fluorescent GECIs & GEVIs exist, but none have been optimized for FONT. Previously, FONT was used to detect GCaMP5 transients in zebrafish but this had yet to be investigated in mice.[9]

The FONT system at Prof. Razanskys lab has a field of view of over  $1\text{cm}^3$ , and an imaging rate of 1.6 KHz.[10] Laser pulses were delivered from a single fibre at the centre of the transducer limiting illumination to one half of the FOV. This limitation was overcome by delivering light uniformly to the FOV from seven fibres mounted in a 3D printed waterproof chamber. The chamber ensured coupling medium (water) for US waves and optimally held the transducer and fibres in place. The system could capture the entire volume (as opposed to half) and internal structures of both the mouse brain and heart with a single laser pulse. This setup was published in the Journal of Biophotonics and is outlined in [Chapter 2](#). [11] The developed system was then used to image the fluorescent GECI, GCaMP6f (neuronal calcium activity) in an isolated mouse brain model with activity being evoked using a seizure inducing drug, pentylenetetrazol (PTZ). [12]

Having established FONTs *ex vivo* capabilities, *in vivo* applications were assessed. Firstly, non-invasive monitoring of hemodynamic activity was investigated. Electrical stimuli were applied to the hind paws of mice with FONT achieving non-invasive 5D (3D, time, multispectral) mapping of the evoked hemodynamic response. Mapping was achieved of cortical hemodynamic responses induced with electrical paw stimuli for all hemodynamic components i.e. oxy-, deoxy- and total hemoglobin (HbO, HbR & HbT respectively). The somatosensory cortex of the mice, particularly the region responsible for hindpaw stimulation, showed elevated activation; the intensity of this activation was found to be statistically significant over all other analysed regions in the brain. These experiments gave a greater insight into how hemoglobin, and how hemodynamic activity can mask GCaMP6f signals, and are outlined in [Chapter 3](#).

Building on the experience gained from hemodynamic imaging with FONT, the detection of GCaMP6f and GCaMP6s transients were investigated are now published in Nature Biomedical Engineering.[13] This was a first of its kind with FONT showing an increased spatiotemporal resolution and FOV compared to fluorescence. The non-invasive capabilities of FONT and the transgenic GCaMP expression highlight the potential for longitudinal (repeated over days or weeks) imaging. To further assess the sensitivity of FONT, a similar system at Prof. Shy Shoham's lab at New York University (NYU) successfully imaged sparsely labelled GCaMP6s/f mice (10% of the expression of previous mice). In line with a publication based dissertation and that these results are unpublished this is only briefly mentioned in the conclusion & outlook.

Experience with these experiments led me to realise that the main disadvantage with imaging transgenic fluorescent proteins with FONT was the absorption wavelength of blue (488nm) light. This resulted in the blood vessels being highly visible in all images which was useful for registration of the data to brain atlases but made detecting GCaMP6 signals cumbersome. Additionally, the inherent noise in the FONT system (~2%) and the low delta (signal change upon activation) in GECIs and GEVIs were limiting factors for FONT. The ideal indicator would have a high delta and absorption in the near infrared (NIR) spectrum of light. Luckily, in collaboration with Prof. Robert Campbell and Prof. Ed Boyden, it was possible to successfully test the first near NIR based GECI (NIR-GECO1) *in vivo*. Detection of NIR-GECO1 transients was achieved via non-invasive mesoscale fluorescence imaging. However, the low delta of the protein seen in fluorescence did not render it suitable for FONT (despite some efforts). This (fluorescent) work was published in Nature Methods and is outlined in [Chapter 4](#). [14] Whilst not suitable for FONT, both forms of the protein (calcium bound & calcium free) can be spectrally distinguished with FONT (unpublished however, included here) but *in vivo* transients could not. Concurrently, the GEVI BUTTERFLY 1.2 (absorbing in the visible at 488 nm) was tested for suitability for FONT but it too suffered from too small a delta in fluorescence imaging. This is mentioned in the final part of the dissertation.

This project has now established a clear and solid platform from which FONT can be used for electrophysiological imaging in the future. Solutions for challenges such as inherent system noise, scattering of visible light, physiological parameters, development and testing of novel proteins and suitable validation mechanisms have been overcome paving the way for a suitable indicator. During the course of this thesis many first of their kinds were achieved such as mapping electrical stimulus evoked hemodynamic activity, detecting direct neuronal activity with FONT via calcium signaling and testing the first NIR GECI.

## References

1. Ferrea, E., et al., *Large-scale, high-resolution electrophysiological imaging of field potentials in brain slices with microelectronic multielectrode arrays*. *Frontiers in neural circuits*, 2012. **6**: p. 80.
2. Dana, H., et al., *Thy1-GCaMP6 transgenic mice for neuronal population imaging in vivo*. *PloS one*, 2014. **9**(9): p. e108697.
3. Bando, Y., et al., *Genetic voltage indicators*. *BMC biology*, 2019. **17**(1): p. 71.
4. Akemann, W., et al., *Two-photon voltage imaging using a genetically encoded voltage indicator*. *Scientific reports*, 2013. **3**: p. 2231.
5. Sanderson, M.J., et al., *Fluorescence microscopy*. *Cold Spring Harbor Protocols*, 2014. **2014**(10): p. pdb. top071795.
6. Nimmerjahn, A., *Optical window preparation for two-photon imaging of microglia in mice*. *Cold Spring Harbor Protocols*, 2012. **2012**(5): p. pdb. prot069286.
7. Deán-Ben, X.L., et al., *Functional optoacoustic neuro-tomography for scalable whole-brain monitoring of calcium indicators*. *Light: Science & Applications*, 2016. **5**(12): p. e16201.
8. Deán-Ben, X., et al., *Advanced optoacoustic methods for multiscale imaging of in vivo dynamics*. *Chemical Society Reviews*, 2017. **46**(8): p. 2158-2198.
9. Deán-Ben, X.L., et al., *Functional optoacoustic neuro-tomography of calcium fluxes in adult zebrafish brain in vivo*. *Optics letters*, 2017. **42**(5): p. 959-962.
10. ÖZBEK, A., X.L. DEÁN-BEN, and D. RAZANSKY, *Optoacoustic imaging at kilohertz volumetric frame rates*. *Optica*, 2018. **in press**.
11. Mc Larney, B., et al., *Uniform light delivery in volumetric optoacoustic tomography*. *Journal of Biophotonics*, 2019. **12**(6): p. e201800387.
12. Gottschalk, S., et al., *Isolated Murine Brain Model for Large-Scale Optoacoustic Calcium Imaging*. *Frontiers in neuroscience*, 2019. **13**: p. 290.
13. Gottschalk, S., et al., *Rapid volumetric optoacoustic imaging of neural dynamics across the mouse brain*. *Nature Biomedical Engineering*, 2019. **3**(5): p. 392-401.
14. Qian, Y., et al., *A genetically encoded near-infrared fluorescent calcium ion indicator*. *Nature Methods*, 2019.

## List of Publications

1. Qian, Y.\*, Piatkevich, K. D.\*, **Mc Larney, B.\***, Abdelfattah, A. S., Mehta, S., Murdock, M. H., ... & Wu, J. (2019). A genetically encoded near-infrared fluorescent calcium ion indicator. *Nature methods*, 16(2), 171.
2. **Mc Larney, B.\***, Rebling, J.\*, Chen, Z., Deán-Ben, X. L., Gottschalk, S., & Razansky, D. (2019). Uniform light delivery in volumetric optoacoustic tomography. *Journal of biophotonics*, e201800387.
3. **Mc Larney, B.\***, Hutter, M.\*, Degtyaruk, O., Deán-Ben, X. L., Razansky, D. (2020) Monitoring of stimulus evoked murine somatosensory cortex hemodynamic activity with five-dimensional functional optoacoustic neuro-tomography. *Frontiers in Neuroscience Brain imaging methods*, 14, p.536.

\* denotes equal contribution

The methodologies and systems used in these papers were also part of further publications. For these publications I am not the first author, but they will be mentioned in the discussion for a more comprehensive understanding of the work carried out in this thesis.

4. Deán-Ben, X. L., Gottschalk, S., **Mc Larney, B.**, Shoham, S., & Razansky, D. (2017). Advanced optoacoustic methods for multiscale imaging of in vivo dynamics. *Chemical Society Reviews*, 46(8), 2158-2198.
5. Gottschalk, S., Degtyaruk, O., **Mc Larney, B.**, Rebling, J., Hutter, M. A., Deán-Ben, X. L., ... & Razansky, D. (2019). Rapid volumetric optoacoustic imaging of neural dynamics across the mouse brain. *Nature biomedical engineering*, 3(5), 392.
6. Gottschalk, S., Degtyaruk, O., **Mc Larney, B.**, Rebling, J., Ben, D., Luis, X., ... & Razansky, D. (2019). Isolated Murine Brain Model for Large-Scale Optoacoustic Calcium Imaging. *Frontiers in neuroscience*, 13, 290.
7. Chen, Z., **Mc Larney, B.**, Rebling, J., Deán-Ben, X. L., Gottschalk, S., & Razansky, D. (2018, November). Multifocal structured illumination fluorescence microscopy with large field-of-view and high spatio-temporal resolution. In *Advanced Optical Imaging Technologies* (Vol. 10816, p. 1081606). International Society for Optics and Photonics.
8. Degtyaruk, O., **Mc Larney, B.**, Deán-Ben, X. L., Shoham, S., & Razansky, D. (2019, June). Optoacoustic Calcium Imaging of Deep Brain Activity in an Intracardially Perfused Mouse Brain Model. In *Photonics* (Vol. 6, No. 2, p. 67). Multidisciplinary Digital Publishing Institute.
9. Chen, Z., **Mc Larney, B.**, Rebling, J., Deán-Ben, X.L., Zhou, Q., Gottschalk, S., Razansky, D. (2019, November). High-Speed Large-Field Multifocal Illumination Fluorescence Microscopy. In *Laser Photonics & Reviews*.

Whilst publications were an integral part of this work it was also important to communicate these results to the wider scientific community at conferences and scientific meetings. Below is the list of presentations I carried out to achieve this.

1. **Benedict Mc Larney**, Johannes Rebling, Zhenyue Chen, Xosé Luís Deán-Ben, Daniel Razansky, (2018, February) Poster Presentation: *Uniform light delivery for quantitative volumetric optoacoustic tomography*, SPIE Photonics West, San Francisco, USA.
2. **Benedict Mc Larney**, Daniel Razansky, (2019, April) Invited Talk: *Making Light Sound – Advances in Multi-Spectral Optoacoustic Tomography*, American Institute of Ultrasound in Medicine, Florida, USA.
3. **Benedict Mc Larney**, Sven Gottschalk, Alexei Degtyaruk, Johannes Rebling, Magdalena Hutter, Xosé Luis Dean-Ben, Daniel Razansky, (2019, April) Poster Presentation: *Rapid volumetric imaging of calcium dynamics across the mouse brain*, NIH Brain Investigators Meeting, Washington D.C., USA.
4. **Benedict Mc Larney**, Sven Gottschalk, Alexei Degtyaruk, Johannes Rebling, Magdalena Hutter, Xosé Luis Dean-Ben, Daniel Razansky, (2019, April) Invited Talk: *Rapid volumetric imaging of calcium dynamics across the mouse brain*, OSA Biophotonics Congress: Optics in the Life Sciences, Tucson, U.S.A.
5. **Benedict Mc Larney**, Sven Gottschalk, Alexei Degtyaruk, Johannes Rebling, Magdalena Hutter, Xosé Luis Dean-Ben, Daniel Razansky, (2019, July) Invited Talk: *Rapid volumetric imaging of calcium dynamics across the mouse brain*, IEEE 41<sup>st</sup> International Engineering in Medicine and Biology Conference, Berlin, Germany.

# 1. Introduction

## 1.1 Fluorescence imaging

Imaging in its various forms is an essential and integral component for the life sciences and medicine.[1-3] Imaging is the process of capturing data from an object and storing this information as discrete values. Medical and biological imaging focuses on capturing information from the internal structures of organisms such as organs and bones.[4] This area of imaging focuses on the interaction of the electromagnetic spectrum (x-rays, light to radio waves) with an organism to reveal information, see Figure 1.1 A). All of this is done to reveal more information about what is happening in an organism from both an anatomical and functional standpoint.[4] In medical imaging a form of electromagnetism is selected, directed toward the object and then its interactions with this object are detected with a flat (2D) method of detection, see Figure 1.1 B).[4, 5] Detection is carried out in various forms e.g. x-rays passing through a body or ultrasound (US) being reflected back to a detector.[5-7] The detected information is then converted to electronic signals and stored as values to make an image on a computer. By rotating the detector around an object, tomographic (2D slices) images can be generated.[8] Acquiring data in the same manner along an axis (translation of the acquisition method or object being imaged) can then be used to build an array of slices resulting in 3D or volumetric tomography.[9] Imaging in general, has evolved from the simple prehistoric drawings on caves, learning how to draw with perspective in the Renaissance and to capturing images from the outside and inside of various objects.[4, 10, 11] Today, imaging can be performed with smartphones with profound implications. For example, phones can be used to capture 3D images that are then used to design prosthetics.[12] Instead of 2D drawings and representations, 3D visualization and imaging can enable a more in depth analysis of an object and in turn, reveal more information. Information is at the heart of science, engineering, and medicine. Before the process of building 3D images from 2D ones is clarified, it is essential to identify and explain the main methods which were used in this dissertation. Both methods centered around the utilization of the electromagnetic spectrum for imaging. The first method that will be discussed is fluorescence. For the applications in this dissertation this method of imaging relies upon the visible spectrum of light (400 – 700 nm), see Figure 1.1 A). All fluorescence imaging carried out in this dissertation employed a common 2D method of imaging with an optical camera.

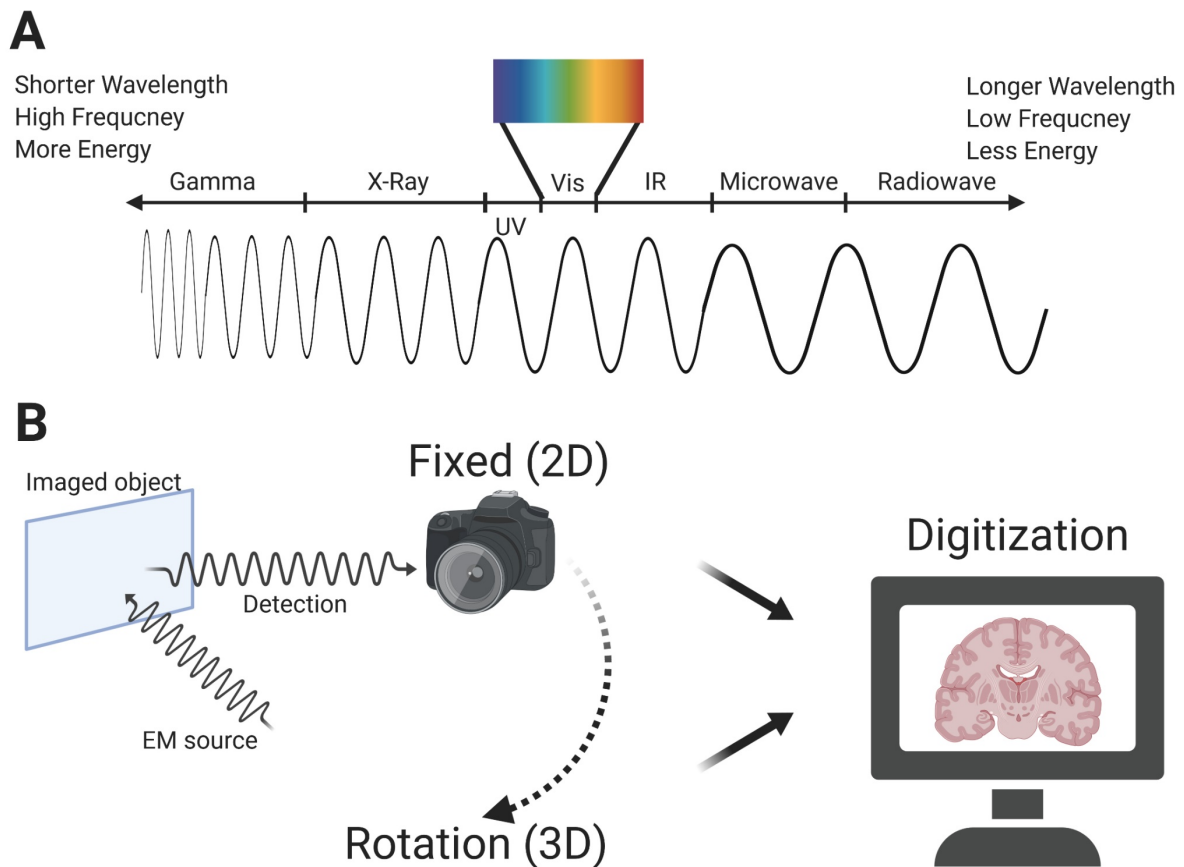


**Figure 1.1 The electromagnetic spectrum and image formation.** A) The electromagnetic (EM) spectrum including those commonly found in medical imaging such as X-rays and the visible spectrum of light. B) Image formation of an object using a detector. An EM source is used to interrogate the object. Reflected or transmitted EM spectrum signals are recorded by the detector converting the physical signals to digital ones. If the detector remains fixed a 2D image is formed, rotating the object or detector along an axis generates a 3D image. The digitized signals are then output to a computer where they can be stored. Image made with Biorender.com.

Fluorescence imaging is a light based (optical) method of imaging with the added advantage of using non-ionizing radiation. This means avoiding putting the sample or patient at risk of tissue damage. It has a long history from concept to current applications in basic research and medical imaging including (but not limited to) antibody labelling, cell structure identification and fluorescence guided surgery.[1, 13-16] The physical process commonly employed in research is explained in Figure 1.2. In short, a wavelength of light ( $\lambda_{exc}$ ) is shone onto a substance e.g. green fluorescent protein (GFP).[17] This light causes electrons in the GFP to be excited to a higher state, where some of the energy is released as heat (through vibrational relaxation). After this, the electron returns to its original energy level and in the process of it doing so, it releases its remaining energy as light ( $\lambda_{em}$ ). The emitted light has less energy than the excitation light, therefore  $\lambda_{em}$  is a longer (weaker) wavelength than  $\lambda_{exc}$ . In the case of GFP, the most commonly used fluorescent protein, 488nm (blue) light is used to excite fluorescence which emits at 532nm (green).[18-20] The difference between the two wavelengths is known as a Stokes shift and the entire process was first described by Aleksander Jabłoński.[13, 21] Numerous animals are able to create similar light emissions (luminescence not fluorescence) but humans have only caught up in the last century thanks to lasers and protein engineering.[22, 23] Fluorescent imaging has now emerged as an integral

part of basic research. It is used in microscopy for immunohistochemistry and various animals have been genetically engineered to express a range of fluorescent proteins covering the visible spectrum of light.[24-27] Fluorescence imaging is now a robust and reliable imaging method, producing rich contrast across a range of spatiotemporal resolutions.[28-32]

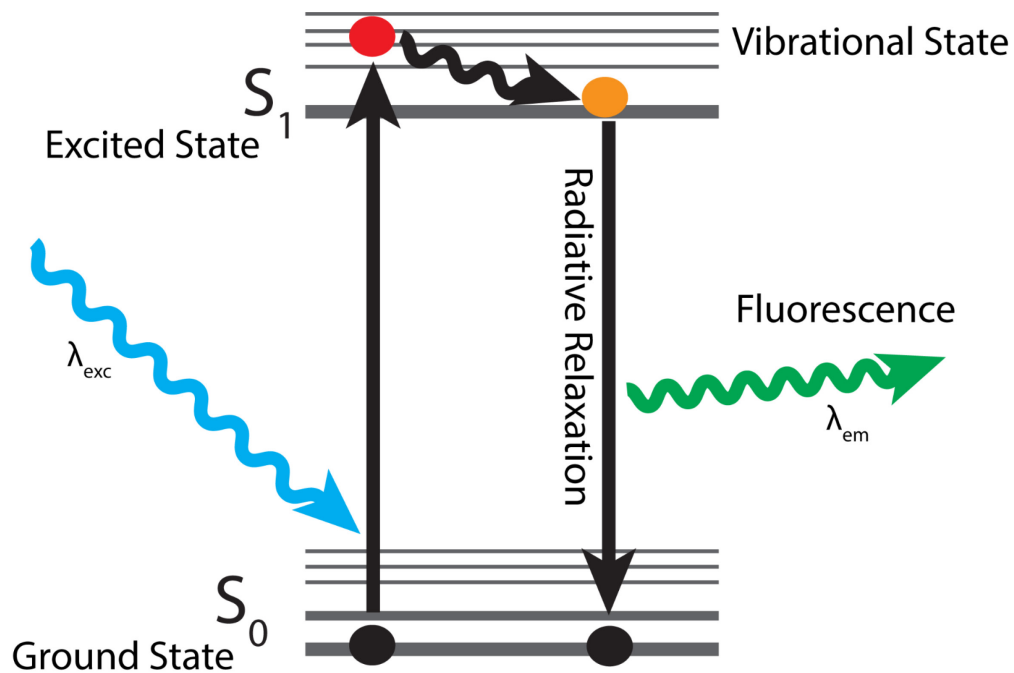


**Figure 1.2 Fluorescence Jablonski diagram.** The process of fluorescence which follows how an electron reaches an excited state via absorbed energy. Once the electron reaches an excited (higher state), it undergoes vibration and energy is lost via heat. Finally, the electron releases the remaining energy as fluorescent light, and it returns to its ground state.[13, 21]

A quick and robust form of fluorescence imaging is a 2D modality known as wide-field fluorescence imaging and is described in Figure 1.3 A). Here, an objective lens is used to focus all the fluorescent light originating from a sample onto a 2D detector. The configuration of this lens and detector will determine whether imaging is carried out in the micro-, meso- or macro-scale (spatial resolution of the system). The system can only focus on a single plane with a determined depth of field. The depth of field of the plane refers to the amount of an object in the Z (or depth) direction from which collected light will be in focus; it has a direct effect on the axial resolution of a system.[33] In a setup like that in Figure. 1.3 A), non-focused light from planes above and below will also be detected and will affect the imaging quality. A confocal setup can be used to mitigate against this see. Fig 1.3 B), but was not used during this work.[34] A confocal system works by only illuminating the sample at either a very specific point (two-photon) within the sample (Z axis) or only detecting light from only a single plane (along the Z axis) and removing out of focus light using pinholes.[34] Confocal systems therefore require point by point (raster) scanning to generate an image which results in high resolution images.[34] Further optical advancements have enabled illumination of entire planes within a sample via single plane illumination microscopy (SPIM).[35] However, in these cases the data capturing process is carried out by moving the 2D imaging plane across a small FOV (such as *Drosophila* embryos) within a 3D object and digitally compiling the single slices (images) into a 3D volume.[36-40] Imaging in this manner is time consuming (low temporal resolution) with increased data loads over relatively small FOVs, on the order of mm's. This is especially true when acquiring 3D data with high-speed imaging (multiple volumes per second).[41] The sample macro fluorescent setup which is most relevant to this dissertation is

outlined in Figure 1.3 A). In this case GFP is used as an example, requiring 488nm excitation laser light and emitting fluorescence at 532nm. Wide-field fluorescence imaging is capable of imaging a larger FOV in 2D at high spatiotemporal resolution, however this comes with the lack of any depth penetration (imaging along the Z axis) and is often of lower spatial resolution than confocal or SPIM methods.[30, 42, 43] The knock-on effect of this means that in comparison to confocal imaging and SPIM, detected signals come from the entire volume and are summed at detection. As a result, it is most suited to thin, non-scattering samples and situations with high motion, such as live organism imaging.[44, 45]

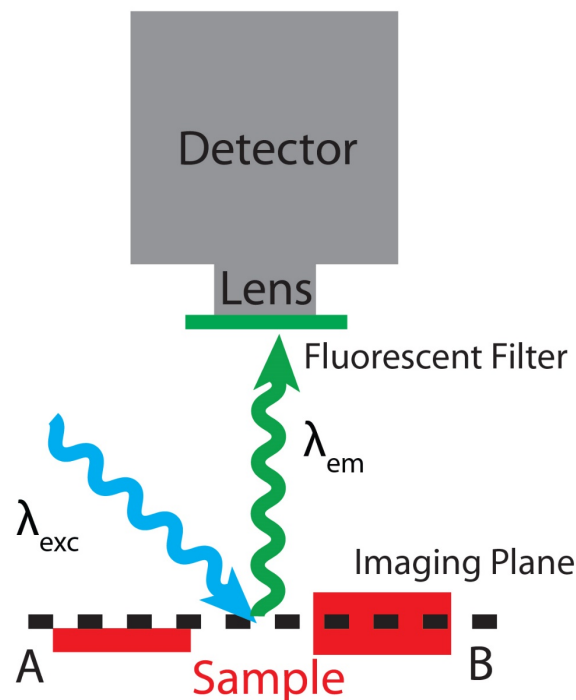


**Figure 1.3 The most common forms of fluorescent imaging.** The same physical process as described in Figure 1.1 is employed in combination with suitable equipment. This includes a suitable detector (camera) coupled with a lens and suitable fluorescent filter. The filter ensures only the emitted fluorescent light is detected. In A) the imaging plane (dotted line) is fixed in a wide field setup. Here signals from below the surface of the object are detected as well as those within the plane. In B) the imaging plane is scanned up and down through the sample (confocal microscopy, two-photon, SPIM). It is notable that in both cases images are acquired in a 2D manner and in B) can be stacked to generate a 3D image.

There are two main physical limitations when imaging with a solely light-based method like fluorescence. Those are the absorption and scattering that both the excitation light and emitted fluorescence will be subject to by tissues and their components. Both of these are more prevalent in the visible regime of light, see Figure 1.4.[46, 47] Absorption reduces the amount of energy a photon has whilst it travels and scattering causes the travel of the photon to diverge randomly.[48, 49] For approximately the first 300 microns in tissues, photons of visible light can travel in a straight line and are known as ballistic photons.[50, 51] This is the case for light used to excite fluorescence or emitted by fluorescence. These photons carry a high amount of information and can be readily recovered to produce diffraction limited (high resolution) images. However, after this short 300  $\mu\text{m}$  distance, the photons enter a diffusive regime and diverge along random paths from their point of entry or generation.[52] It is very difficult to overcome these processes for either the sent photons or the excited fluorescent

photons. The absorption and scattering of light negatively effects image quality in terms of resolution, contrast, achievable imaging depths and ultimately the accuracy of imaging and collected data.[53] Hence, overcoming the limitation imposed by the scattering and absorption properties of tissues has been the subject of intense research, developing numerous modelling methods, imaging techniques and even tissue clearing.[54-59] Advanced optical setups like two and three photon imaging use longer excitation wavelengths outside of the visible regime.[34, 60] These have the advantage of deeper penetration, since longer excitation wavelengths are less affected by scattering or absorption by tissues (Figure 1.4).[61] However, detection is still of emitted fluorescent photons in the visible regime, which are highly affected by scattering and absorption.[62, 63] In cases where laser power is not an issue e.g. phantom or fixed sample imaging where burning and heating due to exposure to IR wavelengths can be ignored, fluorescence can be generated at planes above the focal plane reducing signal to noise ratio (SNR) and blurring of images.[60, 62] Ultimately, this means that when trying to overcome light absorption and scattering there are inherent physical limits to the achievable depths with two and three photon fluorescent microscopy and currently, these limits are being reached. These limits result in being unable to image deep seated tissues especially in e.g. the brain, a highly scattering and absorbing tissue.[61] In turn, this limits data acquisition to cortical structures and small areas (cubic millimeters) of the brain.[64] Further disadvantages of fluorescence imaging often lie in trade-offs between speed, resolution, FOV and achievable depth penetration.

Whilst robust, fluorescence imaging has many drawbacks, namely reduced penetration depths due to the absorption and scattering of visible light in tissues. This is especially noticeable when trying to image over a large scale in scattering tissues such as the entire murine brain or heart. Accordingly, there is a growing need for a modality which can provide similar resolution, contrast, and acquisition speeds over larger fields of view (FOVs). This dissertation will use macroscale setups like that shown in Figure 1.2 A). In this case, fluorescence imaging will be used as a tool to validate results from optoacoustic (OA) imaging.

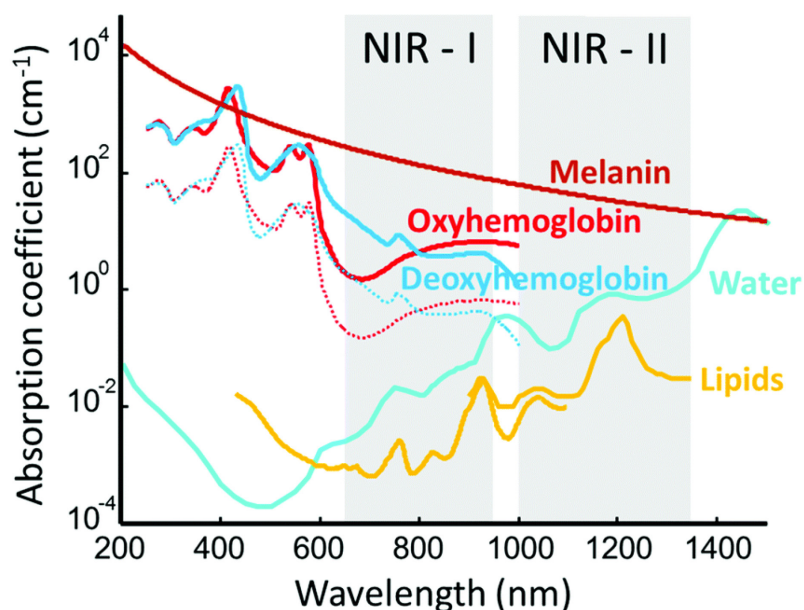


**Figure 1.4 The absorption spectra of various endogenous components of mammalian tissues.** Higher absorption of light (~2 orders of magnitude) is shown in the visible spectrum in comparison with the NIR-I wavelengths. Reproduced via creative commons from Dean-Ben *et al* [53].

## References

- [1] F.-J. Kao, G. Keiser, and A. Gogoi, *Advanced Optical Methods for Brain Imaging*. Springer, 2019.
- [2] S. K. Shrivastava and P. Dubey, "Importance of optical imaging and radioactive isotopes in cancer therapy: Current Needs and Future aspects," *International Journal of Pharmacy & Life Sciences*, vol. 10, no. 3, 2019.
- [3] X. Dang *et al.*, "Deep-tissue optical imaging of near cellular-sized features," *Scientific reports*, vol. 9, no. 1, p. 3873, 2019.
- [4] W. R. Hendee and E. R. Ritenour, *Medical imaging physics*. John Wiley & Sons, 2003.
- [5] J. T. Bushberg and J. M. Boone, *The essential physics of medical imaging*. Lippincott Williams & Wilkins, 2011.
- [6] P. N. Wells and H.-D. Liang, "Medical ultrasound: imaging of soft tissue strain and elasticity," *Journal of the Royal Society Interface*, vol. 8, no. 64, pp. 1521-1549, 2011.
- [7] L. Shamir, S. Ling, S. Rahimi, L. Ferrucci, and I. G. Goldberg, "Biometric identification using knee X-rays," *International journal of biometrics*, vol. 1, no. 3, p. 365, 2009.
- [8] T. M. Buzug, "Computed tomography," in *Springer Handbook of Medical Technology*: Springer, 2011, pp. 311-342.
- [9] E. Seeram, *Computed Tomography-E-Book: Physical Principles, Clinical Applications, and Quality Control*. Elsevier Health Sciences, 2015.
- [10] M. P. Gray, "Cave art and the evolution of the human mind," 2010.
- [11] S. Y. Edgerton, *The mirror, the window, and the telescope: How Renaissance linear perspective changed our vision of the universe*. Cornell University Press, 2009.
- [12] R. Salazar-Gamarra, R. Seelaus, J. V. L. da Silva, A. M. da Silva, and L. L. Dib, "Monoscopic photogrammetry to obtain 3D models by a mobile device: a method for making facial prostheses," *Journal of Otolaryngology-Head & Neck Surgery*, vol. 45, no. 1, p. 33, 2016.
- [13] A. Jablonski, "Efficiency of anti-Stokes fluorescence in dyes," *Nature*, vol. 131, no. 3319, p. 839, 1933.
- [14] G. D. Luker and K. E. Luker, "Optical imaging: current applications and future directions," *Journal of Nuclear Medicine*, vol. 49, no. 1, pp. 1-4, 2008.
- [15] Y. Matsuura, M. Mun, J. Ichinose, M. Nakao, K. Nakagawa, and S. Okumura, "Recent fluorescence-based optical imaging for video-assisted thoracoscopic surgery segmentectomy," *Annals of translational medicine*, vol. 7, no. 2, 2019.
- [16] J. Rao, A. Dragulescu-Andrasi, and H. Yao, "Fluorescence imaging in vivo: recent advances," *Current opinion in biotechnology*, vol. 18, no. 1, pp. 17-25, 2007.
- [17] M. Zimmer, "GFP: from jellyfish to the Nobel prize and beyond," *Chemical Society Reviews*, vol. 38, no. 10, pp. 2823-2832, 2009.
- [18] T. Misteli and D. L. Spector, "Applications of the green fluorescent protein in cell biology and biotechnology," *Nature biotechnology*, vol. 15, no. 10, p. 961, 1997.
- [19] B. A. Pollok and R. Heim, "Using GFP in FRET-based applications," *Trends in cell biology*, vol. 9, no. 2, pp. 57-60, 1999.
- [20] M. Chalfie and S. R. Kain, *Green fluorescent protein: properties, applications and protocols*. John Wiley & Sons, 2005.
- [21] J. R. Lakowicz, *Principles of fluorescence spectroscopy*. Springer Science & Business Media, 2013.

- [22] J. L. Kinsey, "Laser-induced fluorescence," *Annual Review of Physical Chemistry*, vol. 28, no. 1, pp. 349-372, 1977.
- [23] R. Heim and R. Y. Tsien, "Engineering green fluorescent protein for improved brightness, longer wavelengths and fluorescence resonance energy transfer," *Current biology*, vol. 6, no. 2, pp. 178-182, 1996.
- [24] J. Livet *et al.*, "Transgenic strategies for combinatorial expression of fluorescent proteins in the nervous system," *Nature*, vol. 450, no. 7166, p. 56, 2007.
- [25] P. G. Hirrlinger *et al.*, "Expression of reef coral fluorescent proteins in the central nervous system of transgenic mice," *Molecular and Cellular Neuroscience*, vol. 30, no. 3, pp. 291-303, 2005.
- [26] Y. A. Pan, J. Livet, J. R. Sanes, J. W. Lichtman, and A. F. Schier, "Multicolor Brainbow imaging in zebrafish," *Cold Spring Harbor Protocols*, vol. 2011, no. 1, p. pdb. prot5546, 2011.
- [27] S. Hampel, P. Chung, C. E. McKellar, D. Hall, L. L. Looger, and J. H. Simpson, "Drosophila Brainbow: a recombinase-based fluorescence labeling technique to subdivide neural expression patterns," *Nature methods*, vol. 8, no. 3, p. 253, 2011.
- [28] L. Schermelleh *et al.*, "Super-resolution microscopy demystified," *Nature cell biology*, vol. 21, no. 1, p. 72, 2019.
- [29] R. Zhang *et al.*, "Macroscale fluorescence imaging against autofluorescence under ambient light," *Light: Science & Applications*, vol. 7, no. 1, p. 97, 2018.
- [30] Z. Chen *et al.*, "High-Speed Large-Field Multifocal Illumination Fluorescence Microscopy," *Laser & Photonics Reviews*, p. 1900070, 2019.
- [31] S. Stavrakis, G. Holzner, J. Choo, and A. DeMello, "High-throughput microfluidic imaging flow cytometry," *Current opinion in biotechnology*, vol. 55, pp. 36-43, 2019.
- [32] G. Follain, L. Mercier, N. Osmani, S. Harlepp, and J. G. Goetz, "Seeing is believing—multi-scale spatio-temporal imaging towards in vivo cell biology," *J Cell Sci*, vol. 130, no. 1, pp. 23-38, 2017.
- [33] W. E. Ortyn *et al.*, "Extended depth of field imaging for high speed cell analysis," *Cytometry Part A: The Journal of the International Society for Analytical Cytology*, vol. 71, no. 4, pp. 215-231, 2007.
- [34] A. Diaspro, *Confocal and two-photon microscopy: foundations, applications, and advances*. Wiley-Liss New York, 2002.
- [35] J. M. Girkin and M. T. Carvalho, "The light-sheet microscopy revolution," *Journal of Optics*, vol. 20, no. 5, p. 053002, 2018.
- [36] R. Galland, G. Greci, A. Aravind, V. Viasnoff, V. Studer, and J.-B. Sibarita, "3D high- and super-resolution imaging using single-objective SPIM," *Nature methods*, vol. 12, no. 7, p. 641, 2015.
- [37] E. Faure *et al.*, "A workflow to process 3D+ time microscopy images of developing organisms and reconstruct their cell lineage," *Nature communications*, vol. 7, p. 8674, 2016.
- [38] S. Preibisch, S. Saalfeld, J. Schindelin, and P. Tomancak, "Software for bead-based registration of selective plane illumination microscopy data," *Nature methods*, vol. 7, no. 6, p. 418, 2010.
- [39] J. Huisken, J. Swoger, F. Del Bene, J. Wittbrodt, and E. H. Stelzer, "Optical sectioning deep inside live embryos by selective plane illumination microscopy," *Science*, vol. 305, no. 5686, pp. 1007-1009, 2004.

- [40] P. Fei *et al.*, "Subvoxel light-sheet microscopy for high-resolution high-throughput volumetric imaging of large biomedical specimens," *Advanced Photonics*, vol. 1, no. 1, p. 016002, 2019.
- [41] E. G. Reynaud, J. Peychl, J. Huisken, and P. Tomancak, "Guide to light-sheet microscopy for adventurous biologists," *Nature methods*, vol. 12, no. 1, p. 30, 2014.
- [42] A. Nygren, C. Kondo, R. B. Clark, and W. R. Giles, "Voltage-sensitive dye mapping in Langendorff-perfused rat hearts," *American Journal of Physiology-Heart and Circulatory Physiology*, vol. 284, no. 3, pp. H892-H902, 2003.
- [43] R. Jaimes *et al.*, "Lights, camera, path splitter: a new approach for truly simultaneous dual optical mapping of the heart with a single camera," *BMC biomedical engineering*, vol. 1, no. 1, p. 25, 2019.
- [44] G. Silasi, D. Xiao, M. P. Vanni, A. C. Chen, and T. H. Murphy, "Intact skull chronic windows for mesoscopic wide-field imaging in awake mice," *Journal of neuroscience methods*, vol. 267, pp. 141-149, 2016.
- [45] Y. Ma *et al.*, "Wide-field optical mapping of neural activity and brain haemodynamics: considerations and novel approaches," *Philosophical Transactions of the Royal Society B: Biological Sciences*, vol. 371, no. 1705, p. 20150360, 2016.
- [46] S. L. Jacques, "Optical properties of biological tissues: a review," *Phys Med Biol*, vol. 58, no. 11, pp. R37-61, Jun 7 2013.
- [47] S. Johnsen and E. A. Widder, "The physical basis of transparency in biological tissue: ultrastructure and the minimization of light scattering," *Journal of theoretical biology*, vol. 199, no. 2, pp. 181-198, 1999.
- [48] B. Wilson and G. Adam, "A Monte Carlo model for the absorption and flux distributions of light in tissue," *Medical physics*, vol. 10, no. 6, pp. 824-830, 1983.
- [49] M. Xu and R. R. Alfano, "Fractal mechanisms of light scattering in biological tissue and cells," *Optics letters*, vol. 30, no. 22, pp. 3051-3053, 2005.
- [50] M. G. Tanner *et al.*, "Ballistic and snake photon imaging for locating optical endomicroscopy fibres," *Biomedical Optics Express*, vol. 8, no. 9, pp. 4077-4095, 2017/09/01 2017.
- [51] R. Elaloufi, R. Carminati, and J.-J. Greffet, "Diffusive-to-ballistic transition in dynamic light transmission through thin scattering slabs: a radiative transfer approach," *JOSA A*, vol. 21, no. 8, pp. 1430-1437, 2004.
- [52] A. Yaroshevsky, Z. Glasser, E. e. Granot, and S. Sternklar, "Transition from the ballistic to the diffusive regime in a turbid medium," *Optics letters*, vol. 36, no. 8, pp. 1395-1397, 2011.
- [53] X. L. Dean-Ben, S. Gottschalk, B. Mc Larney, S. Shoham, and D. Razansky, "Advanced optoacoustic methods for multiscale imaging of in vivo dynamics," (in English), *Chemical Society Reviews*, vol. 46, no. 8, pp. 2158-2198, Apr 21 2017.
- [54] J. Dawson *et al.*, "A theoretical and experimental study of light absorption and scattering by in vivo skin," *Physics in Medicine & Biology*, vol. 25, no. 4, p. 695, 1980.
- [55] M. G. Giacomelli and A. Wax, "Imaging beyond the ballistic limit in coherence imaging using multiply scattered light," *Optics express*, vol. 19, no. 5, pp. 4268-4279, 2011.
- [56] B. W. Pogue and M. S. Patterson, "Review of tissue simulating phantoms for optical spectroscopy, imaging and dosimetry," *Journal of biomedical optics*, vol. 11, no. 4, p. 041102, 2006.
- [57] K. Chung *et al.*, "Structural and molecular interrogation of intact biological systems," *Nature*, vol. 497, no. 7449, p. 332, 2013.

- [58] F. Martelli, T. Binzoni, A. Pifferi, L. Spinelli, A. Farina, and A. Torricelli, "There's plenty of light at the bottom: statistics of photon penetration depth in random media," *Scientific reports*, vol. 6, p. 27057, 2016.
- [59] A. Badon, D. Li, G. Lerosey, A. C. Boccara, M. Fink, and A. Aubry, "Smart optical coherence tomography for ultra-deep imaging through highly scattering media," *Science Advances*, vol. 2, no. 11, p. e1600370, 2016.
- [60] K. Guesmi *et al.*, "Dual-color deep-tissue three-photon microscopy with a multiband infrared laser," *Light: Science & Applications*, vol. 7, no. 1, p. 12, 2018.
- [61] S. L. Jacques, "Optical properties of biological tissues: a review," *Physics in Medicine & Biology*, vol. 58, no. 11, p. R37, 2013.
- [62] A. Diaspro and M. Robello, "Two-photon excitation of fluorescence for three-dimensional optical imaging of biological structures," *Journal of Photochemistry and Photobiology B: Biology*, vol. 55, no. 1, pp. 1-8, 2000.
- [63] D. G. Ouzounov *et al.*, "In vivo three-photon imaging of activity of GCaMP6-labeled neurons deep in intact mouse brain," *Nature methods*, vol. 14, no. 4, p. 388, 2017.
- [64] T. Wang *et al.*, "Three-photon imaging of mouse brain structure and function through the intact skull," *Nature methods*, vol. 15, no. 10, pp. 789-792, 2018.

## 1.2 Optoacoustic Tomography

Before diving into OA imaging, a brief background in ultrasound (US) is required as it is an integral part of OA imaging. It is important to note that at the heart of every OA system is an US transducer and the development of these transducers have been instrumental to the current success and future of OA.[1] Clinical and pre-clinical US imaging is carried out at frequencies above the hearing limit of humans (max 20 KHz) with a range of transducer (able to send and receive US waves) geometries, often highly sensitive at MHz frequencies.[2, 3] The major developments and research into US devices have transformed it from large and bulky prototypes to compact, hand held and reliable scientific instruments.[4-6] As a result, US is now a routine and dependable tool in clinics around the world with numerous applications from monitoring patient recovery, image guided surgery and even the characterization of gingivitis.[7-11] It is relatively inexpensive, fast (video rate imaging), non-ionizing and safe to use. In comparison to light-based methods, the penetration depth achieved with US in tissues is far larger (in the order of tens of centimeters) at the expense of resolution (in the order of millimeters). Both of which are directly related to the frequency of the transducer, as shown in Figure 1.5, with there being tradeoffs between resolution and penetration depths.[12, 13]

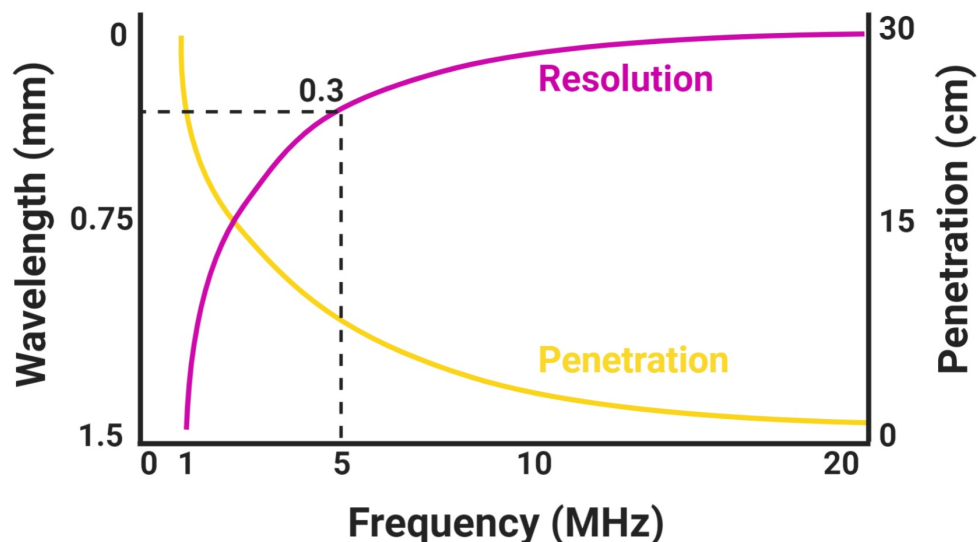


**Figure 1.5 Achievable resolution and penetration depth in tissue as a function of US frequency.** Highlighted is the transducer central frequency used in this work. Adapted from Otto *et al.*[13]

US imaging requires a transducer which sends an ultrasonic wave into tissue. Due to the mismatch in speed of sound in tissues (similar to water  $\sim 1480$  m/s) versus air ( $\sim 330$  m/s), gel (mainly water) is used as a coupling agent to allow ultrasonic waves to enter and exit tissue.[14, 15] The attenuation of ultrasound at 1 MHz ranges from 0.0022 dB/cm in water (tissues) versus 12 dB/cm in air and, the gel ensures US waves pass from one medium to the other without major distortions.[14, 15] Similarly to light based imaging, US waves can undergo reflection, refraction or scattering resulting in numerous artifacts.[16, 17] Subsequently, only components within the tissue which cause the wave to return back to the transducer are detected.[2] When the wave is reflected away from the transducer, no signal is detected and the signals that do return to the transducer are weaker than those emitted.[2] Through various reconstruction algorithms and depending on the transducer geometry, an image is then formed over a large FOV (tens of centimeters).[18]

Using techniques such as time of flight (the length of time between the US wave being emitted and then returning to the transducer) in combination with transducer geometry (2D or 3D) will determine the type of imaging that is performed.[19-21] This image can tell an experienced user numerous things about an object or tissue. Various structures such as ligaments, bone and even blood flow (Doppler) can be determined.[22, 23] Images can be recorded at KHz rates with US but they are severely lacking contrast in comparison with fluorescence imaging.[24] To compensate for this lack of contrast, exogenous contrast mechanisms can be added during imaging such as microbubbles (which resonate at the MHz frequencies used clinically), and these are currently being adopted in clinics.[25, 26] Whilst US is readily capable of imaging scattering tissues on a large scale, the lack of contrast has limited its application to murine research. It predominantly functions as a method for anatomical as opposed to functional imaging, with no current application to image electrophysiology.

Optoacoustics (OA, also known as photoacoustics and thermoacoustics) is an imaging method which can overcome the contrast issue faced by US and the penetration issues faced by fluorescence imaging.[27] This positions it as a possible solution to imaging over a large scale ( $\text{cm}^3$ ) through highly optically scattering tissues such as the murine brain.[27] Current applications in imaging electrophysiology with OA have been limited to proof of concept studies with exogenous dyes *in vivo*, posing difficulties for longitudinal imaging.[28, 29] OA in comparison to US and fluorescence imaging is a relatively new imaging technique. However, it has a long history dating back to Alexander Graham Bell who first described the phenomenon and has undergone accelerated development in recent years.[30, 31] Compared to fluorescence, OA has only been used for imaging in the past three decades, as shown by the timeline depicting the increase in publications of OA imaging (OAI), optoacoustic tomography (OAT) and fluorescence imaging per year in Figure 1.6. There has been a steady increase in the publications per year for OAI while papers focusing on OAT are more recent, dating from the mid-90s. From a practical perspective, OA employs two physical phenomena instead of one. This is in stark contrast to US or fluorescence imaging where sound or light are sent in and sound or light are detected, respectively. For OA imaging, short pulses (nanoseconds) of electromagnetism, light or radio frequencies (RF) are used to generate US waves.[32] The work in this dissertation has focused on OAI that is carried out via pulses of light and so RF will not be discussed. To apply OAI to biomedical imaging certain criteria must be met. One of which is that, light must be delivered to an object in predetermined pulses, less than ten nanoseconds in duration.[27]

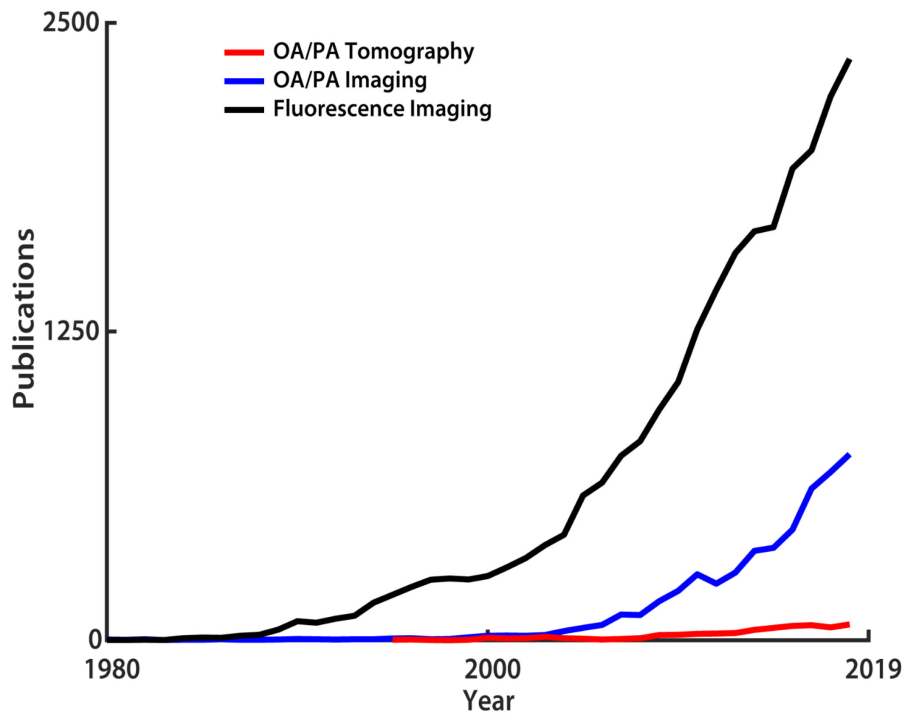


**Figure 1.6 Publications mentioning optoacoustic tomography, optoacoustic imaging and fluorescence imaging per year based on data from SCOPUS.** OA imaging has been around since the 1980s, but OAT is a more recent development from 1995. OAT makes up a small amount of current OA publications, both of which are small in comparison to fluorescence imaging.

When the pulse of light first arrives the object (e.g. an absorber on the molecular scale such as heme in hemoglobin) will absorb the energy from the light causing it to slightly heat up (millikelvin increase) and expand, converting the thermal energy to mechanic energy.[27, 33] This process is known as thermoelastic expansion and the efficiency at which an absorber can convert thermal to mechanic energy is known as its Grüneisen parameter.[34] As the light is only present for <10 ns, the heating stops, and the object will quickly cool and contract to its original size in a process known as thermoelastic contraction.[35] It is this rapid expansion and contraction of the absorber which produces US waves, hence the importance of short light pulses as shown in Figure 1.7. Additionally, as the light exposure is so short, the level of heating and expansion in terms of potential damage to the object is negligible.[36] The short pulses further allow the determination of signals based on time of detection and increase the achievable axial resolution.[34, 37] In comparison, fluorescence, especially wide-field imaging, uses continuous wave (CW) lasers which cause a slow heating of the tissue, and unless modulated, do not meet the requirements to produce US waves.[33, 38]

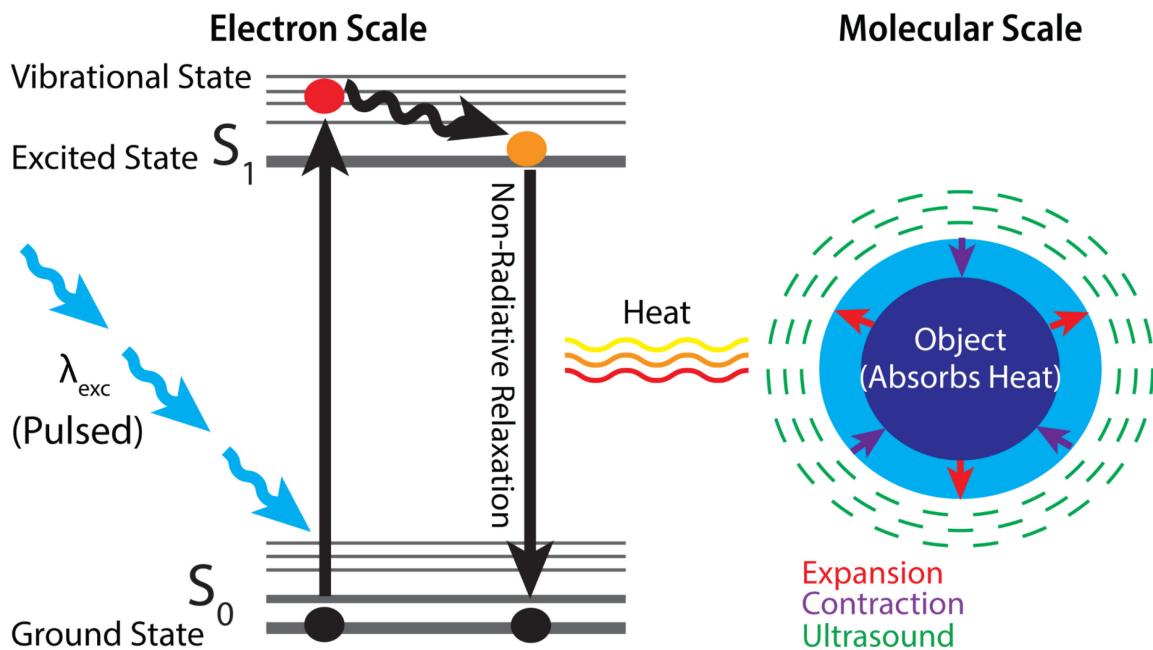


**Figure 1.7 Jablonski diagram explaining the generation of OA waves.** Note that in comparison to Figure 1.2 the excitation light ( $\lambda_{exc}$ ) is pulsed. The generated heat is converted to mechanical potential by the object resulting in thermoelastic expansion and contraction, producing ultrasound.

The physics of OAI have positioned it as a widely applicable imaging method capable of carrying out longitudinal basic research and clinical studies.[27] The amount of heat generated is proportional to the pulse of delivered light and as previously mentioned, is within the milliKelvin range; each milliKelvin ( $0.001^{\circ}\text{C}$ ) increase will produce around 0.8 MPa of pressure in tissues.[34] US imaging is commonly performed from 0.1 to 4 MPa of pressure meaning that only a slight increase in temperature is required to produce similar imaging conditions with OAI.[39] Hence, the amount of light needed to generate US is well below the American National Standards Institute (ANSI) safety limits for light exposure.[33, 40] The mathematical process by which OA waves are produced are not shown here as they were not the focus of this dissertation and have been described in detail numerous times.[36, 41] One of the most important developments is the use of a laser to deliver pulses of light to create OA waves.[42] Since this finding, most applications of OAI have relied on similar lasers for imaging and more recently modulated continuous wave lasers have been employed.[38] This has led to the exponential growth of OAI as seen in Figure 1.6.

As per Figure 1.4, biological components such as hemoglobin, lipid and water will absorb at various rates at distinct wavelengths of light.[27, 43] A good practical example of this is putting a green laser pointer directly against a finger and the light will not go through (it is mostly absorbed by hemoglobin and highly scattered by lipids).[43] However, when this is done with a red laser, some light will be visible through to the other side (less absorption and scattering).[43] OAI takes advantage of this phenomenon and uses pulsed lasers known as optical parametric oscillators (OPOs) to produce specific wavelengths of light that excite the tissue. Illuminating tissues with specific wavelengths prioritizes the US signal from one component over another, creating a map of the optical absorptivity of the tissue.[40, 44]

Performing OAI in this manner enables the multispectral unmixing of the tissue into its separate components and biomarkers e.g. oxy- and deoxygenated hemoglobin, melanin and lipids.[27]

One of the main advantages of OAI over fluorescence imaging is that the light only needs to deposit its energy within the tissue and is not needed for detection. For this reason, optical scattering could be seen as an advantage for acoustic resolution OAI helping to more uniformly disperse energy within the tissue, readily seen within lipid heavy tissues such as the brain. The resulting generated US is far less scattered in comparison to the optical component and can be readily recovered.[45] This has the added benefit of achieving optical based contrast with the reduced scattering and refraction of US in tissues, resulting in molecular imaging across depths, FOVs and spatiotemporal resolutions that neither US nor fluorescence imaging can achieve.[34, 46] This has been advanced to a stage where numerous endogenous (biomarkers such as hemoglobin, lipids) and exogenous (fluorescent dyes, nanoparticles) spectral components can be spectrally unmixed.[27] When carried out using a tomographic system this process is known as multispectral optoacoustic tomography (MSOT).[47] This method is predominantly focused on biomarker unmixing, brain vasculature in small animals and angiogenesis in tumors (with human applications).[27, 48-50]

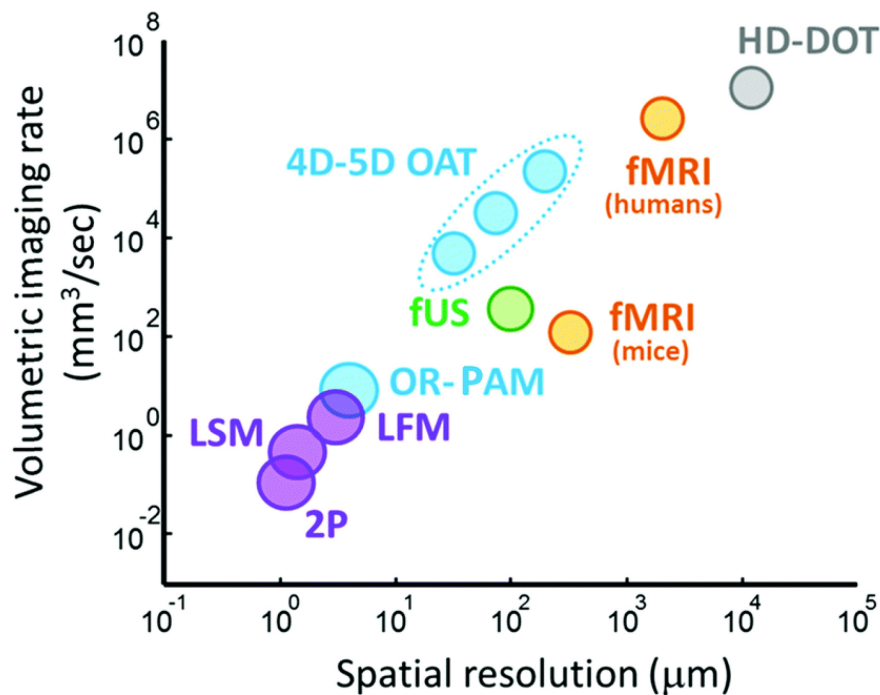


**Figure 1.8 Comparing the imaging capabilities of optoacoustic and other functional imaging modalities in terms of spatial resolution and volumetric imaging rates.** Fluorescence methods are shown in violet; light sheet microscopy (LSM),[51] two photon (2P)[52] & light field microscopy (LFM).[53] Functional ultrasound (fUS) shown in green,[54] functional magnetic resonance imaging (fMRI) shown in orange for both clinical and pre-clinical systems,[55, 56] high-density diffuse optical tomography (HD-DOT) is shown in gray,[57] OA systems are shown in cyan including optical resolution photoacoustic microscopy (OR-PAM)[58] along with 4D and 5D optoacoustic tomography (4D-5D OAT).[59] Reproduced under creative commons license from Dean-Ben *et al.* 2017.[27]

The versatility of OAI has resulted in numerous devices and setups.[27] These range from small FOV (mm<sup>3</sup>) high resolution OA microscopes to large scale (cm<sup>3</sup>) FOV macroscopic tomographic imaging setups with pre-clinical and clinical applications. Conveniently, these applications bridge the gap between high resolution, small FOV methods and low resolution,

large FOV methods.[27] This is shown in Figure 1.8. This work has focused on the implementation of an optoacoustic tomography (OAT) system and so other systems which are outside the scope of this thesis, will not be discussed. The spatiotemporal resolution and volumetric imaging rates of OAT position it as an excellent candidate to image electrophysiology across a large scale in scattering tissues, likely outperforming fUS and fluorescence imaging.

Tomography, as previously described in Chapter 1.1 is the process of imaging an object in 2D slices. By translating the detector or object along an axis, 3D images can be rendered by stacking the 2D slices. Many forms of OAT have been developed including those with cross section-based acquisitions. These have been developed for small animal imaging and function by surrounding the object of interest with optical paths for laser excitation and a circular transducer array to instantaneously capture excited US signals from the entire FOV.[60] An example of such a system is shown in Fig 1.9 A). In this case an animal (such as a mouse) is translated along the Y axis whilst tomographic images are acquired at each section. This technique has already shown the ability to image entire cross sections of mice at video rates, revealing deep-seated internal structures such as the liver and heart.[60, 61]

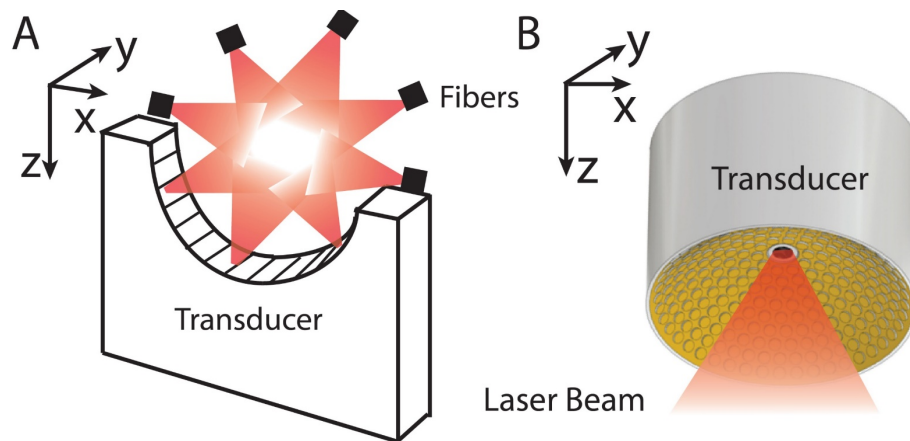


**Figure 1.9 Common OAT setups.** A) A 512 elements hemispherical OAT transducer array with central aperture used to deliver light to the sample. This setup allows volumetric imaging of a large FOV (1-2 cm<sup>3</sup>) B) MSOT setup as is available in commercial systems. The transducer and light sources (fibers) are moved along the y axis imaging the object in slices like MRI and X-Ray CT scanners.

2D OAT has proven to be a highly sensitive method however, the geometry of such transducers requires translation of the object to generate 3D images. By using a geometrically different array e.g. one that is 3D in nature like the hemispherical transducer (cup) shown in Figure. 1.9 B), allows images to be recreated in 3D from a single laser pulse.[62] This transducer geometry has achieved real time (video rate) imaging in 3D.[63] Whilst similar transducer geometries have been present for US imaging, their application to OAT has been limited by the lack of a laser capable of delivering laser pulses at sufficient rates.[64, 65] Recently developed lasers capable of meeting these criteria have catalyzed the adoption of these transducers to OAT.

The transducer array used in this dissertation (see Figure. 1.9 B) is comprised of 512 US point transducers embedded along a hemispherical cup with 140° angular coverage and with a central frequency of 5 MHz.[66-68] The laser light used for excitation was delivered via an optical fiber through a central aperture and the generated US is detected along the hemispherical surface.[66] As the US wave will reach each individual transducer element at

different times with varying intensities, back projection (BP) algorithms can be used to calculate their location of origin (reconstruction).[69] BP algorithms are not computationally demanding and can provide robust data representations of detected US signals.[70] Combining the hemispherical transducer used in this work and implementing BP reconstruction algorithms on graphics processing units (GPUs) has enabled real time 3D imaging.[71, 72] More recent advancements have even enabled 3D imaging at volumetric rates up to 1.6 KHz at a single wavelength.[73] This transducer has previously been shown to be capable of imaging scattering tissues such as the murine heart over a large field of view.[74] However, BP reconstructions are prone to artefacts such as streaks, negative values in the reconstruction and generally hinder quantification.[70] Model based (MB) algorithms overcome the limits of BP approaches by minimizing the error between detected signals and predicted signals from optoacoustic propagation models. In general, MB methods are slower to compute than BP methods but are more suited for quantitative approaches.[70] Numerous approaches are being employed to reduce the time taken for MB methods such as GPU implementation.[75, 76]

When comparing OAT to fluorescence, US and other imaging modalities, its spectroscopic ability i.e. multispectral imaging and biomarker unmixing is one of its greatest strengths.[47] This was of huge advantage for this dissertation, enabling the spectral unmixing of oxygenated, deoxygenated and total hemoglobin (HbO, HbR & HbT) to image hemodynamic activity in Chapter 4 along with a selection of optimum wavelengths for imaging various chromophores.[27] By combining all OAT components, 3D imaging, video rates and multispectral imaging, it is now possible to image in 5D over FOVs and rates which are far superior to comparable techniques.[77, 78] The process of imaging with 5D OAT is summarized in Figure 1.10. Currently, 5D imaging can be carried out at 100Hz using either the visible or NIR spectrum of light for excitation with the system shown in Figure 1.9 B). However, its application to imaging electrophysiology in scattering tissues is yet to be fully realized, especially in murine tissues. In addition, the spatial resolution achievable with the method is in the order of  $\sim 150 \mu\text{m}$  isotropically i.e. the resolution is even across all axes, with a FOV of  $1 \text{ cm}^3$ . [66] The system is capable of spectrally unmixing exogenous contrast agents, including fluorescent ones.[27] This is particularly applicable at wavelengths above 650 nm where the endogenous contrast from hemoglobin is reduced.[43, 60, 63] The high spatiotemporal resolution, which can be carried out across an entire mouse organ such as the brain or heart and 5D imaging position this OAT system as an excellent candidate to image electrophysiology in highly scattering tissues. Achieving this would surpass the current limitations seen in US and fluorescence imaging, combining the strengths of both. The next chapter will outline electrophysiology, current attempts to image it directly or indirectly as well as how 5D OAT in the form of functional optoacoustic neuro-tomography (FONT) can image electrophysiology from genetically encoded proteins like those used in fluorescence imaging.

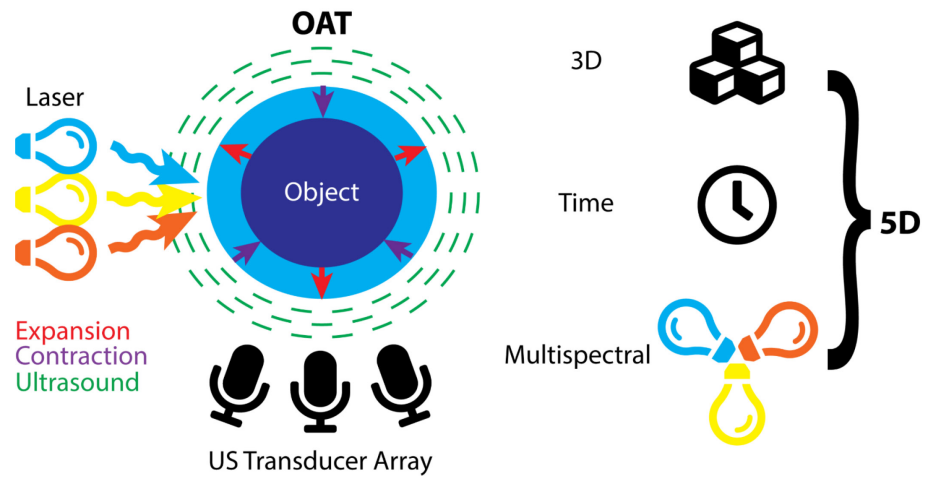


**Figure 1.10 5D OAT.** The process of generating US waves from an object with multispectral excitation and OAT along with the components which make up 5D OAT.

## References

- [1] X. Wang, J. B. Fowlkes, J. M. Cannata, C. Hu, and P. L. Carson, "Photoacoustic imaging with a commercial ultrasound system and a custom probe," *Ultrasound in medicine & biology*, vol. 37, no. 3, pp. 484-492, 2011.
- [2] F. M. Abu-Zidan, A. F. Hefny, and P. Corr, "Clinical ultrasound physics," *Journal of Emergencies, Trauma and Shock*, vol. 4, no. 4, p. 501, 2011.
- [3] P. Wells, "Diagnostic ultrasound: a logical approach," *Lippincott-Raven Publishers*, pp. 1-19, 1997.
- [4] J. H. Holmes, D. H. Howry, G. J. Posakony, and C. R. Cushman, "The ultrasonic visualization of soft tissue structures in the human body," *Transactions of the American Clinical and Climatological Association*, vol. 66, p. 208, 1955.
- [5] J. Wild, "The scientific discovery of sonic reflection by soft tissues and application of ultrasound to diagnostic medicine and tumor screening," in *Third Meeting of the World Federation for Ultrasound in Medicine and Biology (Scientific Exhibit Section) Brighton, England—July, 1982*.
- [6] C. M. Sehgal, S. P. Weinstein, P. H. Arger, and E. F. Conant, "A review of breast ultrasound," *Journal of mammary gland biology and neoplasia*, vol. 11, no. 2, pp. 113-123, 2006.
- [7] V. C. Protopappas, D. A. Baga, D. I. Fotiadis, A. C. Likas, A. A. Papachristos, and K. N. Malizos, "An ultrasound wearable system for the monitoring and acceleration of fracture healing in long bones," *IEEE transactions on biomedical engineering*, vol. 52, no. 9, pp. 1597-1608, 2005.
- [8] Q. Duan, A. F. Laine, and J. S. Suri, "Real-Time 4D Cardiac Segmentation by Active Geometric Functions," in *Ultrasound Imaging*: Springer, 2012, pp. 225-253.
- [9] R. Chifor, M. E. Badea, Ş. C. Vesa, and I. Chifor, "The utility of 40 MHz periodontal ultrasonography in the assessment of gingival inflammation evolution following professional teeth cleaning," *Medical ultrasonography*, vol. 17, no. 1, pp. 34-38, 2015.
- [10] Y. Minami and M. Kudo, "Review of dynamic contrast-enhanced ultrasound guidance in ablation therapy for hepatocellular carcinoma," *World Journal of Gastroenterology: WJG*, vol. 17, no. 45, p. 4952, 2011.
- [11] N. M. Krekel *et al.*, "Intraoperative ultrasound guidance for palpable breast cancer excision (COBALT trial): a multicentre, randomised controlled trial," *The lancet oncology*, vol. 14, no. 1, pp. 48-54, 2013.
- [12] H. Stewart, M. Repacholi, and D. Benwell, "Essentials of medical ultrasound," *MH Repacholi and DA Ben well, eds., Humana Press, Clifton, NJ*, pp. 181-213, 1982.
- [13] C. M. Otto, *Textbook of Clinical Echocardiography E-Book*. Elsevier Health Sciences, 2013.
- [14] K. K. Shung, *Diagnostic ultrasound: Imaging and blood flow measurements*. CRC press, 2015.
- [15] J. A. Zagzebski, "Essentials of ultrasound physics. 1996," *Mosby, St. Louis*.
- [16] R. M. Kirberger, "Imaging artifacts in diagnostic ultrasound—a review," *Veterinary Radiology & Ultrasound*, vol. 36, no. 4, pp. 297-306, 1995.
- [17] L. H. Gimber and M. S. Taljanovic, "Ultrasound Imaging Artifacts," in *Pitfalls in Musculoskeletal Radiology*: Springer, 2017, pp. 33-44.

- [18] O. V. Solberg, F. Lindseth, H. Torp, R. E. Blake, and T. A. N. Hernes, "Freehand 3D ultrasound reconstruction algorithms—a review," *Ultrasound in medicine & biology*, vol. 33, no. 7, pp. 991-1009, 2007.
- [19] H. Yerli and S. Y. Eksioğlu, "Extended field-of-view sonography: evaluation of the superficial lesions," *Canadian Association of Radiologists Journal*, vol. 60, no. 1, pp. 35-39, 2009.
- [20] J. Provost *et al.*, "3D ultrafast ultrasound imaging in vivo," *Physics in Medicine & Biology*, vol. 59, no. 19, p. L1, 2014.
- [21] C. Li, L. Huang, N. Duric, H. Zhang, and C. Rowe, "An improved automatic time-of-flight picker for medical ultrasound tomography," *Ultrasonics*, vol. 49, no. 1, pp. 61-72, 2009.
- [22] J. G. Craig, "Ultrasound of ligaments and bone," *Ultrasound Clinics*, vol. 2, no. 4, pp. 617-637, 2007.
- [23] R. W. Gill, "Measurement of blood flow by ultrasound: accuracy and sources of error," *Ultrasound in medicine & biology*, vol. 11, no. 4, pp. 625-641, 1985.
- [24] M. Tanter and M. Fink, "Ultrafast imaging in biomedical ultrasound," *IEEE transactions on ultrasonics, ferroelectrics, and frequency control*, vol. 61, no. 1, pp. 102-119, 2014.
- [25] J. Ophir and K. J. Parker, "Contrast agents in diagnostic ultrasound," *Ultrasound in medicine & biology*, vol. 15, no. 4, pp. 319-333, 1989.
- [26] D. Cosgrove, "Ultrasound contrast agents: an overview," *European journal of radiology*, vol. 60, no. 3, pp. 324-330, 2006.
- [27] X. Deán-Ben, S. Gottschalk, B. Mc Larney, S. Shoham, and D. Razansky, "Advanced optoacoustic methods for multiscale imaging of in vivo dynamics," *Chemical Society Reviews*, vol. 46, no. 8, pp. 2158-2198, 2017.
- [28] J. Kang *et al.*, "Transcranial recording of electrophysiological neural activity in the rodent brain in vivo using functional photoacoustic imaging of near-infrared voltage-sensitive dye," *Frontiers in neuroscience*, vol. 13, p. 579, 2019.
- [29] B. Rao, R. Zhang, L. Li, J. Y. Shao, and L. V. Wang, "Photoacoustic imaging of voltage responses beyond the optical diffusion limit," *Sci Rep*, vol. 7, no. 1, p. 2560, May 31 2017.
- [30] A. G. Bell, "On the production and reproduction of sound by light," in *Proc. Am. Assoc. Adv. Sci.*, 1881, vol. 29, pp. 115-136.
- [31] A. G. Bell, "The photophone," *Science*, vol. 1, no. 11, pp. 130-134, 1880.
- [32] S. Y. Emelianov, P.-C. Li, and M. O'Donnell, "Photoacoustics for molecular imaging and therapy," *Physics today*, vol. 62, no. 8, p. 34, 2009.
- [33] C. Li and L. V. Wang, "Photoacoustic tomography and sensing in biomedicine," *Physics in Medicine & Biology*, vol. 54, no. 19, p. R59, 2009.
- [34] J. Yao and L. V. Wang, "Sensitivity of photoacoustic microscopy," *Photoacoustics*, vol. 2, no. 2, pp. 87-101, 2014.
- [35] L. V. Wang and J. Yao, "A practical guide to photoacoustic tomography in the life sciences," *Nature methods*, vol. 13, no. 8, p. 627, 2016.
- [36] L. V. Wang, "Tutorial on photoacoustic microscopy and computed tomography," *IEEE Journal of Selected Topics in Quantum Electronics*, vol. 14, no. 1, pp. 171-179, 2008.
- [37] M. Xu and L. V. Wang, "Photoacoustic imaging in biomedicine," *Review of scientific instruments*, vol. 77, no. 4, p. 041101, 2006.

- [38] S. A. Telenkov and A. Mandelis, "Fourier-domain biophotoacoustic subsurface depth selective amplitude and phase imaging of turbid phantoms and biological tissue," *Journal of biomedical optics*, vol. 11, no. 4, p. 044006, 2006.
- [39] D. Dance, S. Christofides, A. Maidment, I. McLean, and K. Ng, "Diagnostic radiology physics," *International Atomic Energy Agency*, 2014.
- [40] L. V. Wang and H.-i. Wu, *Biomedical optics: principles and imaging*. John Wiley & Sons, 2012.
- [41] M. Tang, D. Elson, R. Li, C. Dunsby, and R. Eckersley, "Photoacoustics, thermoacoustics, and acousto-optics for biomedical imaging," *Proceedings of the Institution of Mechanical Engineers, Part H: Journal of Engineering in Medicine*, vol. 224, no. 2, pp. 291-306, 2010.
- [42] L. Kreuzer, "Ultralow gas concentration infrared absorption spectroscopy," *Journal of Applied Physics*, vol. 42, no. 7, pp. 2934-2943, 1971.
- [43] S. L. Jacques, "Optical properties of biological tissues: a review," *Physics in Medicine & Biology*, vol. 58, no. 11, p. R37, 2013.
- [44] K. P. Koestli, M. Frenz, H. P. Weber, G. Paltauf, and H. Schmidt-Kloiber, "Optoacoustic measurements of water, bone, and cartilage with an infrared OPO," in *Laser-Tissue Interaction X: Photochemical, Photothermal, and Photomechanical*, 1999, vol. 3601, pp. 310-318: International Society for Optics and Photonics.
- [45] J. L. Su *et al.*, "Advances in clinical and biomedical applications of photoacoustic imaging," *Expert opinion on medical diagnostics*, vol. 4, no. 6, pp. 497-510, 2010.
- [46] X. L. Dean-Ben, S. Gottschalk, B. Mc Larney, S. Shoham, and D. Razansky, "Advanced optoacoustic methods for multiscale imaging of in vivo dynamics," (in English), *Chemical Society Reviews*, vol. 46, no. 8, pp. 2158-2198, Apr 21 2017.
- [47] V. Ntziachristos and D. Razansky, "Molecular imaging by means of multispectral optoacoustic tomography (MSOT)," *Chemical reviews*, vol. 110, no. 5, pp. 2783-2794, 2010.
- [48] D. Razansky, A. Buehler, and V. Ntziachristos, "Volumetric real-time multispectral optoacoustic tomography of biomarkers," *Nature protocols*, vol. 6, no. 8, p. 1121, 2011.
- [49] J. Laufer, E. Zhang, G. Raivich, and P. Beard, "Three-dimensional noninvasive imaging of the vasculature in the mouse brain using a high resolution photoacoustic scanner," *Applied optics*, vol. 48, no. 10, pp. D299-D306, 2009.
- [50] G. Diot *et al.*, "Multispectral optoacoustic tomography (MSOT) of human breast cancer," *Clinical Cancer Research*, vol. 23, no. 22, pp. 6912-6922, 2017.
- [51] M. B. Bouchard *et al.*, "Swept confocally-aligned planar excitation (SCAPE) microscopy for high-speed volumetric imaging of behaving organisms," *Nature photonics*, vol. 9, no. 2, p. 113, 2015.
- [52] L. Kong *et al.*, "Continuous volumetric imaging via an optical phase-locked ultrasound lens," *Nature methods*, vol. 12, no. 8, pp. 759-762, 2015.
- [53] R. Prevedel *et al.*, "Simultaneous whole-animal 3D imaging of neuronal activity using light-field microscopy," *Nature methods*, vol. 11, no. 7, pp. 727-730, 2014.
- [54] E. Macé, G. Montaldo, I. Cohen, M. Baulac, M. Fink, and M. Tanter, "Functional ultrasound imaging of the brain," *Nature methods*, vol. 8, no. 8, p. 662, 2011.
- [55] S. Moeller *et al.*, "Multiband multislice GE-EPI at 7 tesla, with 16-fold acceleration using partial parallel imaging with application to high spatial and temporal whole-brain fMRI," *Magnetic resonance in medicine*, vol. 63, no. 5, pp. 1144-1153, 2010.

- [56] S. C. Bosshard, F. Stuker, C. Von Deuster, A. Schroeter, and M. Rudin, "BOLD fMRI of C-fiber mediated nociceptive processing in mouse brain in response to thermal stimulation of the forepaws," *PloS one*, vol. 10, no. 5, 2015.
- [57] A. T. Eggebrecht *et al.*, "Mapping distributed brain function and networks with diffuse optical tomography," *Nature photonics*, vol. 8, no. 6, p. 448, 2014.
- [58] J. Yao *et al.*, "High-speed label-free functional photoacoustic microscopy of mouse brain in action," *Nature methods*, vol. 12, no. 5, p. 407, 2015.
- [59] X. L. Dean-Ben *et al.*, "Functional optoacoustic neuro-tomography for scalable whole-brain monitoring of calcium indicators," (in English), *Light-Science & Applications*, vol. 5, Dec 2016.
- [60] A. Taruttis, S. Morscher, N. C. Burton, D. Razansky, and V. Ntziachristos, "Fast Multispectral Optoacoustic Tomography (MSOT) for Dynamic Imaging of Pharmacokinetics and Biodistribution in Multiple Organs," *PLOS ONE*, vol. 7, no. 1, p. e30491, 2012.
- [61] A. Karlas *et al.*, "Cardiovascular optoacoustics: From mice to men – A review," *Photoacoustics*, vol. 14, pp. 19-30, 2019/06/01/ 2019.
- [62] J. Gateau, A. Chekkoury, and V. Ntziachristos, "Ultra-wideband three-dimensional optoacoustic tomography," *Optics letters*, vol. 38, no. 22, pp. 4671-4674, 2013.
- [63] A. Buehler, E. Herzog, D. Razansky, and V. Ntziachristos, "Video rate optoacoustic tomography of mouse kidney perfusion," *Optics Letters*, vol. 35, no. 14, pp. 2475-2477, 2010/07/15 2010.
- [64] A. Buehler, X. L. Deán-Ben, J. Claussen, V. Ntziachristos, and D. Razansky, "Three-dimensional optoacoustic tomography at video rate," *Optics Express*, vol. 20, no. 20, pp. 22712-22719, 2012/09/24 2012.
- [65] X. L. Dean-Ben, H. Lopez-Schier, and D. Razansky, "Optoacoustic micro-tomography at 100 volumes per second," (in English), *Scientific Reports*, vol. 7, Jul 31 2017.
- [66] B. Mc Larney, J. Rebling, Z. Chen, X. L. Deán-Ben, S. Gottschalk, and D. Razansky, "Uniform light delivery in volumetric optoacoustic tomography," *Journal of Biophotonics*, vol. 12, no. 6, p. e201800387, 2019.
- [67] S. Gottschalk *et al.*, "Rapid volumetric optoacoustic imaging of neural dynamics across the mouse brain," *Nature Biomedical Engineering*, vol. 3, no. 5, pp. 392-401, 2019/05/01 2019.
- [68] S. Gottschalk *et al.*, "Isolated Murine Brain Model for Large-Scale Optoacoustic Calcium Imaging," *Frontiers in neuroscience*, vol. 13, p. 290, 2019.
- [69] G. Paltauf, R. Nuster, and P. Burgholzer, "Weight factors for limited angle photoacoustic tomography," (in English), *Physics in Medicine and Biology*, vol. 54, no. 11, pp. 3303-3314, Jun 7 2009.
- [70] X. L. Dean-Ben, A. Buehler, V. Ntziachristos, and D. Razansky, "Accurate model-based reconstruction algorithm for three-dimensional optoacoustic tomography," *IEEE Transactions on Medical Imaging*, vol. 31, no. 10, pp. 1922-1928, 2012.
- [71] X. L. Dean-Ben, A. Ozbek, and D. Razansky, "Volumetric real-time tracking of peripheral human vasculature with GPU-accelerated three-dimensional optoacoustic tomography," *IEEE Trans Med Imaging*, vol. 32, no. 11, pp. 2050-5, Nov 2013.
- [72] X. L. Deán-Ben and D. Razansky, "Functional optoacoustic human angiography with handheld video rate three dimensional scanner," *Photoacoustics*, vol. 1, no. 3-4, pp. 68-73, 2013.
- [73] A. Özbek, X. L. Deán-Ben, and D. Razansky, "Optoacoustic imaging at kilohertz volumetric frame rates," *Optica*, vol. 5, no. 7, pp. 857-863, 2018/07/20 2018.

- [74] X. L. Deán-Ben, S. J. Ford, and D. Razansky, "High-frame rate four dimensional optoacoustic tomography enables visualization of cardiovascular dynamics and mouse heart perfusion," *Scientific reports*, vol. 5, p. 10133, 2015.
- [75] L. Ding, X. L. Dean-Ben, and D. Razansky, "Efficient 3-D Model-Based Reconstruction Scheme for Arbitrary Optoacoustic Acquisition Geometries," *IEEE Trans Med Imaging*, vol. 36, no. 9, pp. 1858-1867, Sep 2017.
- [76] L. Ding, X. L. Deán-Ben, and D. Razansky, "20 frames per second model-based reconstruction in cross-sectional optoacoustic tomography," in *Photons Plus Ultrasound: Imaging and Sensing 2017*, 2017, vol. 10064, p. 100641A: International Society for Optics and Photonics.
- [77] X. Luís Deán-Ben and D. Razansky, "Adding fifth dimension to optoacoustic imaging: volumetric time-resolved spectrally enriched tomography," *Light: Science & Applications*, Original Article vol. 3, p. e137, 01/31/online 2014.
- [78] S. Gottschalk, T. Felix Fehm, X. Luís Deán-Ben, and D. Razansky, "Noninvasive real-time visualization of multiple cerebral hemodynamic parameters in whole mouse brains using five-dimensional optoacoustic tomography," *Journal of Cerebral Blood Flow & Metabolism*, vol. 35, no. 4, pp. 531-535, 2015.

### 1.3 Neuroimaging

Neuroimaging is a main stay of both basic research in neuroscience and applied research in the medical field.[1] It has a range of applications from rudimentary imaging of rapid action potentials in cells on the order of milliseconds to observing long term processes like hemodynamic activity, on the order of tens of seconds to minutes.[2-4] Ultimately, all neuroimaging aims to further understand the brain. As neurodegenerative diseases are increasingly becoming more prevalent and debilitating in older populations, further insights into the brain are of huge importance.[5] A basic understanding of the brain and how it works as a whole rather than in small sections is hugely lacking.[6] Developing a tool capable of doing so in real time and across the entirety of a brain (especially for mice) would significantly progress neuroscience research.[6] In this chapter electrophysiology will be briefly introduced, which in this case means the communication of the brain and the current neuroimaging approaches that are used to image electrophysiological activity. Finally, the shortcomings of current applications will be noted and how FONT may provide a solution to these problems.

Electrophysiology is the process of recording or generating an electrical potential or impulse in cells or tissues.[7] It is an integral part of neuroscience and basic research. Electrophysiology elucidates how cells function, how communication in the brain is carried out and how well a heart is beating.[7, 8] Currently, the basic functions of single neurons are well understood.[9] A neuron receives input from various other neurons it is connected to. Based on the sum of these inputs and various factors it is able to relay the signal to the next neuron(s) it is connected to. This is achieved via electrical (voltage) potential across the cell membrane of the neuron as it travels across the cell like a wave carrying the signal (electrical or chemical relays) to the next cell, as shown in Figure 1.11.[9] These signals form the building blocks of complex neuroanatomical structures such as the human brain, yet much is still not understood about this organ and billions have been spent on elucidating brain function as a whole.[6] However, it is known that neuronal communication is a metabolically intensive process requiring a ready supply of oxygen, nutrients and glucose where 2% of body mass consumes almost 20% of body energy.[10] For decades, neuroscience has relied on simplifying the model of the brain to single cells, *in vivo* work in mice and monkeys and more recently in organoids.[11-13] Currently, there are a myriad of ways to detect direct and indirect forms of electrophysiology. However, imaging is coming to the forefront in terms of speed, resolution and FOV with advancements in detection and genetically encoded calcium and voltage indicators (GECIs & GEVIs).[1, 12, 14, 15] Despite this, there remains a need for improved imaging speed across a FOV as large as the entire mouse brain ( $\text{cm}^3$ ) which, will likely be achieved by improved GECIs & GEVIs and new imaging modalities.[5, 6]

One of the first methods for detecting electrophysiology was carried out via rudimentary setups on single neurons connected to muscles.[16] Electrical shocks were applied to neurons and the attached muscle twitched or moved in response. Further experiments on squid axons led to deeper insights to the function of neurons.[17] It was determined that higher potassium and anion concentrations were present inside the cell in contrast to higher sodium and chloride concentrations outside the cell. This concentration gradient allows neurons to build up a resting state negative charge across the cell membrane (resting potential). Depolarization of the neurons begins by an electrical impulse causing a voltage gated sodium ion channel ( $\text{Na}_v$ ) to open with sodium entering the cell. The potential across the membrane then increases and above a certain threshold will cause the cell to depolarize. This results in an electrical wave propagating along the cell membrane (action potential).[7, 18]

Whilst synapses can be electrical (ion-based communication), the majority are chemical (neurotransmitter based). Synapses can be divided into three main components, the presynaptic terminal which is the section of the neuron's membrane at the synapse (neurotransmitter releasing neuron), the synaptic cleft (extracellular space between neurons, ~40 nm for chemical synapses) and the postsynaptic terminal which is the section of the membrane from the receiving neuron (opposite side of the synaptic cleft).[9, 19] An example synapse is outlined in Figure 1.11. The action potential in a presynaptic neuron results in the opening of voltage-gated calcium channels, resulting in the rapid influx of  $\text{Ca}^{2+}$  ions from the extracellular matrix into the neuron.[20] The  $\text{Ca}^{2+}$  ions then facilitate the binding of vesicles containing neurotransmitters such as dopamine to the presynaptic terminal where they are then released across the synaptic cleft. These neurotransmitters such as dopamine or gamma-Aminobutyric acid (GABA), will bind to receptors along the membrane of the postsynaptic neuron. In turn, the receptors cause ion channels to open and positively charged ions will flow into the postsynaptic neuron, causing the membrane to depolarize and triggering an action potential. Calcium ions ( $\text{Ca}^{2+}$ ) are essential for this neurotransmitter release.[21]

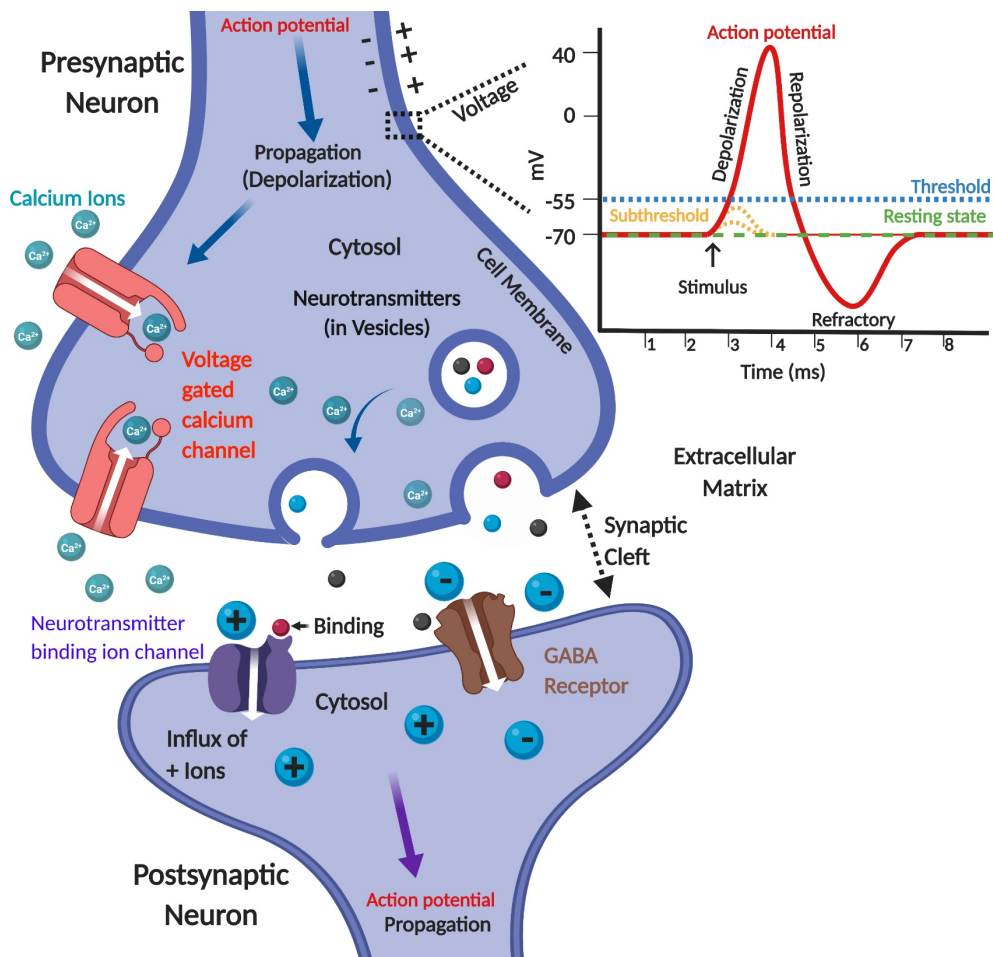


**Figure 1.11 The synaptic cleft during activation between neurons with the electrophysiological profile of a recorded action potential along the membrane.** Neuronal activation stimulates the influx of  $\text{Ca}^{2+}$  ions into the presynaptic neuron via the opening of voltage-gated calcium channels. The  $\text{Ca}^{2+}$  ions then bind to vesicles loaded with neurotransmitters, facilitating them to bind to the presynaptic terminal and release numerous neurotransmitters (e.g. GABA) into the synaptic cleft. The neurotransmitters then bind to receptive ion channels along the membrane of the postsynaptic neuron (postsynaptic terminal). This causes the ion channels to open, prompting an influx of positively charged ions,

depolarizing the membrane of the postsynaptic neuron. An action potential across the neuronal membrane, which is the key component of neuronal communication, is briefly described on the top right including resting state and sub threshold events. Created with BioRender.com.

Electrophysiological readings (detecting the voltage change during action potentials on the membrane using an electrode) are commonly performed using a technique known as patch clamping. Patch clamping requires the use of small glass pipettes, connected to suitable recording equipment that are attached to the membrane of the cell and is often carried out under a microscope.[22] Due to its direct physical attachment to the neuronal membrane, patch clamping can read highly sensitive information from a single or groups of neurons (field potential) and is the current gold standard in electrophysiology.[23-25] The achieved temporal resolution of electrophysiology is as fast as the neuronal communication itself (1-2 KHz), but the assessed population of neurons is only a fraction of a percent of all neurons in the brain. Due to its high spatial resolution and need for direct contact with neurons of interest, the method is highly effective and suited to recordings from single neurons, dendritic spines, and small neuronal populations. However, due to its highly invasive nature (electrodes must be inserted into the brain for *in vivo* studies) it struggles to achieve truly large scale recordings.[26]

More recent developments have tried to achieve large scale electrophysiology by developing needle arrays covered in electrodes which can be inserted into the mouse brain with little to no adverse effects.[27] Certain variants, such as graphene based electrodes, can record action potentials from multiple neurons across all layers of the cortex.[28] Nevertheless, these methods of array insertion remain highly invasive and have not yet achieved highly coveted whole-brain recording.[7] Whole brain (large-scale) electrophysiological recordings are now a necessary step for further understanding of brain function.[6] Non-invasive techniques like electroencephalogram (EEG) caps are carried out by placing a “helmet” like device containing numerous electrodes on the heads of subjects and can be used in mice and humans.[29, 30] These methods have the ability to record electrophysiological signals from much larger areas, such as the entire cortex.[29] However, recordings from such large areas causes a reduction in spatial resolution and in some cases (in mice) still requires invasive surgery for device attachment.[31] Advanced methods can enable more precise 3D mapping but these require reference MRI images.[32] As a result there is high demand for a modality which is sensitive to electrophysiological signals over a large scale, ideally the entire mouse brain.

The most common method of large-scale brain imaging is functional magnetic resonance imaging (fMRI).[33] MRI functions by exposing protons to a high magnetic field. Protons are subatomic particles which spin and have a small magnetic potential with hydrogen (the nucleus of which is a single proton and is highly present in water i.e. tissues), being the main agent used to image with MRI.[34] The high magnetic field causes all the protons to align along an axis and once aligned, a radiofrequency (RF) pulse is used to push the protons to spin at an axis 90° or 180° from the magnetic field. The RF is then stopped, the protons realign to the magnetic field and in doing so, release EM energy.[34] This EM energy is then detected by the MRI machine with different tissues releasing energy at different rates that the MRI can distinguish producing anatomical images.[34] fMRI uses blood as an agent to determine metabolism in a tissue and thus provides anatomical and functional imaging, especially in the brain.[33]

fMRI relies on the fact that HbO has weak paramagnetic potential but HbR has strong paramagnetic potential i.e. HbR produces far more magnetic signal than HbO does when

exposed to a magnetic field like that in MRI.[35] When a neuron or region of a brain is active, it consumes a large amount of oxygen and thus an increase of HbO occurs at the site of activation reducing HbR.[36] As a result, the decrease in HbO corresponds to a decrease in detected fMRI signal in that area.[36] Imaging hemodynamic activity in this form is known as the blood oxygenation level dependent (BOLD) response, which is in fact an inverted response to an increase in activity. BOLD fMRI is widely practiced in humans and mice to non-invasively map brain (neuronal electrophysiology) activity.[36-38] Although the BOLD response has been widely adapted, it is an indirect measure of electrophysiological activity which in truth only shows an increase in metabolic activity in the area.[39] It cannot conclusively be said that the BOLD response images solely neuronal (electrophysiological) activity as other cells (e.g. glial cells which provide nutrients to neurons) in the region may undergo increased metabolic activity.

Whilst it is assumed that neuronal synaptic activity consumes 85% of glucose consumption in the brain it is not currently possible to separate the metabolic activity of one cell type from the other in the brain with fMRI and the reliability of the BOLD signal has been the subject of wide debate.[40-42] fMRI has the ability to image the brain non-invasively but it has significant challenges, especially in small animal imaging.[43] The spatial resolution of fMRI (on the order of mm's) is low in comparison to fluorescence methods (on the order of microns) and is further amplified when imaging small animals like mice where the brain is an order of magnitude smaller than that of humans.[44, 45] Both the spatial and the temporal resolution of fMRI leaves a uncertainty with devices achieving 1 Hz rates across their FOVs. Recent developments have achieved sub-second acquisitions with voxel (volumetric/3D pixels) sizes of 1.5 mm<sup>3</sup>. [46]

Optical imaging (OI) is one method that can overcome many of the limitations seen in fMRI and classic electrophysiology. OI has the advantage of being able to detect both hemodynamic signals (e.g. diffuse optical tomography - DOT) and direct electrophysiological changes with both fluorescent GECIs and GEVIs and suitable voltage and calcium sensitive dyes.[47-51] OI of fluorescent changes from calcium and voltage transients (GECIs and GEVIs) has given many insights into neuronal communication within the brain.[52] These insights include connecting animal behavior with neuronal activity, somatosensory and olfactory responses as well as awake mouse imaging.[53-57] Developments in high speed cameras can easily achieve 1-2 KHz temporal resolution with advancements in optics allowing varying degrees of spatial resolution, including dendrites on single cells and wide field brain imaging.[3] Two and three photon imaging methods even allow for 3D imaging to be achieved at varying depths across the cortex and in some cases, reaching the hippocampus.[58-60]

However, there are numerous drawbacks to OI. The most obvious issues include achievable depth (approx. 1mm) and the invasive nature of the method.[61] Methods like two and three photon imaging require removal of the scalp and additional steps like skull thinning, skull clearing or the implantation of a glass cover slip (craniotomy).[62-64] This ensures matching of the refractive indices of the tissue with the optics and allows for repeated measurements.[65] Optical imaging tends to cover two regimes, such as high resolution imaging across a small FOV (portion of the cortex) or low resolution macro imaging across a large FOV with high temporal resolution. There are consistent tradeoffs between FOV, speed and spatial resolution and no one method is capable of delivering sufficient results in all three. Macro imaging, that is not capable of optical sectioning has the added disadvantage that signals are recorded from all depths and as a result, a maximum intensity image (MIP) is produced of all activity. This means that the origin of signals cannot be determined, and it

remains unknown if a neuron fired in the cortex or hippocampus. For “deep” two photon imaging, an endoscope setup is often used. This is highly invasive and requires the removal or displacement of brain tissue.[66]

Advancements in OI setups have resulted in countless discoveries regarding brain function. Many of these discoveries in modern day neuroimaging were achieved thanks to the development of GECIs, GEVIs and glutamate sensors along with voltage and calcium sensitive dyes.[12, 51, 67-70] The most common of these are GECIs because of their high sensitivity, quick response times and transgenic lines. Many of these are possible thanks to the ground breaking work of Tsien.[71, 72] Tsien and his team discovered that calcium sensors could be inserted into a fluorescent protein (GFP) to detect cytosolic calcium changes.[73] The fluorescent proteins are predominantly derived from aqueous organisms like jelly fish and anemones.[74, 75] Dyes (e.g. Fura2) capable of detecting calcium and voltage have been used for decades but these are considered a brute force approach with loading, dispersion and toxicity causing numerous problems.[51, 76, 77] Dye imaging is further complicated by the need for intracranial loading, meaning dyes must be loaded through the skull before an experiment or require opening of the blood brain barrier (BBB).[78, 79]

In comparison to dyes, genetically encoded indicators are more reliable, are made by the cell itself and can be targeted to specific sub population of neurons such as inhibitory or excitatory neurons.[80, 81] Consequently, researchers can establish lines of transgenic animals that can be used for experiment replications. The process in which GECIs work is now well established but took years to develop, with green calmodulin protein (GCaMP) emerging as the most successful of these.[48, 82] The GCaMP protein works so that a calmodulin (CaM) group, sensitive to calcium is coupled to a GFP molecule.[83] The expression of the GCaMP is designed to be present in the cytoplasm of the cell, where the influx and efflux of calcium during neuronal activity can be readily detected as per Figure 1.12. Without calcium, the protein exists in a poorly light absorbent and therefore poorly fluorescence state. Upon binding of the calcium, the calmodulin group (hinge-like, sometimes replaced by troponin C) undergoes a conformational change and binds to a target peptide such as M13 or RS20.[84, 85] This peptide then restores the absorption of the circularly permuted GFP protein and therefore results in increased fluorescence. Many GCaMP have increased fluorescence by using circularly permuted enhanced GFP (cpEGFP).[86] Circularly permuted versions of GFP enable the insertion of calcium sensitive domains close to the chromophore whilst retaining and sometimes enhancing the folding properties of the protein i.e. it is easier for the protein to form in the cell, the protein remains stable and retains its desired optical properties.[87] In the case of GCaMP the fluorescent modulation of GFP is achieved via M13 or RS20 which in turn are dependent upon the  $\text{Ca}^{2+}$  binding of CaM. This directly relates the fluorescence to cellular calcium changes enabling the visualization of cellular activity on a micro-, meso- and macroscopic scale.[73, 86-88]

As previously mentioned, and shown in Figure 1.11, calcium is one of the main neurotransmitters involved in neuronal communication (influx of calcium during activation) and is a direct method of imaging electrophysiology, albeit at a slightly reduced rate (onset times of 10 to 100ms vs 1ms for GEVIs). It is important to note that more recent GCaMPs have dramatically increased the kinetics of the protein so that the fluorescent response matches the real time fluctuations of  $\text{Ca}^{2+}$  ions in the cell.[85, 89, 90] The binding mechanism of calcium to Calmodulin and the rapid change in cellular calcium concentration (increases of nano to micro molar) enables detected signals to be amplified.[91] This feature of the GCaMP series has enabled high delta values (signal change over baseline activity) with newer versions like

GCaMP6 achieving delta changes of 100s of % in single neurons during activation in comparison to 10s of % in older versions such as GCaMP3.[82]

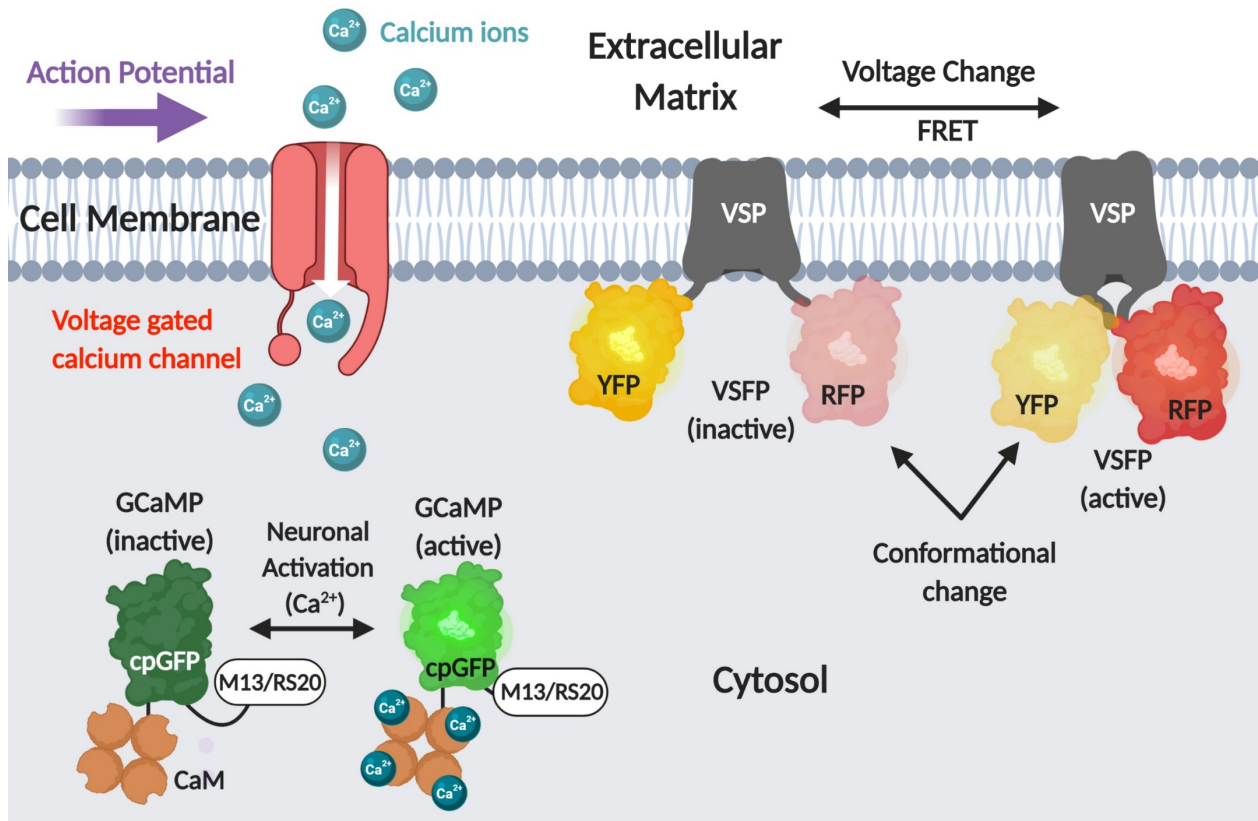


**Figure 1.12 The cellular location and fluorescent function of the GECI; GCaMP and GEVI; Butterfly 1.2.** Action potentials trigger the opening of voltage gated calcium channels, prompting an influx of Ca<sup>2+</sup> ions increasing intracellular Ca<sup>2+</sup> levels from nano to micro molar levels. Calmodulin (CaM) binds this calcium altering the location of residues M13 or RS20. This location change alters the cpGFP molecule increasing its fluorescence. In this way neuronal electrophysiological activity can be visualized with fluorescence. In the case of Butterfly 1.2 the voltage change on the membrane also causes a structural change. Upon activation the voltage sensitive protein (VSP) embedded within the membrane decreases the distance between two fluorescent proteins yellow fluorescent protein (YFP) and red fluorescent protein (RFP). This enables increased efficiency in Förster resonance energy transfer (FRET) between the proteins with YFP donating energy to the RFP. The YFP protein undergoes a dip in recorded fluorescence with the RFP protein undergoing an increase in fluorescence. The ratio between the two proteins can then be determined visualizing the electrophysiology of the neuron. Created with Biorender.com.

GEVIs have enabled accurate and repetitive electrophysiology imaging.[2] These voltage sensitive proteins are targeted to embed in the membrane of the cell where voltage changes are most prevalent.[15, 89] Their fluorescent or absorption changes in response to the voltage change across the membrane and are a more accurate indicator of electrophysiological activity than GECIs.[92] There are inherent delays involved in Ca<sup>2+</sup> imaging as Ca<sup>2+</sup> needs to flow into the cell which voltage imaging is not reliant on, resulting in GECIs sometimes misreporting rapid consecutive neuronal activations.[93] GEVIs are predominantly based on voltage sensing domains (VSD) in the form of a voltage sensitive protein (VSP). VSPs are predominantly rhodopsins and chemogenetic structures and have

undergone rapid development as a result of protein engineering and high throughput screening.[2, 89, 94, 95] The consequent fluorescence changes tend to be lower than those seen in calcium sensors, with deltas on the order of 1 to 100% in single cell recordings, especially for Förster resonance energy transfer (FRET) based proteins such as Butterfly 1.2, see Figure 1.12.[49] More recent advancements have led to the development of GEVIs like Archon1, with delta values in the range of 100% with onset times of ~1ms.[89] GEVIs essentially react as quickly as the neuronal communication itself.[89, 96] In many cases, voltage imaging across the whole brain is often seen as a pinnacle of neuroimaging. Achieving this would enable research to peer into the brain in real time and observe behavioral processes and changes as they happen.[95] However, many of the GEVIs need further development with GECIs having superior delta changes due to the influx of  $Ca^{2+}$  ions during neuronal activation. Furthermore, GEVIs often do not function for two and three photon imaging and are coupled to the same fluorescent molecules like GFP.[95]

As discussed in the previous section, OAT has the capability to image fluorescent proteins, especially those which absorb in the NIR and IR range of the light spectrum. Additionally, it can take advantage of endogenous contrast to image hemodynamic activity. However, this endogenous contrast is one of the main issues for imaging fluorescent GECIs, GEVIs and voltage/calcium sensitive dyes with FONT. The majority have an absorption profile lying within the visible spectrum of light (400 – 700 nm), where the background absorption of tissues can mask the signal derived from the functional protein/dye.[95] In addition, nearly all indicators have been designed for fluorescence (optical) imaging which may reduce their FONT potential.[85, 89] Interestingly, many of the proteins developed may have been perfect FONT indicators in their first iterations, showing an absorption change in response to their sensing domain with minor fluorescence. The ideal indicator for voltage or calcium imaging with FONT would be one that is good at absorbing light (ideally in the NIR region) and converting it to heat. In many cases this would mean developing GECIs and GEVIs that are not based on GFP as it currently exists but rather a NIR absorbing version or new candidate fluorescent protein. A suitable GECI or GEVI for FONT would also need to act as a poor fluorescent agent (bad at converting light to light), undergo strong absorption changes during neuronal activation and be genetically encoded. Many dyes have shown promise for electrophysiological imaging with FONT, but problems surrounding their loading, distribution and toxicity do not make them suitable for repetitive and repeatable imaging.[77, 79, 97, 98]

The next chapters will center around the investigation and application of an 5D OAT system optimized for FONT and the neuroimaging of genetically encoded electrophysiological indicators at Prof. Razanskys group at IBMI, home of the chair for Biological and Medical Imaging at TUM. This will revolve around determining whether the system can image an entire *ex vivo* murine brain via uniform illumination to provide large scale imaging; how the system can be used to detect the GECI GCaMP6s/f activity; imaging hemodynamic activity with the system; the *in vivo* detection of GCaMP6s/f; and the further testing of two proteins for their suitability for FONT.[99-101] The first is a GEVI known as Butterfly 1.2 (absorbing in the visible range) and the second is a GECI NIR-GECO1, the first NIR GECI of its kind.[15, 102] The testing of the proteins is outlined along with the reasons why they are not currently suitable for *in vivo* FONT and what steps should be taken to realize this.

## References

- [1] T. Morita, M. Asada, and E. Naito, "Contribution of neuroimaging studies to understanding development of human cognitive brain functions," *Frontiers in Human Neuroscience*, vol. 10, p. 464, 2016.
- [2] T. Knöpfel, Y. Gallero-Salas, and C. Song, "Genetically encoded voltage indicators for large scale cortical imaging come of age," *Current opinion in chemical biology*, vol. 27, pp. 75-83, 2015.
- [3] Y. Ma *et al.*, "Wide-field optical mapping of neural activity and brain haemodynamics: considerations and novel approaches," *Philosophical Transactions of the Royal Society B: Biological Sciences*, vol. 371, no. 1705, p. 20150360, 2016.
- [4] S. C. Bosshard, C. Baltes, M. T. Wyss, T. Mueggler, B. Weber, and M. Rudin, "Assessment of brain responses to innocuous and noxious electrical forepaw stimulation in mice using BOLD fMRI," *PAIN®*, vol. 151, no. 3, pp. 655-663, 2010.
- [5] T. R. Insel, S. C. Landis, and F. S. Collins, "The NIH brain initiative," *Science*, vol. 340, no. 6133, pp. 687-688, 2013.
- [6] M. C. Mott, J. A. Gordon, and W. J. Koroshetz, "The NIH BRAIN Initiative: Advancing neurotechnologies, integrating disciplines," *PLoS biology*, vol. 16, no. 11, p. e3000066, 2018.
- [7] H. N. Rubaiy, "A short guide to electrophysiology and ion channels," *Journal of Pharmacy & Pharmaceutical Sciences*, vol. 20, pp. 48-67, 2017.
- [8] J. E. Hall, *Guyton and Hall textbook of medical physiology e-Book*. Elsevier Health Sciences, 2015.
- [9] H. Lodish, A. Berk, S. L. Zipursky, P. Matsudaira, D. Baltimore, and J. Darnell, "Overview of neuron structure and function," *Molecular Cell Biology*, vol. 4, 2000.
- [10] S. Herculano-Houzel, "Scaling of brain metabolism with a fixed energy budget per neuron: implications for neuronal activity, plasticity and evolution," *PloS one*, vol. 6, no. 3, 2011.
- [11] G. J. Stuart and L. M. Palmer, "Imaging membrane potential in dendrites and axons of single neurons," *Pflügers Archiv*, vol. 453, no. 3, pp. 403-410, 2006.
- [12] H. Dana *et al.*, "Thy1-GCaMP6 transgenic mice for neuronal population imaging in vivo," *PloS one*, vol. 9, no. 9, p. e108697, 2014.
- [13] A. Marom, E. Shor, S. Levenberg, and S. Shoham, "Spontaneous activity characteristics of 3D "optonets"," *Frontiers in neuroscience*, vol. 10, p. 602, 2017.
- [14] T. Deffieux, C. Demene, M. Pernot, and M. Tanter, "Functional ultrasound neuroimaging: a review of the preclinical and clinical state of the art," *Current opinion in neurobiology*, vol. 50, pp. 128-135, 2018.
- [15] Y. Mishina, H. Mutoh, C. Song, and T. Knöpfel, "Exploration of genetically encoded voltage indicators based on a chimeric voltage sensing domain," *Frontiers in molecular neuroscience*, vol. 7, p. 78, 2014.
- [16] L. Galvani, *Aloysii Galvani De viribus electricitatis in motu musculari commentarius*. Apud Societatem Typographicam, 1792.
- [17] A. L. Hodgkin and A. F. Huxley, "A quantitative description of membrane current and its application to conduction and excitation in nerve," *The Journal of physiology*, vol. 117, no. 4, pp. 500-544, 1952.
- [18] A. Fletcher, "Action potential: generation and propagation," *Anaesthesia & Intensive Care Medicine*, vol. 12, no. 6, pp. 258-262, 2011.

- [19] L. P. Savtchenko and D. A. Rusakov, "The optimal height of the synaptic cleft," *Proceedings of the National Academy of Sciences*, vol. 104, no. 6, pp. 1823-1828, 2007.
- [20] T. C. Südhof, "Calcium control of neurotransmitter release," *Cold Spring Harbor perspectives in biology*, vol. 4, no. 1, p. a011353, 2012.
- [21] M. Khvotchev, G. Lonart, and T. Südhof, "Role of calcium in neurotransmitter release evoked by  $\alpha$ -latrotoxin or hypertonic sucrose," *Neuroscience*, vol. 101, no. 3, pp. 793-802, 2000.
- [22] A. Verkhratsky and V. Parpura, "History of electrophysiology and the patch clamp," in *Patch-Clamp Methods and Protocols*: Springer, 2014, pp. 1-19.
- [23] Y. Zhao, S. Inayat, D. Dikin, J. Singer, R. Ruoff, and J. B. Troy, "Patch clamp technique: review of the current state of the art and potential contributions from nanoengineering," *Proceedings of the Institution of Mechanical Engineers, Part N: Journal of Nanoengineering and Nanosystems*, vol. 222, no. 1, pp. 1-11, 2008.
- [24] L. A. Annecchino and S. R. Schultz, "Progress in automating patch clamp cellular physiology," *Brain and Neuroscience Advances*, vol. 2, p. 2398212818776561, 2018.
- [25] O. Herreras, "Local field potentials: myths and misunderstandings," *Frontiers in neural circuits*, vol. 10, p. 101, 2016.
- [26] N. A. Steinmetz, C. Koch, K. D. Harris, and M. Carandini, "Challenges and opportunities for large-scale electrophysiology with Neuropixels probes," *Current opinion in neurobiology*, vol. 50, pp. 92-100, 2018.
- [27] E. Ferrea *et al.*, "Large-scale, high-resolution electrophysiological imaging of field potentials in brain slices with microelectronic multielectrode arrays," *Frontiers in neural circuits*, vol. 6, p. 80, 2012.
- [28] E. Masvidal-Codina *et al.*, "High-resolution mapping of infraslow cortical brain activity enabled by graphene microtransistors," *Nature materials*, vol. 18, no. 3, p. 280, 2019.
- [29] B. He, L. Yang, C. Wilke, and H. Yuan, "Electrophysiological Imaging of Brain Activity and Connectivity—Challenges and Opportunities," *IEEE Transactions on Biomedical Engineering*, vol. 58, no. 7, pp. 1918-1931, 2011.
- [30] D. Kim, C. Yeon, E. Chung, and K. Kim, "A non-invasive flexible multi-channel electrode for in vivo mouse EEG recording," in *SENSORS, 2014 IEEE*, 2014, pp. 1111-1114: IEEE.
- [31] M. Lee, D. Kim, H.-S. Shin, H.-G. Sung, and J. H. Choi, "High-density EEG recordings of the freely moving mice using polyimide-based microelectrode," *JoVE (Journal of Visualized Experiments)*, no. 47, p. e2562, 2011.
- [32] C. M. Michel and D. Brunet, "EEG Source Imaging: a practical review of the analysis steps," *Frontiers in neurology*, vol. 10, 2019.
- [33] E. A. DeYoe, P. Bandettini, J. Neitz, D. Miller, and P. Winans, "Functional magnetic resonance imaging (fMRI) of the human brain," *Journal of neuroscience methods*, vol. 54, no. 2, pp. 171-187, 1994.
- [34] W. R. Hendee and E. R. Ritenour, *Medical imaging physics*. John Wiley & Sons, 2003.
- [35] L. Pauling and C. D. Coryell, "The Magnetic Properties and Structure of Hemoglobin, Oxyhemoglobin and Carbonmonoxyhemoglobin," (in eng), *Proceedings of the National Academy of Sciences of the United States of America*, vol. 22, no. 4, pp. 210-216, 1936.
- [36] S.-G. Kim and P. A. Bandettini, "Principles of BOLD functional MRI," in *Functional Neuroradiology*: Springer, 2011, pp. 293-303.

- [37] J. M. Adamczak, T. D. Farr, J. U. Seehafer, D. Kalthoff, and M. Hoehn, "High field BOLD response to forepaw stimulation in the mouse," *Neuroimage*, vol. 51, no. 2, pp. 704-712, 2010.
- [38] S. Boussida, A. S. Traoré, and F. Durif, "Mapping of the brain hemodynamic responses to sensorimotor stimulation in a rodent model: A BOLD fMRI study," *PLoS one*, vol. 12, no. 4, p. e0176512, 2017.
- [39] D. Attwell and C. Iadecola, "The neural basis of functional brain imaging signals," *Trends in neurosciences*, vol. 25, no. 12, pp. 621-625, 2002.
- [40] G. Iannetti and R. G. Wise, "BOLD functional MRI in disease and pharmacological studies: room for improvement?," *Magnetic resonance imaging*, vol. 25, no. 6, pp. 978-988, 2007.
- [41] O. J. Arthurs and S. Boniface, "How well do we understand the neural origins of the fMRI BOLD signal?," *Trends in neurosciences*, vol. 25, no. 1, pp. 27-31, 2002.
- [42] M. Jueptner and C. Weiller, "does measurement of regional cerebral blood flow reflect synaptic activity? Implications for PET and fMRI," *Neuroimage*, vol. 2, no. 2, pp. 148-156, 1995.
- [43] C. Hoyer, N. Gass, W. Weber-Fahr, and A. Sartorius, "Advantages and challenges of small animal magnetic resonance imaging as a translational tool," *Neuropsychobiology*, vol. 69, no. 4, pp. 187-201, 2014.
- [44] X. L. Dean-Ben, S. Gottschalk, B. Mc Larney, S. Shoham, and D. Razansky, "Advanced optoacoustic methods for multiscale imaging of in vivo dynamics," (in English), *Chemical Society Reviews*, vol. 46, no. 8, pp. 2158-2198, Apr 21 2017.
- [45] G. H. Glover, "Overview of functional magnetic resonance imaging," *Neurosurgery Clinics*, vol. 22, no. 2, pp. 133-139, 2011.
- [46] P. E. Yoo *et al.*, "7T-fMRI: Faster temporal resolution yields optimal BOLD sensitivity for functional network imaging specifically at high spatial resolution," *Neuroimage*, vol. 164, pp. 214-229, 2018.
- [47] J. P. Culver, A. M. Siegel, J. J. Stott, and D. A. Boas, "Volumetric diffuse optical tomography of brain activity in rat," in *Biomedical Topical Meeting*, 2004, p. WF1: Optical Society of America.
- [48] L. Tian *et al.*, "Imaging neural activity in worms, flies and mice with improved GCaMP calcium indicators," *Nature methods*, vol. 6, no. 12, p. 875, 2009.
- [49] W. Akemann, M. Sasaki, H. Mutoh, T. Imamura, N. Honkura, and T. Knöpfel, "Two-photon voltage imaging using a genetically encoded voltage indicator," *Scientific reports*, vol. 3, p. 2231, 2013.
- [50] I. Ferezou, F. Matyas, and C. C. Petersen, "Imaging the brain in action: real-time voltage-sensitive dye imaging of sensorimotor cortex of awake behaving mice," in *In Vivo Optical Imaging of Brain Function. 2nd edition*: CRC Press/Taylor & Francis, 2009.
- [51] B. J. Baker *et al.*, "Imaging brain activity with voltage-and calcium-sensitive dyes," *Cellular and molecular neurobiology*, vol. 25, no. 2, pp. 245-282, 2005.
- [52] L.-D. Liao *et al.*, "Neurovascular coupling: in vivo optical techniques for functional brain imaging," *Biomedical engineering online*, vol. 12, no. 1, p. 38, 2013.
- [53] J. Oh, C. Lee, and B.-K. Kaang, "Imaging and analysis of genetically encoded calcium indicators linking neural circuits and behaviors," *The Korean Journal of Physiology & Pharmacology*, vol. 23, no. 4, pp. 237-249, 2019.
- [54] T. Shuman *et al.*, "Breakdown of spatial coding and neural synchronization in epilepsy," *bioRxiv*, p. 358580, 2018.

- [55] E. C. Emery, A. P. Luiz, S. Sikandar, R. Magnúsdóttir, X. Dong, and J. N. Wood, "In vivo characterization of distinct modality-specific subsets of somatosensory neurons using GCaMP," *Science advances*, vol. 2, no. 11, p. e1600990, 2016.
- [56] D. A. Storace, L. B. Cohen, and Y. Choi, "Using Genetically Encoded Voltage Indicators (GEVIs) to study the input-output transformation of the mammalian olfactory bulb," *Frontiers in cellular neuroscience*, vol. 13, p. 342, 2019.
- [57] Q. Chen *et al.*, "Imaging neural activity using Thy1-GCaMP transgenic mice," *Neuron*, vol. 76, no. 2, pp. 297-308, 2012.
- [58] H. Dana *et al.*, "High-performance calcium sensors for imaging activity in neuronal populations and microcompartments," *Nature methods*, 2019.
- [59] D. G. Ouzounov *et al.*, "In vivo three-photon imaging of activity of GCaMP6-labeled neurons deep in intact mouse brain," *Nature methods*, vol. 14, no. 4, p. 388, 2017.
- [60] N. G. Horton, K. Wang, C.-C. Wang, and C. Xu, "In vivo three-photon imaging of subcortical structures of an intact mouse brain using quantum dots," in *The European Conference on Lasers and Electro-Optics*, 2013, p. CL\_4\_1: Optical Society of America.
- [61] Z. J. Wang, T.-T. Chang, and R. Slauter, "Use of Imaging for Preclinical Evaluation," in *A Comprehensive Guide to Toxicology in Nonclinical Drug Development*: Elsevier, 2017, pp. 921-938.
- [62] A. Nimmerjahn, "Optical window preparation for two-photon imaging of microglia in mice," *Cold Spring Harbor Protocols*, vol. 2012, no. 5, p. pdb. prot069286, 2012.
- [63] A. Holtmaat *et al.*, "Long-term, high-resolution imaging in the mouse neocortex through a chronic cranial window," *Nature protocols*, vol. 4, no. 8, p. 1128, 2009.
- [64] Y.-J. Zhao *et al.*, "Skull optical clearing window for in vivo imaging of the mouse cortex at synaptic resolution," *Light: Science & Applications*, vol. 7, no. 2, p. 17153, 2018.
- [65] M. Alieva, L. Ritsma, R. J. Giedt, R. Weissleder, and J. van Rheenen, "Imaging windows for long-term intravital imaging: General overview and technical insights," *Intravital*, vol. 3, no. 2, p. e29917, 2014.
- [66] G. Meng *et al.*, "High-throughput synapse-resolving two-photon fluorescence microendoscopy for deep-brain volumetric imaging in vivo," *Elife*, vol. 8, p. e40805, 2019.
- [67] M. Wachowiak, C. X. Falk, L. B. Cohen, and M. R. Zochowski, "Voltage and Calcium Imaging of Brain Activity: Examples from the Turtle and the Mouse," in *Brain Mapping: The Methods*: Elsevier, 2002, pp. 77-95.
- [68] M. S. Rad *et al.*, "Voltage and calcium imaging of brain activity," *Biophysical journal*, vol. 113, no. 10, pp. 2160-2167, 2017.
- [69] W. Akemann, H. Mutoh, A. Perron, Y. K. Park, Y. Iwamoto, and T. Knöpfel, "Imaging neural circuit dynamics with a voltage-sensitive fluorescent protein," *Journal of neurophysiology*, vol. 108, no. 8, pp. 2323-2337, 2012.
- [70] N. Helassa *et al.*, "Ultrafast glutamate sensors resolve high-frequency release at Schaffer collateral synapses," *Proceedings of the National Academy of Sciences*, vol. 115, no. 21, pp. 5594-5599, 2018.
- [71] A. Miyawaki *et al.*, "Fluorescent indicators for Ca<sup>2+</sup> based on green fluorescent proteins and calmodulin," *Nature*, vol. 388, no. 6645, p. 882, 1997.
- [72] R. Y. Tsien, "The 2009 Lindau Nobel Laureate Meeting: Roger Y. Tsien, Chemistry 2008," *JoVE (Journal of Visualized Experiments)*, no. 35, p. e1575, 2010.

- [73] G. S. Baird, D. A. Zacharias, and R. Y. Tsien, "Circular permutation and receptor insertion within green fluorescent proteins," *Proceedings of the National Academy of Sciences*, vol. 96, no. 20, pp. 11241-11246, 1999.
- [74] D. C. Prasher, V. K. Eckenrode, W. W. Ward, F. G. Prendergast, and M. J. Cormier, "Primary structure of the *Aequorea victoria* green-fluorescent protein," *Gene*, vol. 111, no. 2, pp. 229-233, 1992.
- [75] D. Yarbrough, R. M. Wachter, K. Kallio, M. V. Matz, and S. J. Remington, "Refined crystal structure of DsRed, a red fluorescent protein from coral, at 2.0-Å resolution," *Proceedings of the National Academy of Sciences*, vol. 98, no. 2, pp. 462-467, 2001.
- [76] M. Canepari, K. Vogt, and D. Zecevic, "Combining voltage and calcium imaging from neuronal dendrites," *Cellular and molecular neurobiology*, vol. 28, no. 8, p. 1079, 2008.
- [77] R. Homma *et al.*, "Wide-field and two-photon imaging of brain activity with voltage and calcium-sensitive dyes," in *Dynamic Brain Imaging*: Springer, 2009, pp. 43-79.
- [78] O. Garaschuk, R.-I. Milos, and A. Konnerth, "Targeted bulk-loading of fluorescent indicators for two-photon brain imaging in vivo," *Nature protocols*, vol. 1, no. 1, p. 380, 2006.
- [79] R. W. Pak *et al.*, "Voltage-sensitive dye delivery through the blood brain barrier using adenosine receptor agonist regadenoson," *Biomedical optics express*, vol. 9, no. 8, pp. 3915-3922, 2018.
- [80] L. L. Looger and O. Griesbeck, "Genetically encoded neural activity indicators," *Current opinion in neurobiology*, vol. 22, no. 1, pp. 18-23, 2012.
- [81] T. L. Daigle *et al.*, "A suite of transgenic driver and reporter mouse lines with enhanced brain-cell-type targeting and functionality," *Cell*, vol. 174, no. 2, pp. 465-480. e22, 2018.
- [82] T.-W. Chen *et al.*, "Ultrasensitive fluorescent proteins for imaging neuronal activity," *Nature*, vol. 499, no. 7458, p. 295, 2013.
- [83] J. Nakai, M. Ohkura, and K. Imoto, "A high signal-to-noise Ca<sup>2+</sup> probe composed of a single green fluorescent protein," *Nature biotechnology*, vol. 19, no. 2, p. 137, 2001.
- [84] J. Akerboom *et al.*, "Optimization of a GCaMP Calcium Indicator for Neural Activity Imaging," *The Journal of Neuroscience*, vol. 32, no. 40, pp. 13819-13840, 2012.
- [85] X. R. Sun *et al.*, "Fast GCaMPs for improved tracking of neuronal activity," *Nature Communications*, vol. 4, no. 1, p. 2170, 2013/07/18 2013.
- [86] J. Akerboom *et al.*, "Crystal structures of the GCaMP calcium sensor reveal the mechanism of fluorescence signal change and aid rational design," *Journal of biological chemistry*, vol. 284, no. 10, pp. 6455-6464, 2009.
- [87] A. I. Kostyuk, A. D. Demidovich, D. A. Kotova, V. V. Belousov, and D. S. Bilan, "Circularly Permuted Fluorescent Protein-Based Indicators: History, Principles, and Classification," *International journal of molecular sciences*, vol. 20, no. 17, p. 4200, 2019.
- [88] Q. Wang, B. Shui, M. I. Kotlikoff, and H. Sondermann, "Structural basis for calcium sensing by GCaMP2," *Structure*, vol. 16, no. 12, pp. 1817-1827, 2008.
- [89] K. D. Piatkevich *et al.*, "A robotic multidimensional directed evolution approach applied to fluorescent voltage reporters," *Nature chemical biology*, vol. 14, no. 4, p. 352, 2018.
- [90] Y. Yang *et al.*, "Improved calcium sensor GCaMP-X overcomes the calcium channel perturbations induced by the calmodulin in GCaMP," *Nature Communications*, vol. 9, no. 1, p. 1504, 2018/04/17 2018.

- [91] X. Gu, E. C. Olson, and N. C. Spitzer, "Spontaneous neuronal calcium spikes and waves during early differentiation," *Journal of Neuroscience*, vol. 14, no. 11, pp. 6325-6335, 1994.
- [92] H. H. Yang and F. St-Pierre, "Genetically encoded voltage indicators: opportunities and challenges," *Journal of Neuroscience*, vol. 36, no. 39, pp. 9977-9989, 2016.
- [93] F. Ali and A. C. Kwan, "Interpreting in vivo calcium signals from neuronal cell bodies, axons, and dendrites: a review," *Neurophotonics*, vol. 7, no. 1, p. 011402, 2019.
- [94] A. S. Abdelfattah *et al.*, "A bright and fast red fluorescent protein voltage indicator that reports neuronal activity in organotypic brain slices," *Journal of Neuroscience*, vol. 36, no. 8, pp. 2458-2472, 2016.
- [95] Y. Bando, C. Grimm, V. H. Cornejo, and R. Yuste, "Genetic voltage indicators," *BMC biology*, vol. 17, no. 1, p. 71, 2019.
- [96] Z. Chen, T. Truong, and H.-w. Ai, "Illuminating brain activities with fluorescent protein-based biosensors," *Chemosensors*, vol. 5, no. 4, p. 32, 2017.
- [97] H. K. Zhang *et al.*, "Listening to membrane potential: photoacoustic voltage-sensitive dye recording," *Journal of biomedical optics*, vol. 22, no. 4, p. 045006, 2017.
- [98] B. Rao, R. Zhang, L. Li, J. Y. Shao, and L. V. Wang, "Photoacoustic imaging of voltage responses beyond the optical diffusion limit," *Sci Rep*, vol. 7, no. 1, p. 2560, May 31 2017.
- [99] B. Mc Larney, J. Rebling, Z. Chen, X. L. Deán-Ben, S. Gottschalk, and D. Razansky, "Uniform light delivery in volumetric optoacoustic tomography," *Journal of Biophotonics*, vol. 12, no. 6, p. e201800387, 2019.
- [100] S. Gottschalk *et al.*, "Isolated Murine Brain Model for Large-Scale Optoacoustic Calcium Imaging," *Frontiers in neuroscience*, vol. 13, p. 290, 2019.
- [101] S. Gottschalk *et al.*, "Rapid volumetric optoacoustic imaging of neural dynamics across the mouse brain," *Nature Biomedical Engineering*, vol. 3, no. 5, pp. 392-401, 2019/05/01 2019.
- [102] Y. Qian *et al.*, "A genetically encoded near-infrared fluorescent calcium ion indicator," *Nature Methods*, 2019/01/21 2019.

## 2. Uniform light delivery in volumetric optoacoustic tomography

### 2.1 Summary and author contribution

This work presents a rapidly prototyped fuse deposition modelling based solution to provide uniform illumination for volumetric optoacoustic tomography. Light delivery in OAT is an essential component for both accurate image reconstruction and quantification. The majority of OAT setups do not correctly account for the illumination profile and thus acquire suboptimal results. This often results in a reduced field of view as in the case of the detector here where only half of the volume was correctly illuminated. My idea was that by combining 3D printing and ray simulation the optimal location of optical fibers could be achieved to enable illuminating the entire FOV of the transducer. The main challenge with this project was to effectively seal a hollow plastic printed chamber to make it waterproof whilst also ensuring its strength to accurately hold both the transducer and fibers in place. Numerous prototypes could be quickly trialed and improved upon leading to an experimental setup that doubled the effective field of view of the setup. The illumination profile was in good agreement with simulated data for uniform illumination and allowed single laser pulse acquisitions of the murine heart and brain. This provided high resolution anatomical images of both organs.

This work combined 3D design and printing, *ex vivo* animal imaging work, understanding the fundamental limitations of OAT and provides a solution for uniform illumination for volumetric OAT. The developed system provided an easy-to-use platform that found uses in functional brain and heart imaging and highlights the importance of correct sample illumination in OAT.

My contribution to the presented manuscript was the following:

**Conception and design:** The setup and experiment were designed by Prof. Razansky, Dr. Rebling and I.

**Development of methodology:** The implementation, printing, sealing and testing of the setup was carried out by Dr. Rebling and I.

**Acquisition of data:** I performed the imaging, reconstruction and analysis of the data.

**FULL ARTICLE**

# Uniform light delivery in volumetric optoacoustic tomography

Benedict Mc Larney<sup>1,2</sup>  | Johannes Rebling<sup>1,2,3,4</sup> | Zhenyue Chen<sup>1</sup> | Xosé Luís Deán-Ben<sup>1,3,4</sup> | Sven Gottschalk<sup>1</sup>  | Daniel Razansky<sup>1,2,3,4\*</sup> 

<sup>1</sup>Institute for Biological and Medical Imaging, Helmholtz Center Munich, Neuherberg, Germany

<sup>2</sup>Faculty of Medicine, Technical University of Munich, Munich, Germany

<sup>3</sup>Faculty of Medicine and Institute of Pharmacology and Toxicology, University of Zurich, Zurich, Switzerland

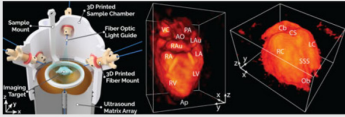
<sup>4</sup>Institute for Biomedical Engineering and Department of Information Technology and Electrical Engineering, ETH Zurich, Zurich, Switzerland

**\*Correspondence**

Daniel Razansky, Institute for Biomedical Engineering, University and ETH Zurich, Wolfgang-Pauli-Str. 27, 8093 Zurich, Switzerland. Email: daniel.razansky@uzh.ch

**Funding information**

European Research Council, Grant/Award Number: ERC-2015-CoG-682379



Accurate image reconstruction in volumetric optoacoustic tomography implies the efficient generation and collection of ultrasound signals around the imaged object. Non-uniform delivery of the excitation light is a common problem in optoacoustic imaging often leading to a diminished field of view, limited dynamic range and penetration, as well as impaired quantification abilities. Presented here is an optimized illumination concept for volumetric tomography that utilizes additive manufacturing via 3D printing in combination with custom-made optical fiber illumination. The custom-designed sample chamber ensures convenient access to the imaged object along with accurate positioning of the sample and a matrix array ultrasound transducer used for collection of the volumetric image data. Ray tracing is employed to optimize the positioning of the individual fibers in the chamber. Homogeneity of the generated light excitation field was confirmed in tissue-mimicking agar spheres. Applicability of the system to image entire mouse organs *ex vivo* has been showcased. The new approach showed a clear advantage over conventional, single-sided illumination strategies by eliminating the need to correct for illumination variances and resulting in enhancement of the effective field of view, greater penetration depth and significant improvements in the overall image quality.

**KEYWORDS**

3d-printing, fibers, illumination, imaging, optoacoustics, organs

## 1 | INTRODUCTION

In optoacoustic (OA) imaging and tomography, tissue contrast arises from the absorption of intermittent (pulsed) light that is transformed into a broadband ultrasound (US) wave field. There are many advantages in this technique over conventional imaging methods such as magnetic resonance imaging and US. Examples of such advantages are improved contrast along with higher spatiotemporal resolution and the ability to select for and quantify separate biological components based on their light absorption [1, 2]. Numerous embodiments have been suggested for OA imaging of areas located at depths ranging from superficial layers to

centimeters within biological tissues [3–6]. In all implementations, the optimal illumination strategy implies confining the excitation light to the region of interest, while avoiding light exposure levels that may cause cell toxicity or other damage to the imaged tissues [7, 8]. For depths beyond the ballistic regime of light (~1 mm in biological tissues), image formation relies on acoustic image reconstruction methods. Light pulses in the millijoule range are typically required to achieve at least several millimeters of imaging depth in the near-infrared spectral window without employing extensive signal averaging [9]. Real-time 2D and 3D imaging can then be achieved via parallel acquisition of signals by means of US arrays [2, 10].

At present, curved US arrays employing cylindrically focused or spherical matrix geometries are fostering the

clinical translation of this technology by combining powerful real-time hand-held imaging capabilities with highly compelling image quality [11–17]. The unique advantages of the curved array technology for optimal collection of high-quality OA tomographic data have also been exploited in many applications involving small animals. For example, hemodynamic changes in the entire brain of rodents have been mapped via single-wavelength and multispectral light excitation [17–19]. By delivering light with pulse repetition frequencies of hundreds or thousands of Hertz, it was possible to accurately track the motion of freely swimming zebrafish larvae in 3D [20, 21]. Imaging of isolated brains of adult zebrafish has further revealed neural activity patterns by capturing absorption changes of genetically encoded calcium indicators [22].

To this end, several experimental and algorithmic strategies have been attempted in order to mitigate image artifacts related to suboptimal object illumination [23–28]. Here, we introduce an optimized design for light delivery in three-dimensional OA tomography based on the combination of a custom-made optical fiber bundle with a 3D-printed (fused deposition modeling (FDM)) sample chamber providing homogenous sample illumination.

## 2 | MATERIALS AND METHODS

### 2.1 | Fiber bundle light delivery

The proposed design is based on an in-house fabricated optical fiber bundle. This bundle allows a more flexible and cost-effective light-guiding approach in comparison to commonly used bundles comprised of thousands of small multimode fibers with fused end-facets. Homogenous light delivery to the imaging target is achieved with a few, large core, step-index multimode fibers. The optimum number and arrangement of the individual fibers to provide uniform illumination on a spherical surface with a 10-mm diameter were determined with ray-tracing simulations performed in TracePro (version 7.3; Lambda Research Corporation, Littleton, Massachusetts). The simulations included the fiber's characteristics (numerical aperture (NA), core diameter) as well as the geometrical constraints posed by the transducer array's geometry and accessibility for sample placement. The estimated optimal arrangement of seven fibers is shown (Figure 1A and B). This arrangement is based on the simulation results of the detector geometries and possible fiber placement around the detector (Figure S1). The distal ends of the individual fibers were arranged in three groups with respect to the spherical array (Figure S2). The first group consisted of a single fiber illuminating the sample from below through an aperture in the transducer. A further two groups, comprised of three fibers each were positioned above and around the sample with equal azimuthal separation of 120°. The lower three fibers were positioned at an

elevational angle of 5.7° with respect to the horizontal plane, while the second group was set at a steeper angle of 37°. Both groups were rotated in the azimuthal direction by 60° with respect to each other (see Figure S2).

The specifications of the fibers used in the proposed design are summarized in Table S1. The bundle is comprised of seven multimode step-index fibers, each with a 600- $\mu\text{m}$  core diameter (FT600EMT; Thorlabs, Newton, New Jersey) and with a total length of approximately 1.5 m. These fibers offer a broad transmission bandwidth (400 to 2200 nm). Their technology-enhanced clad silica cladding makes them particularly mechanically robust, further providing improved bending performance and a large NA of 0.39 for efficient coupling of the excitation light at a reduced cost in comparison to conventional silica-clad fibers [29]. The individual fibers were stripped of their coating to increase the fill factor at the coupling facet (i.e. the percentage area of the proximal end of the fiber into which light can be coupled which is the total area of fiber cores divided by the sum of fiber cores). They were bundled and connectorized to a conventional SMA905 multimode fiber connector (11580A; Thorlabs). The connector's central bore was drilled to a size of 2 mm to accommodate the circularly packed fibers, which were glued in place using high-temperature epoxy (353NDPK; Thorlabs). The fiber end-facets were polished to optical quality using a conventional fiber polishing procedure with a final grit size of 0.3  $\mu\text{m}$  [30]. The resulting proximal end-facet is shown in Figure 1A). The separate fibers were then additionally protected using a reinforced jacket (FT020; Thorlabs), and the individual sensitive glass end-facets of the distal end were cleaved and protected using small steel ferrules. The fiber core diameter of 600  $\mu\text{m}$  provides good mechanical stability, whilst keeping the fibers sufficiently flexible for handling and alignment. Using only seven fibers results in a bundle with sufficient light transmission (64% theoretical transmission), yet making its assembly, handling and alignment at the distal end more straightforward than for bundles with a larger number of fibers.

### 2.2 | 3D-printed sample chamber

A watertight sample chamber for mounting the US transducer array, the optical fibers and the imaged sample was designed and manufactured while accounting for mechanical constraints as well as for the optimum fiber positioning, as previously described. The base of the sample chamber is a cylinder having the diameter of the US transducer array casing and with watertight double O-ring seals between the chamber and the transducer (Figure 1C). The sample chamber has further openings through which separate 3D-printed fiber mounts were inserted under the previously determined optimal angles. The imaged samples were placed in the field of view (FOV) of the transducer on a thin polyethylene film clamped onto a 3D-printed ring mount. This film allowed unobstructed propagation of the OA signals toward the US

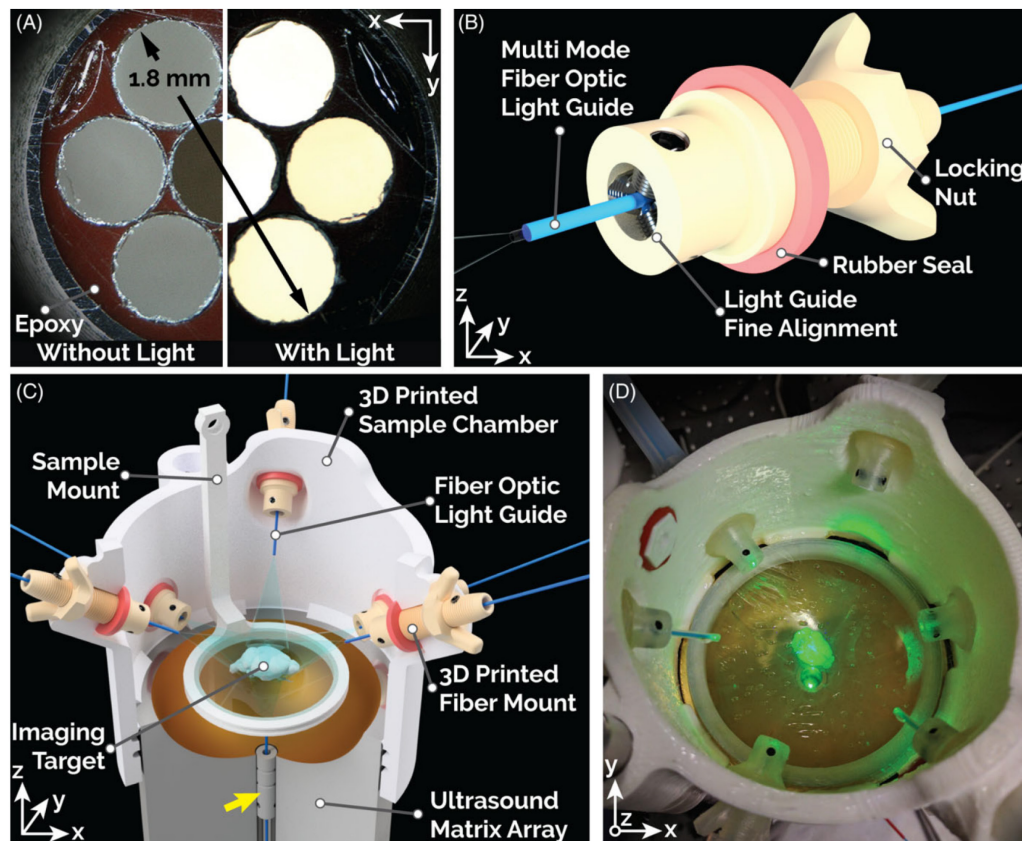


**FIGURE 1** (A) Fabricated and polished fiber bundle (coupling end) with a final diameter of 1.8 mm. It is comprised of seven 600- $\mu\text{m}$  multimode glass fibers. (B) Enlarged rendering of the fiber mount including seals, alignment bolts and the fiber itself. (C) Rendering of the assembly of the entire holder, ultrasound matrix array transducer and the imaged sample. The yellow arrow indicates the single fiber used for single side illumination. For uniform illumination all seven fibers were used. (D) Color photograph of the printed, sealed and assembled 3D-printed holder accommodating the transducer

transducer active surface, while holding the sample in place (Figure 1C).

The separately designed fiber mounts (Figure 1B) and Figure S2) enable a watertight, adjustable and interchangeable fixation for the individual fiber ends. They are comprised of a central cylinder with a rubber sealing and an external M10 thread onto which a 3D-printed locking nut for a watertight fixation of the mount to the sample chamber is placed. The fibers protrude through a central hole in the fiber mount where they were fixed near the end with an M4 plastic set-screw (not shown). The end of the mount facing the sample additionally features three set-screws for fine-alignment of the fiber position. These fine-alignment screws were used prior to the imaging experiments to ensure a homogenous illumination of the sample in the FOV of the US transducer array.

Computer-aided design (CAD) was performed using Inventor Professional 2017 (Autodesk, San Rafael, California). All 3D-printing was carried out in-house using two separate FDM 3D-printers. The sample chamber was manufactured using an RF1000 3D-printer (Conrad Electronic SE, Hirschau, Germany) with a large 0.6 mm nozzle. The large nozzle diameter results in fast printing speeds with improved mechanical strength. The smaller parts, such as the fiber and sample mounts and the locking nuts, were printed using an Ultimaker 2+ 3D-printer (Ultimaker, Geldermalsen, Netherlands) with a 0.2 mm nozzle diameter. This small nozzle provided the required accuracy for these small parts. All parts were prepared for printing using Simplify3D 3.0 software (Simplify3D, Cincinnati, Ohio). The threads on the fiber mounts and in the locking nuts were cut in the 3D-printed parts using conventional metal taps and dies.

### 2.3 | Volumetric OA tomography

A detailed description of the OA signal acquisition protocol is available elsewhere and is briefly summarized here for the sake of completeness [31]. The spherical matrix array transducer consists of 512 circular individual detection elements having a diameter of 2.5 mm and >80% detection bandwidth around a central frequency of 5 MHz (Imasonic SaS, Voray, France). The elements are distributed along a spherical surface with a 40-mm radius and  $140^\circ$  of angular coverage ( $1.31\pi$  solid angle). The OA signals captured by all the array elements were simultaneously digitized at 40 mega samples per second with a custom-made 512-channel data acquisition unit (Falkenstein Mikrosysteme GmbH, Taufkirchen, Germany). Optical excitation was provided with an optical parametric oscillator-based laser (SpitLight; Innolas Laser GmbH, Krailling, Germany), whose Q-switch output was used for triggering the signal acquisition. The laser beam was coupled into the proximal end (Figure 1A) of the custom-made fiber bundle using an aspheric lens ( $f = 50$  mm, AL2550M; Thorlabs). The fiber mounts were secured in the sample chamber, and the individual fiber ends were adjusted and fixed in place for optimal illumination. The US transducer array was placed at the bottom of the sample chamber, and the chamber was filled with water to ensure acoustic coupling between the sample and transducer. For single-sided illumination, only the fiber marked located within the detector was used (yellow arrow in Figure 1A). The laser was tuned to a wavelength of 532 nm for sphere phantom imaging, a highly absorbing wavelength for blood and commonly used for phantom testing in OA tomography [32, 33]. Excitation wavelength of 590 nm was used for both heart and brain imaging, as it has been previously shown to attain high contrast for elucidating organ structures [6]. The laser was operated at a pulse repetition frequency of 10 Hz. The total per-pulse energy at the output of the fiber bundle was measured as 7.7 mJ (approximately 1.1 mJ per fiber, 48% coupling efficiency). Visualization in real-time during data acquisition was enabled by a graphics processing unit implementation of a back-projection formula [34].

### 2.4 | Phantom preparation and imaging

Illumination uniformity with the proposed design was first tested by imaging a spherical, tissue-mimicking agar phantom. This phantom was designed to mimic highly absorbing biological tissue over a broad range of visible wavelengths in order to easily determine the uniformity of the illumination across the surface of the sphere. For this, an agar solution (1.5% agar powder dissolved in distilled water, 30391049; ThermoFisher Scientific, Waltham, Massachusetts) was mixed to contain a final concentration of 6% Intralipid from a 20% emulsion (68890-65-3; SigmaAldrich, St. Louis, Missouri) to mimic highly scattering tissue with reduced scattering coefficient  $\mu'_s \sim 10 \text{ cm}^{-1}$  [33]. Black India

ink (Higgins Ink, Leeds, Massachusetts) with an optical absorption coefficient  $\mu_a \sim 4 \text{ cm}^{-1}$  was further added to the agar solution to simulate absorption of blood in the visible range [32]. This liquid solution was injected into a custom-made spherical polyvinyl chloride mold. The solidified spherical phantom was then removed from the mold, placed in the sample chamber and imaged as described previously.

The resolution of the system was tested by randomly embedding spheres with an approximate diameter of 90  $\mu\text{m}$  (BKPMS-1.2 90-106  $\mu\text{m}$ ; Black Paramagnetic Polyethylene Microspheres; Cospheric, Santa Barbara, California) in a cylindrical phantom with 16 mm diameter consisting of 1.5% agar dissolved in distilled water (30391049; ThermoFisher Scientific). The microspheres were mainly distributed across a cross-section of the phantom, which was placed in the center of the detector's FOV and scanned along the axial direction with 0.5 mm steps. Imaging was performed at 532 nm. The resolution was estimated as the mean square difference between the measured full width at half maximum (FWHM) of a microsphere and its diameter. Note that the measured FWHM may be affected by negative values in the images associated to limited-view effects, particularly along the  $z$ -direction [35]. Thereby, the actual resolution of the system can be slightly lower.

### 2.5 | Numerical simulation

A numerical simulation was performed in order to facilitate interpretation of the obtained experimental results in tissue phantoms. For this, OA images corresponding to a uniformly illuminated sphere with the same optical properties as the one used in the experiments were reconstructed. The light fluence distribution within the sphere was estimated considering the light diffusion approximation using a constant fluence on the surface of the sphere as a boundary condition. Under these assumptions, the light fluence distribution is described by a modified spherical Bessel function given by

$$U(r) = \frac{U_0}{\frac{\sinh(kR)}{kR}} \times \frac{\sinh(kr)}{kr} \quad (1)$$

where  $U_0$  is the fluence at the surface of the sphere,  $r$  is the distance from the center of the sphere with radius  $R$ . The photon diffusion wavenumber is defined as  $k = \sqrt{\mu_a/D}$ , where the photon diffusion coefficient  $D = 1/3(\mu_a + \mu'_s)$  and  $\mu_a$  and  $\mu'_s$  are the absorption and reduced scattering coefficients, respectively. Considering a uniform absorption coefficient and a uniform Grüneisen parameter, the spatial distribution of the initial OA pressure is equivalent to that of the light fluence. The OA signals were then estimated with a discretized version of the time-domain OA model [36]. Note that limited-view effects are expected to affect the reconstructed images for the angular coverage of the array ( $140^\circ$ ), so that a reconstructed uniform sphere is not expected. The detection array was modeled by splitting its  $140^\circ$  spherical

aperture into 512 individual elements, 2.5 mm diameter each. The effects of the finite aperture of the transducer elements (~2.5 mm in diameter) was accounted for by segmenting the surface of each element into 150 subelements and summing up the corresponding signals across the element [37].

The simulated datasets were reconstructed using a model-based reconstruction iterative method, as reported elsewhere [36]. Prior to reconstruction, the signals were band-pass filtered between 0.1 and 6 MHz. Note that the model used for the tomographic reconstruction was also used as a forward model for simulations, but filtering prevents the inverse crime. The experimental signals were further deconvolved with the impulse response of the transducer. All reconstructions were performed on a  $15 \times 15 \times 15 \text{ mm}^3$  3D Cartesian grid consisting of  $150 \times 150 \times 150$  voxels.

## 2.6 | Biological tissues imaging

The system's performance was further demonstrated in actual biological samples by imaging a murine heart and brain *ex vivo*.

### 2.6.1 | Brain imaging

The brain was extracted from a female wild type CD1 mouse (approximately 10 weeks old). The mouse was euthanized using a lethal dose of Ketamine/Xylazine. Once euthanasia was completed, an incision was made along the *linea alba* for the length of the *peritoneum*. The chest cavity was opened and the mouse was perfused with artificial cerebrospinal fluid (ACSF) via insertion of a needle into the left ventricle. The right ventricle of the heart was then cut to allow fluid to flow out. Perfusion was carried out until the liver turned white, indicating complete blood removal. The solution was then changed to high sucrose-containing ACSF for further perfusion and finally to paraformaldehyde (PFA) [38]. Next, the head was removed via decapitation. After removal of the skull, the brain was isolated and stored in high-sucrose ACSF. Due to the orientation of the brain within the skull cavity a portion of the olfactory bulbs detached from the structure, and hence is reduced in size in comparison to a secondary brain which is shown in Figure S3. The brain was then quick frozen and stored at  $-80^\circ\text{C}$ , with the sucrose preventing the formation of ice crystals. Prior to the imaging experiment, the brain was defrosted and imaged at room temperature.

### 2.6.2 | Heart imaging

For heart isolation, a mouse with the same characteristics as described in Section 2.6.1 was euthanized. Once euthanasia was completed, the chest cavity was opened and the heart was extracted. Excess fatty tissue around the heart was cut away. The heart was placed in phosphate-buffered saline (PBS) buffer until it stopped beating, so that any remaining

blood in the heart was removed. The heart was then placed into PFA for fixation. Imaging was then carried out in PBS at room temperature.

## 3 | RESULTS

### 3.1 | Phantom imaging

The maximum intensity projections (MIPs) of the reconstructed OA images from a scattering and absorbing sphere phantom are shown in Figure 2. The top row displays projections along the  $z$ -axis, while the second row shows side views with projections along the  $y$ -axis. The third row shows single  $x$ - $y$  slices through the sphere at a depth of 5 mm from the surface. The normalized maximum intensity for each  $z$  slice (circumference) of the respective sphere is shown in Figure 2J). Automated code was implemented to fit a circle to the circumference and plot its corresponding maximum signal intensity. Clearly, only part of the hemisphere facing the illuminating bundle is visible in the images obtained with single-sided illumination (Figure 2A, D and G). In this case, the image quality is flawed by the excessive dispersion of OA signal magnitude, whereas the intensity values decay rapidly with increasing distance from the fiber (Figure 2A, D, G and J, blue line) resulting in a “dark side of the moon” effect. The corresponding images obtained for the uniformly illuminated sphere are shown (Figure 2B, E and H). Here, pressure waves are generated equally along the entire sphere surface since the illumination is evenly distributed across the object (Figure 2J, green line). The signal intensity at the top side of the sphere ( $z \sim 8 \text{ mm}$ ), corresponding to the most distant area from the transducer, is approximately 75% of the maximum. In comparison, the reconstructed image for single side illumination has a signal intensity at this position of less than 5% of the maximum (Figure 2J). Moreover, the images reconstructed from simulated datasets closely resemble the experimental results (Figure 2C, F and I). Note that both the experimentally and theoretically rendered images exhibit significant signal decay toward the central area (equator) of the sphere (Figure 2J), green and orange lines). However, these effects are not illumination related and are rather attributed to the limited-view artifact caused by the restricted  $140^\circ$  tomographic coverage of the spherical array detector [35, 39]. Herein, we provide a detailed characterization of the resolution at different points within the FOV. It is shown that the estimated resolution along all directions is generally confined in the 150- to 250- $\mu\text{m}$  range for a cylindrical field of view of 10-mm length and 10-mm diameter (Figure S4).

### 3.2 | Tissue imaging

MIPs of the reconstructed OA images of the *ex vivo* murine brain and heart are shown in Figures 3 and 4. Both the brain and the heart can be visualized in their entirety with key anatomical structures clearly discernible, including both atria and

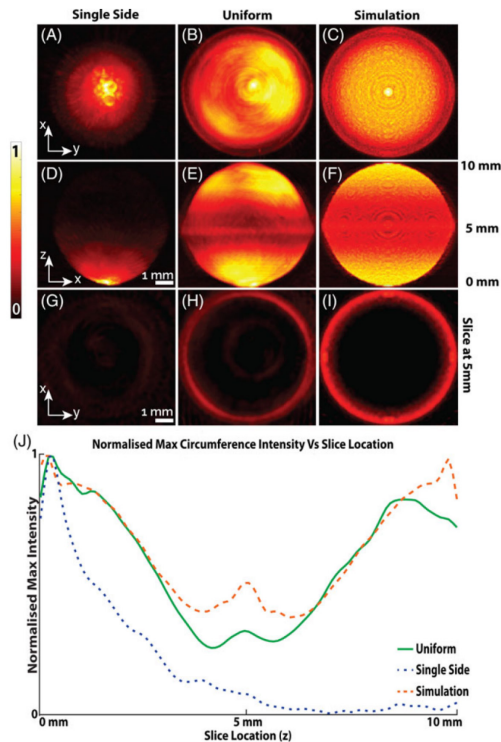


**FIGURE 2** Comparison between experimental and simulated volumetric optoacoustic reconstructions. (A)–(C) MIP images looking from the top of each sphere for the single side, uniform and simulated (perfect) illumination scenarios, respectively. (D)–(F) The corresponding side view MIPs. (G)–(I) Single cross-sectional slices through the centre of each sphere. (J) Max circumference signal intensity in each Z slice of the respective spheres

ventricles as well as the coronary artery in the heart (Figure 3A and B) [40–44]. In the brain, both right and left cortices, the medulla and the cerebellum are visible along with additional deep seated structures, as labeled (Figure 4A and B) [45, 46]. In addition, individual image cross sections taken from both organs (Figures 3C–E and 4C–E) show that superficial as well as deep structures can be clearly discerned when referenced to widely available atlases [39–45] and gross anatomical images (Figure S3A–C). The relatively uniform OA signal and contrast exhibited in the cross-sectional views of the heart and the brain was achieved despite significant light attenuation due to absorption and scattering (Figures 3F and G and 4F and G), thus clearly evincing the importance of uniform light delivery in volumetric OA tomography.

#### 4 | DISCUSSION AND CONCLUSIONS

In this work, we have demonstrated the implementation of a uniform illumination solution for volumetric OA tomography

and showcased its advantages in tissue-mimicking phantoms and mouse organs *ex vivo*. The uniform sample illumination was achieved with a custom-designed bundle of multimode optical fibers. The high NA of the fibers enables high signal-to-noise ratio with single-shot excitations, while efficiently covering the entire surface of the imaged sample. The optimum configuration of the fibers was established with ray-tracing-based simulations. It should be noted that while further illumination improvements tailored to specific applications may be possible, the current configuration was deemed appropriate for a generally applicable case. The accurate fiber positioning was ensured with a 3D-printed mount designed ad hoc for holding the US transducer and the fiber outputs. The mount was printed using 3D-printing technology based on a CAD design and sealed to prevent water leakage during the experiments. Proper water enclosing provides an optimum platform for minimizing light energy loss as well as guaranteeing acoustic coupling of the optoacoustically excited pressure waves. By availing of the freedom of design afforded by the 3D printing technique, the design could be readily adjusted to a different illumination configuration, size and orientation of the detection array, sample location, etc.

The enhancement in imaging performance was quantified using a spherical object having uniform absorption. When the sphere was uniformly illuminated, its entire surface became visible with the reconstructed images, accurately resembling the theoretically predicted (simulated) values. Even though it has been shown that OA images can, in principle, be corrected for nonuniform illumination and light attenuation, it was not necessary in this case [25, 47–50]. Such correction for limited-view conditions or for a relatively low number of measuring positions can be still hampered by streak-type artifacts associated with strong nonuniformity of the excitation light field (hot spots) [51]. Besides suboptimal light delivery, which is known to greatly affect quantification in OA imaging and tomography [52], the reconstruction accuracy may also be conditioned by other factors, such as limited coverage of the tomographic detection geometry [35]. Indeed, the incomplete ( $140^\circ$ ) tomographic coverage of the spherical matrix array was responsible for the image distortions in the central part of the reconstructed sphere, irrespective of the light illumination uniformity. Quantification can also be hampered by acoustic attenuation and scattering in the object. Further challenges for quantification are related to the finalized aperture and narrow frequency response of the US sensors, which may result in signal decay at deeper regions, signal broadening and resolution degradation [37, 53–56].

Optimal light delivery can benefit a number of biological applications involving OA imaging studies, as it will improve upon the reconstruction accuracy and capacity for identifying and quantifying presence of biological compounds. One example that was showcased in this work is the imaging of entire extracted tissue samples, such as murine

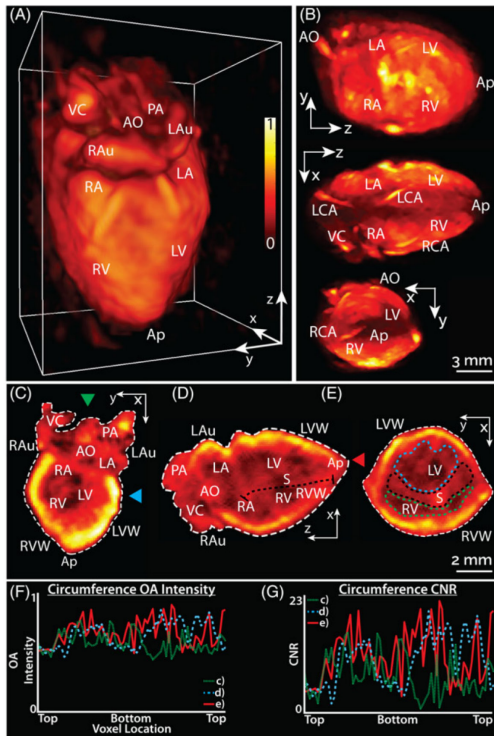


**FIGURE 3** Validation of the uniform light delivery approach in an *ex vivo* murine heart. (A) Single shot volumetric optoacoustic tomography rendering from an excised murine heart. (B) MIP views along the coronal, sagittal and transverse orthoslices of the murine heart. The green arrow shows the slice location for (D), the blue arrow for (E) and red arrow for (C). Indications of gross anatomical structures are labelled. AO: Aorta, VC: Vena Cava, LA: Left Atrium, LV: Left Ventricle, LVW: Left Ventricular Wall, RA: Right Atrium, RV: Right Ventricle, RVW: Right Ventricular Wall, Ap: Apex, LAu: Left Auricle, RAu: Right Auricle, S: Septum, LCA: Left Coronary Artery, RCA: Right Coronary Artery. The black line highlights the septum. (F) OA circumference intensity values for corresponding sectional views as listed. (G) Corresponding contrast-to-noise ratios (CNR) for the voxels shown in (F)

organs. In this way, *in vivo* imaging results could be corroborated in intact blood-free samples *ex vivo* using the same type of contrast and particularly concerning gross external and internal anatomical heart and brain structures, may remove the need for time-consuming histology [57]. Some isolation techniques, such as isolated brain [22] or Langendorff heart preparations [58, 59], enable preserving the organ functionality after extraction and thus could potentially benefit from the improved illumination design suggested in our work. Herein, it was shown that murine hearts and brains, when cleared from blood and fixed in PFA can be imaged in their entirety with a single pulse data. The same imaging strategy could be applied to malignant masses dissected from

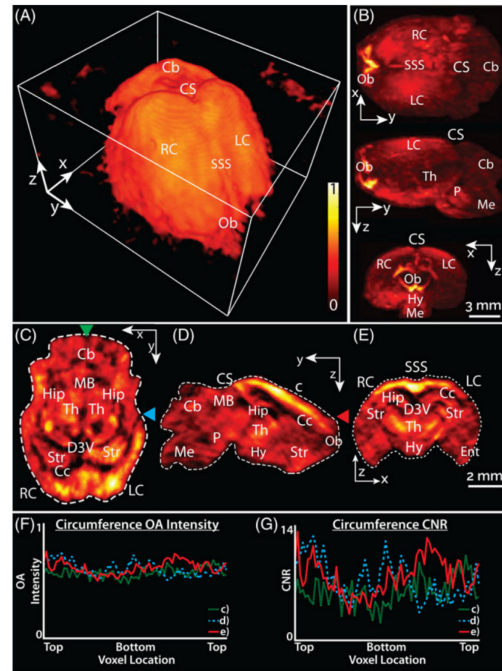


**FIGURE 4** Single shot validation of the uniform light delivery approach in an *ex vivo* murine brain. (A) Volumetric optoacoustic tomography rendering from an excised murine brain. (B) MIP views along the coronal, sagittal and transverse orthoslices of the murine brain are shown. (C,D,E) The corresponding coronal, sagittal and transverse orthoslices of the murine brain are shown. The green arrow shows the slice location for (D), the blue arrow for (E) and red arrow for (C). Indications of gross anatomical structures are labelled. Ob: Olfactory bulbs, SSS: Superior Sagittal Sinus, RC: Right Cortex, LC: Left Cortex, Cb: Cerebellum, Th: Thalamus, P: Pons, Me: Medulla, Hy: Hypothalamus, Hip: Hippocampus, D3V: Dorsal Third Ventricle, Th: Thalamus, RV: Right Ventricle, LV: Left Ventricle, Ent: Entorhinal Cortex, Str: Striatum, CS: Confluence of Sinuses, MB: Mid-Brain (F) OA circumference intensity values for corresponding sectional views as listed. (G) Corresponding contrast-to-noise ratios (CNR) for the voxels shown in (F)

patients [13]. Homogenous illumination is also key in achieving artifact-free 3D and 4D imaging of behaving small organisms, such as freely swimming zebrafish larvae [20]. Our approach can effectively enhance the FOV and hence the region where fish motion can be tracked in three dimensions. Optimal light delivery can further facilitate more accurate identification and quantification of bio-markers in tumors visualized with volumetric OA tomography [60, 61]. Homogenous light delivery would also aid functional studies which rely upon spectral unmixing in multispectral OA tomography. The main advantage of the current system is its ability to achieve high spatiotemporal resolution (max isotropic resolution of 150  $\mu\text{m}$  at 100 Hz). Future developments could see the system be adapted not only for imaging isolated organs but potentially also for whole-body small

animal imaging with a single laser pulse. This would, however, certainly necessitate development of a dedicated detection array matching the geometry of the entire imaged object. Alternatively, previous studies have rotated the detector with a single illumination fiber around the animal to acquire tomographic whole-body data or translated a ring-shaped transducer array along the entire mouse [62, 63].

In conclusion, optimum light delivery can significantly enhance the effective FOV, quantitiveness and overall performance of volumetric OA tomography. Considering the unique spatiotemporal resolution range covered with the imaging system employed in the current work [5], the suggested approach can facilitate more accurate interpretation of OA images in numerous ex vivo, in vivo and in vitro studies, especially when it comes to functional imaging studies where more homogenous light delivery could result in more accurate spectral unmixing and quantification of specific chromophores [64].

#### ACKNOWLEDGMENTS

This study was supported by the European Research Council Consolidator grant ERC-2015-CoG-682379.

#### AUTHOR BIOGRAPHIES

Please see Supporting Information online.

#### ORCID

Benedict Mc Larney  <https://orcid.org/0000-0002-6165-7431>

Sven Gottschalk  <https://orcid.org/0000-0003-1604-1854>

Daniel Razansky  <https://orcid.org/0000-0001-8676-0964>

#### REFERENCES

- [1] J. Xia, J. Yao, L. V. Wang, *Electromagnet. Waves* **2014**, *147*, 1.
- [2] J. Xia, L. V. Wang, *I.E.E.E. Trans. Biomed. Eng.* **2014**, *61*, 1380.
- [3] P. Beard, *Interface Focus* **2011**, *1*, 602.
- [4] L. H. V. Wang, S. Hu, *Science* **2012**, *335*, 1458.
- [5] X. L. Dean-Ben, S. Gottschalk, B. Mc Larney, S. Shoham, D. Razansky, *Chem. Soc. Rev.* **2017**, *46*, 2158.
- [6] L. Li, J. Xia, G. Li, A. Garcia-Uribe, Q. Sheng, M. A. Anastasio, L. V. Wang, *Neurophotonics* **2016**, *3*, 035001.
- [7] K. Kim, H. Park, K. M. Lim, *Toxicol Res.* **2015**, *31*, 97.
- [8] P. P. Laissue, R. A. Alghamdi, P. Tomancak, E. G. Reynaud, H. Shroff, *Nat Methods.* **2017**, *14*, 657.
- [9] L. V. Wang, J. Yao, *Nat. Methods.* **2016**, *13*, 627.
- [10] A. Taruttis, V. N. Tziachristos, *Nat Photonics.* **2015**, *9*, 219.
- [11] A. Dima, V. N. Tziachristos, *Photoacoustics* **2016**, *4*, 65.
- [12] V. Neuschmelting, N. C. Burton, H. Lockau, A. Urich, S. Harmsen, V. Ntziachristos, M. F. Kircher, *Photoacoustics* **2016**, *4*, 1.
- [13] I. Stoffels, S. Morscher, I. Helfrich, U. Hillen, J. Leyh, N. C. Burton, T. C. Sardella, J. Claussen, T. D. Poeppel, H. S. Bachmann, A. Roesch, K. Griewank, D. Schadendorf, M. Gunzer, J. Klode, *Sci. Transl. Med.* **2015**, *7*, 317ra199.
- [14] G. Diot, S. Metz, A. Noske, E. Liapis, B. Schroeder, S. V. Ovsepian, R. Meier, E. Rummeny, V. Ntziachristos, *Clin. Cancer Res.* **2017**, *23*, 6912.
- [15] J. Reber, M. Willershauser, A. Karlas, K. Paul-Yuan, G. Diot, D. Franz, T. Fromme, S. V. Ovsepian, N. Beziere, E. Dubikovskaya, D. C. Karampinos, C. Holzapfel, H. Hauner, M. Klingenspor, V. N. Tziachristos, *Cell Metab.* **2018**, *27*, 689.
- [16] F. T. Felix, D. B. X. Luis, S. Peter, S. Ronald, R. Daniel, *J. Biophotonics* **2016**, *9*, 934.
- [17] L. Xiang, B. Wang, L. Ji, H. Jiang, *Sci. Rep.* **2013**, *3*, 1113.
- [18] S. Gottschalk, T. F. Fehm, X. L. Dean-Ben, D. Razansky, *J. Cerebr. Blood F. Met.* **2015**, *35*, 531.
- [19] S. Gottschalk, T. F. Fehm, X. L. Deán-Ben, V. Tsytarev, D. Razansky, *Neurophotonics* **2016**, *4*, 011007.
- [20] X. L. Dean-Ben, H. Lopez-Schier, D. Razansky, *Sci. Rep.* **2017**, *7*, 6850.
- [21] A. Özbek, X. L. Deán-Ben, D. Razansky, *Optica* **2018**, *5*, 857.
- [22] X. L. Dean-Ben, G. Sela, A. Lauri, M. Kneipp, V. Ntziachristos, G. G. Westmeyer, S. Shoham, D. Razansky, *Light-Sci. Appl.* **2016**, *5*, e16201.
- [23] L. Lin, J. Xia, T. T. W. Wong, L. Li, L. V. Wang, *J. Biomed. Opt.* **2015**, *20*, 016019.
- [24] M. Omar, J. Rebling, K. Wicker, T. Schmitt-Manderbach, M. Schwarz, J. Gateau, H. Lopez-Schier, T. Mappes, V. N. Tziachristos, *Light-Sci. Appl.* **2017**, *6*, e16186.
- [25] K. G. Held, M. Jaeger, J. Ricka, M. Frenz, H. G. Akarçay, *Photoacoustics* **2016**, *4*, 70.
- [26] C. W. Hupple, S. Morscher, N. C. Burton, M. D. Pagel, L. R. McNally, J. Cárdenas-Rodríguez, *Photoacoustics* **2018**, *10*, 54.
- [27] J. Gateau, T. Chaigne, O. Katz, S. Gigan, E. Bossy, *Opt. Lett.* **2013**, *38*, 5188.
- [28] W. F. Xia, D. Piras, M. K. A. Singh, J. C. G. van Hespren, T. G. van Leeuwen, W. Steenbergen, S. Manohar, *Biomed. Opt. Express* **2013**, *4*, 2555.
- [29] D. A. Krohn, B. P. McCann. Silica optical fibers: technology update. *Proc. Volume 2396, Biomedical Optoelectronic Instrumentation, SPIE*, San Jose, CA, **1995**, p. 10.
- [30] S. Royer, B. V. Zemelman, M. Barbic, A. Losonczy, G. Buzsaki, J. C. Magee, *Eur. J. Neurosci.* **2010**, *31*, 2279.
- [31] X. L. Dean-Ben, A. Özbek, D. Razansky, *IEEE Trans. Med. Imaging* **2013**, *32*, 2050.
- [32] W.-F. Cheong, S. A. Prah, A. J. Welch, *IEEE J. Quantum Electron.* **1990**, *26*, 2166.
- [33] P. Lai, X. Xu, L. V. Wang, *J. Biomed. Opt.* **2014**, *19*, 35002.
- [34] A. Özbek, X. Deán-Ben, D. Razansky. Realtime parallel back-projection algorithm for three-dimensional optoacoustic imaging devices. *Proc. SPIE, The International Society for Optical Engineering*, **2013**, p. 880001.
- [35] X. L. Deán-Ben, D. Razansky, *Photoacoustics* **2016**, *4*, 133.
- [36] L. Ding, X. L. Dean-Ben, D. Razansky, *IEEE Trans. Med. Imaging* **2017**, *36*, 1858.
- [37] D. Queiros, X. L. Dean-Ben, A. Buehler, D. Razansky, A. Rosenthal, V. Ntziachristos, *J. Biomed. Opt.* **2013**, *18*, 076014.
- [38] G. J. Gage, D. R. Kipke, W. Shain, *J. Vis. Exp.* **2012**, *65*, e3564.
- [39] Y. Xu, L. V. Wang, G. Ambartsoumian, P. Kuchment, *Med. Phys.* **2004**, *31*, 724.
- [40] C. Dullin, R. Ufartes, E. Larsson, S. Martin, M. Lazzarini, G. Tromba, J. Missbach-Guentner, D. Pinkert-Leetsch, D. M. Katschinski, F. Alves, *PLoS One* **2017**, *12*, e0170597.
- [41] C. T. Badea, B. Fubara, L. W. Hedlund, G. A. Johnson, *Mol. Imaging* **2005**, *4*, 153535002005041.
- [42] A. N. Tullio, D. Accili, V. J. Ferrans, Z.-X. Yu, K. Takeda, A. Grinberg, H. Westphal, Y. A. Preston, R. S. Adelstein, *Proc. Natl. Acad. Sci. U S A* **1997**, *94*, 12407.
- [43] A. Yoldas, E. Ozmen, V. Ozdemir, *J. S. Afr. Vet. Assoc.* **2010**, *81*, 247.
- [44] I. Takamasa, Y. Hiroshi, H. Toshiyuki Braintree Scientific. *A Color atlas of sectional anatomy of the Mouse*, **2001**.
- [45] S. W. Oh, J. A. Harris, L. Ng, B. Winslow, N. Cain, S. Mihalas, Q. Wang, C. Lau, L. Kuan, A. M. Henry, M. T. Mortrud, B. Ouellette, T. N. Nguyen, S. A. Sorensen, C. R. Slaughterbeck, W. Wakeman, Y. Li, D. Feng, A. Ho, E. Nicholas, K. E. Hirokawa, P. Bohn, K. M. Joines, H. Peng, M. J. Hawrylycz, J. W. Phillips, J. G. Hohmann, P. Wohnoutka, C. R. Gerfen, C. Koch, A. Bernard, C. Dang, A. R. Jones, H. Zeng, *Nature* **2014**, *508*, 207.
- [46] E. S. Lein, M. J. Hawrylycz, N. Ao, M. Ayres, A. Bensinger, A. Bernard, A. F. Boe, M. S. Boguski, K. S. Brockway, E. J. Byrnes, L. Chen, L. Chen, T.-M. Chen, M. Chi Chin, J. Chong, B. E. Crook, A. Czaplinska, C. N. Dang, S. Datta, N. R. Dee, A. L. Desaki, T. Desta, E. Diep,

- T. A. Dolbear, M. J. Donelan, H.-W. Dong, J. G. Dougherty, B. J. Duncan, A. J. Ebbert, G. Eichele, L. K. Estin, C. Faber, B. A. Facer, R. Fields, S. R. Fischer, T. P. Fliss, C. Frenshley, S. N. Gates, K. J. Glattfelder, K. R. Halverson, M. R. Hart, J. G. Hohmann, M. P. Howell, D. P. Jeung, R. A. Johnson, P. T. Karr, R. Kawal, J. M. Kidney, R. H. Knapik, C. L. Kuan, J. H. Lake, A. R. Laramée, K. D. Larsen, C. Lau, T. A. Lemon, A. J. Liang, Y. Liu, L. T. Luong, J. Michaels, J. J. Morgan, R. J. Morgan, M. T. Mortrud, N. F. Mosqueda, L. L. Ng, R. Ng, G. J. Orta, C. C. Overly, T. H. Pak, S. E. Parry, S. D. Pathak, O. C. Pearson, R. B. Puchalski, Z. L. Riley, H. R. Rockett, S. A. Rowland, J. J. Royall, M. J. Ruiz, N. R. Sarno, K. Schaffnit, N. V. Shapovalova, T. Sivisay, C. R. Slaughterbeck, S. C. Smith, K. A. Smith, B. I. Smith, A. J. Sodt, N. N. Stewart, K.-R. Stumpf, S. M. Sunkin, M. Sutram, A. Tam, C. D. Teemer, C. Thaller, C. L. Thompson, L. R. Varnam, A. Visel, R. M. Whitlock, P. E. Wohnoutka, C. K. Wolkey, V. Y. Wong, M. Wood, M. B. Yaylaoglu, R. C. Young, B. L. Youngstrom, X. Feng Yuan, B. Zhang, T. A. Zwingman, A. R. Jones, *Nature* **2006**, *445*, 168.
- [47] A. Q. Bauer, R. E. Nothdurft, J. P. Culver, T. N. Epelding, L. V. Wang, *J. Biomed. Opt.* **2011**, *16*, 096016.
- [48] T. Harrison, P. Shao, R. J. Zemp *Biomed. Opt. Express* **2013**, *4*, 2224.
- [49] M. Kirillin, V. Perekatova, I. Turchin, P. Subochev, *Photoacoustics* **2017**, *8*, 59.
- [50] X. L. Deán-Ben, A. C. Stiel, Y. Jiang, V. Ntziachristos, G. G. Westmeyer, D. Razansky, *Opt. Lett.* **2015**, *40*, 4691.
- [51] G. Paltauf, R. Nuster, P. Burgholzer, *Phys. Med. Biol.* **2009**, *54*, 3303.
- [52] B. Cox, J. G. Laufer, S. R. Arridge, P. C. Beard, *J. Biomed. Opt.* **2012**, *17*, 061202.
- [53] X. L. Deán-Ben, D. Razansky, V. Ntziachristos, *Phys. Med. Biol.* **2011**, *56*, 6129.
- [54] N. Baddour, A. Mandelis, *Photoacoustics* **2015**, *3*, 132.
- [55] E. Filoux, J. Mamou, O. Aristizábal, J. A. Ketterling, *IEEE Trans. Ultrason. Ferroelectr. Freq. Control* **2011**, *58*, 994.
- [56] H. K. Zhang, A. Cheng, N. Bottenus, X. Guo, G. E. Trahey, E. M. Boctor, *J. Med. Imaging* **2016**, *3*, 027001.
- [57] J. W. McGowan, G. L. Bidwell. The Use of Ex Vivo Whole-organ Imaging and Quantitative Tissue Histology to Determine the Bio-distribution of Fluorescently Labeled Molecules. *J. Vis. Exp.* **2016**. DOI: 10.3791/54987.
- [58] R. M. Bell, M. M. Mocanu, D. M. Yellon, *J. Mol. Cell. Cardiol.* **2011**, *50*, 940.
- [59] D. Lang, M. Sulkin, Q. Lou, I. R. Efimov, Optical mapping of action potentials and calcium transients in the mouse heart, *J. Vis. Exp.* **2011**, 3275. DOI: 10.3791/3275.
- [60] L. Kirscher, X. L. Deán-Ben, M. Scadeng, A. Zaremba, Q. Zhang, C. Kober, T. F. Fehm, D. Razansky, V. Ntziachristos, J. Stritzker, A. A. Szalay, *Theranostics* **2015**, *5*, 1045.
- [61] V. Ermolayev, X. L. Deán-Ben, S. Mandal, V. Ntziachristos, D. Razansky, *Eur. Radiol.* **2016**, *26*, 1843.
- [62] X. L. Deán-Ben, T. F. Fehm, S. J. Ford, S. Gottschalk, D. Razansky, *Light-Sci. Appl.* **2017**, *6*, e16247.
- [63] A. Taruttis, S. Morscher, N. C. Burton, D. Razansky, V. Ntziachristos, *PLoS One* **2012**, *7*, e30491.
- [64] X. Luís Deán-Ben, D. Razansky, *Light-Sci. Appl.* **2014**, *3*, e137.

#### SUPPORTING INFORMATION

Additional supporting information may be found online in the Supporting Information section at the end of the article.

**How to cite this article:** Mc Larney B, Rebling J, Chen Z, Deán-Ben XL, Gottschalk S, Razansky D. Uniform light delivery in volumetric optoacoustic tomography. *J. Biophotonics*. 2019;e201800387. <https://doi.org/10.1002/jbio.201800387>

## Supporting Information

Additional supporting information may be found in the online version of this article at the publisher's website.

### **Uniform light delivery in volumetric optoacoustic tomography**

Benedict Mc Larney<sup>1,2,¶</sup>, Johannes Rebling<sup>1,2,3,4,¶</sup>, Zhenyue Chen<sup>1</sup>, Xosé Luis Deán-Ben<sup>1,3,4</sup>, Sven Gottschalk<sup>1</sup> & Daniel Razansky<sup>1,2,3,4\*</sup>

<sup>1</sup>Institute for Biological and Medical Imaging (IBMI), Helmholtz Center Munich, Ingolstädter Landstr. 1, 85764 Neuherberg, Germany

<sup>2</sup>Faculty of Medicine, Technical University of Munich, Ismaninger Str. 22, 81675 Munich, Germany

<sup>3</sup>Faculty of Medicine and Institute of Pharmacology and Toxicology, University of Zurich, Switzerland

<sup>4</sup>Institute for Biomedical Engineering and Department of Information Technology and Electrical Engineering, ETH Zurich, Switzerland

\*Corresponding Author: E-mail: [daniel.razansky@uzh.ch](mailto:daniel.razansky@uzh.ch)

¶ Contributed equally

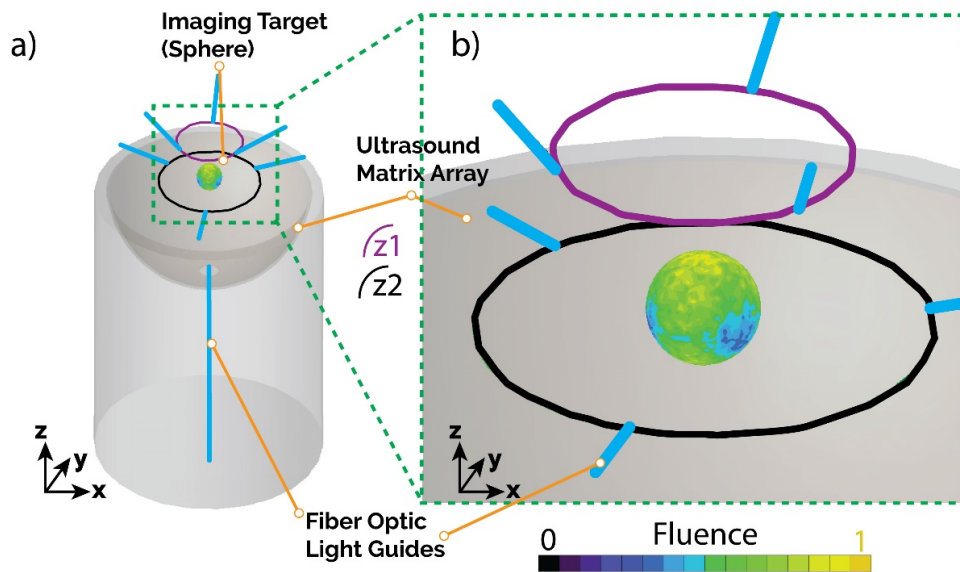


**Figure S1** Simulation results showing the optimum location for 7 fibers located around the detector evenly illuminating a 1cm diameter sphere. (a) Fiber arrangement for achieving an even illumination across the sphere. (b) Close up view of the spherical object showing light intensity distribution on its surface.

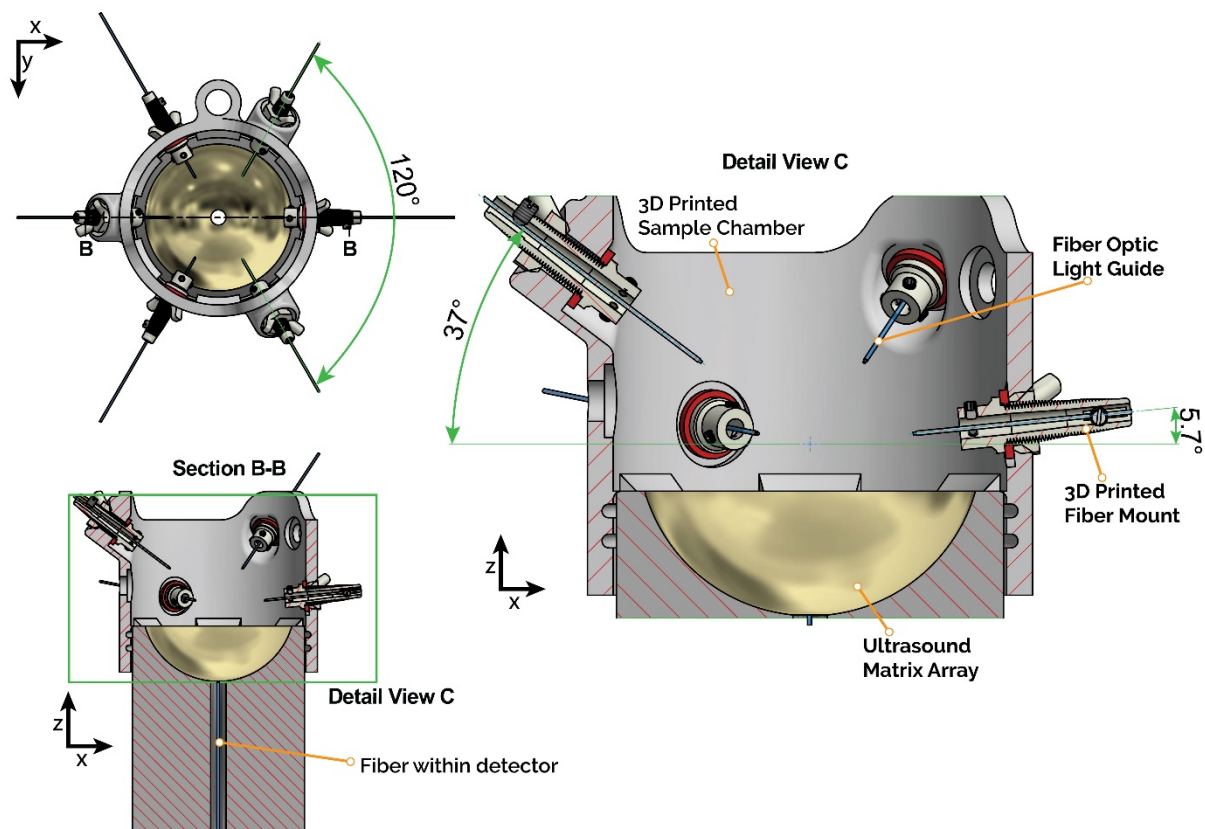


**Figure S2** Technical CAD drawing of the sample chamber, including fiber illumination angles and the holders. The fiber within the detector was utilised for single sided illumination. CAD files available online at <https://bit.ly/2zelv8J>.

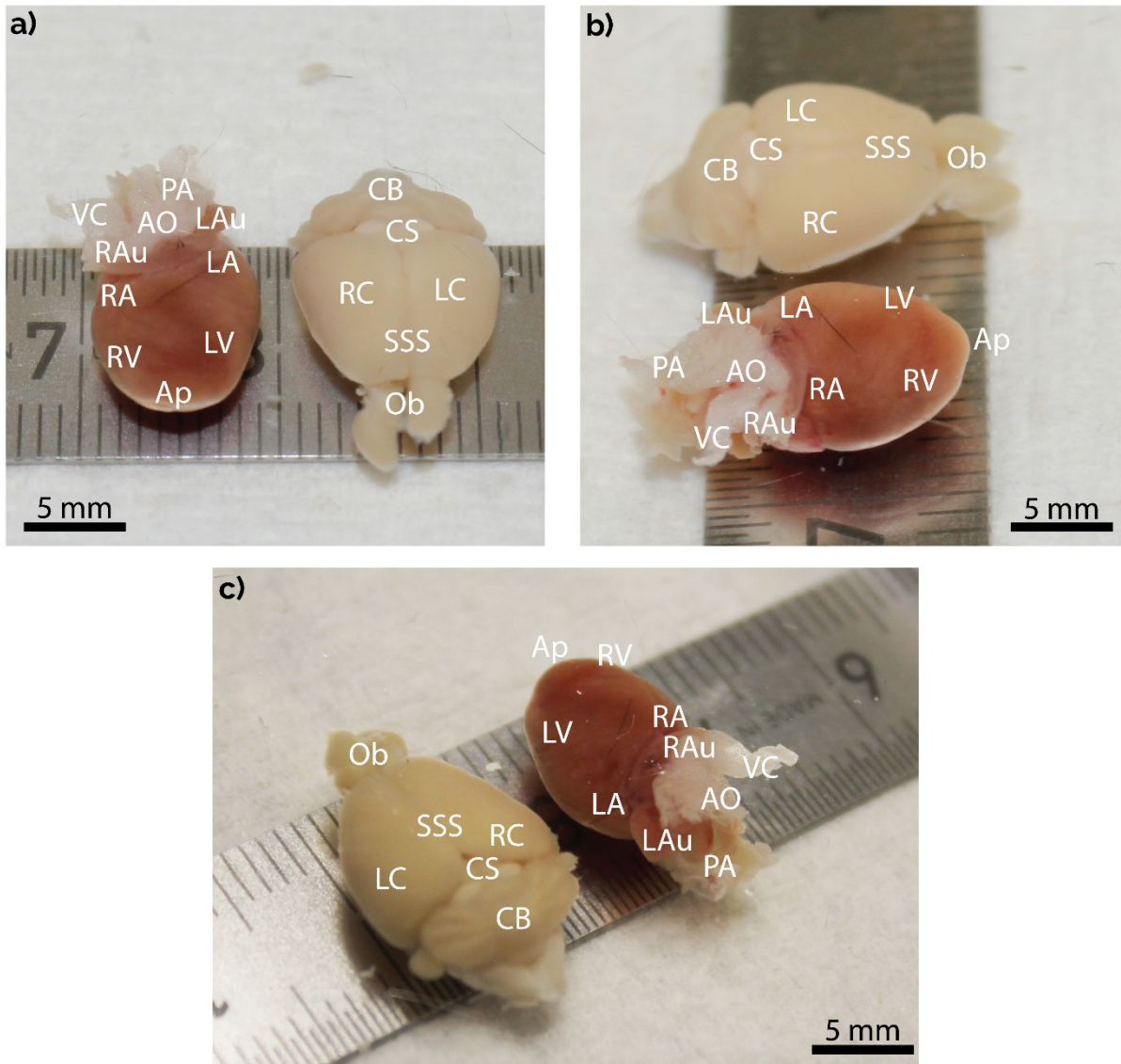


**Figure S3** Gross anatomical images of an excised heart and brain. a) to c) Varying orientations of the organs and the labelled structures. RAu: Right Auricle, LAu: Left Auricle, RA: Right Atrium, LA: Left Atrium, RV: Right Ventricle, LV: Left Ventricle, Ap: Apex, VC: Vena Cava, PA: Pulmonary Artery, AO: Aorta, CB: Cerebellum, CS: Confluence of sinuses, RC: Right Cortex, LC: Left Cortex, SSS: Location of Superior Sagittal Sinus (removed during extraction), Ob: Olfactory bulbs.

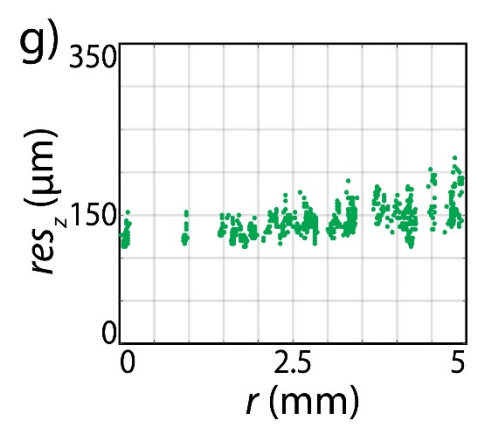
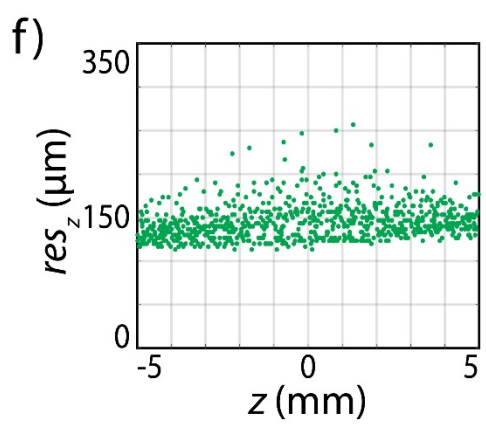
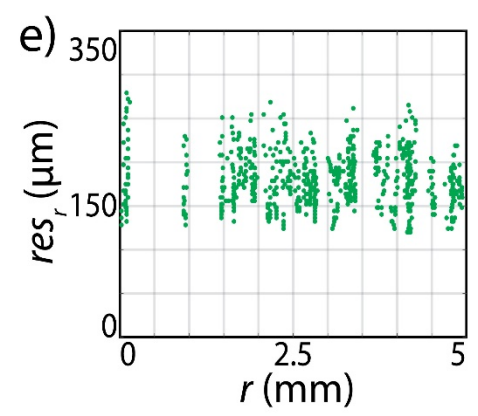
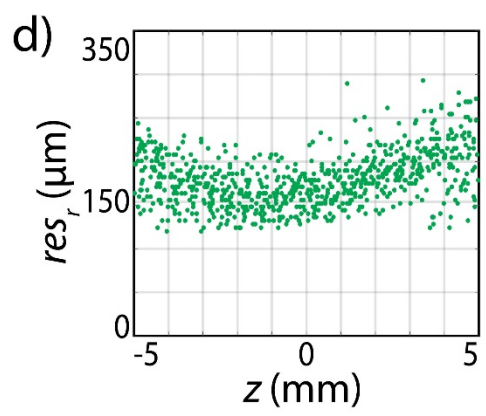
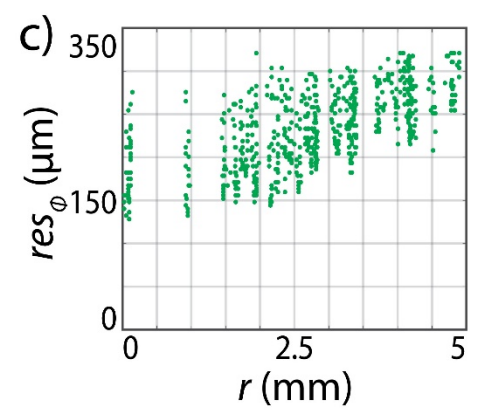
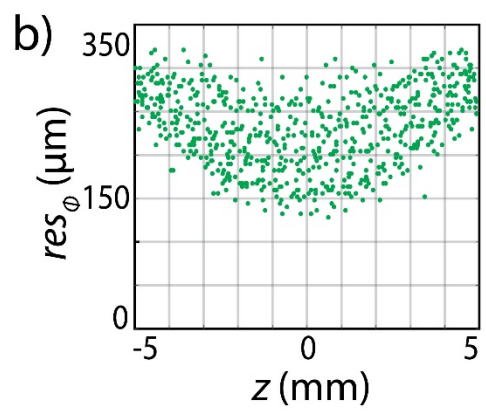
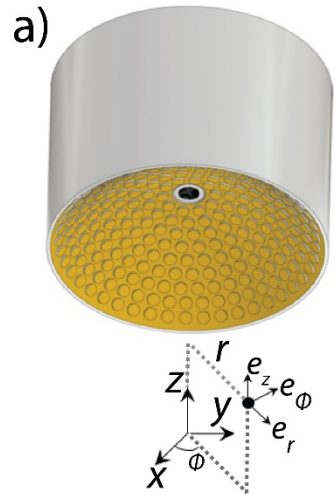


**Figure S4** Characterization of the spatial resolution of the system. (a) Position of a point of the field of view in a cylindrical coordinate system positioned at the centre of the spherical array. (b-g) Mean square difference between the measured full width half maximum (FWHM) of a microsphere and its diameter ( $\sim 90$  microns) along the directions of the cylindrical unit vectors shown in (a) as a function of the radial and axial coordinates. The measured values barely change with the angular position due to the axial symmetry of the array. Note that the measured FWHM may be affected by negative values in the images associated to limited view effects, particularly along the z direction, so that the actual resolution can be slightly lower.

<b>Optical fibers</b>	Multimode, step-index (FT600EMT, Thorlabs, USA)
<b>Number of fibers</b>	7
<b>Fiber core/cladding/coating diameter</b>	600 / 630 / 1040 $\mu\text{m}$
<b>Fiber/Bundle NA</b>	0.39
<b>Bundle aperture diameter</b>	1040 $\mu\text{m}$
<b>Bend radius (short/long term)</b>	30 mm / 60 mm
<b>Single fiber protection</b>	Reinforced PVC/Kevlar/PP jacket (FT020, Thorlabs, USA)
<b>Bundle length</b>	~1.5 m
<b>Proximal end aperture</b>	2 mm
<b>Proximal end termination</b>	SMA905 (11580A, Thorlabs, USA)
<b>Distal end termination</b>	Jacketed fiber with additional steel ferule protection
<b>Theoretical bundle transmission</b>	64.32 %
<b>Wavelength range</b>	400 - 2200 nm

**Table S1**      Optical and mechanical specifications of the custom-made optical fiber bundle.

### 3. Monitoring of stimulus evoked murine somatosensory cortex hemodynamic activity with volumetric multi-spectral optoacoustic tomography

#### 3.1 Summary and author contribution

This work presents a method and image analysis pipeline for elucidating the hemodynamic response and recording the evoked signals using Functional optoacoustic neurotomography. Electrical paw stimulation, a well-established method in neuroimaging, was employed based on a paradigm from fMRI. The strong contrast from hemoglobin positions FONT as an optimal method to observe functional hemodynamic changes in the brain in response to stimuli. However, these hemodynamic changes are subtle and often highly localized to a contralateral side to stimulation. Accurate recordings of such changes require the optimum selection of light wavelengths for unmixing and the correct physiological parameters for the mouse.

This work provides a method to account for the variations that are inherent to FONT namely, laser fluctuations arising from cooling systems and pulse to pulse changes. By correcting for these changes and implementing a generalizable analysis regime hemodynamic changes were shown in the three major hemodynamic components (HbO, HbR & HbT). The changes were shown to be contralaterally weighted in some cases and positions FONT as a suitable replacement for fMRI and other optical methods achieving high spatiotemporal resolution across the mouse cortex, completely non-invasively. My idea of efficiently characterizing the sources of noise in the FONT system, accounting and correcting for them eased detection of hemodynamic changes. Furthermore, automating the unmixing and analysis methods further provided ease of detection with correlation mapping from select voxels highlighting the extent of activity across the cortex.

This work combined laser alignment, *in vivo* animal imaging work, furthering the applications of FONT, optimizing experimental settings, MATLAB scripting and automation, investigative neuroscience. The developed methodology modified a protocol from fMRI studies to highlight the inherent advantages of FONT over conventional methods for neuroimaging.

My contribution to the presented manuscript was the following:

**Conception and design:** I designed the experiment along with Prof. Razansky and Ms. Hutter.

**Development of methodology:** The methodology was outlined and refined by I and Ms. Hutter.

**Acquisition of data:** I performed all mouse imaging. Data reconstruction & analysis was performed by both Magdalena Hutter and I.



OPEN ACCESS

**Edited by:**

Itamar Ronen,  
Leiden University Medical Center,  
Netherlands

**Reviewed by:**

Itamar Kahn,  
Technion Israel Institute  
of Technology, Israel  
Adrian Rodriguez-Contreras,  
City College of New York (CUNY),  
United States  
Saak V. Ovsepian,  
National Institute of Mental Health,  
Czechia  
Stratis Tzoumas,  
Carl Zeiss, Germany

**\*Correspondence:**

Daniel Razansky  
daniel.razansky@uzh.ch

**† Present address:**

Benedict Mc Lamey,  
Molecular Pharmacology Program,  
Department of Radiology, Memorial  
Sloan Kettering Cancer Center,  
New York, NY, United States

‡ These authors have contributed  
equally to this work

**Specialty section:**

This article was submitted to  
Brain Imaging Methods,  
a section of the journal  
Frontiers in Neuroscience

**Received:** 03 January 2020

**Accepted:** 01 May 2020

**Published:** 03 June 2020

**Citation:**

Mc Lamey B, Hutter MA,  
Degtyaruk O, Deán-Ben XL and  
Razansky D (2020) Monitoring  
of Stimulus Evoked Murine  
Somatosensory Cortex Hemodynamic  
Activity With Volumetric Multi-Spectral  
Optoacoustic Tomography.  
Front. Neurosci. 14:536.  
doi: 10.3389/fnins.2020.00536

# Monitoring of Stimulus Evoked Murine Somatosensory Cortex Hemodynamic Activity With Volumetric Multi-Spectral Optoacoustic Tomography

Benedict Mc Lamey<sup>1,2†</sup>, Magdalena Anastasia Hutter<sup>2†</sup>, Oleksiy Degtyaruk<sup>2,3</sup>,  
Xosé Luis Deán-Ben<sup>3,4</sup> and Daniel Razansky<sup>1,2,3,4\*</sup>

<sup>1</sup> Faculty of Medicine, Technical University of Munich, Munich, Germany, <sup>2</sup> Institute for Biological and Medical Imaging, Helmholtz Center Munich, Munich, Germany, <sup>3</sup> Faculty of Medicine and Institute of Pharmacology and Toxicology, University of Zurich, Zurich, Switzerland, <sup>4</sup> Institute for Biomedical Engineering and Department of Information Technology and Electrical Engineering, Eidgenössische Technische Hochschule (ETH) Zürich, Zurich, Switzerland

Sensory stimulation is an attractive paradigm for studying brain activity using various optical-, ultrasound- and MRI-based functional neuroimaging methods. Optoacoustics has been recently suggested as a powerful new tool for scalable mapping of multiple hemodynamic parameters with rich contrast and previously unachievable spatio-temporal resolution. Yet, its utility for studying the processing of peripheral inputs at the whole brain level has so far not been quantified. We employed volumetric multi-spectral optoacoustic tomography (vMSOT) to non-invasively monitor the HbO, HbR, and HbT dynamics across the mouse somatosensory cortex evoked by electrical paw stimuli. We show that elevated contralateral activation is preserved in the HbO map (invisible to MRI) under isoflurane anesthesia. Brain activation is shown to be predominantly confined to the somatosensory cortex, with strongest activation in the hindpaw region of the contralateral sensorimotor cortex. Furthermore, vMSOT detected the presence of an initial dip in the contralateral hindpaw region in the delta HbO channel. Sensorimotor cortical activity was identified over all other regions in HbT and HbO but not in HbR. Pearson's correlation mapping enabled localizing the response to the sensorimotor cortex further highlighting the ability of vMSOT to bridge over imaging performance deficiencies of other functional neuroimaging modalities.

**Keywords:** optoacoustics, hemodynamics, somatosensory, cortex, initial-dip

## INTRODUCTION

Imaging the brain with high resolution, both at functional and anatomical levels, and in real time is essential for unraveling the mysteries of how we think and act. In the last few decades, vast efforts have been directed to the development of new approaches for scalable imaging of brain activity (Markram et al., 2011; Insel et al., 2013). The brain is known to consist of billions of cells, predominantly neurons, glia, and endothelial cells, where neuronal communication is achieved

through electrical signals transmitted across a hugely dense network. Monitoring these orchestral interactions at a global level in mammalian brains remains a major challenge in neuroscience and current research efforts are transitioning to enable imaging the functioning brain in its entirety as opposed to focusing on single or small numbers of cells (Fornito et al., 2015; Mott et al., 2018). Current limiting factors of this transition are the need for high spatio-temporal resolution across the entire brain, non-invasivity and specificity of the recorded responses (He et al., 2011).

Neuronal activity is highly demanding in terms of energy consumption (Herculano-Houzel, 2011). The brain vasculature provides neurons with a continuous supply of oxygen and nutrients to satisfy the local demand in activated areas (Buxton et al., 1998; Yablonskiy et al., 2013) resulting in rapid hemodynamic changes that are known to be linked to neuronal activation via neurovascular coupling (Filosa and Blanco, 2007). Functional magnetic resonance imaging (fMRI) is the predominant method used to image these changes (Bosshard et al., 2010; Yablonskiy et al., 2013). However, the method's spatial and temporal resolution is limited while quantification of hemodynamic responses further relies upon theoretical models to extract reduced hemoglobin (HbR) levels from the measured blood oxygenated level dependent (BOLD) signals, the relationship of which to neuronal activity is still not fully understood (Arthurs and Boniface, 2002; Iannetti and Wise, 2007; Logothetis, 2008).

Recently, alternative functional brain imaging approaches based on optical and ultrasound methods have shown great promise. In particular, optical methods capable of imaging hemodynamic responses include optical intrinsic signal imaging (OISI), laser speckle imaging (LSI) and diffusion optical tomography (DOT) (Culver et al., 2004; Kazmi et al., 2015; Reisman et al., 2017). These methods enable enhanced contrast, increased speed and significantly reduced costs with respect to fMRI. However, they are strongly affected by the scattering of light within biological tissues, which limits their applicability to superficial layers of the cortex (Hielscher, 2005), even for state of the art approaches that do not require removal of the scalp or skull (Reisman et al., 2017). Due to weak scattering of ultrasound waves in soft tissues, functional ultrasound (fUS) is able to achieve imaging of deep brain areas with diffraction-limited ultrasonic resolution but skull removal is often required for high resolution studies. Furthermore, its contrast primarily relies on cerebral blood flow (Macé et al., 2011; Deffieux et al., 2018), making it insensitive to changes in other relevant hemodynamic parameters occurring during brain activation, such as oxygenation changes.

Multi-spectral optoacoustic tomography (MSOT) has recently emerged as a powerful approach for studying brain activity in rodents (Ovsepian et al., 2019b). The endogenous contrast provided by the optical absorption of blood enables mapping multiple hemodynamic parameters (Hu and Wang, 2010; Li et al., 2010; Gottschalk et al., 2015, 2017; Yao et al., 2015), while the penetration depth and resolution are comparable to those achieved with fUS. MSOT systems facilitate real-time volumetric (three-dimensional) imaging with scalable spatial resolution

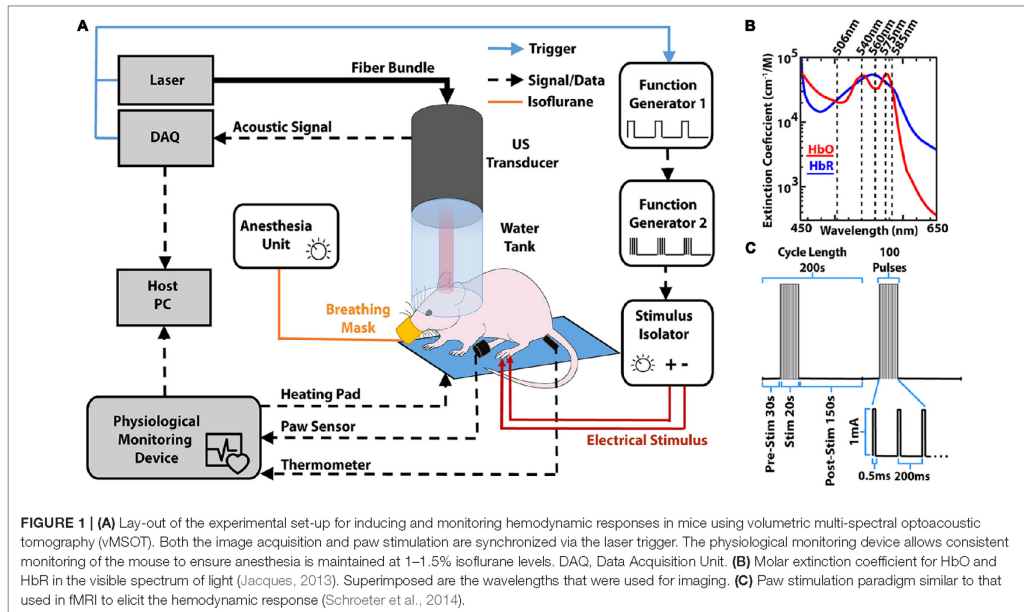
and field of view (FOV) not easily achievable with other optical modalities such as OISI, DOT or LSI. Therefore, MSOT effectively bridges the gap between cellular resolution microscopy on a sub-millimeter scale and macroscopic neuroimaging observations with poor spatial resolution (Dean-Ben et al., 2016; Deán-Ben et al., 2017; Ovsepian et al., 2019a). To date, various stimulation paradigms, including optogenetic, paw and whisker, have been imaged with MSOT. These enabled readily detecting functional activation via hemodynamics with anatomic landmarks (Hu and Wang, 2010; Olefir et al., 2019; Ovsepian et al., 2019a,b). Previous studies have shown capabilities of non-invasive imaging through the skull and scalp linking epileptic seizure activity to electrophysiological activity (Gottschalk et al., 2017). The fast imaging speed and spectroscopic differentiation capacity have further enabled imaging of calcium dynamics *in vivo* (Dean-Ben et al., 2016; Gottschalk et al., 2019).

Despite its promising imaging performance showcased in initial studies, the utility of MSOT for studying the processing of peripheral inputs has only been achieved at small cerebral FOVs and its application to the whole brain has so far not been quantified (Olefir et al., 2019; Ovsepian et al., 2019a). In this work, we employ a state-of-the-art volumetric MSOT (vMSOT) system providing five dimensional (5D, three-dimensional, real-time and multi-spectral) imaging capabilities in order to map cerebral hemodynamic changes in mice in response to a standard electrical paw stimulation paradigm commonly used in fMRI (Schroeter et al., 2014). Electrical paw stimulation has the added advantage of being applicable to a wide variety of model organisms, providing a robust and replicable method of investigating brain responses to peripheral stimuli. As opposed to fMRI and other conventional neuroimaging methods, high-resolution imaging was achieved over the entire isocortex. This enabled mapping of real time simultaneous responses of all hemodynamic components (oxy- and deoxy-hemoglobin, blood volume) to peripheral stimuli across multiple brain regions. The high contrast of the vMSOT images corresponding to visible optical wavelengths facilitates detecting signals from small cortical arterioles and venules, which are known to undergo greater changes than larger vessels during the hemodynamic response (Ma et al., 2016a; He et al., 2018).

## MATERIALS AND METHODS

### vMSOT Imaging

The imaging set-up used in the experiments has been previously described in detail (Gottschalk et al., 2019). In summary, the 512-element hemispherical transducer array (Imasonic SaS, Voray, France) has a central aperture through which a fiber optic bundle is placed (CeramOptec GmbH, Bonn, Germany). The bundle is coupled to a short-pulsed (<10 ns) optical parametric oscillator laser capable of sweeping wavelengths from 420 to 680 nm (Innolas Laser GmbH, Krailling, Germany) on a per-pulse basis. Visible wavelengths of light were chosen for an optimal signal-to-noise ratio (SNR) of the cortical vasculature. The pulse repetition frequency (PRF) of the laser was set to 20 Hz, with five wavelengths (506, 540, 560, 575, and 585 nm, see **Figure 1B**)



being repeated in succession to efficiently cover the relatively slow hemodynamic changes for a trial length of 200 s with multiple repeats (see section “Stimulation Paradigm”). The vMSOT images featuring endogenous blood contrast were processed via linear spectral unmixing to isolate the oxygenated hemoglobin (HbO), reduced hemoglobin (HbR) and total hemoglobin (HbT) components using the spectral absorption profile of hemoglobin (Jacques, 2013). Note that the linear unmixing approach is prone to spectral coloring artifacts when rendering concentrations of exogenous agents and blood oxygenation values in deep tissues (Cox et al., 2012; Tzoumas et al., 2016; Tzoumas and Ntzachristos, 2017). In our case, the light fluence distribution at the mouse cortex, where hemodynamic changes were mapped, was assumed to be approximately the same for all wavelengths due to the relatively superficial imaging depth, in a way that linear unmixing provides sufficiently accurate readings. In addition, no quantitative sO<sub>2</sub> values were extracted in our study, which solely relied on relative readings of the individual HbO and HbR components (Laufer et al., 2005; Li et al., 2008; Cox et al., 2012).

**Animal Preparation and Paw Stimulation**

Experiments were performed in 4–6-week-old female athymic nude *FoxN1<sup>tm</sup>* mice (*n* = 4, Envigo, New Jersey, United States, *Foxn1<sup>tm</sup>* 069, weight range 16–20 g). Mice were housed in transparent cages (GM500 IVC Green Line, Tecniplast Deutschland GmbH, Hohenpeissenberg, Germany) which in line with institutional guidelines could house up to 5 mice per cage. The housing ensured a 12 h day and night system with lights turning on at 8 am. Temperature was controlled at 24 ± 1°C

with a relative humidity range between 40 and 60%. Animals had access to food and water *ad libitum*. This study was carried out in full compliance with the institutional guidelines of the Institute for Biological and Medical Imaging and with approval from the Government District of Upper Bavaria. The mice were anesthetized by placing them in a chamber containing isoflurane at a concentration of 3% v/v isoflurane in 100% O<sub>2</sub>. Subsequently, they were transferred to a stereotaxic head holding frame (Narishige International Limited, London, United Kingdom) and ultrasound gel (Aquasonic Clear Ultrasound Gel, Parker Laboratories Inc., NJ, United States) was applied on top of the scalp of the animals after being cleaned of any dirt.

The imaging equipment comprising of a water tank and a hemispherical transducer array was then placed above the head of the mice as schematically depicted in **Figure 1A**. Physiological conditions [heart and breathing rates, temperature and peripheral capillary oxygen saturation (SpO<sub>2</sub>)] were monitored and maintained using an *ad hoc* apparatus (PhysioSuite®, Kent Scientific, Torrington, CT, United States). During all experiments the heart rate of the mice was maintained at ~400 beats per minute (bpm). The PhysioSuite apparatus provided real time information of the heart bpm and this was continually monitored during data acquisition. The anesthesia level was reduced to between 1 and 1.5% v/v isoflurane in 100% O<sub>2</sub> during the measurements, whilst monitoring heart pace and altering anesthesia depth to maintain a heart rate of ~400 bpm. Sufficient anesthesia depth was ensured by testing the toe pinch reflex of the non-stimulated paw (both before and after trials). Following data acquisition, all mice were removed from the head holder

and allowed to recover from anesthesia. No adverse effects such of the experiment were noted in any of the mice.

### Stimulation Paradigm

Electrical stimulation was performed by placing two stainless steel electrodes beneath the skin of one of the hind paws of the mouse. The electrodes were connected to a stimulus isolator (Model A365R, World Precision Instruments, Sarasota, FL, United States) that delivered a train of 100 pulses (0.5 ms, 1 mA) at 5 Hz for 20 s (Schroeter et al., 2014). The total trial time was 200 s, with a 30 s baseline (pre-stimulation), 20 s of stimulation and 150 s of recovery (post-stimulation, see **Figure 1C**). For each measurement, the trial was repeated consecutively two times. Measurements were also carried out in the same fashion but without applying any electrical stimulation for a single trial prior to the stimulation experiment (negative control) where no activation was detected, as shown in **Supplementary Figure S3**.

### Data Analysis

All data was reconstructed offline using a graphics processing unit (GPU) implementation of the back-projection algorithm, as previously described (Ozbek et al., 2013). In brief, the signals were band-pass filtered between 100 kHz and 6 MHz to remove both low frequency bias and high frequency noise components. The reconstructed images were normalized on a frame by frame basis to compensate for laser fluctuations as well as for the wavelength-dependent energy of the pulse. This was achieved by constantly measuring the optoacoustic signal from of a  $\sim 150$   $\mu\text{m}$  sphere (Cospheric LLC, Santa Barbara, CA, United States) located on the foil separating the water tank from the head of the mouse. Following unmixing, the relative changes of each component (%) were calculated. This was done by subtracting the baseline image, estimated as the average of the first 30 s of the trial, from the image at each time point and subsequently normalizing by such baseline. Stimulation trials were recorded consecutively from each mouse with responses being detected in all cases. Coronal slices were chosen within the approximate locations of visual (VC), somatosensory (SS) and somatomotor (SM) cortical regions in relation to the anatomical landmark bregma and within the isocortex, for each mouse ( $-2.0$  mm from bregma – VC, bregma – SS and  $+2.0$  mm – SM, respectively, see **Figure 2A**) and **Supplementary Figure S2A**) (Takamasa et al., 2001; Oh et al., 2014; Paxinos and Franklin, 2019). Using available atlases, the coronal slices were compared to known regions and ROIs ( $5 \times 5 \times 3$  voxels) were chosen for analysis, including the primary SS region corresponding to lower limbs (SIHL or SSp-II) (Oh et al., 2014; Paxinos and Franklin, 2019). The mean value from all voxels within the ROI was used to compute traces. Single trials were analyzed and the response from each mouse for HbO, HbR, and HbT was averaged into a single representative trace for each mouse. Finally, the averaged responses from all mice for each component and respective region were averaged to determine the population response from the stimulation and non-stimulation trials.

Statistical analysis was carried out via custom code in Matlab (2018b, Mathworks, MA, United States) on the trace data from both stimulation trials from all mice (8 trials in total). The code

automatically sorted through each trace to find its peak activation percentage (P%), peak dip percentage (Dip%) and the times taken to reach peak activation (TTP), the dip (DTTP) and decay time (DeT). All times were calculated on the 10th and 90th percentile change. Statistical significance was determined via a Wilcoxon signed-rank test where  $p < 0.05$  was determined as statistically significant (Liao et al., 2012). Note that for HbO and HbT a dip would constitute a downward trend before reaching peak activation and for HbR a dip would constitute an upward trend before reaching peak activation. Each contralateral (CL) region was compared to its ipsilateral (IL) counterpart and finally the region of the SS known to correspond to contralateral hindpaw (CL-HP) stimulation region was tested for significance over all other regions (Takamasa et al., 2001; Oh et al., 2014; Paxinos and Franklin, 2019).

### Functional Cortical Mapping

Pearson's correlation coefficient mapping was carried out on the HbO data (any data likely to include the scalp and skull was removed) to determine the extent of activation (Huppert et al., 2006; Cui et al., 2017). The correlation map of the brain was generated by using the time trace of the CL-HP SS ROI within the activated region and then calculating the time correlation coefficient of this trace to all other voxels in the brain. For correlation mapping, a ROI of  $1 \times 3$  voxels was selected from the previous ROI used to determine the activity traces. Activation data from both trials of each mouse were averaged into a single representative trial. Smoothing was applied to the entire imaged FOV prior to calculating the correlation map using a  $3 \times 3 \times 3$  kernel of ones and any data outside the brain was removed via thresholding. To allow for a slight time shift but still correlated signals a permissible lag of  $\pm 2$  s was included. The maximum value of each correlation coefficient was then chosen to compose a three-dimensional map of correlation values. To visualize the data more clearly the map was thresholded to only include positive correlation values where 0 corresponds to no correlation and 1 corresponds to maximum correlation.

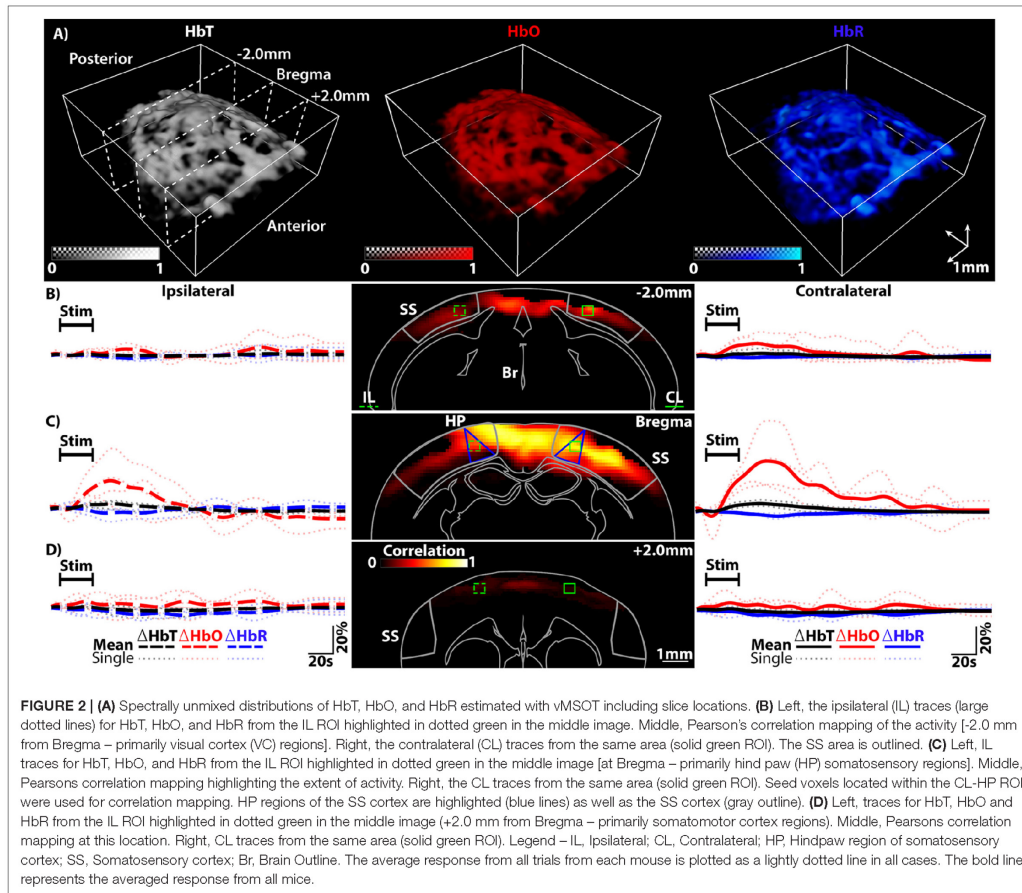
### Hemodynamic Imaging

The set-up to both evoke and comprehensively capture numerous components of the hemodynamic response is outlined in **Figures 1A–C**. The current set-up allows for complete movement of the mouse head (all axes and rotation) to ensure optimal placement. The ability to monitor the heart rate and other physiological states ensured that the heart rate was maintained at  $\sim 400$  bpm throughout the experiments whilst also keeping the mouse anesthetized. To ensure synchronization of both the imaging and stimulus paradigm the laser trigger was used to control the entire experiment.

## RESULTS

### Preserved Contralateral Activity

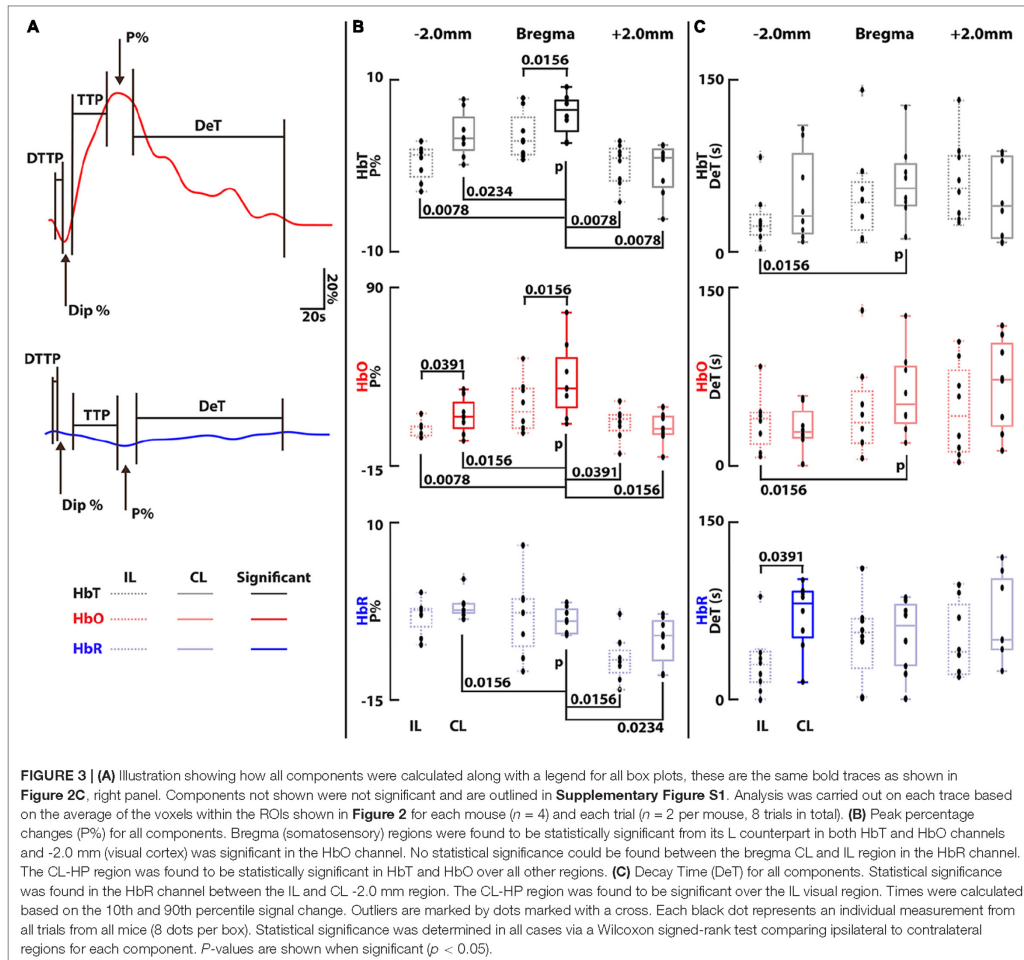
For all experiments the paw stimulation paradigm was carried out as outlined in the methods section. As shown in **Figure 2** (A – representative of  $n = 4$  mice), vMSOT is readily capable of



rendering the HbO, HbR, and HbT components after unmixing the multi-spectral data. The field of view (FOV) covers the cortical regions. For ease of visualization all IL traces are bold dotted lines on the left hand side of **Figures 2B–D**, left panels and all CL are solid lines on the right (**Figures 2B–D**, right panels), irrespective of their original orientation. In all cases ROIs were chosen within the VC, SS, or SM regions of the isocortex [**Figures 2B–D**, middle panels, dotted (IL) and solid (CL) green lines]. Note that blue segmented regions highlight the HP region of the SS cortex. The corresponding time courses for HbO, HbR, and HbT averaged over both trials from each mouse are shown (lighter colored dotted lines, **Figures 2B–D**), including the average response from all mice (population response, bold lines **Figures 2B–D**). The traces have been cropped to show 5 s before stimulation, the stimulation window and then the remaining 150 s recovery period. As can be seen in the traces the hemodynamic changes clearly evince that stimulating the

paw results in hemodynamic activity across the entire isocortex, with the CL side of the brain undergoing the strongest reaction, especially the CL-HP region.

Having extracted numerous activation traces from each trial and each mouse, quantitative evaluation of the detected activations in each region and the CL and IL counterparts was carried out. Five components of the traces from all trials and all mice were investigated: the peak percentage change (P%), the time to this peak (TTP), the decay time (DeT), the dip percentage (Dip%) if seen and the dip time to peak (DTTP) – see **Figure 3A**. P% and DeT were found to be consistently significant and are shown in **Figures 3B,C**. Data is plotted with IL traces for each region on the left (dotted lines) and CL regions on the right (solid lines). Each CL region was tested for significance over its IL counterpart and the CL-HP region was tested for significance over all regions (CL and IL). The strongest activity is located within the SS CL-HP region of the brain (Bregma –



HP regions are outlined by the additional blue triangular line in **Figure 2C**, middle panel.

The magnitude of the measured  $\Delta\text{HbO}$ ,  $\Delta\text{HbR}$ , and  $\Delta\text{HbT}$  responses for the CL-HP SS region (Bregma) achieves a median P% change of 31.4, -3.5, and 6.6% with a TTP of 20.5, 22.6, and 21 s HbO, HbR, and HbT, respectively. These values are in line with previous studies (Adamczak et al., 2010; Yao et al., 2013). In comparison, the IL-HP region only reaches P% changes of 17.4, -2.6, and 3.0% with a TTP of 18.6, 19.25, and 14.4 s for the respective components. These responses are in line with previous studies (Masamoto et al., 2006; Chen et al., 2011; Ma et al., 2016b). Of note is the presence of an initial dip in the HbO channel of both the IL-HP and CL-HP SS traces (**Figure 2C**, left and right panels). However, in this study there was no statistical

significance between these dips, and they did not occur in all cases. The Dip% and DTTP for these dips are summarized in **Supplementary Figure S1**. The median decay times (DeT) for the CL-HP region was longer in all cases in comparison to the IL-HP region (52.1, 61.5, and 50.25 s vs. 36.75, 55.85, and 38.85 s for HbO, HbR, and HbT, respectively) but statistical significance was only found in the HbT component (**Figure 3C**). It was also found that the P% of the CL-HP region was statistically significant over not only its IL counterpart but all other regions in both HbT and HbO (**Figure 3B**). This was not the case for HbR, which failed to show significance over its IL counterpart (**Figure 3B**). In general, the IL hemisphere of the brain in comparison to the CL side undergoes a less localized and more generic activation in terms of temporal dynamics and extent of the activation across the VC,

SS and SM areas (see **Figure 3C** and **Supplementary Figure S1**). As expected, recordings without paw stimulation resulted in no activation (see **Supplementary Figures S3A–C**).

### Functional Mapping of Cortical Activity

To further demonstrate the capabilities of vMSOT to map cortical hemodynamic responses, Pearson's correlation mapping was carried out on the HbO data. Due to the dynamic range of the delta values seen in the HbO data (up to 65% in one case), the presence of the initial dip and the difficulty in determining CL and IL activity in the HbR and HbT channels, it was determined this would give the most reliable and accurate result for the mapping process. Additionally, vMSOT is unique in its ability to map HbO at such a scale and resolution. Following the correlation mapping process outlined in the methods, a resulting correlation matrix representative of all mice for each region is displayed in **Figures 2B–D**, middle panels. Using the delta map as a guide, highly activated seed voxels located within the CL-HP SS region were chosen for correlation mapping (Oh et al., 2014; Paxinos and Franklin, 2019). Coronal slices are shown overlaid on the outline of a brain (Oh et al., 2014). The activation is strongest within the CL-HP SS area, yet a clear global response remains that ranges across a dominant section of the VC, SS cortex, and small portion of the SM.

### DISCUSSION

Numerous imaging modalities currently exist to monitor functional hemodynamic changes in the brain. These range from high resolution small FOV microscopy-based techniques to lower resolution macroscopic MRI- and US-based techniques. Closing the scaling gap between single cell neuronal imaging and a network level visualization approaches remains a pressing challenge. The results presented in this study corroborate and complement common BOLD studies using a similar stimulation paradigm (Schroeter et al., 2014). This was carried out with the added benefit of being able to detect more comprehensive functional information (namely, HbO, HbR, and HbT). The characteristics of the hemodynamic responses detected with vMSOT (including P%, TTP, DeT, Dip%, and DTTP shown in **Figures 2B–D**, **3B,C** and **Supplementary Figure S1**) are generally comparable to those measured with BOLD and optical techniques (Schroeter et al., 2014; Ma et al., 2016b), although modality cross-validation under the same anesthesia, mouse line and stimulation paradigm was outside the scope of the current investigation. It should be noted that the dynamic range of the  $\Delta$ HbR signal is approximately twice that of BOLD (3% vs. 1.5%). This increase in detection is likely due to the fact that while HbR is a valid paramagnetic agent, its physical properties in terms of light absorption capabilities are likely stronger than its paramagnetic potential (Pauling and Coryell, 1936; Jacques, 2013). These unique features of vMSOT, achieved by capitalizing on the synergistic combination of strong optical contrast and high diffraction-limited ultrasonic resolution, enables a comprehensive representation of brain metabolism and function

and is poised to provide new insights on the understanding of brain activity.

The traces seen for HbO, HbR, and HbT further allude to previously observed hemodynamic changes with HbO overshooting and then undershooting to levels below the baseline after recovery. The presence of an initial dip in the HbO component located in both of the SS CL and IL-HP regions with stronger dynamics on the CL side, a contentious issue in fMRI, further highlights the strength of vMSOT for hemodynamic monitoring (Hu and Yacoub, 2012). However, this study did not find any statistical significance between the CL and IL dips for either Dip% or DTTP (**Supplementary Figures S1B,C**). Our results show little to no increase in the HbR before it decreases whilst the HbT increase and slow return to baseline corresponds to the dilation of vessels attributed to the increase in total CBV, similar to what is achieved with fUS (Culver et al., 2005). The vMSOT system employed in this work additionally provides anatomical information that can be efficiently used for co-registration with established atlases of the mouse brain and hence facilitate localizing the activated areas (**Figures 2B–D**, middle panels and **Supplementary Figure S2**). This was utilized to show that the activity is strongest not only within the CL-HP region (as expected, **Figure 2C**, right panel) but a diffuse global response was seen across the isocortex including the VC, SS, and SM regions (**Figures 2B–D** and **Supplementary Figures S2A,B**). By quantitatively analyzing the traces for all components, all trials and across all regions it was shown that the CL side of the brain showed consistently stronger activation (P%, **Figure 3B**) than the IL side along with longer TTP values and DeT values (**Supplementary Figure S1A** and **Figure 3C**). However, statistical significance could only be determined in the HbO and HbT channel for P% (**Figure 3B**). Of particular importance is the fact that the P% of the CL-HP SS region was statistically significant from all other brain regions for HbT and HbO (**Figure 3B**). Future experiments could likely take advantage of this fact to aid in mapping and localizing activated areas, along with other stimulation paradigms e.g., whisker and optogenetic stimulation (Olefir et al., 2019; Ovsepian et al., 2019a,b). Future studies may further aim at investigating how the hemodynamic responses outlined here vary across different lines and sexes within the same model organism and in comparison to other model organisms (Constantinides et al., 2011; Li and Zhang, 2018; Ovsepian et al., 2019a). It should also be noted that the experiments were carried out in a completely non-invasive manner with skull and scalp remaining intact and without the need for exogenous contrast agents, thus highlighting vMSOT's applicability in neuroimaging studies and potential implications for the imaging of small animal disease models.

A potential limitation of the study described in this work stems from the use of isoflurane anesthesia, which may hinder the hemodynamic responses due to its vasodilatory effect (Constantinides et al., 2011). Other anesthesia methods, such as ketamine or urethane, may result in better mapping and a reduced global response than that shown here (**Figures 2B–D**, middle panels; Kober et al., 2005). However, due to the added dynamic range of all hemodynamic components, vMSOT is readily able to overcome these anesthesia artifacts.

This is proven by the fact the while correlation mapping showed widespread activation, this activation was strongest within the CL-HP SS region. Deeper mapping of the brain could be carried out by employing near-infrared (650–1350 nm) light illumination. However, the weaker absorption of blood at these wavelengths will likely lead to a lower SNR of vascular structures (Jacques, 2013). This is especially true in the case of smaller arterioles and venules that undergo greater hemodynamic changes than larger vessels (Ma et al., 2016a; He et al., 2018). Visible light was then chosen as the more suitable imaging paradigm for mapping the activity within the superficial location of the SS cortex. Due to the recent advent of calcium imaging with vMSOT in the mouse brain and the current limited palette of suitable near-infrared probes the ability to distinguish endogenous contrast over exogenous probes in the visible regime of light is of great importance (Gottschalk et al., 2019).

Having replicated similar results to those seen in fMRI with a similar stimulation and mapping method, future work should aim at using the suggested methodology to study neurovascular and neurometabolic coupling mechanisms. This may be of especial importance in the postnatal development of mice and in neurodegenerative models. The method could be utilized for research on neuro-degenerative diseases such as Alzheimer's, where the non-invasive aspect could be of particular use in longitudinal studies (Camandola and Mattson, 2017; Yin et al., 2017). The suggested vMSOT platform combines the contrast-related strengths of optical imaging with the penetration depths and high resolution of ultrasound. As shown in **Figure 1A**, brain imaging with vMSOT is achieved with only an ultrasound gel applied to the scalp, which may facilitate experiments in head-fixed awake mice and simultaneous or consecutive stimulation of multiple paws (Morales-Botello et al., 2012; Vanni et al., 2017; Desjardins et al., 2019). vMSOT also has greater sensitivity to hemodynamic activity than fMRI via the increased dynamic range of delta activity and visualization of multiple hemodynamic components. All in all, vMSOT's ability to combine functional and anatomical imaging at superior spatio-temporal resolution

across the whole mouse cortex is expected to be of significant advantage to neuroimaging.

## DATA AVAILABILITY STATEMENT

The datasets generated for this study are available on request to the corresponding author.

## ETHICS STATEMENT

This study was carried out in full compliance with the institutional guidelines of the Institute for Biological and Medical Imaging and with approval from the Government District of Upper Bavaria.

## AUTHOR CONTRIBUTIONS

BM, MH, and DR conceived the study. BM carried out all experiments. BM and MH carried out the analysis of the data. DR and XD-B supervised the study and data analysis. All authors were involved in writing the manuscript and discussed the results.

## FUNDING

This project has received funding from the European Research Council under Consolidator Grant ERC-2015-CoG-682379 and the Human Frontier Science Program Young Investigator Grant HFSP-RGY070.

## SUPPLEMENTARY MATERIAL

The Supplementary Material for this article can be found online at: <https://www.frontiersin.org/articles/10.3389/fnins.2020.00536/full#supplementary-material>

## REFERENCES

- Adamczak, J. M., Farr, T. D., Seehafer, J. U., Kalthoff, D., and Hoehn, M. (2010). High field BOLD response to forepaw stimulation in the mouse. *Neuroimage* 51, 704–712. doi: 10.1016/j.neuroimage.2010.02.083
- Arthurs, O. J., and Boniface, S. (2002). How well do we understand the neural origins of the fMRI BOLD signal? *Trends Neurosci.* 25, 27–31. doi: 10.1016/s0166-2236(00)01995-0
- Bosshard, S. C., Balthes, C., Wyss, M. T., Mueggler, T., Weber, B., and Rudin, M. (2010). Assessment of brain responses to innocuous and noxious electrical forepaw stimulation in mice using BOLD fMRI. *PAIN* 151, 655–663. doi: 10.1016/j.pain.2010.08.025
- Buxton, R. B., Wong, E. C., and Frank, L. R. (1998). Dynamics of blood flow and oxygenation changes during brain activation: the balloon model. *Magn. Reson. Med.* 39, 855–864. doi: 10.1002/mrm.1910390602
- Camandola, S., and Mattson, M. P. (2017). Brain metabolism in health, aging, and neurodegeneration. *EMBO J.* 36, 1474–1492. doi: 10.15252/embj.201695810
- Chen, B. R., Bouchard, M. B., McCaslin, A. F., Burgess, S. A., and Hillman, E. M. (2011). High-speed vascular dynamics of the hemodynamic response. *Neuroimage* 54, 1021–1030. doi: 10.1016/j.neuroimage.2010.09.036
- Constantinides, C., Mean, R., and Janssen, B. J. (2011). Effects of isoflurane anesthesia on the cardiovascular function of the C57BL/6 mouse. *ILAR J.* 52:e21.
- Cox, B. T., Laufer, J. G., Beard, P. C., and Arridge, S. R. (2012). Quantitative spectroscopic photoacoustic imaging: a review. *J. Biomed. Opt.* 17, 061202. doi: 10.1117/1.jbo.17.6.061202
- Cui, M.-H., Suzuka, S. M., Branch, N. A., Ambadipudi, K., Thangaswamy, S., Acharya, S. A., et al. (2017). Brain neurochemical and hemodynamic findings in the NY1DD mouse model of mild sickle cell disease. *NMR Biomed.* 30:e3692. doi: 10.1002/nbm.3692
- Culver, J. P., Siegel, A. M., Franceschini, M. A., Mandeville, J. B., and Boas, D. A. (2005). Evidence that cerebral blood volume can provide brain activation maps with better spatial resolution than deoxygenated hemoglobin. *Neuroimage* 27, 947–959. doi: 10.1016/j.neuroimage.2005.05.052
- Culver, J. P., Siegel, A. M., Stott, J. J., and Boas, D. A. (2004). Volumetric diffuse optical tomography of brain activity. *Opt. Lett.* 28, 2061–2063.
- Deán-Ben, X. L., Gottschalk, S., Mc Larney, B., Shoham, S., and Razansky, D. (2017). Advanced optoacoustic methods for multiscale imaging of in vivo dynamics. *Chemical Society Reviews* 46, 2158–2198. doi: 10.1039/c6cs00765a

- Dean-Ben, X. L., Sela, G., Lauri, A., Kneipp, M., Ntziachristos, V., Westmeyer, G. G., et al. (2016). Functional photoacoustic neuro-tomography for scalable whole-brain monitoring of calcium indicators. *Light Sci. Appl.* 5:e16201. doi: 10.1038/lsa.2016.201
- Defieux, T., Demene, C., Pernot, M., and Tanter, M. (2018). Functional ultrasound neuroimaging: a review of the preclinical and clinical state of the art. *Curr. Opin. Neurobiol.* 50, 128–135. doi: 10.1016/j.conb.2018.02.001
- Desjardins, M., Kılıç, K., Thunemann, M., Mateo, C., Holland, D., Ferri, C. G., et al. (2019). Awake mouse imaging: from two-photon microscopy to blood oxygen level-dependent functional magnetic resonance imaging. *Biol. Psychiatry* 4, 533–542. doi: 10.1016/j.bpsc.2018.12.002
- Filosa, J. A., and Blanco, V. M. (2007). Neurovascular coupling in the mammalian brain. *Exp. Physiol.* 92, 641–646. doi: 10.1113/expphysiol.2006.03.6368
- Fornito, A., Zalesky, A., and Breakspear, M. (2015). The connectomics of brain disorders. *Nat. Rev. Neurosci.* 16:159. doi: 10.1038/nrn3901
- Gottschalk, S., Degtyaruk, O., Mc Larney, B., Rebling, J., Hutter, M. A., Deán-Ben, X. L., et al. (2019). Rapid volumetric photoacoustic imaging of neural dynamics across the mouse brain. *Nat. Biomed. Eng.* 3, 392–401. doi: 10.1038/s41551-019-0372-9
- Gottschalk, S., Fehm, T. F., Dean-Ben, X. L., and Razansky, D. (2015). Noninvasive real-time visualization of multiple cerebral hemodynamic parameters in whole mouse brains using five-dimensional photoacoustic tomography. *J. Cereb. Blood Flow Metab.* 32, 938–951. doi: 10.1038/jcbfm.2014.249
- Gottschalk, S., Fehm, T. F., Dean-Ben, X. L., Tsytarev, V., and Razansky, D. (2017). Correlation between volumetric oxygenation responses and electrophysiology identifies deep thalamocortical activity during epileptic seizures. *Neurophotonics* 4:011007. doi: 10.1117/1.nph.4.1.011007
- He, B., Yang, L., Wilke, C., and Yuan, H. (2011). Electrophysiological Imaging of Brain activity and connectivity—challenges and opportunities. *IEEE Trans. Biomed. Eng.* 58, 1918–1931. doi: 10.1109/TBME.2011.2139210
- He, Y., Wang, M., Chen, X., Pohmann, R., Polimeni, J. R., Scheffler, K., et al. (2018). Ultra-slow single-Vessel BOLD and CBV-Based fMRI spatiotemporal dynamics and their correlation with neuronal intracellular calcium signals. *Neuron* 97, 925.e–939.e. doi: 10.1016/j.neuron.2018.01.025
- Herculano-Houzel, S. (2011). Scaling of brain metabolism with a fixed energy budget per neuron: implications for neuronal activity, plasticity and evolution. *PLoS One* 6:e17514. doi: 10.1371/journal.pone.0017514
- Hielscher, A. H. (2005). Optical tomographic imaging of small animals. *Curr. Opin. Biotechnol.* 16, 79–88.
- Hu, S., and Wang, L. V. (2010). Neurovascular photoacoustic tomography. *Front. Neuroeng.* 2:10. doi: 10.3389/fneng.2010.00010
- Hu, X., and Yacoub, E. (2012). The story of the initial dip in fMRI. *Neuroimage* 62, 1103–1108. doi: 10.1016/j.neuroimage.2012.03.005
- Huppert, T. J., Hoge, R. D., Diamond, S. G., Franceschini, M. A., and Boas, D. A. (2006). A temporal comparison of BOLD, ASL, and NIRS hemodynamic responses to motor stimuli in adult humans. *Neuroimage* 29, 368–382.
- Iannetti, G., and Wise, R. G. (2007). BOLD functional MRI in disease and pharmacological studies: room for improvement? *Magn. Reson. Imaging* 25, 978–988.
- Insel, T. R., Landis, S. C., and Collins, F. S. (2013). The NIH brain initiative. *Science* 340, 687–688.
- Jacques, S. L. (2013). Optical properties of biological tissues: a review. *Phys. Med. Biol.* 58, R37–R61. doi: 10.1088/0031-9155/58/11/R37
- Kazmi, S. S., Richards, L. M., Schrandt, C. J., Davis, M. A., and Dunn, A. K. (2015). Expanding applications, accuracy, and interpretation of laser speckle contrast imaging of cerebral blood flow. *J. Cereb. Blood Flow Metab.* 35, 1076–1084. doi: 10.1038/jcbfm.2015.84
- Kober, F., Iltis, I., Cozzone, P. J., and Bernard, M. (2005). Myocardial blood flow mapping in mice using high-resolution spin labeling magnetic resonance imaging: influence of ketamine/xylazine and isoflurane anesthesia. *Magn. Reson. Med.* 53, 601–606.
- Laufer, J., Elwell, C., Delpy, D., and Beard, P. (2005). In vitro measurements of absolute blood oxygen saturation using pulsed near-infrared photoacoustic spectroscopy: accuracy and resolution. *Phys. Med. Biol.* 50, 4409.
- Li, C., Aguirre, A., Gamelin, J. K., Maurudis, A., Zhu, Q., and Wang, L. V. (2010). Real-time photoacoustic tomography of cortical hemodynamics in small animals. *J. Biomed. Opt.* 15:010509. doi: 10.1117/1.3302807
- Li, C.-X., and Zhang, X. (2018). Evaluation of prolonged administration of isoflurane on cerebral blood flow and default mode network in macaque monkeys anesthetized with different maintenance doses. *Neurosci. Lett.* 662, 402–408. doi: 10.1016/j.neulet.2017.10.034
- Li, M.-L., Oh, J.-T., Xie, X., Ku, G., Wang, W., Li, C., et al. (2008). Simultaneous molecular and hypoxia imaging of brain tumors in vivo using spectroscopic photoacoustic tomography. *Proc. IEEE* 96, 481–489.
- Liao, L.-D., Lin, C.-T., Shih, Y.-Y. I., Duong, T. Q., Lai, H.-Y., Wang, P.-H., et al. (2012). Transcranial imaging of functional cerebral hemodynamic changes in single blood vessels using in vivo photoacoustic microscopy. *J. Cereb. Blood Flow Metab.* 32, 938–951. doi: 10.1038/jcbfm.2012.42
- Logothetis, N. K. (2008). What we can do and what we cannot do with fMRI. *Nature* 453, 869. doi: 10.1038/nature06976
- Ma, Y., Shaik, M. A., Kim, S. H., Kozberg, M. G., Thibodeaux, D. N., Zhao, H. T., et al. (2016a). Wide-field optical mapping of neural activity and brain haemodynamics: considerations and novel approaches. *Philos. Trans. R. Soc. B* 371:20150360.
- Ma, Y., Shaik, M. A., Kozberg, M. G., Kim, S. H., Portes, J. P., Timerman, D., et al. (2016b). Resting-state hemodynamics are spatiotemporally coupled to synchronized and symmetric neural activity in excitatory neurons. *Proc. Natl. Acad. Sci. U.S.A.* 113, E8463–E8471. doi: 10.1073/pnas.1525369113
- Macé, E., Montaldo, G., Cohen, I., Baulac, M., Fink, M., and Tanter, M. (2011). Functional ultrasound imaging of the brain. *Nat. Methods* 8:662.
- Markram, H., Meier, K., Lippert, T., Grillner, S., Frackowiak, R., Dehaene, S., et al. (2011). Introducing the human brain project. *Proc. Comput. Sci.* 7, 39–42.
- Masamoto, K., Kim, T., Fukuda, M., Wang, P., and Kim, S.-G. (2006). Relationship between neural, vascular, and BOLD signals in isoflurane-anesthetized rat somatosensory cortex. *Cereb. Cortex* 17, 942–950.
- Morales-Botello, M., Aguilar, J., and Foffani, G. (2012). Imaging the spatio-temporal dynamics of supragranular activity in the rat somatosensory cortex in response to stimulation of the paws. *PLoS One* 7:e40174. doi: 10.1371/journal.pone.0040174
- Mott, M. C., Gordon, J. A., and Koroshetz, W. J. (2018). The NIH BRAIN Initiative: advancing neurotechnologies, integrating disciplines. *PLoS Biol.* 16:e3000066. doi: 10.1371/journal.pbio.3000066
- Oh, S. W., Harris, J. A., Ng, L., Winslow, B., Cain, N., Mihalas, S., et al. (2014). A mesoscale connectome of the mouse brain. *Nature* 508, 207. doi: 10.1038/nature13186
- Olefir, I., Ghazaryan, A., Yang, H., Malekzadeh-Najafabadi, J., Glasl, S., Symvoulidis, P., et al. (2019). Spatial and spectral mapping and decomposition of neural dynamics and organization of the mouse brain with multispectral photoacoustic tomography. *Cell Rep.* 26, 2833–2846. doi: 10.1016/j.celrep.2019.02.020
- Ovsepian, S. V., Jiang, Y., Sardella, T. C., Malekzadeh-Najafabadi, J., Burton, N. C., Yu, X., et al. (2019a). Visualizing cortical response to optogenetic stimulation and sensory inputs using multispectral handheld photoacoustic imaging. *Photoacoustics* 2019:100153. doi: 10.1016/j.pacs.2019.100153
- Ovsepian, S. V., Olefir, I., and Ntziachristos, V. (2019b). Advances in photoacoustic neurotomography of animal models. *Trends Biotechnol.* 37, 1315–1326. doi: 10.1016/j.tibtech.2019.07.012
- Ozbek, A., Deán-Ben, X., and Razansky, D. (2013). Realtime parallel back-projection algorithm for three-dimensional photoacoustic imaging devices, European Conference on Biomedical Optics. *Opt. Soc. Am.* 8800:880001.
- Pauling, L., and Coryell, C. D. (1936). The magnetic properties and structure of hemoglobin, oxyhemoglobin and carbonmonoxyhemoglobin. *Proc. Natl. Acad. Sci. U.S.A.* 22, 210–216.
- Paxinos, G., and Franklin, K. B. (2019). *Paxinos and Franklin's The Mouse Brain in Stereotaxic Coordinates*. Cambridge, MA: Academic Press.
- Reisman, M. D., Markow, Z. E., Bauer, A. Q., and Culver, J. P. (2017). Structured illumination diffuse optical tomography for noninvasive functional neuroimaging in mice. *Neurophotonics* 4:021102. doi: 10.1117/1.NPh.4.2.021102
- Schroeter, A., Schlegel, F., Seuwen, A., Grandjean, J., and Rudin, M. (2014). Specificity of stimulus-evoked fMRI responses in the mouse: the influence of

- systemic physiological changes associated with innocuous stimulation under four different anesthetics. *Neuroimage* 94, 372–384. doi: 10.1016/j.neuroimage.2014.01.046
- Takamasa, I., Hiroshi, Y., and Toshiyuki, H. (2001). A Color atlas of sectional anatomy of the mouse. *Braintree Sci.*
- Tzoumas, S., and Ntziachristos, V. (2017). Spectral unmixing techniques for optoacoustic imaging of tissue pathophysiology. *Philos. Trans. R. Soc. A* 375, 20170262. doi: 10.1098/rsta.2017.0262
- Tzoumas, S., Nunes, A., Olefir, I., Stangl, S., Symvoulidis, P., Glasl, S., et al. (2016). Eigenspectra optoacoustic tomography achieves quantitative blood oxygenation imaging deep in tissues. *Nat. Commun.* 7, 12121. doi: 10.1038/ncomms12121
- Vanni, M. P., Chan, A. W., Balbi, M., Silasi, G., and Murphy, T. H. (2017). Mesoscale mapping of mouse cortex reveals frequency-dependent cycling between distinct macroscale functional modules. *J. Neurosci.* 37, 7513–7533. doi: 10.1523/JNEUROSCI.3560-16.2017
- Yablonskiy, D. A., Sukstanskii, A. L., and He, X. (2013). Blood oxygenation level-dependent (BOLD)-based techniques for the quantification of brain hemodynamic and metabolic properties—theoretical models and experimental approaches. *NMR Biomed.* 26, 963–986. doi: 10.1002/nbm.2839
- Yao, J., Wang, L., Yang, J.-M., Maslov, K. I., Wong, T. T., Li, L., et al. (2015). High-speed label-free functional photoacoustic microscopy of mouse brain in action. *Nat Methods* 12:407. doi: 10.1038/nmeth.3336
- Yao, J., Xia, J., Maslov, K. I., Nasirivanaki, M., Tsytsarev, V., Demchenko, A. V., et al. (2013). Noninvasive photoacoustic computed tomography of mouse brain metabolism in vivo. *Neuroimage* 64, 257–266. doi: 10.1016/j.neuroimage.2012.08.054
- Yin, F., Yao, J., Brinton, R. D., and Cadenas, E. (2017). The metabolic-inflammatory axis in brain aging and neurodegeneration. *Front. Aging Neurosci.* 9:209.
- Conflict of Interest:** The authors declare that the research was conducted in the absence of any commercial or financial relationships that could be construed as a potential conflict of interest.
- Copyright © 2020 Mc Larney, Hutter, Degtyaruk, Deán-Ben and Razansky. This is an open-access article distributed under the terms of the Creative Commons Attribution License (CC BY). The use, distribution or reproduction in other forums is permitted, provided the original author(s) and the copyright owner(s) are credited and that the original publication in this journal is cited, in accordance with accepted academic practice. No use, distribution or reproduction is permitted which does not comply with these terms.

## Monitoring of stimulus evoked murine somatosensory cortex hemodynamic activity with volumetric multi-spectral optoacoustic tomography

Benedict Mc Larney<sup>1,2†‡</sup>, Magdalena Hutter<sup>2,‡</sup>, Oleksiy Degtyaruk<sup>2,3</sup>, Xosé Luís Dean Ben<sup>3,4</sup>, Daniel Razansky<sup>1,2,3,4\*</sup>

<sup>1</sup>Faculty of Medicine, Technical University of Munich, Munich, Germany

<sup>2</sup>Institute of Biological and Medical Imaging, Helmholtz Center Munich, Neuherberg, Germany

<sup>3</sup>Faculty of Medicine and Institute of Pharmacology and Toxicology, University of Zurich, Switzerland

<sup>4</sup>Institute for Biomedical Engineering and Department of Information Technology and Electrical Engineering, ETH Zurich, Switzerland

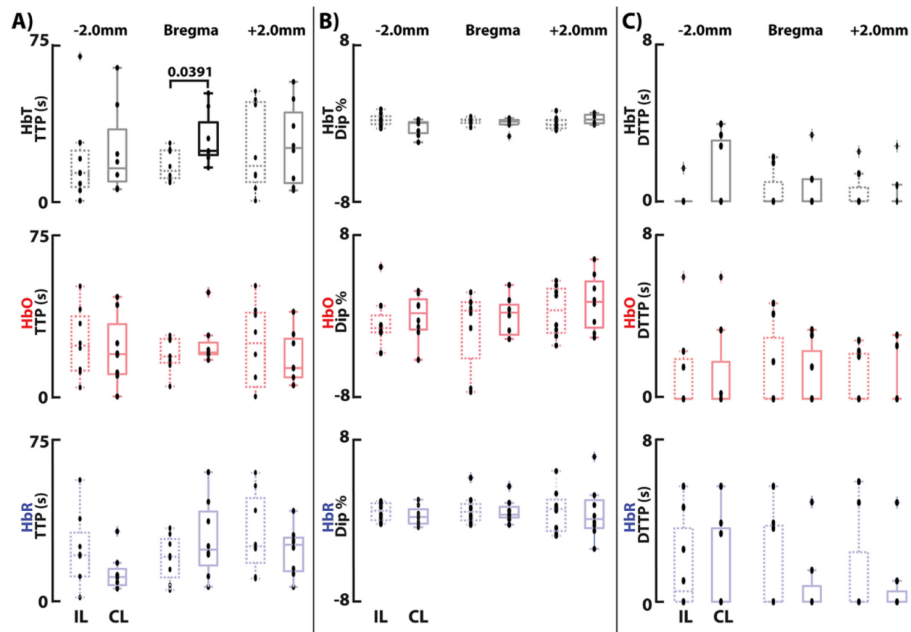
<sup>‡</sup>These authors have contributed equally to this work

<sup>†</sup>Present address: Benedict Mc Larney, Molecular Pharmacology Program, Department of Radiology, Memorial Sloan Kettering Cancer Center, New York, NY, United States

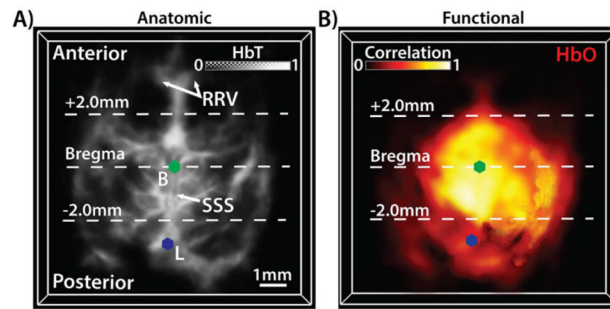
**\* Correspondence:**

Daniel Razansky

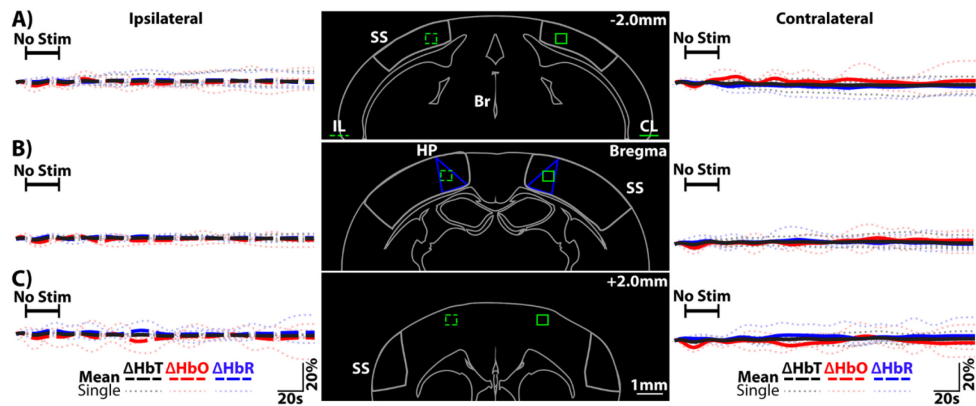
[daniel.razansky@uzh.ch](mailto:daniel.razansky@uzh.ch)



**Supplemental Figure 1. A - C)** Box plots of all components for each respective region. P values are shown when significant ( $p < 0.05$ ). Analysis was carried out on each trace based on the average of the voxels within the ROIs shown in Figure 2 for each mouse ( $n = 4$ ) and each trial ( $n = 2$  per mouse, 8 trials in total). **(A)** Time to peak (TTP) for each component. Statistical significance was only found in the HbT channel between the IL & CL Bregma regions. **(B)** Dip percentage (Dip %) for all regions and components. **(C)** Dip time to peak (DTTP) for each component and region. The median and standard deviation are shown, and whiskers extend to adjacent values. Each black dot represents an individual measurement from all cycles from all mice (8 dots per box). Statistical significance was determined via a Wilcoxon signed-rank test comparing ipsilateral to contralateral regions for each component.



**Supplemental Figure 2 A – B** MIPs of 3D Anatomic (HbT) and functional (HbO correlation mapping data). (A) Anatomic data (Transverse view, based on vMSOT spectrally unmixed HbT distribution) highlighting the slice locations as shown in Figure 2. Highlighted are anatomical landmarks lambda (L, blue hexagon) and bregma (B, green hexagon). Also highlighted are the superior sagittal sinus (SSS) and rostral rhinal vein (RRV). (B) The corresponding MIP of Pearson's correlated HbO data with the anatomical locations identified in A) superimposed. The ability to visualize anatomical landmarks aids in identifying the location of activated areas.



**Supplemental Figure 3.** A - C) Control data (electrodes inserted but no stimulation applied) for a single cycle from each mouse for HbT, HbO and HbR respectively across all previously analysed brain regions, including anatomical references. These are based on the same mice and ROIs as shown in Figure 2. For ease of comparison, the window in which paw stimulation would be applied is left visible however, no paw stimulation was applied in this case. (A) Left, the ipsilateral (IL) traces (large dotted lines) for HbT, HbO and HbR from the IL ROI highlighted in dotted green in the middle image. Middle, reference brain outline image with ROIs. Right, the contralateral (CL) traces from the same area (solid green ROI). The SS area is outlined. (B) Left, IL traces for HbT, HbO and HbR from the IL ROI highlighted in dotted green in the middle image (at Bregma - primarily hind paw (HP) somatosensory regions). Middle, reference brain outline image with ROIs. Right, the CL traces from the same area (solid green ROI). HP regions of the SS cortex are highlighted (blue lines) as well as the SS cortex (grey outline). (C) Left, traces for HbT, HbO and HbR from the IL ROI highlighted in dotted green in the middle image (+2.0mm from Bregma - primarily somatomotor cortex regions). Middle, reference brain outline with ROIs at this location. Right, CL traces from the same area (solid green ROI). In all cases no activity like that seen during electrical stimulation is observed with fluctuations likely resulting from resting state changes. The response from a single cycle from each mouse is plotted as a lightly dotted line in all cases. The bold line represents the averaged response from all mice. Legend - IL: Ipsilateral, CL: Contralateral, HP: Hindpaw region of somatosensory cortex, SS: Somatosensory cortex, Br: Brain Outline. The average response from all trials from each mouse is plotted as a lightly dotted line in all cases. The bold line represents the averaged response from all mice.

## 4. A genetically encoded near-infrared fluorescent calcium ion indicator

### 4.1 Summary and Author Contribution

One of the current limitations for both purely optical based methods and optoacoustics is the inherent scattering and absorption of light within the visible spectrum (400 – 650nm). GFP, one of the main workhorses of fluorescence microscopy absorbs light at 488 nm where the effects of scattering and absorption are orders of magnitude higher than in the NIR range. Due to its success and established methods the majority of calcium and voltage genetically encoded indicators incorporate GFP or one of its derivatives and thus are limited to the visible spectrum of light. This poses further drawbacks in the acquisition of optogenetic data where actuators and sensors have high spectral overlap. As shown in previous work, OAT imaging at red and NIR wavelengths could allow non-invasive imaging of the entire mouse brain however no such indicator existed. Having established that GCaMP6s/f could be detected with FONT even in the presence of high hemoglobin background absorption, attempting similar experiments with an NIR GECI would be of high importance. This work outlines the development and testing of the first NIR GECI, NIR-GECO1. The protein undergoes a change in fluorescence (decrease) upon binding to  $\text{Ca}^{2+}$  (the opposite of GCaMP6). NIR-GECO1 absorbs light at 671nm and emits at 702 nm, within the NIR spectrum of light. Unfortunately, it did not provide a detectable response with FONT.

This work provides a method for the development, transfection and *in vivo* testing of the first NIR GECO. Detection of the protein required the development of a sensitive macro scale fluorescent setup for imaging the entire mouse head and the use of a highly stable laser due to the low delta of the protein. NIR GECO1 requires biliverdin as a co-factor in order to fluoresce, unlike GFP which can be fully formed in a fluorescent state by mammalian cells. As a result, the majority of NIR-GECO1 expressed *in vivo* is non-fluorescent and bleaches at a much faster rate than GFP. Additionally, as NIR-GECO1 is in its first iteration compared to GCaMP6s/f which has undergone decades of improvement, it is ~1 order of magnitude less sensitive when directly compared. Successful mesoscale detection of NIR-GECO1 with fluorescence required careful selection of viral injection into the S1HL region of the mouse cortex along with data processing to account for the rapid bleaching of the protein.

This work combined laser alignment, *in vivo* animal imaging work, neurosurgery, optimization of NIR-GECO1 expression *in vivo*, optimizing experimental settings, MATLAB scripting and automation and investigative neuroscience. The developed methodology took account of current AAV transient expression methods and further optimized the paw stimulation pattern to get the maximum possible response out of the protein.

My contribution to the presented manuscript was the following:

**Conception and design:** I designed the *in vivo* mesoscale experiments along with Prof. Razansky and Dr. Gottschalk.

**Development of methodology:** I outlined and refined the methodology.

**Acquisition of data:** I performed all mouse imaging and injections with the assistance of Mr. Michael Reiss. I performed all mesoscale *in vivo* analysis.

# A genetically encoded near-infrared fluorescent calcium ion indicator

Yong Qian<sup>1,12</sup>, Kiryl D. Piatkevich<sup>2,12</sup>, Benedict Mc Larney<sup>3,4,12</sup>, Ahmed S. Abdelfattah<sup>5</sup>, Sohun Mehta<sup>6</sup>, Mitchell H. Murdock<sup>7</sup>, Sven Gottschalk<sup>3</sup>, Rosana S. Molina<sup>7</sup>, Wei Zhang<sup>1</sup>, Yingche Chen<sup>1</sup>, Jiahui Wu<sup>1</sup>, Mikhail Drobizhev<sup>7</sup>, Thomas E. Hughes<sup>7</sup>, Jin Zhang<sup>6</sup>, Eric R. Schreiter<sup>5</sup>, Shy Shoham<sup>8</sup>, Daniel Razansky<sup>3,4,9,10</sup>, Edward S. Boyden<sup>2</sup> and Robert E. Campbell<sup>1,11\*</sup>

**We report an intensimetric, near-infrared fluorescent, genetically encoded calcium ion (Ca<sup>2+</sup>) indicator (GECI) with excitation and emission maxima at 678 and 704 nm, respectively. This GECI, designated NIR-GECO1, enables imaging of Ca<sup>2+</sup> transients in cultured mammalian cells and brain tissue with sensitivity comparable to that of currently available visible-wavelength GECIs. We demonstrate that NIR-GECO1 opens up new vistas for multicolor Ca<sup>2+</sup> imaging in combination with other optogenetic indicators and actuators.**

GECIs are often used together with optogenetic actuators for simultaneous recording and control of biological processes with high spatiotemporal resolution. However, substantial spectral overlap among currently available GECIs, optogenetic actuators and other genetically encoded indicators limits the possibilities for multiplexing. Most genetically encoded fluorophores fall into two classes: visibly fluorescent  $\beta$ -barrel fluorescent proteins that are homologs of the *Aequorea* green fluorescent protein<sup>1</sup>, and far-red to near-infrared (NIR) fluorescent biliverdin-binding fluorescent proteins (BV-FPs) derived from bacteriophytochromes (BphPs)<sup>2</sup> or other biliverdin-binding proteins<sup>3</sup>. Fluorescent proteins have emission peaks in the visible range (~450–670 nm), and BV-FPs have emission peaks in the NIR range (~670–720 nm)<sup>4</sup>. While many GECIs and other indicators have been engineered from fluorescent proteins, examples of BV-FP-based indicators are limited. Examples include BV-FPs as donors and acceptors in fluorescence resonance energy transfer (FRET)-based indicators, and the use of split BV-FPs in protein complementation assays<sup>5</sup>.

To expand the range of GECI colors into the NIR range, we have engineered an intensimetric GECI on the basis of the monomeric BV-FP, mIFP<sup>6</sup>. We pursued a design with a Ca<sup>2+</sup>-binding domain (calmodulin (CaM)-RS20), inserted into mIFP such that Ca<sup>2+</sup> binding would modulate the biliverdin chromophore environment and fluorescence intensity (Supplementary Note 1). We chose four potential insertion sites (between residues 9/10, 57/58, 138/139 and 170/176) based on inspection of the X-ray crystal structure of *Deinococcus radiodurans* BphP (PDB ID: 2O9B)<sup>7</sup>, which has 35% sequence identity with mIFP<sup>6</sup>. Only the replacement of residues 171–175 with CaM-RS20 yielded a protein with a Ca<sup>2+</sup>-dependent

change in fluorescence in vitro (a twofold decrease) (Fig. 1a,b and Supplementary Fig. 1). To improve the indicator properties, we systematically optimized the insertion site (leading to deletion of mIFP residues 176 and 177) and the N- and C-terminal linkers (ultimately the sequences GAL and RRHD, respectively) connecting CaM-RS20 to mIFP.

To facilitate iterative rounds of improvement on the basis of fluorescence screening of randomly mutated variants in bacterial colonies followed by functional tests in mammalian cells, we created a vector (*pcDuEx2*) for expression in both *Escherichia coli* and mammalian cells (Supplementary Fig. 2a). Following 12 rounds of library expression and screening (Supplementary Figs. 2b and 3), we designated our best variant as NIR genetically encoded Ca<sup>2+</sup> indicator for optical imaging (NIR-GECO1; Supplementary Figs. 2c and 4). A parallel effort to engineer a GECI from the smURFP<sup>8</sup> BV-FP was not successful (Supplementary Fig. 5). NIR-GECO1 has absorbance and emission peaks at 678 and 704 nm, respectively, and undergoes a 90% decrease in fluorescence intensity upon binding Ca<sup>2+</sup> ( $K_d=215$  nm) (Fig. 1c–e and Supplementary Fig. 6). The fluorescence change and  $K_d$  are comparable to those of GCaMP3 ( $F_{max}/F_{min}=13.6$ ;  $K_d=405$  nm), which was the first broadly useful single-fluorescent-protein-based GECI<sup>8</sup>. Key differences include the opposite directions of the responses to Ca<sup>2+</sup> and NIR-GECO1's lower Hill coefficient ( $n=1.03$ ). As an inverse response indicator, NIR-GECO1 is in its more brightly fluorescent form in resting cells (low Ca<sup>2+</sup>), and is therefore more susceptible to photobleaching under continuous illumination. In addition, excitation of resting cells above and below the imaging plane will contribute to an increased background signal. As expected when comparing an FP to a BV-FP, the Ca<sup>2+</sup>-bound state of GCaMP3 is approximately sixfold brighter than the Ca<sup>2+</sup>-free state of NIR-GECO1 (Supplementary Table 1)<sup>8</sup>.

To evaluate the performance of NIR-GECO1 in cultured neurons, we compared intracellular fluorescence brightness and photostability to those of the spectrally similar BV-FPs, iRFP682<sup>9</sup> and miRFP<sup>10</sup> (Supplementary Table 1). All three BV-FPs distributed evenly within the cytosol, dendrites and nucleus of neurons, with no apparent puncta or localized accumulations (Fig. 1f). NIR-GECO1 baseline intracellular brightness was similar to that of miRFP and

<sup>1</sup>Department of Chemistry, University of Alberta, Edmonton, Alberta, Canada. <sup>2</sup>Media Lab and McGovern Institute for Brain Research, MIT, Cambridge, MA, USA. <sup>3</sup>Institute for Biological and Medical Imaging, Helmholtz Center Munich, Neuherberg, Germany. <sup>4</sup>Faculty of Medicine, Technical University of Munich, Munich, Germany. <sup>5</sup>Janelia Research Campus, Howard Hughes Medical Institute, Ashburn, VA, USA. <sup>6</sup>Department of Pharmacology, University of California San Diego, La Jolla, CA, USA. <sup>7</sup>Department of Cell Biology and Neuroscience, Montana State University, Bozeman, MT, USA. <sup>8</sup>Departments of Ophthalmology and of Neuroscience and Physiology, New York University Langone Health, New York City, NY, USA. <sup>9</sup>Faculty of Medicine and Institute of Pharmacology and Toxicology, University of Zurich, Zurich, Switzerland. <sup>10</sup>Department of Information Technology and Electrical Engineering and Institute for Biomedical Engineering, ETH Zurich, Zurich, Switzerland. <sup>11</sup>Department of Chemistry, Graduate School of Science, The University of Tokyo, Tokyo, Japan. <sup>12</sup>These authors contributed equally: Yong Qian, Kiryl D. Piatkevich, Benedict Mc Larney. \*e-mail: [robert.e.campbell@ualberta.ca](mailto:robert.e.campbell@ualberta.ca)

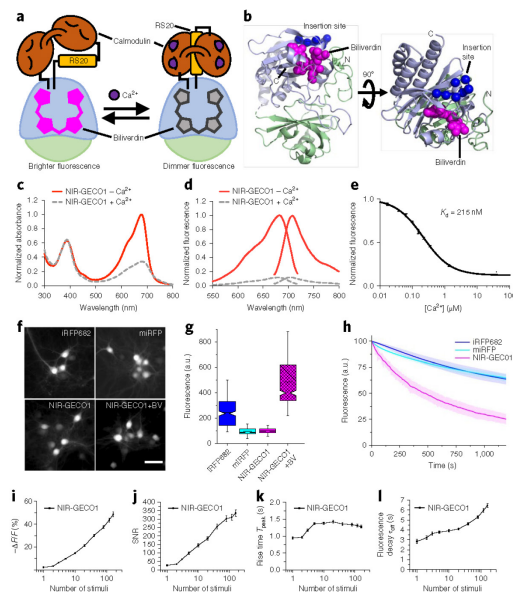


**Fig. 1 | Structure and characterization of NIR-GECO1.** **a**, Schematic representation of NIR-GECO1 and its mechanism of response to  $\text{Ca}^{2+}$ . The PAS domain is colored light green, and the biliverdin-binding GAF domain is colored light blue. RS20 is the CaM-binding peptide of smooth muscle myosin light chain kinase. **b**, Orthogonal views of the structure of DrBphP (PDB 2O9B), a close homolog of mRFP. The PAS and GAF domains are colored as in **a**, biliverdin is shown as magenta spheres, and the  $\text{Ca}^{2+}$  atoms of the seven residues that were replaced with CaM-RS20 are shown as blue spheres. **c**, Absorbance spectra in the presence ( $39\ \mu\text{M}$ ) and absence of  $\text{Ca}^{2+}$ . **d**, Fluorescence excitation and emission spectra in the presence ( $39\ \mu\text{M}$ ) and absence of  $\text{Ca}^{2+}$ . **e**, Fluorescence of NIR-GECO1 as a function of  $\text{Ca}^{2+}$  concentration. Center values are the mean, and error bars are s.d.  $n=3$  independent experiments. **f**, Representative wide-field fluorescence images ( $631/28\ \text{nm}$  excitation (Ex) at  $38\ \text{mW}\ \text{mm}^{-2}$  and  $664\ \text{LP}$  emission (Em)) of mouse neurons expressing iRFP682, miRFP, NIR-GECO1 and NIR-GECO1 supplemented with exogenous biliverdin ( $25\ \mu\text{M}$ ) ( $n=263, 326, 367$  and  $473$  neurons for iRFP682, miRFP, NIR-GECO1 and NIR-GECO1+ biliverdin, respectively, from two cultures). The dynamic ranges of these images have been normalized to facilitate visual comparison of protein localization. Fluorescence brightness quantification provided in **g**. Scale bar,  $50\ \mu\text{m}$ . **g**, Relative fluorescence intensity for neurons shown in **f** (BV, biliverdin). Box plots with notches are used. The narrow part of notch is the median; the top and bottom of the notch denote the 95% confidence interval of the median; the horizontal line is the mean; the top and bottom horizontal lines are the 25th and 75th percentiles for the data; and the whiskers extend  $1 \times 1.5$  the interquartile range from the 25th and 75th percentiles. **h**, Photobleaching curves for iRFP682, miRFP and NIR-GECO1 ( $n=84, 69$  and  $88$  neurons, respectively, from two cultures;  $631/28\ \text{nm}$  Ex at  $38\ \text{mW}\ \text{mm}^{-2}$ ; solid lines represent mean value, shaded areas represent s.d.). **i-l**, NIR-GECO1 response amplitude (**i**), signal-to-noise ratio (SNR) (**j**), rise time (actually a fluorescence decrease) for  $\text{Ca}^{2+}$  binding (**k**) and decay time (actually a fluorescence increase) for  $\text{Ca}^{2+}$  dissociation (**l**), as a function of the number of field stimulation-induced action potentials. Center values are the mean, and error bars are s.e.m.  $n=55$  neurons.

2.5-fold lower than that of iRFP682 (Fig. 1g). Administration of  $25\ \mu\text{M}$  exogenous biliverdin for 3 h resulted in an approximately fivefold increase in the NIR-GECO1 baseline fluorescence (Fig. 1g),

indicating that  $\sim 80\%$  of NIR-GECO1 was not bound to biliverdin. The addition of biliverdin also resulted in a slight increase in the mean value of the NIR-GECO1 fluorescence changes during spontaneous activity ( $16 \pm 6\%$  versus  $20 \pm 8\%$   $-\Delta F/F_0$  for NIR-GECO1 and NIR-GECO1 + biliverdin, respectively; mean  $\pm$  s.d. throughout; Supplementary Fig. 7a,b). This biliverdin-free fraction is not fluorescent but presumably participates in contra-productive  $\text{Ca}^{2+}$  buffering. Coexpression of heme-oxygenase 1 (HO1) with NIR-GECO1<sup>+</sup> resulted in only a 1.4-fold enhancement of fluorescence intensity (Supplementary Fig. 7c,d). Under continuous wide-field illumination at  $38\ \text{mW}\ \text{mm}^{-2}$  (about two to four times higher than typically used for NIR-GECO1 imaging), the photobleaching rate of NIR-GECO1 was approximately fourfold higher than those of miRFP and iRFP682 (Fig. 1h and Supplementary Table 1).

To characterize the fluorescence response of NIR-GECO1 to electric field stimulation-evoked action potentials, we delivered field stimuli ( $50\ \text{V}$ ,  $83\ \text{Hz}$ ,  $1\ \text{ms}$ ) in trains of 1, 2, 3, 5, 10, 20, 40, 80, 120 and 160 to transfected neurons (Supplementary Fig. 8a). The resulting fluorescence changes, recorded from cell bodies, revealed that  $-\Delta F/F_0$ , SNR, rise time and decay time all increased with the number of stimuli (Fig. 1i-l). Relative to GCaMP3, NIR-GECO1 has similar  $-\Delta F/F_{\text{min}}$  for 1–10 action potentials and an approximately twofold higher SNR, but these values are around tenfold lower than those for GCaMP6s (Supplementary Fig. 9a–d). The near-linear stimulus response over the range of approximately 2–40 stimuli is consistent with the near-unity Hill coefficient<sup>11</sup>. In cells, the rise and decay times of NIR-GECO1 appeared substantially slower than those of GCaMP6s. This observation is inconsistent with the fast  $\text{Ca}^{2+}$ -dissociation kinetics measured in vitro ( $\text{Ca}^{2+}$ -dissociation kinetic constant  $k_{\text{off}} = 1.93\ \text{s}^{-1}$  for NIR-GECO1 versus  $1.08\ \text{s}^{-1}$  for GCaMP6s; Supplementary Fig. 6b). With no targeting sequence attached, NIR-GECO1 distributes throughout the cytoplasm and nucleus. Measuring from the cell body, we found that nuclear-excluded NIR-GECO1 (NES-NIR-GECO1) exhibited similar kinetics as NIR-GECO1, ruling out slow  $\text{Ca}^{2+}$  diffusion in and out of the nucleus as an explanation for slower response kinetics (Supplementary Fig. 9c,d). When coexpressed in cultured neurons, NIR-GECO1 and GCaMP6s both reported spontaneous oscillations in  $\text{Ca}^{2+}$  concentration with opposite fluorescence changes (Supplementary Fig. 9e,f).

To evaluate in vivo expression of NIR-GECO1, we induced expression of the gene in layer 2/3 (L2/3) of mouse motor cortex via in utero electroporation (IUE). Imaging of brain slices revealed fluorescence through neuronal cell bodies and processes (Fig. 2a and Supplementary Fig. 8b) and no punctate structures. Stimulation of action potentials with whole-cell patch-clamp electrophysiology gave  $-\Delta F/F_0$  of  $7.2 \pm 2.8\%$ ,  $13.4 \pm 3.8\%$  and  $27.6 \pm 2.8\%$  for 5, 10 and 20 action potentials, respectively (Fig. 2b, Supplementary Fig. 8c). Stimulation of neuronal activity with 4-aminopyridine resulted in mean maximal  $-\Delta F/F_0$  of  $\sim 20\%$  and mean averaged  $-\Delta F/F_0$  of  $\sim 10\%$  (Fig. 2c,d). To determine whether NIR-GECO1 could be used for one-photon in vivo imaging, we injected adeno-associated virus (AAV) carrying the NIR-GECO1 gene (AAV2/9-hSyn1-NIR-GECO1) in the sensorimotor cortex of mice. Mesoscale fluorescence imaging through the intact skin (hair removed) and skull of anesthetized mice during two paradigms of paw stimuli revealed transient stimuli- and NIR-GECO1-dependent fluorescence changes (decreases) of approximately 0.3% (Fig. 2e–g, Supplementary Figs. 10 and 11 and Supplementary Videos 1 and 2). Under similar conditions, GCaMP6s exhibited approximately tenfold greater fluorescence changes (increases). We attribute the better performance of GCaMP6s to its inherently larger  $\text{Ca}^{2+}$ -dependent fluorescence response ( $\times 30$  versus  $\times 8$  under identical conditions; Supplementary Table 1), its higher Hill coefficient (2.4 versus 1.0) and lower  $K_d$  ( $144$  versus  $215\ \text{nm}$ ) that has been empirically optimized for neuronal activity imaging.

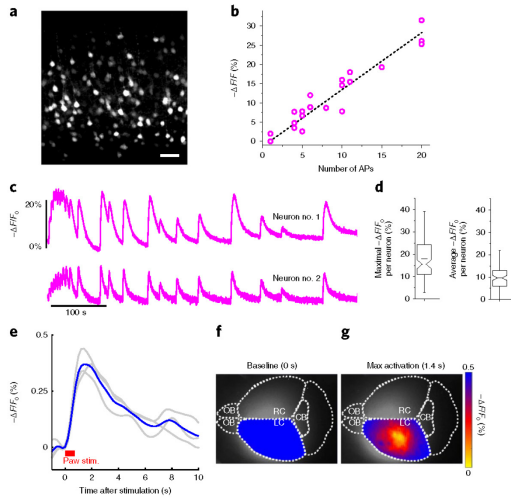


**Fig. 2 | Imaging of in vivo expressed NIR-GECO1.** **a**, Representative confocal image of live brain slice expressing NIR-GECO1 (641 nm Ex; 664LP Em;  $n = 4$  slices from two mice at P11–22). Scale bar, 50  $\mu\text{m}$ . **b**, NIR-GECO1 fluorescence responses to action potential (AP) trains evoked by current injections ( $n = 6$  neurons from four mice at P11–22; dashed line indicates linear regression). **c**, Single-trial wide-field imaging of 4-aminopyridine (1 mM final concentration) evoked neuronal activity from the cell bodies of two representative neurons (631/28 nm Ex and 664LP Em; acquisition rate 20 Hz;  $n = 129$  neurons from two slices from one mouse). **d**, Maximal (left) and average (right)  $-\Delta F/F_0$  for the experiment of **c**. Box plots are used as described in Fig. 1g. For experiments in **a–d**, NIR-GECO1 was expressed in vivo by IUE at E15.5. **e–g**, In vivo mesoscale imaging of foot-shock responses in mouse sensorimotor cortex. Three mice (4 weeks old) were injected with AVV2/9-hSyn1-NIR-GECO1 in either the right or the left side of the brain and imaged (671 nm Ex; 721/42 nm Em) 10–21 d later. **e**, Response to a paw stimulation paradigm of ten pulses in 700 ms (0.5 mA, 20 ms on and 50 ms off). Each gray line represents the averaged response of a mouse across 19 cycles, and the blue line represents the mean response from all three mice ( $n = 3$ ; that is, 57 cycles). **f**, Activation map of mouse brain, injected in left cortex, before stimulation. Diffuse fluorescence in the right cortex is attributed to diffusion of viral particles and light scattering. **g**, Activation map of mouse brain at max activation 1.4 s after stimulation. Scale bar, 2 mm. OB, olfactory bulb; CB, cerebellum; L/Rc, left or right cortex.

Owing to its spectrally distinct fluorescence, NIR-GECO1 should be particularly useful for in vitro imaging in combination with optogenetic actuators and fluorescent-protein-based indicators. To explore such applications, we attempted two-photon imaging of NIR-GECO1 and GCaMP6f. NIR-GECO1 two-photon brightness at both 1,250 nm and 880 nm excitation is sufficient to image neurons in culture and in mouse brain tissue ex vivo and in vivo (Fig. 3a,b and Supplementary Fig. 12). With 1,250-nm excitation we observed neuronal-activity-dependent changes in NIR-GECO1 fluorescence in cultured neurons, as confirmed by coexpression of GCaMP6f, with average  $-\Delta F/F_0$  of  $48 \pm 28\%$  ( $n = 37$  neurons from one culture; Fig. 3c). With two-photon excitation at 880 nm (11.4 mW of total light power), both the intracellular brightness and the photostability of NIR-GECO1 ( $t_{1/2} = 20$  s) were slightly higher than those of mRFP, but lower than those of iRFP682 (Supplementary

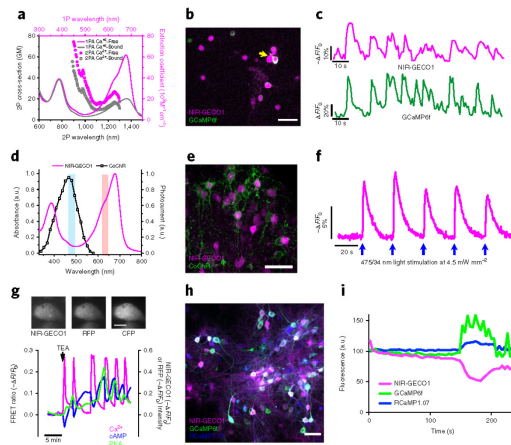


**Fig. 3 | Spectral multiplexing of NIR-GECO1 with optogenetic indicators and actuators.** **a**, One-photon (solid line; identical to Fig. 1c) and two-photon (open circles) absorption spectra of NIR-GECO1 in the presence and absence of  $\text{Ca}^{2+}$ . Two-photon absorption spectra are presented versus laser wavelength used for excitation. GM, Goepfert–Mayer units. **b**, Representative fluorescence image of cultured neurons expressing NIR-GECO1 (magenta) and GCaMP6f (green) acquired under two-photon excitation (imaging condition: NIR-GECO1 1,250 nm Ex, 705/90 nm Em; GCaMP6f 920 nm Ex, 518/45 nm Em;  $n = 2$  cultures). Scale bar, 50  $\mu\text{m}$ . **c**, Representative single-trial fluorescence recording of 4-aminopyridine (1 mM final concentration) evoked neuronal activity using NIR-GECO1 and GCaMP6f under imaging conditions as in **b** ( $n = 32$  neurons from two cultures; yellow arrow indicates the neuron the fluorescence traces were obtained from; image acquisition rate, 1 Hz). **d**, Action spectrum of channelrhodopsin from *Chloromonas oogama* (CoChR) (black line; adapted with permission from ref. 17) and NIR-GECO1 absorbance spectrum (magenta line; identical to Fig. 1c with no free  $\text{Ca}^{2+}$ ) with wavelengths used for CoChR activation (475/34 nm; cyan bar) and NIR-GECO1 excitation (638/14 nm; orange bar). **e**, Representative confocal images of neurons in L2/3 of motor cortex coexpressing NIR-GECO1 (magenta) and CoChR-mTagBFP2-Kv2.2<sup>motif</sup> (green) targeted by IUE at E15.5 (imaging conditions: NIR-GECO1 641 nm Ex, 664LP Em; CoChR-mTagBFP2-Kv2.2<sup>motif</sup> 405 nm Ex and 452/45 nm Em). Scale bar, 50  $\mu\text{m}$ . **f**, Single-trial wide-field imaging of NIR-GECO1 responses to CoChR activation (fluorescence excitation and activation as in **d**; 664LP Em; blue arrows, CoChR stimulation with 200 ms light pulses; image acquisition rate 5 Hz). Similar results were obtained with CheRiff<sup>10</sup> (Supplementary Fig. 13d,e). **g**, Top, representative fluorescence images of MIN6  $\beta$ -cell coexpressing AKAR4 (left, 420/20 nm Ex and 475/40 nm Em for CFP and 535/25 nm Em for YFP), NIR-GECO1 (middle, 640/30 nm Ex and 700/75 nm Em) and Pink Flamingo<sup>16</sup> (right, 555/25 nm Ex and 605/52 nm Em). Scale bar, 10  $\mu\text{m}$ . Bottom, simultaneous visualization of  $\text{Ca}^{2+}$  (NIR-GECO1;  $-\Delta F/F_0$ , magenta line), cyclic AMP (Pink Flamingo;  $\Delta F/F_0$ , blue line), and PKA (AKAR4; FRET emission ratio  $\Delta R/R_0$ , green line) in a MIN6 cell treated with 20 mM tetraethylammonium chloride (TEA) at  $t = 0$  (arrow). Traces for four additional representative cells are provided in Supplementary Fig. 14. **h**, Representative overlaid fluorescence image of dissociated neurons coexpressing NIR-GECO1, GCaMP6f and RCaMP1.07. **i**, Simultaneous detection of spontaneous neuronal activity reported by GCaMP6f, RCaMP1.07 and NIR-GECO1, in a single cell as in **h**. The percentage of responding cells (during a 3-min imaging session) was 92% for GCaMP6f ( $n = 271$  neurons), 79% for RCaMP1.07 ( $n = 178$  neurons) and 59% for NIR-GECO1 ( $n = 331$  neurons).

Fig. 12a,b). However, when we used 880-nm excitation, we did not observe characteristic fluorescence changes of NIR-GECO1 associated with neuronal  $\text{Ca}^{2+}$  dynamics in neurons either in culture or in live brain slices (Supplementary Fig. 12c). We have not succeeded in demonstrating *in vivo* imaging of neuronal activity using NIR-GECO1 with either 880-nm or 1,250-nm two-photon excitation.

To explore the combined use of NIR-GECO1 and an optogenetic actuator, we prepared live brain slices expressing NIR-GECO1 and the high-photocurrent channelrhodopsin CoChR<sup>12,13</sup> (Fig. 3d). Activation of CoChR with cyan-colored light produced  $\text{Ca}^{2+}$  transients that were reliably reported by NIR-GECO1 (Fig. 3e,f), and there was no evidence of photophysical artifacts attributable to the illumination conditions (Supplementary Fig. 13a–c)<sup>14</sup>.

To demonstrate NIR-GECO1's utility for use with fluorescent-protein-based indicators, we performed three-indicator (four-color) imaging using NIR-GECO1, the cyan- and yellow-fluorescent-protein-based protein kinase A indicator AKAR<sup>15</sup> and the red-fluorescent-protein-based cAMP indicator Pink Flamindo<sup>16</sup>. Pharmacological stimulation of  $\text{Ca}^{2+}$  oscillations in MIN6  $\beta$ -cells *in vitro* led to rapid and synchronous oscillations in  $\text{Ca}^{2+}$ , cAMP and PKA activity (Fig. 3g, Supplementary Fig. 14 and Supplementary Video 3). Coexpression of NIR-GECO1 with GCaMP6f<sup>17</sup> and RCaMP1.07<sup>18</sup> enabled three-color *in vitro* imaging of spontaneous neuronal activity (Fig. 3h,i and Supplementary Video 4).

We have demonstrated that NIR-GECO1 is a useful new addition to the GECI palette. As a first-generation indicator, NIR-GECO1 falls short of the most extensively optimized fluorescent-protein-based GECIs in several critical performance parameters. Accordingly, NIR-GECO1 is not generally useful for *in vivo* imaging of neuronal activity. However, NIR-GECO1 does provide a robust inverse response to  $\text{Ca}^{2+}$  concentration changes in cultured cells, primary neurons and acute slices roughly on par with GCaMP3. In addition, because of its highly red-shifted excitation maximum, it is the preferred  $\text{Ca}^{2+}$  indicator for pairing with blue-light-activated optogenetic actuators, to minimize actuator activation during imaging<sup>19</sup>. Finally, it creates a multitude of new opportunities for multiparameter imaging in conjunction with multiple fluorescent-protein-based intensimetric or ratiometric FRET-based indicators.

As with many BV-FPs, NIR-GECO1 is substantially dimmer than state-of-the-art fluorescent-protein-derived GECIs such as GCaMP6s (10.7 times brighter)<sup>17</sup> and jRGECO1a (three times brighter)<sup>19</sup>. To enable general utility for *in vivo* imaging, future iterations of NIR-GECO1 should be optimized for brighter fluorescence (for example, improved biliverdin-binding efficiency could provide up to an approximately fivefold increase), increased affinity for  $\text{Ca}^{2+}$ , increased photostability and faster kinetics. We expect NIR-GECO1 to be just as amenable to further improvements as the GCaMP series, and for these advancements to be soon realized through protein-engineering efforts.

#### Online content

Any methods, additional references, Nature Research reporting summaries, source data, statements of data availability and associated accession codes are available at <https://doi.org/10.1038/s41592-018-0294-6>.

Received: 10 May 2018; Accepted: 4 December 2018;  
Published online: 21 January 2019

#### References

1. Tsien, R. Y. *Annu. Rev. Biochem.* **67**, 509–544 (1998).
2. Shu, X. et al. *Science* **324**, 804–807 (2009).
3. Rodriguez, E. A. et al. *Nat. Methods* **13**, 763–769 (2016).
4. Piatkevich, K. D. et al. *Biophys. J.* **113**, 2299–2309 (2017).
5. Shcherbakova, D. M., Stepanenko, O. V., Turoverov, K. K. & Verkhusha, V. V. *Trends Biotechnol.* **36**, 1230–1243 (2018).
6. Yu, D. et al. *Nat. Methods* **12**, 763–765 (2015).
7. Wagner, J. R., Zhang, J., Brunzelle, J. S., Vierstra, R. D. & Forest, K. T. *J. Biol. Chem.* **282**, 12298–12309 (2007).
8. Tian, L. et al. *Nat. Methods* **6**, 875–881 (2009).
9. Shcherbakova, D. M. & Verkhusha, V. V. *Nat. Methods* **10**, 751–754 (2013).
10. Piatkevich, K. D. et al. *Nat. Chem. Biol.* **14**, 352–360 (2018).
11. Inoue, M. et al. *Nat. Methods* **12**, 64–70 (2015).
12. Shemesh, O. A. et al. *Nat. Neurosci.* **20**, 1796–1806 (2017).
13. Klapoetke, N. C. et al. *Nat. Methods* **11**, 338–346 (2014).
14. Wu, J. et al. *ACS Chem. Neurosci.* **4**, 963–972 (2013).
15. Depry, C., Allen, M. D. & Zhang, J. *Mol. Biosyst.* **7**, 52–58 (2011).
16. Harada, K. et al. *Sci. Rep.* **7**, 7351 (2017).
17. Chen, T.-W. W. et al. *Nature* **499**, 295–300 (2013).
18. Ohkura, M., Sasaki, T., Kobayashi, C., Ikegaya, Y. & Nakai, J. *PLoS ONE* **7**, e39933 (2012).
19. Dana, H. et al. *eLife* **5**, e12727 (2016).
20. Hochbaum, D. R. et al. *Nat. Methods* **11**, 825–833 (2014).

#### Acknowledgements

The authors thank the University of Alberta Molecular Biology Services Unit; Y. Li, H. Zhou and A. Aggarwal, for technical support; A. Holt for providing access to the stopped-flow spectrophotometer; and M. Vanni, T. Murphy, A. Nimmerjahn and S. Chen for preliminary AAV testing. We thank M.-E. Paquet at the University of Laval Molecular Tools Platform and the Janelia Research Campus (JRC) Virus core for AAV production. We thank V. Rancic and the JRC Histology group for preparing cultured neurons. We thank D. Park and H.J. Suk for help with characterization of NIR-GECO1 in brain-slice and two-photon imaging. We thank M. Reiss for assistance with the mouse handling. X.L. Deán-Ben for help with the *in vivo* mesoscale data analysis, M. Davidson and X. Shu for the mIFP gene, and E. Rodriguez for the smURFP gene. Work in R.E.C.'s lab was supported by grants from NSERC (RGPIN 288338-2010), CIHR (MOP 123514 and FS 154310), Brain Canada and NIH (U01 NS090565). D.R. acknowledges support from the European Research Council (ERC-2015-CoG-682379). The work of D.R. and S.S. was also supported by the NIH (R21-EY026382 and U01-NS107680). Work in J.Z.'s lab was supported by NIH (R01-DK073368 and R35-CA197622). E.S.B. was supported by J. Doerr, the HHMI-Simons Faculty Scholars Program, the Open Philanthropy Project, Human Frontier Science Program (RGP0015/2016), US Army Research Laboratory and the US Army Research Office (W911NF1510548), US-Israel Binational Science Foundation (2014509) and NIH (2R01-DA029639 and 1R01-GM104948).

#### Author contributions

Y.Q. developed NIR-GECO1 and performed *in vitro* characterization. Y.Q., K.D.P., A.S.A. and M.H.M. performed characterization in hippocampal neurons. K.D.P. and M.H.M. characterized NIR-GECO1 in intact brain slices. B.M.L. and S.G. performed *in vivo* mesoscale imaging. S.M. performed live-cell imaging in MIN6  $\beta$ -cells. R.S.M. and M.D. measured two-photon spectra. W.Z. built the pcDuEx2 vector. Y.C. and J.W. worked on development of the smURFP-based GECI. M.D., T.E.H., J.Z., E.R.S., S.S., D.R., E.S.B. and R.E.C. supervised research. All authors were involved in data analysis. Y.Q., K.D.P. and R.E.C. wrote the manuscript.

#### Competing interests

The University of Alberta has non-exclusively licensed NIR-GECO1 to LumiSTAR Biotechnology.

#### Additional information

Supplementary information is available for this paper at <https://doi.org/10.1038/s41592-018-0294-6>.

Reprints and permissions information is available at [www.nature.com/reprints](http://www.nature.com/reprints).

Correspondence and requests for materials should be addressed to R.E.C.

**Publisher's note:** Springer Nature remains neutral with regard to jurisdictional claims in published maps and institutional affiliations.

© The Author(s), under exclusive licence to Springer Nature America, Inc. 2019

## Methods

**General methods and materials.** Synthetic DNA oligonucleotides were purchased from Integrated DNA Technologies. Q5 high-fidelity DNA polymerase (New England Biolabs) was used for routine PCR amplifications, and Taq DNA polymerase (New England Biolabs) was used for error-prone PCR. The QuikChange mutagenesis kit (Agilent Technologies) was used for site-directed mutagenesis. Restriction endonucleases, rapid DNA ligation kits and GeneJET miniprep kits were from Thermo Fisher Scientific. PCR products and products of restriction digests were purified using agarose gel electrophoresis and the GeneJET gel extraction kit (Thermo Fisher Scientific). All DNA sequences were confirmed using the BigDye Terminator v.3.1 cycle sequencing kit (Applied Biosystems). Reactions were analyzed at the University of Alberta Molecular Biology Service Unit. Absorbance measurements were made with a DU-800 UV-visible spectrophotometer (Beckman), and fluorescence spectra were recorded on a Safire2 plate reader (Tecan).

**Engineering of NIR-GECO1.** The gene encoding mIFP (a gift from Michael Davidson and Xiaokun Shu; Addgene plasmid no. 54,620)<sup>37</sup> was inserted between BamHI and EcoRI of a pBAD vector (Life Technologies) that expressed cyanobacteria *Synechocystis* HO-1 to convert an endogenous heme in bacteria into biliverdin, as previously described<sup>31</sup>.

The DNA sequence encoding CaM and RS20 (a peptide that corresponds to the CaM-binding peptide of smooth muscle myosin light chain kinase; VDSRRKWNKAGHAVRAIGRSS) portions of REX-GECO1 (ref.<sup>32</sup>), with mutations Q306D and M339F borrowed from jRGECO1a<sup>33</sup>, were genetically fused by overlap extension PCR using a DNA sequence that encodes for the flexible peptide linker GGGGS<sup>33</sup>.

For each site (X) of mIFP targeted for CaM-RS20 insertion, the full-length gene (encoding mIFP<sub>1-10X</sub>-CaM-RS20-mIFP<sub>X+1-10320</sub>) was assembled by overlap extension PCR and then inserted into the pBAD vector. Variants were expressed in *E. coli* strain DH10B (Thermo Fisher Scientific) in LB media supplemented with 100 µg ml<sup>-1</sup> ampicillin and 0.0016% L-arabinose. Proteins were extracted using B-PER bacterial protein extraction reagent (Thermo Fisher Scientific) and tested for fluorescence brightness and Ca<sup>2+</sup>-dependent response.

The most promising variant was subjected to an iterative process of library generation and screening in *E. coli*. The pBAD vector was used in the first three rounds. From the fourth round, pCDuEx2 was used to enable expression in both *E. coli* and mammalian cells. Libraries were generated by error-prone PCR of the whole gene<sup>34</sup> or site-directed mutagenesis using Quikchange (Agilent Technologies) and degenerate codons at the targeted positions.

For libraries generated by random mutagenesis, approximately 10,000 colonies were screened in a given round. For libraries generated by randomization of one or more codons, a number of colonies that was approximately threefold the theoretical number of gene variants were screened. For each round, the top 2% of colonies with high fluorescence intensity were picked, cultured and tested on 396-well plates. Approximately 25% of those picked variants were further screened in HeLa cells on the basis of fluorescence. In a given round, screening was stopped when a substantially improved variant was identified. There were 12 rounds of screening before NIR-GECO1 was identified.

**NIR-GECO1 expression vectors.** pCDuEx2 was constructed based on the pCDNA3.1 backbone. The Tac promoter and a gene sequence containing Kpn2I and XbaI sites was inserted immediately after the CMV promoter by overlap extension PCR. A DNA fragment containing the T7 promoter, the gene encoding NIR-GECO1 and the gene encoding HO-1 was amplified from the pBAD vector and inserted into the Kpn2I and XbaI sites.

For HeLa cell expression, the pCDuEx2 vector was used. For expression in dissociated neurons, either an AAV2 vector or a lentivirus containing NIR-GECO1 was used. For AAV2 vector preparation, NIR-GECO1 was cloned from pCDuEx2 into BamHI and HindIII sites of an AAV2 vector (a gift from Roger Tsien; Addgene plasmid no. 50970)<sup>35</sup>. To create lentivirus expressing NIR-GECO1, the gene for NIR-GECO1 or NIR-GECO1-T2A-HO1 was cloned into the BamHI and EcoRI sites of FCK lentivirus vector (Addgene plasmid no. 2217). HEK293FT cells at 80% confluency in 35-mm cell-culture dishes (Corning) were transfected with 1.5 µg of FCK-CMV-NIR-GECO1 or FCK-CMV-NIR-GECO1-T2A-HO1, 1.0 µg of psPAX2 (a gift from D. Trono; Addgene plasmid no. 12,260), 0.5 µg of pMD2.G (a gift from D. Trono; Addgene plasmid no. 12,259) and 0.2 µg of pAdvantage (Promega), with 9 µl of Turbofect transfection reagent in 2 ml of Opti-MEM medium (Thermo Fisher Scientific). Opti-MEM medium containing Turbofect and DNA mix were replaced with 2 ml of complete cell-culture medium containing 110 mg ml<sup>-1</sup> sodium pyruvate at 24 h post-transfection. At 48 h post-transfection, the virus-containing supernatant was collected, spun at 400g (relative centrifugal force) for 5 min and filtered through a 0.45-µm PVDF syringe filter unit (EMD Millipore) to get rid of pellet cellular debris. Dissociated neurons in 24-well plates were transduced with 2 ml of virus-containing supernatant.

**Protein purification and in vitro characterization.** The gene encoding NIR-GECO1, with a poly-histidine tag on the C terminus, was expressed from the pBAD vector. Bacteria were lysed with a cell disruptor (Constant Systems Ltd)

and then centrifuged at 15,000g for 30 min, and proteins were purified by Ni-NTA affinity chromatography (Agarose Bead Technologies). The buffer was typically exchanged to 10 mM MOPS, 100 mM KCl (pH 7.2) with centrifugal concentrators (GE Healthcare Life Sciences). We determined extinction coefficients by comparing the absorbance value at 678 nm to the absorbance value at the 391 nm and assuming an extinction coefficient of 39,900 M<sup>-1</sup> cm<sup>-1</sup> at 391 nm<sup>36</sup>. For determination of quantum yields ( $\Phi$ ), purified mIFP ( $\Phi = 0.08$ ) was used as a standard. The concentration of NIR-GECO1 (Ca<sup>2+</sup>-free), NIR-GECO1 (Ca<sup>2+</sup>-saturated) and mIFP was adjusted to have absorbance of 0.2–0.6 at 650 nm. A series of dilutions, with absorbance ranging from 0.01 to 0.05, were prepared, and integrated emission intensity versus absorbance was plotted. Quantum yields were determined from the slopes ( $S$ ) of each line using the equation  $\Phi_{\text{protein}} = \Phi_{\text{standard}} \times (S_{\text{protein}}/S_{\text{standard}})$ . We carried out pH titrations by diluting protein into buffers (pH from 2 to 11) containing 30 mM trisodium citrate, 30 mM sodium borate and either 10 mM CaCl<sub>2</sub> or 10 mM EGTA. Fluorescence intensities as a function of pH were then fitted by a sigmoidal binding function to determine the apparent pK<sub>a</sub>. Ca<sup>2+</sup> titrations were carried out using EGTA-buffered Ca<sup>2+</sup> solutions (Calcium Calibration Buffer Kit no. 1, Life Technologies). We prepared buffers by mixing a CaEGTA buffer (30 mM MOPS, 100 mM KCl, 10 mM EGTA, 10 mM CaCl<sub>2</sub>) and an EGTA buffer (30 mM MOPS, 100 mM KCl, 10 mM EGTA) to give free Ca<sup>2+</sup> concentrations ranging from 0 nM to 39 µM at 25 °C. Fluorescence intensities were plotted against Ca<sup>2+</sup> concentrations and fitted by a sigmoidal binding function to determine the Hill coefficient and K<sub>d</sub>. To determine k<sub>off</sub>, we used an SX20 stopped-flow spectrometer (Applied Photophysics). Briefly, protein samples with 10 µM CaCl<sub>2</sub> (30 mM MOPS, 100 mM KCl, pH 7.2) were rapidly mixed with 10 mM EGTA (30 mM MOPS, 100 mM KCl, pH 7.2) at room temperature, and an absorption growth curve was measured and fitted by a single exponential equation.

Two-photon spectra and cross-sections were measured using femtosecond excitation as described in Supplementary Note 2.

**Animal care.** For experiments performed at Massachusetts Institute of Technology (MIT), all methods for animal care and use were approved by the MIT Committee on Animal Care and were in accordance with the National Institutes of Health Guide for the Care and Use of Laboratory Animals. Four time pregnant Swiss Webster mice (Taconic) were used for this study, as were five C57BL/6 mice (Taconic), ages 4–12 weeks. Mice were used without regard to gender.

For experiments performed at Technical University of Munich, all animal in vivo experimentation was done in full compliance with the institutional guidelines of the Institute for Biological and Medical Imaging and with approval from the Government District of Upper Bavaria. A total of 12 mice were used for these experiments: 3 female FOxN1 nude mice that were injected with the NIR-GECO1 virus, 3 female FOxN1 nude mice that were injected with the mIFP virus, 3 female Black6 (C57BL/6) transgenic mice expressing GCaMP6s, and 3 mice (2 female FOxN1 and 1 female Black6) that were injected with PBS as negative controls.

All experiments at University of Alberta for obtaining the cortical neurons were approved by the University of Alberta Animal Care and Use Committee and carried out in compliance with guidelines of the Canadian Council for Animal Care and the Society for Neuroscience's Policies on the Use of Animals and Humans in Neuroscience Research.

For experiments at HHMI Janelia Research Campus, all surgical and experimental procedures were in accordance with protocols approved by the HHMI Janelia Research Campus Institutional Animal Care and Use Committee and Institutional Biosafety Committee.

**Imaging of NIR-GECO1 in HeLa cells and dissociated neuron cultures.** HeLa cells (40–60% confluent) in 24-well glass-bottom plates (Cellvis) were transfected with 0.5 µg of the NIR-GECO1-pCDuEx2 plasmid and 2 µl of TurboFect (Thermo Fisher Scientific) in Dulbecco's modified Eagle's medium (DMEM; Gibco Fisher Scientific). Following 2 h of incubation, the media was changed to DMEM supplemented with 10% fetal bovine serum (FBS; Sigma-Aldrich), 2 mM GlutaMax (Thermo Fisher Scientific) and 1% penicillin–streptomycin (Gibco). The cells were then incubated for 48 h at 37 °C in a CO<sub>2</sub> incubator. Before imaging, culture medium was changed to Hanks' Balanced Salt Solution (HBSS).

For dissociated hippocampal mouse neuron culture preparation, postnatal day 0 or 1 Swiss Webster mice (Taconic Biosciences) were used as previously described<sup>38</sup>. Briefly, dissected hippocampal tissue was digested with 50 units of papain (Worthington Biochem) for 6–8 min at 37 °C, and the digestion was stopped by incubation with ovomucoid trypsin inhibitor (Worthington Biochem) for 4 min at 37 °C. Tissue was gently dissociated with Pasteur pipettes, and dissociated neurons were plated at a density of 20,000–30,000 per glass coverslip coated with Matrigel (BD Biosciences). Neurons were seeded in 100 µl of plating medium containing MEM (Life Technologies), glucose (33 mM; Sigma), transferrin (0.01%; Sigma), HEPES (10 mM; Sigma), GlutaGro (2 mM; Corning), insulin (0.13%; Millipore), B27 supplement (2%; Gibco) and heat-inactivated FBS (7.5%; Corning). After cell adhesion, additional plating medium was added. AraC (0.002 mM; Sigma) was added when glia density was 50–70% of confluence. Neurons were grown at 37 °C and 5% CO<sub>2</sub> in a humidified atmosphere. We

transduced cultured neurons at 4–5 days in vitro (DIV) by administering  $\sim 10^{10}$  viral particles of rAAV8-hSyn-iRFP682, rAAV8-hSyn-miRFP (both from Vector Core, University of North Carolina) or rAAV9-hSyn-NIR-GECO1 (Department of Biochemistry and Microbiology, University of Laval) per well (the rAAV genome titer was determined by dot blot). For coexpression of the GECIs, the rAAV8-hSyn-GCaMP6f, rAAV8-hSyn-RCaMP1.07 (both from Vector Core, University of North Carolina) and rAAV9-hSyn-NIR-GECO1 viral particles were added in a 1/1/3 ratio, respectively. A biliverdin hydrochloride (Sigma-Aldrich) solution in dimethylsulfoxide (25 mM) was used as a  $1,000\times$  stock ( $25\mu\text{M}$  final concentration) for the experiments shown in Fig. 1g and Supplementary Fig. 7a,b. All measurements on neurons were taken after DIV 16.

For dissociated rat cortical neuron culture preparation, postnatal day 0 or 1 Sprague Dawley rats were used. Dissected cortices were digested in Papain solution (50 units; Sigma) for 10 min at  $37^\circ\text{C}$  and then incubated with DNase ( $0.15\text{ mg ml}^{-1}$ ; Sigma) for 5 min at  $37^\circ\text{C}$ . After washing the tissue with FBS (Sigma) and removing supernatant, we added neurobasal B27 (Thermo Fisher Scientific) to tissue. Tissue was then gently dissociated with Pasteur pipettes, and dissociated neurons were plated at a density of  $\sim 1.5\times 10^5$  on collagen-coated 24-well glass-bottom dishes containing NbActi4 culture medium (BrainBits LLC) supplemented with 2% FBS, penicillin-G potassium salt (50 units per ml), and streptomycin sulfate ( $50\text{ mg ml}^{-1}$ ). Half of the culture media was replaced every 4–5 d. Neuronal cells were infected using the NIR-GECO1 lentivirus on day 8. Before imaging, the culture medium was changed to HBSS.

Wide-field fluorescence imaging of cultured neurons was performed using an epifluorescence inverted microscope (Eclipse Ti-E, Nikon) equipped with a Photometrics QuantEM 512SC camera and a 75-W Xenon lamp or a Zyla5.5 sCMOS (scientific complementary metal-oxide semiconductor) camera (Andor) and a SPECTRA X light engine (Lumencor). NIS-Elements Advanced Research (Nikon) was used for automated microscope and camera control. Cells were imaged with  $60\times/1.49\text{-NA}$  (numerical aperture) oil or  $20\times/0.75\text{-NA}$  air objective lenses (Nikon) at room temperature. For dual-color imaging with GCaMP6s, NIR ( $650/60\text{ nm Ex}$  and  $720/50\text{ nm Em}$ ) and green ( $490/15\text{ nm Ex}$  and  $525/50\text{ nm Em}$ ) filter sets were rotated into the emission light path. Three-color Ca imaging with GCaMP6f and RCaMP1.07 was performed using an inverted Nikon Eclipse Ti microscope equipped with a spinning disk sCSUW1 confocal scanner unit (Yokogawa), 488-, 561- and 642-nm solid state lasers, 525/25-nm, 579/34-nm and 664LP emission filters, a  $20\times/0.75\text{-NA}$  air objective lens (Nikon) and a 4.2 PLUS Zyla camera (Andor), controlled by NIS-Elements AR software. One cautionary note for confocal imaging is that gallium-arsenide-phosphide photomultiplier tube detectors have poor sensitivity at wavelengths greater than 700 nm.

Two-photon imaging (as shown in Fig. 3b,c and Supplementary Fig. 12c) was performed using an Olympus FVMPE-RS equipped with two lasers for fluorescence excitation. An InSight X3 laser (Spectra-Physics) tuned to  $1,250\text{ nm}$  at 8.0% transmissivity was used to excite NIR-GECO1, and a Mai-Tai HP Ti:Sapphire laser (Spectra-Physics) tuned to  $920\text{ nm}$  at 17.4% transmissivity was used to excite GCaMP6f. The laser beams were focused by a  $25\times/1.05\text{-NA}$  water-immersion objective lens (Olympus). NIR-GECO1 emission was separated using a  $660\text{--}750\text{-nm}$  filter, GCaMP6f emission was separated using a  $495\text{--}540\text{-nm}$  filter, and signals were collected onto separate photomultiplier tubes. Imaging was performed at a sampling speed of  $2.0\mu\text{s}$  per pixel with one-way galvanic scanning. Raw scanner data were converted to an image z-stack using ImageJ (NIH).

Two-photon imaging for Supplementary Fig. 12a,b,d–f was performed using a two-photon laser scanning microscope (Ultima IV, Prairie Technologies) with a mode-locked Ti:Sapphire laser (Mai-Tai, Spectra-Physics) and a  $16\times/0.8\text{-NA}$  water-immersion objective (CFI75 LWD 16; Nikon). For image acquisition, the laser was set to emit  $880\text{ nm}$  at a total light power of  $11.4\text{ mW}$ , and  $535/50\text{-nm}$  and  $731/137\text{-nm}$  emission filters (Semrock) were used. The microscope was operated using the ScanImage 3.8 software package<sup>66</sup>.

**Electrophysiology and  $\text{Ca}^{2+}$  imaging in dissociated hippocampal neurons.** The genes encoding NIR-GECO1 and GCaMP6s were expressed under the control of a synapsin promoter in cultured rat hippocampal neurons. Neurons were stimulated using a custom-built field stimulator using a stimulus isolator (A385, World Precision Instruments) with platinum wires. Field stimuli ( $50\text{ V}$ ,  $83\text{ Hz}$ ,  $1\text{ ms}$ ) were delivered in trains of 1, 2, 3, 5, 10, 20, 40, 80, 120 and 160 to the cultured neurons. Neurons were imaged using a Nikon Eclipse Ti2 inverted microscope equipped with a  $40\times/1.4\text{-NA}$  objective (Nikon). A quad bandpass filter (set number, 89,000; Chroma) was used along with a  $480\text{-nm}$  light-emitting diode (LED) (Spectra X light engine, Lumencor) or a  $640\text{-nm}$  LED (Spectra X light engine, Lumencor) to image GCaMP6s or NIR-GECO1, respectively. Fluorescence was collected using an sCMOS camera (Orca-Flash4.0, Hamamatsu) at  $34\text{ Hz}$ . For GCaMP6s, the response amplitude ( $\Delta F/F_{\text{min}}$ ) was quantified as the change in fluorescence divided by baseline fluorescence over the  $0.5\text{-s}$  period preceding the stimulus. For NIR-GECO1, the response amplitude was quantified as the change in fluorescence divided by peak fluorescence during the stimulus ( $-\Delta F/F_{\text{min}}$ ). SNR was quantified as the peak change in fluorescence over the s.d. of the signal over the  $0.5\text{-s}$  period preceding stimulation.

**Multiplexed live-cell imaging with NIR-GECO1 in MIN6  $\beta$ -cells.** MIN6 pancreatic  $\beta$ -cells were cultured in DMEM containing  $4.5\text{ g l}^{-1}$  glucose, supplemented with

$10\%$  (v/v) FBS,  $1\%$  (v/v) Pen-Strep and  $50\mu\text{M}$   $\beta$ -mercaptoethanol, and maintained at  $37^\circ\text{C}$  with a  $5\%$   $\text{CO}_2$  atmosphere. Cells were plated onto  $35\text{-mm}$  glass-bottom dishes, grown to  $40\text{--}60\%$  confluence and then transfected with  $0.5\mu\text{g}$  each of plasmids encoding AKAR4<sup>65</sup>, Pink Flamingo<sup>66</sup> and NIR-GECO1 using Lipofectamine 2000 (Invitrogen). After 48 h, cells were washed twice with HBSS (Gibco) and imaged in HBSS at  $37^\circ\text{C}$  using a Zeiss AxioObserver Z1 inverted epifluorescence microscope (Carl Zeiss) equipped with a  $40\times/1.3\text{-NA}$  objective, a Lambda 10–2 filter-changer (Sutter Instruments) and a Photometrics Evolve 512 EMCCD (electron-multiplying charge-coupled device) (Photometrics) controlled by METAFLUOR v7.7 software (Molecular Devices). Filters for cyan/yellow emission ratio were a 420DF20 excitation filter, a 450DRLP dichroic mirror and two emission filters (475DF40 for CFP and 535DF25 for YFP). Filters for RFP were a 555DF25 excitation filter, a ZT568RDC dichroic mirror and a 605DF52 emission filter. Filters for NIR-GECO1 were a 640DF30 excitation filter, a 700DF75 excitation filter and a T660LPXR dichroic mirror. Exposure times ranged between 50 and 500 ms, with EM gain set from 10–50, and images were acquired every 20 s. Fluorescence intensities were corrected by background subtraction. The emission ratio change ( $R - R_0$ ) or fluorescence intensity change ( $F - F_0$ ) was divided by the initial ratio or intensity to obtain  $\Delta R/R_0$  or  $\Delta F/F_0$ , with time zero defined as the time point immediately preceding drug addition. Graphs were plotted using GraphPad Prism 7 (GraphPad Software).

**In utero electroporation.** Embryonic day (E) 15.5 timed-pregnant female Swiss Webster (Taconic) mice were deeply anesthetized with  $2\%$  isoflurane. Uterine horns were exposed and periodically rinsed with warm sterile PBS. A plasmid encoding NIR-GECO1 or a mixture of plasmids encoding NIR-GECO1 and CoChR (pCAG-NIR-GECO1-WPRE, pCAG-CoChR-mTagBFP2-Kv2.2motif-WPRE; at a total DNA concentration of  $\sim 1\text{--}2\mu\text{g}\mu\text{l}^{-1}$ ) diluted with PBS were injected into the lateral ventricle of one cerebral hemisphere of an embryo. Five voltage pulses ( $50\text{ V}$ ,  $50\text{-ms}$  duration,  $1\text{ Hz}$ ) were delivered using round plate electrodes (ECM 830 electroporator, Harvard Apparatus). Injected embryos were placed back into the dam, and allowed to mature to delivery. The P0 pups were screened for corresponding fluorescence and negative pups were excluded for further experiments. All experimental manipulations were performed in accordance with protocols approved by the Massachusetts Institute of Technology Committee on Animal Care, following guidelines described in the US National Institutes of Health Guide for the Care and Use of Laboratory Animals.

**Acute brain slice preparation.** Acute brain slices were obtained from Swiss Webster (Taconic) mice at P11 to P22, using standard techniques. Mice were used without regard for sex. No statistical methods were used to estimate sample size for animal studies throughout. No randomization or blinding were used for animal studies throughout. Mice were anaesthetized by isoflurane inhalation, decapitated and cerebral hemispheres were quickly removed and placed in cold choline-based cutting solution consisting of (in mM): 110 choline chloride, 25  $\text{NaHCO}_3$ , 2.5 KCl, 7  $\text{MgCl}_2$ , 0.5  $\text{CaCl}_2$ , 1.25  $\text{NaH}_2\text{PO}_4$ , 25 glucose, 11.6 ascorbic acid and 3.1 pyruvic acid ( $339\text{--}341\text{ mOsm per kg}$ ; pH 7.75 adjusted with NaOH) for 2 min, blocked and transferred into a slicing chamber containing ice-cold choline-based cutting solution. Coronal slices ( $300\mu\text{m}$  thick) were cut with a Compresstome VF-300 slicing machine, transferred to a holding chamber with artificial cerebrospinal fluid (ACSF) containing (in mM) 125 NaCl, 2.5 KCl, 25  $\text{NaHCO}_3$ , 2  $\text{CaCl}_2$ , 1  $\text{MgCl}_2$ , 1.25  $\text{NaH}_2\text{PO}_4$  and 11 glucose ( $300\text{--}310\text{ mOsm per kg}$ ; pH 7.35 adjusted with NaOH) and recovered for 10 min at  $34^\circ\text{C}$  followed by another 30 min at room temperature. Slices were subsequently maintained at room temperature until use. Both cutting solution and ACSF were constantly bubbled with  $95\%$   $\text{O}_2$  and  $5\%$   $\text{CO}_2$ .

**Concurrent electrophysiology and  $\text{Ca}^{2+}$  imaging in acute brain slice.** Slices were transferred to a recording chamber on an Olympus BX51WI upright microscope and superfused ( $2\text{--}3\text{ ml min}^{-1}$ ) with ACSF at room temperature. Whole-cell patch-clamp recordings were acquired via an Axopatch 700B amplifier (Molecular Devices) and Digidata 1440 digitizer (Molecular Devices). For recordings, borosilicate glass pipettes (Warner Instruments) with an outer diameter of  $1.2\text{ mm}$  and a wall thickness of  $0.255\text{ mm}$  were pulled to a resistance of  $3\text{--}5\text{ M}\Omega$  with a P-97 Flaming/Brown micropipette puller (Sutter Instruments) and filled with a solution containing 155 mM K-gluconate, 8 mM NaCl,  $0.1\text{ mM}$   $\text{CaCl}_2$ ,  $0.6\text{ mM}$   $\text{MgCl}_2$ ,  $10\text{ mM}$  HEPES,  $4\text{ mM}$  Mg-ATP and  $0.4\text{ mM}$  Na-GTP. The pipette solution pH was adjusted to 7.3 with KOH and the osmolarity was adjusted to  $298\text{ mOsm}$  with sucrose. Cells were visualized through a  $40\times/0.8\text{-NA}$  water-immersion objective with epifluorescence. Whole-cell current-clamp recordings were obtained from NIR-GECO1-positive neurons in layer 2/3 of motor cortex. Fluorescence was excited by a SPECTRA X light engine (Lumencor) with  $638/14\text{-nm}$  excitation filter (Semrock), fluorescence was collected through the same objective, passed through a 664LP emission filter and imaged onto an Orca-Flash4.0 v2 sCMOS camera (Hamamatsu) at  $50\text{-Hz}$  acquisition frequency.

**In vivo imaging of NIR-GECO1.** Methods for in vivo two-photon imaging to acquire the image shown in Supplementary Fig. 12f are provided as Supplementary Note 3. Methods for in vivo mesoscale imaging to acquire data

and images shown in Fig. 2e–g and Supplementary Figs. 10 and 11 are provided as Supplementary Note 4.

**Statistics and reproducibility.** All data are expressed as mean  $\pm$  s.d. or mean  $\pm$  s.e.m., as specified in figure legends. Box plots with notches<sup>27</sup> are used for Figs. 1g and 2d and Supplementary Figs. 7b, 12a and 13c. In these plots, the narrow part of the notch is the median; the top and bottom of the notch denote the 95% confidence interval of the median; the horizontal line is the mean; the top and bottom horizontal lines are the 25th and 75th percentiles for the data; and the whiskers extend 1.5 times the interquartile range from the 25th and 75th percentiles. Sample sizes ( $n$ ) are listed with each experiment. No samples were excluded from analysis and all experiments were reproducible. For experiments for which representative data are shown, the number of times each experiment was repeated independently with similar results is summarized in Supplementary Note 5. No randomization or blinding was used. All attempts at replication of the experiments were successful.

**Reporting Summary.** Further information on research design is available in the Nature Research Reporting Summary linked to this article.

#### Data availability

The NIR-GECO1 gene sequence is available through GenBank (submission no. MK134690), pDuEx2-NIR-GECO1 (plasmid no. 113,680) and pAAV-hSyn-NES-NIR-GECO1 (plasmid no. 113,683) are available via Addgene according to the terms of the Uniform Biological Material Transfer Agreement. Source data for Figs. 1–3 and Supplementary Figs. 5–14 are available online.

#### References

- Gambetta, G. A. & Lagarias, J. C. *Proc. Natl Acad. Sci. USA* **98**, 10566–10571 (2001).
- Wu, J. et al. *Nat. Commun.* **5**, 5262 (2014).
- Heckman, K. L. & Pease, L. R. *Nat. Protoc.* **2**, 924–932 (2007).
- Cirino, P. C., Mayer, K. M. & Umeno, D. in *Directed Evolution Library Creation: Methods and Protocols* (eds Arnold, F. H. & Georgiou, G.) 3–9 (Humana, Totowa, NJ, 2003).
- Lin, J. Y. et al. *Neuron* **79**, 241–253 (2013).
- Pologruto, T. A., Sabatini, B. L. & Svoboda, K. *Biomed. Eng. Online* **2**, 13 (2003).
- Krzywinski, M. & Altman, N. *Nat. Methods* **11**, 119–120 (2014).

## Reporting Summary

Nature Research wishes to improve the reproducibility of the work that we publish. This form provides structure for consistency and transparency in reporting. For further information on Nature Research policies, see [Authors & Referees](#) and the [Editorial Policy Checklist](#).

### Statistical parameters

When statistical analyses are reported, confirm that the following items are present in the relevant location (e.g. figure legend, table legend, main text, or Methods section).

n/a | Confirmed

- The **exact sample size** ( $n$ ) for each experimental group/condition, given as a discrete number and unit of measurement
- An indication of whether measurements were taken from distinct samples or whether the same sample was measured repeatedly
- The statistical test(s) used AND whether they are one- or two-sided  
*Only common tests should be described solely by name; describe more complex techniques in the Methods section.*
- A description of all covariates tested
- A description of any assumptions or corrections, such as tests of normality and adjustment for multiple comparisons
- A full description of the statistics including **central tendency** (e.g. means) or other basic estimates (e.g. regression coefficient) AND **variation** (e.g. standard deviation) or associated **estimates of uncertainty** (e.g. confidence intervals)
- For null hypothesis testing, the test statistic (e.g.  $F$ ,  $t$ ,  $r$ ) with confidence intervals, effect sizes, degrees of freedom and  $P$  value noted  
*Give  $P$  values as exact values whenever suitable.*
- For Bayesian analysis, information on the choice of priors and Markov chain Monte Carlo settings
- For hierarchical and complex designs, identification of the appropriate level for tests and full reporting of outcomes
- Estimates of effect sizes (e.g. Cohen's  $d$ , Pearson's  $r$ ), indicating how they were calculated
- Clearly defined error bars  
*State explicitly what error bars represent (e.g. SD, SE, CI)*

*Our web collection on [statistics for biologists](#) may be useful.*

### Software and code

Policy information about [availability of computer code](#)

Data collection

Molecular Devices MetaMorph and MetaFluor 7.7, NIS-Elements AR software, LabView, Andor Solis 4.21, OLYMPUS FLUOView 3000

Data analysis

Graphpad Prism 6.0 and 7.0, Origin9, Microsoft Excel, Clampfit 10.7, MatLab2017b, ImageJ, MetaFluor 7.7

For manuscripts utilizing custom algorithms or software that are central to the research but not yet described in published literature, software must be made available to editors/reviewers upon request. We strongly encourage code deposition in a community repository (e.g. GitHub). See the Nature Research [guidelines for submitting code & software](#) for further information.

### Data

Policy information about [availability of data](#)

All manuscripts must include a [data availability statement](#). This statement should provide the following information, where applicable:

- Accession codes, unique identifiers, or web links for publicly available datasets
- A list of figures that have associated raw data
- A description of any restrictions on data availability

One page 15 of the Supplementary Material we state: "Data Availability. Gene sequence data will be deposited in GenBank with accession codes that are TBD. Plasmids will be distributed via Addgene according to the terms of the Uniform Biological Material Transfer Agreement. Source data for Figs. 1-2, and Supplementary Figs. 5-7, 9, 11 will be included in the final version of the paper."

## Field-specific reporting

Please select the best fit for your research. If you are not sure, read the appropriate sections before making your selection.

Life sciences  Behavioural & social sciences  Ecological, evolutionary & environmental sciences

For a reference copy of the document with all sections, see [nature.com/authors/policies/ReportingSummary-flat.pdf](https://www.nature.com/authors/policies/ReportingSummary-flat.pdf)

## Life sciences study design

All studies must disclose on these points even when the disclosure is negative.

Sample size	On page 9 of Supplementary Material we state: "No statistical methods were used to estimate sample size for animal studies throughout." As noted in Dell et al ILAR. J (2002) and recommended by the NIH, "In experiments based on the success or failure of a desired goal, the number of animals required is difficult to estimate..." As noted in the aforementioned paper, "The number of animals required is usually estimated by experience instead of by any formal statistical calculation, although the procedures will be terminated [when the goal is achieved]." On page 15 of the Supplementary Material we include the following statement: "Statistical analysis. All data are expressed as mean $\pm$ s.d or mean $\pm$ s.e.m, as specified in figure legends. Box plots with notches are used for Figs. 1g, 2d, and Supplementary Figs. 7b, 12a and 13c. In these plots, the narrow part of notch is the median; the top and bottom of the notch is the 95% confidence interval of the median; the horizontal line is the mean; the top and bottom horizontal lines are the 25% and 75% percentiles for the data; and the whiskers extend 1.5 $\times$ the interquartile range from the 25th and 75th percentiles. Sample sizes (n) are listed with each experiment. No samples were excluded from analysis and all experiments were reproducible. No randomization or blinding was used."
Data exclusions	P31. The P0 pups were screened for corresponding fluorescence, negative pups were excluded for further experiments.
Replication	P33. All attempts at replication were successful.
Randomization	P33. No randomization or blinding was used
Blinding	P33. No randomization or blinding was used

## Reporting for specific materials, systems and methods

Materials & experimental systems		Methods	
n/a	Included in the study	n/a	Included in the study
<input checked="" type="checkbox"/>	<input type="checkbox"/> Unique biological materials	<input checked="" type="checkbox"/>	<input type="checkbox"/> ChIP-seq
<input checked="" type="checkbox"/>	<input type="checkbox"/> Antibodies	<input checked="" type="checkbox"/>	<input type="checkbox"/> Flow cytometry
<input type="checkbox"/>	<input checked="" type="checkbox"/> Eukaryotic cell lines	<input checked="" type="checkbox"/>	<input type="checkbox"/> MRI-based neuroimaging
<input checked="" type="checkbox"/>	<input type="checkbox"/> Palaeontology		
<input type="checkbox"/>	<input checked="" type="checkbox"/> Animals and other organisms		
<input checked="" type="checkbox"/>	<input type="checkbox"/> Human research participants		

## Eukaryotic cell lines

Policy information about [cell lines](#)

Cell line source(s)	HeLa (ATCC), HEK293FT (Thermo Fisher Scientific), MIN6 (Miyazaki laboratory, Osaka University)
Authentication	Cell lines were not authenticated
Mycoplasma contamination	MIN6 cells were tested weekly for Mycoplasma using DNA staining. Other cell lines were not tested.
Commonly misidentified lines (See <a href="#">ICLAC</a> register)	HEK293FT cells were used for production of lentivirus due to the following advantages: fast-growing, high transfection efficiency and tolerance of high levels of proteins.

## Animals and other organisms

Policy information about [studies involving animals](#); [ARRIVE guidelines](#) recommended for reporting animal research

Laboratory animals	Pages 4 and 5 of Supplementary material. We state: "Animal care. For experiments performed at Massachusetts Institute of
--------------------	--

Laboratory animals

Technology (MIT), all methods for animal care and use were approved by the MIT Committee on Animal Care and were in accordance with the National Institutes of Health Guide for the Care and Use of Laboratory Animals. Four time pregnant Swiss Webster mice (Taconic) were used for this study, as were five C57BL/6 mice (Taconic), ages 4–12 weeks. Mice were used without regard to gender.

For experiments performed at Technical University of Munich, all animal in vivo experimentation was done in full compliance with the institutional guidelines of the Institute for Biological and Medical Imaging and with approval from the Government District of Upper Bavaria. A total of twelve mice were used for these experiments: three female FOXP1 nude mice that were injected with the NIR-GECO1 virus; three female FOXP1 nude mice that were injected with the miRFP virus; three female Black6 (C57BL/6J) transgenic mice expressing GCaMP6s and three mice (two female FOXP1 and one female Black6) that were injected with PBS as negative controls.

All experiments at University of Alberta for obtaining the cortical neurons were approved by the University of Alberta Animal Care and Use Committee and carried out in compliance with guidelines of the Canadian Council for Animal Care and the Society for Neuroscience's Policies on the Use of Animals and Humans in Neuroscience Research.

For experiments at HHMI Janelia Research Campus, all surgical and experimental procedures were in accordance with protocols approved by the HHMI Janelia Research Campus Institutional Animal Care and Use Committee and Institutional Biosafety Committee."



Wild animals

The study did not involve wild animals.

Field-collected samples

The study did not involve sample collected from the field.

Corresponding author(s): Robert E. Campbell  
 Initial submission  Revised version  Final submission

## Editorial Policy Checklist

This form is used to ensure compliance with Nature Research editorial policies related to research ethics and reproducibility. For further information, please see our [Authors & Referees](#) site. All relevant questions on the form must be answered.

### ▶ Competing interests

Policy information about [competing interests](#)

#### Competing interests declaration

In the interest of transparency and to help readers form their own judgements of potential bias, Nature Research journals require authors to declare any competing financial and/or non-financial interest in relation to the work described in the submitted manuscript.

- No, I declare that the authors have no competing financial or non-financial interests as defined by Nature Research.  
 Yes, I declare that the authors have a competing interest as defined by Nature Research

The University of Alberta has non-exclusively licensed NIR-GECO1 to LumiSTAR Biotechnology.

### ▶ Data availability

Policy information about [availability of data](#)

#### Data availability statement

All manuscripts must include a [data availability statement](#). This statement should provide the following information, where applicable:

- Accession codes, unique identifiers, or web links for publicly available datasets
- A list of figures that have associated raw data
- A description of any restrictions on data availability

- A full data availability statement is included in the manuscript.

#### Mandated accession codes (where applicable)

Confirm that all relevant data are deposited into a public repository and that accession codes are provided.

- All relevant accession codes are provided  Accession codes will be available before publication  No data with mandated deposition

### ▶ Data presentation

#### Image integrity

- Confirm that all images comply with our [image integrity policy](#).

Unprocessed data must be provided upon request. Please double-check figure assembly to ensure that all panels are accurate (e.g. all labels are correct, no inadvertent duplications have occurred during preparation, etc.).

#### Data distribution

Present data in a format that shows data distribution (dot-plots or box-and-whisker plots).

Define all box-plot elements (e.g. center line, median; box limits, upper and lower quartiles; whiskers, 1.5x interquartile range; points, outliers). If using bar graphs, overlay the corresponding dot plots.

- Confirm that all data presentation meets these requirements and that individual data points are shown.

## Specific policy considerations

Some types of research require additional policy disclosures. Please indicate whether these apply to your study. If you are not certain, please read the appropriate section before selecting a response.

Does not apply	Involved in the study
<input type="checkbox"/>	<input checked="" type="checkbox"/> Custom software or computer code
<input checked="" type="checkbox"/>	<input type="checkbox"/> Macromolecular structural data
<input type="checkbox"/>	<input checked="" type="checkbox"/> Research animals and/or animal-derived materials that require ethical approval
<input checked="" type="checkbox"/>	<input type="checkbox"/> Human research participants
<input checked="" type="checkbox"/>	<input type="checkbox"/> Clinical data

### ▶ Code availability

Policy information about [availability of computer code](#)

#### Code availability statement

For all studies using custom code, the Methods section must include a statement under the heading "Code availability" describing how readers can access the code, including any access restrictions.

A full code availability statement is included in the manuscript

### ▶ Research animals

Policy information about [studies involving animals](#); [ARRIVE guidelines](#) recommended for reporting animal research

#### Ethical compliance

Confirm that you have complied with all relevant ethical regulations and that a statement affirming this is included in the manuscript.

#### Ethics committee

Confirm that the manuscript states the name(s) of the board and institution that approved the study protocol.

I certify that all the above information is complete and correct.

Typed signature Robert E. Campbell

Date November 20, 2018

This checklist template is licensed under a Creative Commons Attribution 4.0 International License, which permits use, sharing, adaptation, distribution and reproduction in any medium or format, as long as you give appropriate credit to the original author(s) and the source, provide a link to the Creative Commons license, and indicate if changes were made. The images or other third party material in this article are included in the article's Creative Commons license, unless indicated otherwise in a credit line to the material. If material is not included in the article's Creative Commons license and your intended use is not permitted by statutory regulation or exceeds the permitted use, you will need to obtain permission directly from the copyright holder. To view a copy of this license, visit <http://creativecommons.org/licenses/by/4.0/>

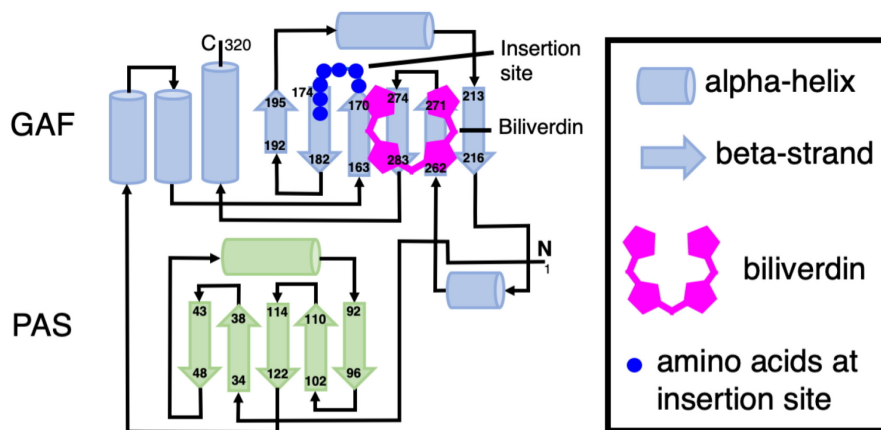


In the format provided by the authors and unedited.

## A genetically encoded near-infrared fluorescent calcium ion indicator

Yong Qian<sup>1,12</sup>, Kiryl D. Piatkevich<sup>2,12</sup>, Benedict Mc Larney<sup>3,4,12</sup>, Ahmed S. Abdelfattah<sup>5</sup>, Sohun Mehta<sup>6</sup>, Mitchell H. Murdock<sup>2</sup>, Sven Gottschalk<sup>3</sup>, Rosana S. Molina<sup>7</sup>, Wei Zhang<sup>1</sup>, Yingche Chen<sup>1</sup>, Jiahui Wu<sup>1</sup>, Mikhail Drobizhev<sup>7</sup>, Thomas E. Hughes<sup>8</sup>, Jin Zhang<sup>6</sup>, Eric R. Schreiter<sup>5</sup>, Shy Shoham<sup>8</sup>, Daniel Razansky<sup>3,4,9,10</sup>, Edward S. Boyden<sup>2</sup> and Robert E. Campbell<sup>1,11\*</sup>

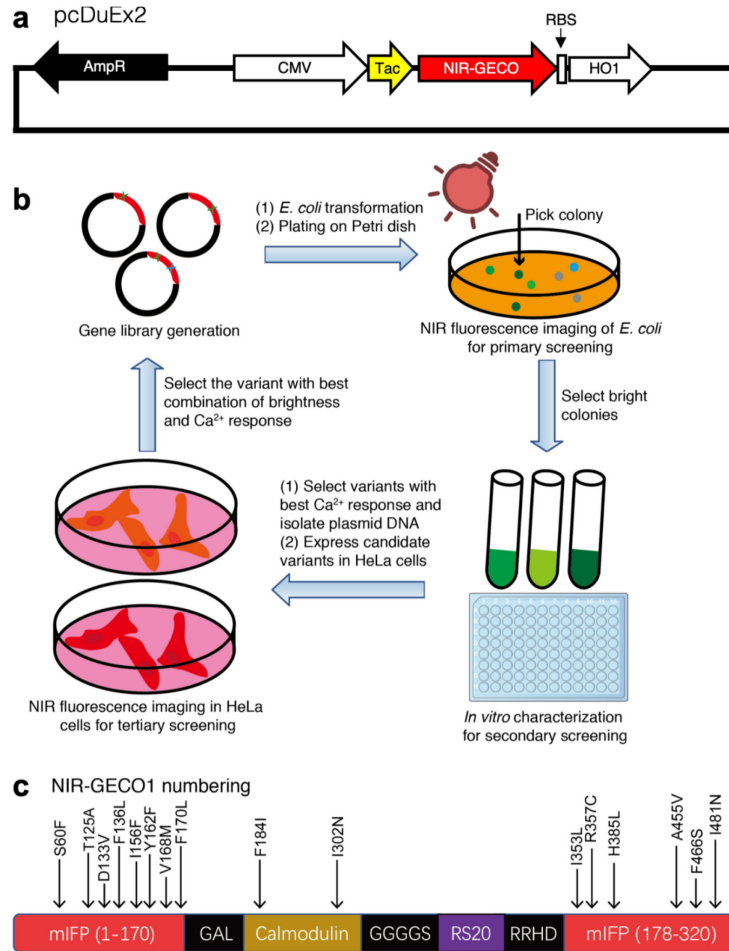
<sup>1</sup>Department of Chemistry, University of Alberta, Edmonton, Alberta, Canada. <sup>2</sup>Media Lab and McGovern Institute for Brain Research, MIT, Cambridge, MA, USA. <sup>3</sup>Institute for Biological and Medical Imaging, Helmholtz Center Munich, Neuherberg, Germany. <sup>4</sup>Faculty of Medicine, Technical University of Munich, Munich, Germany. <sup>5</sup>Janelia Research Campus, Howard Hughes Medical Institute, Ashburn, VA, USA. <sup>6</sup>Department of Pharmacology, University of California San Diego, La Jolla, CA, USA. <sup>7</sup>Department of Cell Biology and Neuroscience, Montana State University, Bozeman, MT, USA. <sup>8</sup>Departments of Ophthalmology and of Neuroscience and Physiology, New York University Langone Health, New York City, NY, USA. <sup>9</sup>Faculty of Medicine and Institute of Pharmacology and Toxicology, University of Zurich, Zurich, Switzerland. <sup>10</sup>Department of Information Technology and Electrical Engineering and Institute for Biomedical Engineering, ETH Zurich, Zurich, Switzerland. <sup>11</sup>Department of Chemistry, Graduate School of Science, The University of Tokyo, Tokyo, Japan. <sup>12</sup>These authors contributed equally: Yong Qian, Kiryl D. Piatkevich, Benedict Mc Larney. \*e-mail: [robert.e.campbell@ualberta.ca](mailto:robert.e.campbell@ualberta.ca)



### Supplementary Figure 1

The topology of mIFP (i.e., bacteriophytochrome).

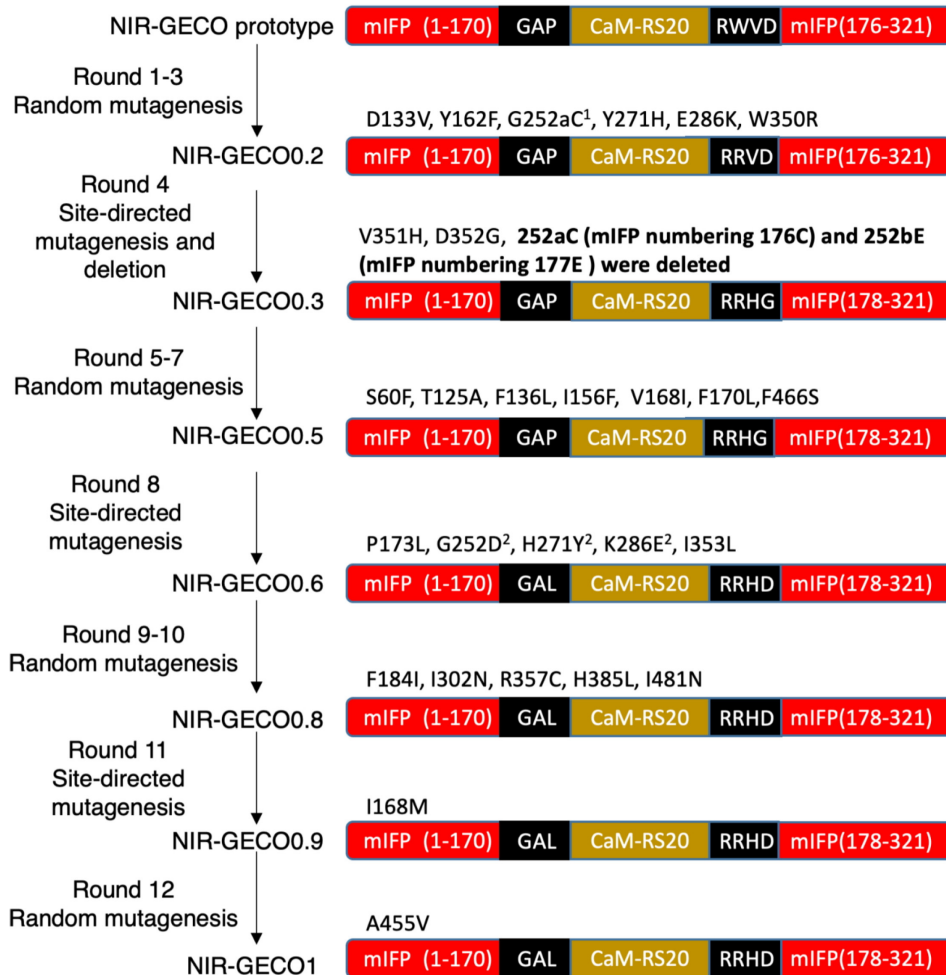
Scheme is based on alignment of the sequence of mIFP (320 residues; GenBank accession number AKH03689.1; *Nat. Methods* **12**, 763–765, 2015), with the crystal structure of the chromophore-binding domain of *Deinococcus radiodurans* BphP (PDB 2O9B; *J. Biol. Chem.* **282**, 12298–12309, 2007). Representation is adapted from Takala et al. (*Nature* **509**, 245–248; 2014), with  $\beta$ -strands represented as arrows and  $\alpha$ -helical regions represented as cylinders. The PAS domain is colored in light green, and the BV-binding GAF domain is colored in light blue, as in Fig. 1a,b. The approximate position of the bound BV is represented by a magenta structure. Numbers at the ends of  $\beta$ -strands correspond to mIFP numbering (see Supplementary Figs. 2c, 3 and 4), based on alignment with the crystal structure. To engineer NIR-GECO1, 5 residues (171–175, DEEGN) in the loop between the first two  $\beta$ -strands of the GAF domain were initially replaced with a 182-residue CaM-RS20 domain (a 3-residue linker followed by 147-residue CaM followed by a 5-residue linker followed by 23-residue RS20 followed by a 4-residue linker). Systematic optimization of the insertion site to improve the  $\text{Ca}^{2+}$ -dependent fluorescence change led to the deletion of residues 176G and 177E of mIFP, resulting in an overall replacement of 7 residues (171–177, DEEGNGE) with the CaM-RS20 domain.



**Supplementary Figure 2**

Directed evolution of NIR-GECO1 by library screening.

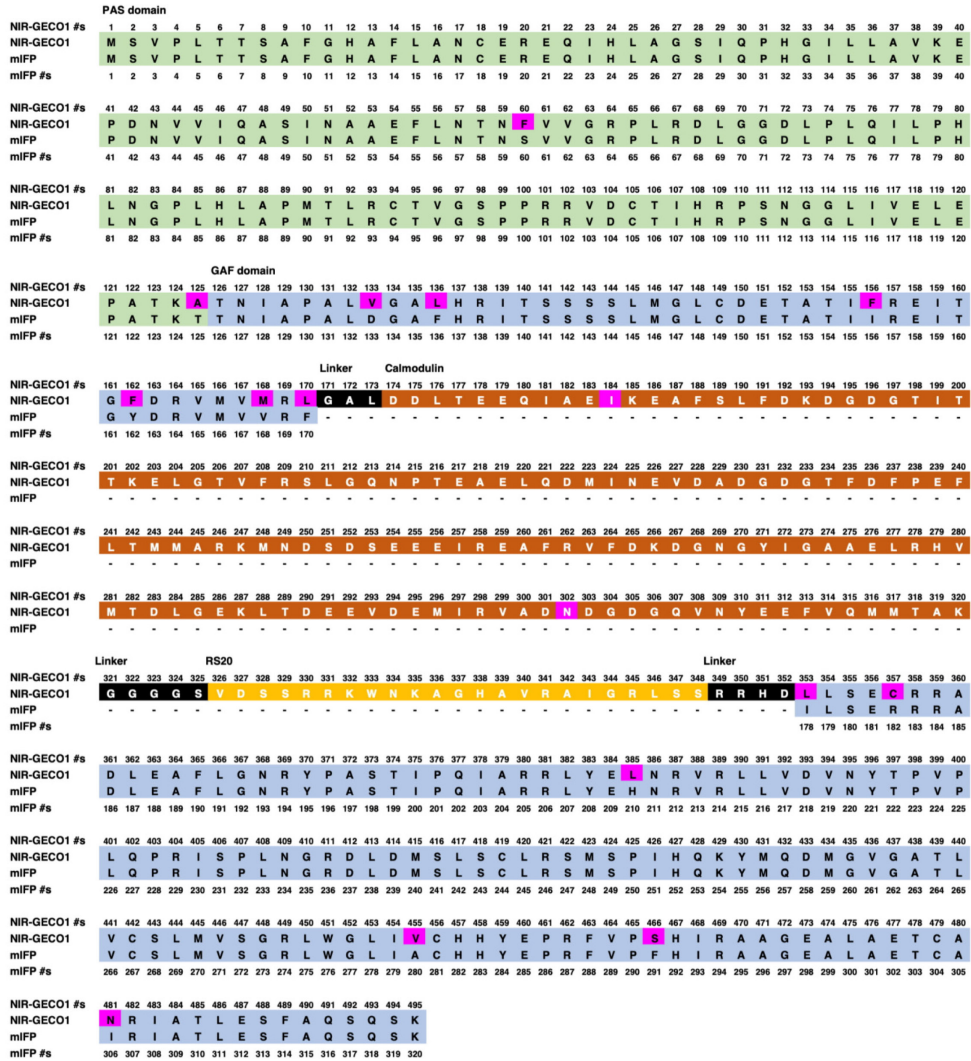
(a) Representation of the pcDuEx2 vector used for expression of genes in both bacteria and mammalian cells. Cytomegalovirus (CMV) promoter is used for mammalian expression, while the *Tac* promoter (a hybrid promoter derived from the *trp* and *lac* promoters) is used for bacterial expression. HO1 is expressed in bacteria but, because of the presence of a stop codon after NIR-GECO1 and the lack of a promoter before HO1, it is not expressed in mammalian cells. RBS, ribosome binding site; HO1, heme-oxygenase 1. (b) Workflow of the screening process. Briefly, *E. coli* DH10B was transformed with a gene library in pcDuEx2 and grown on LB plates, and then bright colonies were picked and cultured. Proteins were extracted from overnight cultures of bacteria and then tested for fluorescence and  $\text{Ca}^{2+}$  response in 384-well plates. Variants with reasonable brightness and  $\text{Ca}^{2+}$  response were selected, and the corresponding plasmids were purified. HeLa cells were transfected with the selected plasmids, and live-cell fluorescence imaging was used to evaluate both brightness and  $\text{Ca}^{2+}$  response. HeLa cells were not supplemented with BV. (c) Mutations of NIR-GECO1 acquired during directed evolution.

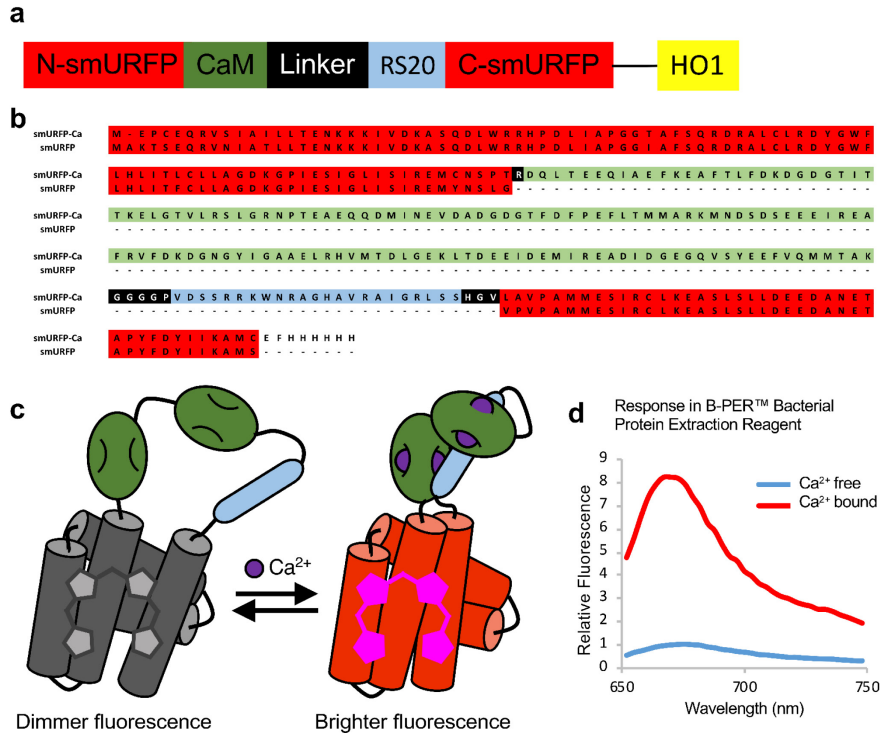


Supplementary Figure 3

Lineage of improved NIR-GECO variants.

Key mutations included deletion of 252aC and 252bE, which substantially improved the Ca<sup>2+</sup>-dependent fluorescence change; F184I and I302N, which increased affinity for Ca<sup>2+</sup>; and W350R and R357C, A455V which substantially improved the brightness. Footnotes: <sup>1</sup>This residue was deleted in round 4. <sup>2</sup>These mutations were reversions.

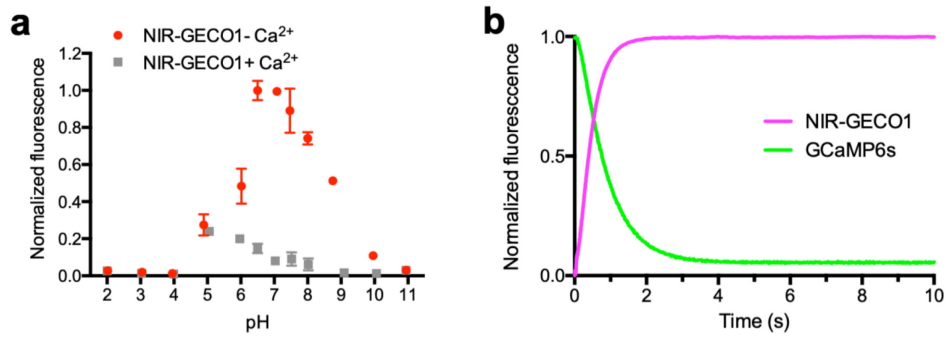




**Supplementary Figure 5**

Attempted engineering of a smURFP-based Ca<sup>2+</sup> indicator.

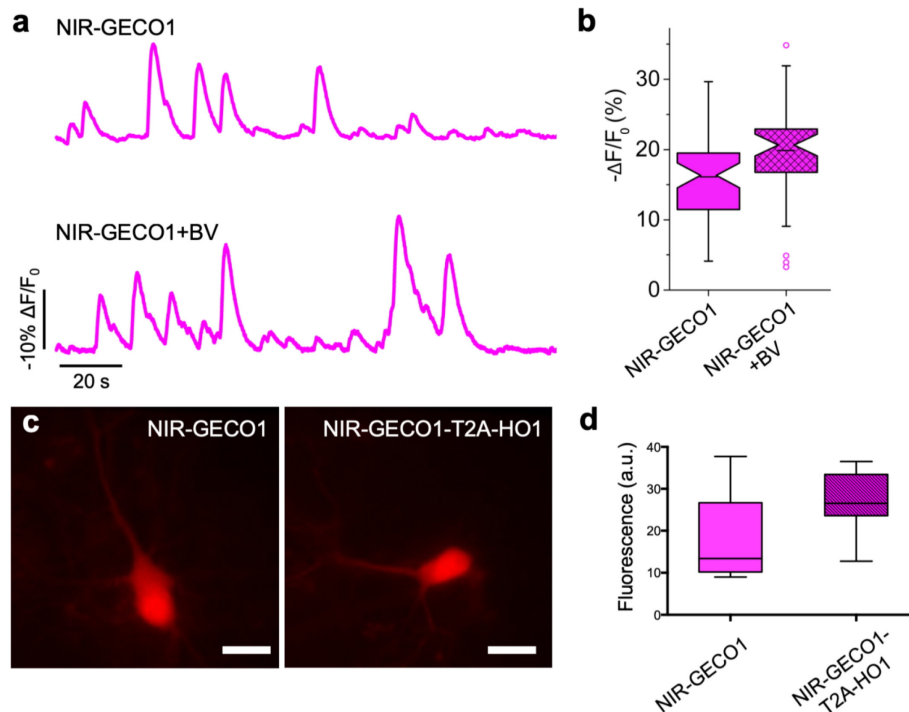
Using methods analogous to those used to develop NIR-GECO1, we attempted to engineer a smURFP-based (*Nat. Methods* **13**, 763-769; 2016) Ca<sup>2+</sup> indicator. During each round of screening, the protein was tested for Ca<sup>2+</sup>-dependent fluorescent response in crude bacterial lysate prepared with B-PER protein extraction reagent (Thermo Fisher). Under these conditions, this indicator exhibited a substantial fluorescence increase upon binding Ca<sup>2+</sup>. Unfortunately we were unable to functionally express this indicator in mammalian cells. (a) Schematic representation of the smURFP-based Ca<sup>2+</sup> indicator structure. (b) Sequence of the indicator after the eighth round of directed evolution. (c) Schematic representation of the protein structure and response. CaM-RS20 was inserted between the fourth and fifth helix of smURFP. The best variant exhibited an approximately eightfold change in fluorescence intensity (Ca<sup>2+</sup>-bound/Ca<sup>2+</sup>-free) at the maximum emission (670 nm). (d) Emission spectra for the protein after the eighth round, normalized to the Ca<sup>2+</sup>-free state.



**Supplementary Figure 6**

Additional in vitro characterization of NIR-GECO1.

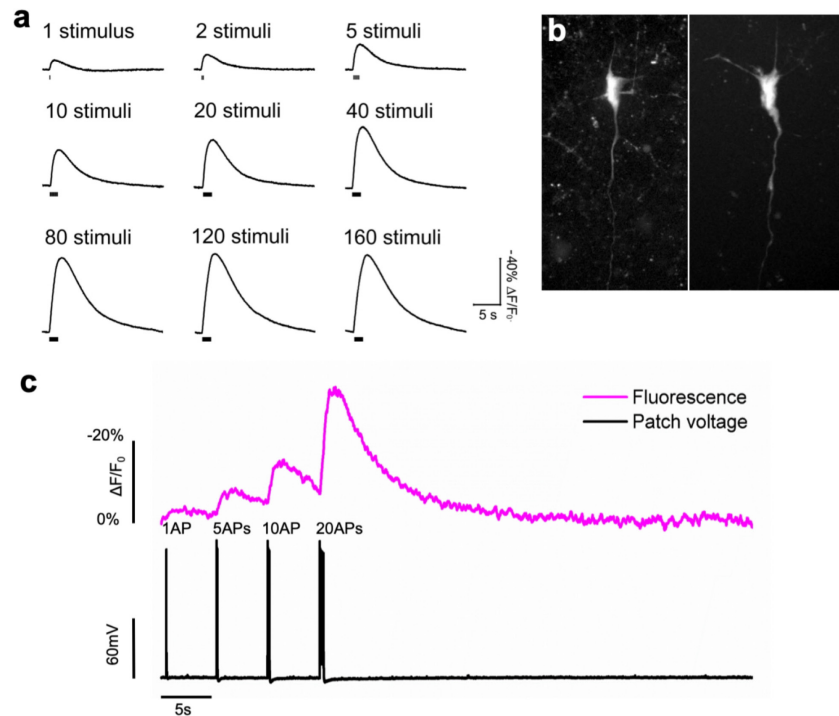
(a) pH titration curves of NIR-GECO1 in the presence and absence of Ca<sup>2+</sup>. *n* = 3 independent experiments; values are mean ± s.d. (b) Ca<sup>2+</sup> dissociation kinetics of NIR-GECO1 (magenta) and GCaMP6s (green).



#### Supplementary Figure 7

Increasing intracellular BV concentration has a modest effect on NIR-GECO1 brightness.

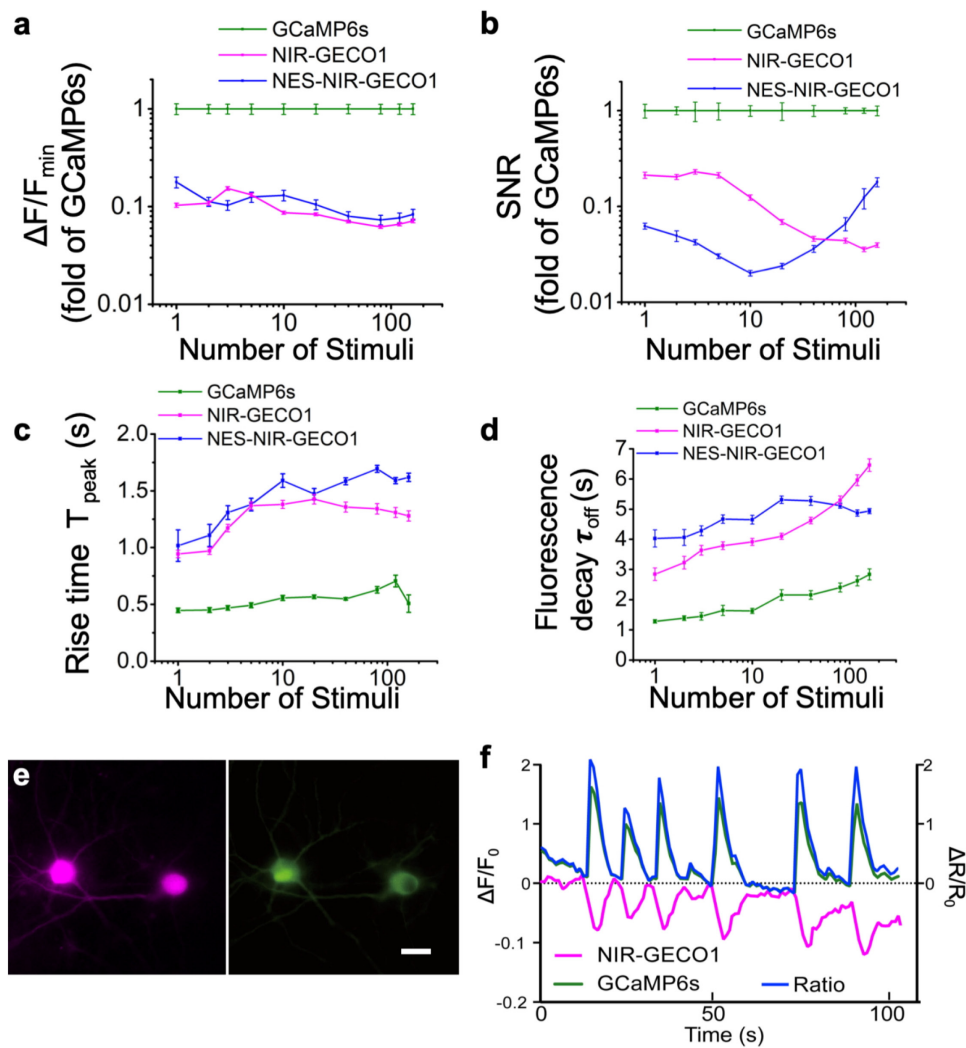
(a) Representative fluorescence traces of NIR-GECO1 (top) and NIR-GECO1 supplied with 25  $\mu$ M exogenous BV (bottom) in response to neuronal spontaneous activities.  $n = 51$  neurons for NIR-GECO and  $n = 39$  neurons for NIR-GECO1 + BV. (b) Quantification of  $-\Delta F/F_0$  corresponding to the experiment of a. Values are  $16 \pm 6\%$  for NIR-GECO1 and  $20 \pm 8\%$  for NIR-GECO1 + BV (mean  $\pm$  s.d.). (c) Representative wide-field fluorescence images of neurons expressing NIR-GECO1 (left) and NIR-GECO1-T2A-HO1 (right). The human HO1 gene was used. Scale bar, 20  $\mu$ m. (d) Relative normalized fluorescence of NIR-GECO1 ( $n = 15$  neurons) and NIR-GECO1-T2A-HO1 ( $n = 15$  neurons). Values are  $18.3 \pm 10.2$  (a.u.) for NIR-GECO1 and  $27.1 \pm 7.0$  (a.u.) for NIR-GECO1-T2A-HO1 (mean  $\pm$  s.d.). Fluorescence was normalized by coexpression of EGFP (NIR channel, 650/60 nm Ex and 720/60 nm Em; green channel, 490/15 nm Ex and 525/50 nm Em). Box plots are used where the top and bottom horizontal lines mark the 25th and 75th percentiles for the data; whiskers extend to the maximum and minimum for the data; and the black horizontal bar is the median.



**Supplementary Figure 8**

Characterization of NIR-GECO1 in cultured neurons and in intact brain tissues.

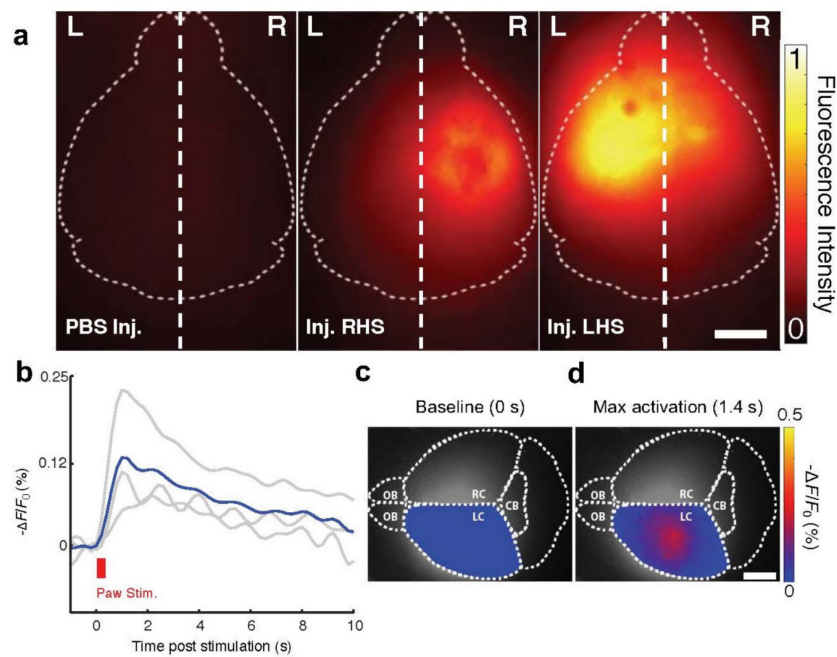
(a) Representative traces of single trial NIR-GECO1 fluorescence responses to field stimulation in cultured rat hippocampal neurons. (b) Representative confocal images of neurons in L2/3 of motor cortex expressing NIR-GECO1 (641 nm Ex and 664LP Em;  $n = 4$  slices from 2 mice). Such neurons were imaged during electrophysiological current injections as in c. (c) Representative single-trial wide-field optical recording of NIR-GECO1 fluorescence responses (magenta; 631/28 nm Ex and 664LP Em; acquisition rate 50 Hz) to 1, 5, 10, and 20 action potentials trains evoked by current injections in neurons in L2/3 of motor cortex (as in b;  $n = 6$  neurons from 4 mice at P11-22). Patch voltage is shown in black.



**Supplementary Figure 9**

Comparison of NIR-GECO1, NES-NIR-GECO1 and GCaMP6s.

(a) Response amplitude of NIR-GECO1 ( $n = 55$  neurons) and NES-NIR-GECO1 ( $n = 147$  neurons) as a fraction of GCaMP6s ( $n = 31$  neurons). The average  $-\Delta F/F_{\min}$  of NIR-GECO1 was  $2.4 \pm 0.12\%$ ,  $3.4 \pm 0.16\%$ ,  $6.6 \pm 0.29\%$ ,  $11 \pm 0.44\%$ ,  $17 \pm 0.65\%$ ,  $27 \pm 0.9\%$ ,  $43 \pm 1.4\%$ ,  $60 \pm 2.0\%$ ,  $77 \pm 3.0\%$ , and  $94 \pm 4.2\%$  for 1, 2, 3, 5, 10, 20, 40, 80, 120 and 160 APs, respectively. Relative to GCaMP6s, the  $-\Delta F/F_{\min}$  of NIR-GECO1 was 10% of GCaMP6s for 1 and 2 APs and increased to 15% and 13% for 3 and 5 APs and then went down to 7% for APs from 10 to 160 APs. Elsewhere in the paper we have consistently used  $\Delta F/F_0$  to describe fluorescence changes. Here we use  $\Delta F/F_{\min}$  to enable the values for NIR-GECO1 and GCaMP6s to be easily compared. (b) Signal-to-noise ratio (SNR) of NIR-GECO1 and NES-NIR-GECO1 compared to GCaMP6s. The SNR of NIR-GECO1 was  $26.7 \pm 1.98$ ,  $34.4 \pm 2.15$ ,  $62.2 \pm 3.42$ ,  $98.6 \pm 6.37$ ,  $145 \pm 9.29$ ,  $185 \pm 10.9$ ,  $256 \pm 15.3$ ,  $302 \pm 18.0$ ,  $311 \pm 16.9$  and  $335 \pm 18.8$  for 1, 2, 3, 5, 10, 20, 40, 80, 120 and 160 APs, respectively. Relative to GCaMP6s, the SNR of NIR-GECO1 was 20% of GCaMP6s for APs from 1 to 5 and then goes down to 12% to 4% of GCaMP6s for APs from 10 to 100. (c) Fluorescence rise time of NIR-GECO1 and NES-NIR-GECO1 (actually a fluorescence decrease) compared to GCaMP6s for binding of  $\text{Ca}^{2+}$ . The average rise time of NIR-GECO1 was  $0.94 \pm 0.033$  s,  $1.4 \pm 0.038$  s,  $1.4 \pm 0.044$  s for 1, 10 and 40 APs. (d) Fluorescence decay time of NIR-GECO1 and NES-NIR-GECO1 (actually a fluorescence increase) compared to GCaMP6s for dissociation of  $\text{Ca}^{2+}$ . The average decay time of NIR-GECO1 was  $2.8 \pm 0.21$  s,  $3.9 \pm 0.12$  s,  $4.6 \pm 0.11$  s for 1, 10 and 40 APs. For a-d, the NIR-GECO1 data are identical to data represented in Fig. 1i-l. For a-d, center values are the mean, and error bars are s.e.m.  $n = 55$  neurons for NIR-GECO1 and  $n = 31$  neurons for GCaMP6s. (e) Representative wide-field fluorescence images of coexpressed NIR-GECO1 (left) and GCaMP6s (right).  $n = 5$  neurons from two cultures. Scale bar, 20  $\mu\text{m}$ . (f) Spontaneous  $\text{Ca}^{2+}$  oscillations in dissociated cortical neurons coexpressing NIR-GECO1 and GCaMP6s (NIR channel, 650/60 nm Ex and 720/60 nm Em; green channel, 490/15 nm Ex and 525/50 nm Em; acquisition rate is 1 Hz). Also shown is  $\Delta R/R_0$ , where  $R$  is the normalized GCaMP6s intensity divided by normalized NIR-GECO1 intensity.  $n = 5$  neurons from two cultures.

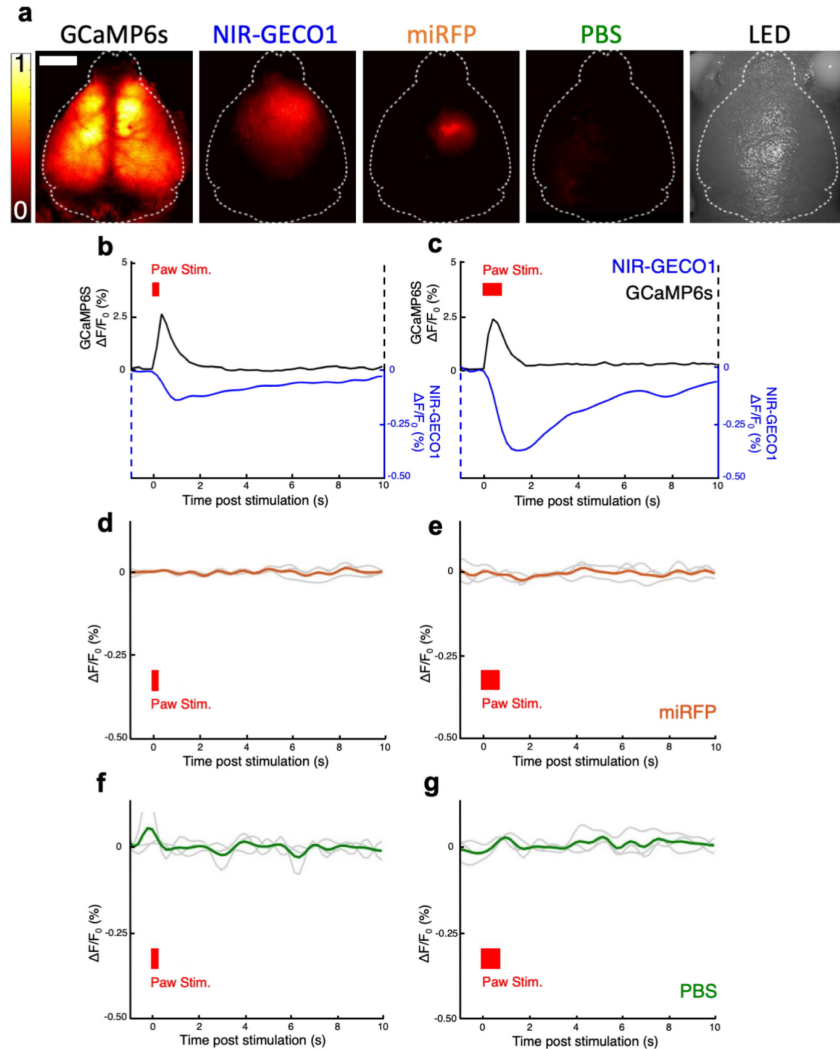


### Supplementary Figure 10

In vivo mesoscale imaging of footshock responses in mice using NIR-GECO1.

(a) Mesoscale fluorescence images (671 nm Ex and 721/42 nm Em) of the mouse sensorimotor cortex injected with AAV2/9-hSyn1-NIR-GECO1 (as in Fig. 2e–g). Left, negative control with no viral expression on the right side of mouse brain (PBS injection). Middle, viral expression of NIR-GECO1 on the right side of mouse brain. Right, viral expression of NIR-GECO1 on the left side of mouse brain. Scale bar, 2 mm. (b) Fluorescence response of NIR-GECO1 in response to a paw stimulation paradigm with a single 50-ms pulse (0.5 mA). As in Fig. 2e, each gray line represents the averaged response of a mouse across 19 cycles, and the blue line represents the mean response from all 3 mice ( $n = 3$ , or  $3 \times 19 = 57$  cycles). (c) Activation map of mouse brain before stimulation. The estimated brain outline was manually superimposed onto the fluorescence images to facilitate determining the site of injection and activation in relation to bregma and the sensorimotor cortex. (d) Activation map of mouse brain at max activation. Scale bar, 2 mm. OB, olfactory bulb; CB,

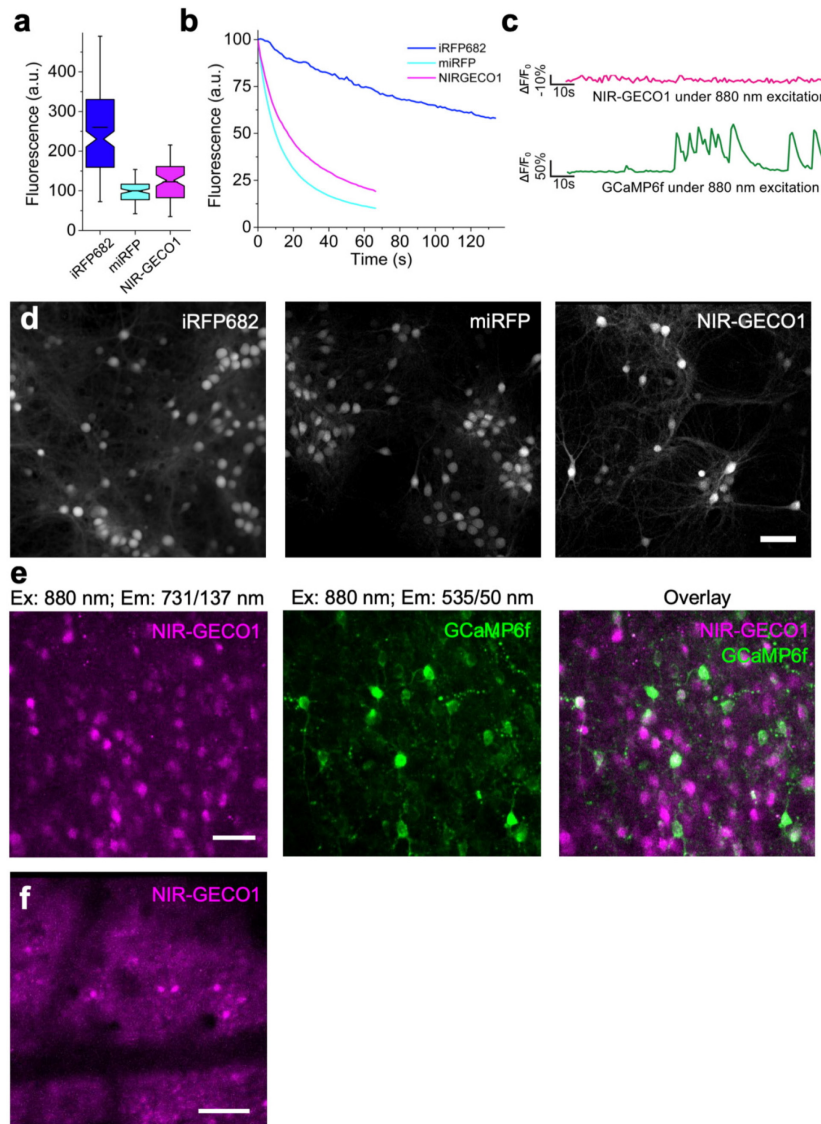
cerebellum; L/R, left or right cortex.



**Supplementary Figure 11**

Control experiments for in vivo mesoscale imaging using GCaMP6s and miRFP.

**(a)** Comparative fluorescence images of a transgenic Bl6-GCaMP6s mouse and FoxN1 nude NIR-GECO1, miRFP and PBS injected mice. All fluorescence images are normalized to the GCaMP image shown. Direct comparison of the NIR-GECO1 and miRFP brightness is complicated by the fact that the AAVs were different serotypes (AAV2/9 and AAV2, respectively) and the NIR-GECO1 stock had 10 $\times$  more genome copies/mL. Also shown is a representative white light image of the imaging area. Scale bar, 2 mm. **(b, c)** Positive control experiment with imaging of GCaMP6s in response to paw stimulations. For **b**, a stimulation paradigm of a single 50-ms pulse (0.5 mA) was used. For **c**, a stimulation paradigm of 10 pulses in 700 ms (0.5 mA, 20 ms on and 50 ms off) was used. The mean value from 3 mice is shown in each case. NIR-GECO1 curves are the same as in Supplementary Fig. 10b and Fig. 2e. **(d, e)** A negative control experiment with imaging of miRFP fluorescence in response to paw stimulations. Stimulations in **d** and **e** are the same as in **b** and **c**, respectively. Orange line represents the mean value from 3 mice, and gray lines represent the average response of 1 mouse across 19 cycles. **(f, g)** A negative control with fluorescence imaging PBS-injected mouse in response to paw stimulations. Filter set is the same as for NIR-GECO1. The green line represents the mean value of 3 measurements (an average of 19 cycles) from 2 mice, and the gray lines represent the average response averaged for 1 mouse measured once and 1 mouse measured twice. Stimulations in **f** and **g** are the same as in **b** and **c**, respectively. The GCaMP6s mice are a transgenic line, and the mice were approximately 2 months older than other mice used in these experiments.

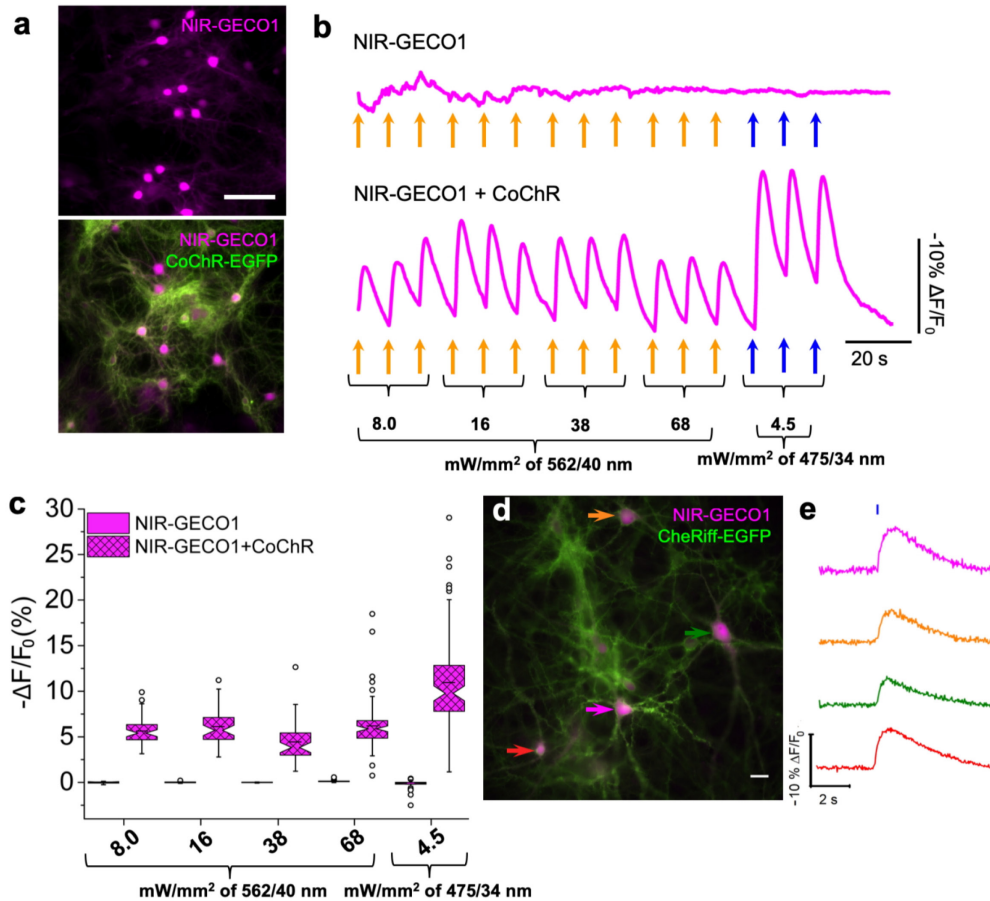


**Supplementary Figure 12**

Two-photon fluorescence microscopy of NIR-GECO1.

BV-FPs can be visualized using two-photon fluorescence microscopy (*Biophys. J.* **113**, 2299–2309; 2017), a widely used technique for *in vivo*  $\text{Ca}^{2+}$  imaging. (a) Relative normalized fluorescence and (b) raw photobleaching curves for iRFP682 (blue), miRFP (cyan), and

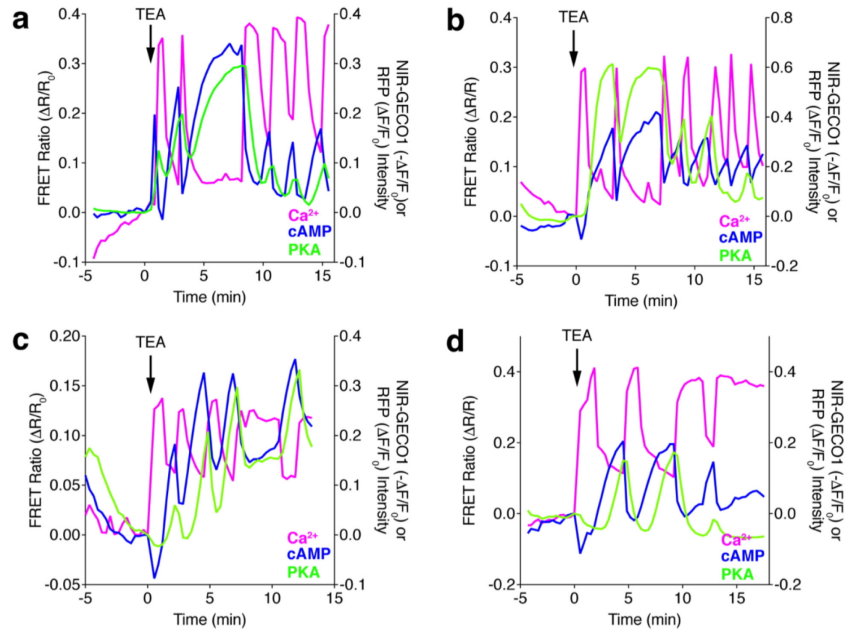
NIR-GECO1 (magenta) in cultured mouse neurons ( $n = 184$ , 106, and 77 cells, respectively, from one culture) under 880-nm two-photon excitation and 4.05 mW of total light power. For a, a box plot with notches is used as described in Fig. 1g. (c) Representative fluorescence recording of 4-aminopyridine (1 mM final concentration)-evoked neuronal activity using NIR-GECO1 and GCaMP6f fluorescence under 880-nm two-photon excitation. Excitation for both NIR-GECO1 and GCaMP6f was 880 nm, and emission filters for NIR-GECO1 and GCaMP6f were 705/90 nm and 518/45 nm, respectively. (d) Representative two-photon fluorescence images of cultured mouse neurons expressing iRFP682 (left), miRFP (middle) and NIR-GECO1 (right), under 880-nm two-photon excitation (731/137 nm Em;  $n = 184$ , 106, and 77 cells, respectively, from one culture). Scale bar, 50  $\mu\text{m}$ . (e) Two-photon fluorescence images of live mouse brain slice coexpressing NIR-GECO1 (left; magenta) and GCaMP6f (middle; green) under 880-nm excitation (right, overlay).  $n = 2$  slices from one mouse. Scale bar, 50  $\mu\text{m}$ . (f) *In vivo* two-photon microscopy of NIR-GECO1-expressing neurons in mouse primary visual cortex.  $n = 3$  fields of view from one mouse. Scale bar, 50  $\mu\text{m}$ .



Supplementary Figure 13

Combined use of channelrhodopsins (CoChR and CheRiff) and NIR-GECO1 for optogenetic stimulation and imaging of activity.

Representative wide-field fluorescent images of cultured hippocampal mouse neurons expressing NIR-GECO1 (top; magenta; 631/28 nm Ex and 664LP Em), and both NIR-GECO1 (magenta; 631/28 nm Ex and 664LP Em) and CoChR-EGFP (*Nat. Methods* **11**, 338–346, 2014; *Nat. Neurosci.* **20**, 1796–1806, 2017) (green; bottom; 475/34 nm Ex and 525/50 nm Em). Scale bar, 50  $\mu$ m. **(b)** Representative single trial traces for single neurons (as in **a**;  $n = 45$  and 93 neurons for NIR-GECO1 and NIR-GECO1 + CoChR-EGFP, respectively, from two cultures) illuminated with 562/40 nm (orange arrows) or 475/34 nm (blue arrows) at indicated light intensities with 200-ms duration per pulse. **(c)** Quantification of NIR-GECO1 fluorescence changes in response to activation of CoChR under the conditions described in **b** ( $n = 45$  and 93 neurons for NIR-GECO1 and NIR-GECO1 + CoChR-EGFP, respectively, from 2 cultures). Box plots with notches are used as described in Fig. 1g. **(d)** Image of cultured rat hippocampal neurons expressing CheRiff-EGFP (*Nat. Methods* **11**, 825–833; 2014) (green, 480 nm Ex and 525/36 nm Em) and NIR-GECO1 (magenta, 640 nm Ex and 705/50 nm Em). CheRiff is localized to the plasma membrane, whereas NIR-GECO1 fills the cytoplasm and nucleus of the neurons. Scale bar, 20  $\mu$ m. **(e)** NIR-GECO1 fluorescence traces from 4 neurons, indicated with correspondingly colored arrows in **d**, in response to optical stimulation. Blue bar indicates a 10-ms blue light (490/20 nm at 4 mW/mm<sup>2</sup>) illumination.



**Supplementary Figure 14**

Additional representative single-cell traces for multiplexed imaging of MIN6  $\beta$ -cells.

Conditions are identical to those described for Fig. 3g. A video of the cell shown in panel **d** is provided as Supplementary Video 3.

**Supplementary Table 1.** Spectral, photochemical and biochemical properties of NIR-GECO1 in comparison with iRFP682, miRFP, GCaMP6s and GCaMP3.

Protein	[Ca <sup>2+</sup> ] (mM)	Ex (nm)	Em (nm)	EC (×10 <sup>3</sup> mM <sup>-1</sup> cm <sup>-1</sup> )	QY (%)	Photost ability t <sub>1/2</sub> <sup>a</sup> (s)	pK <sub>a</sub>	Dynamic range <sup>b</sup>	Hill coeff. (n)	K <sub>d</sub> (nM)	k <sub>off</sub> (s <sup>-1</sup> )
NIR-GECO1	0 <sup>e</sup>	678	704	62	6.3	480	6.03	8×	1.03	215	1.93
	5	678	704	20	1.9		4.68				
iRFP682 <sup>d</sup>	N/A	670	682	69	11.3	1860 <sup>e</sup>	4.6	N/A	N/A	N/A	N/A
miRFP <sup>d</sup>	N/A	674	703	92	9.7	2040 <sup>e</sup>	4.3	N/A	N/A	N/A	N/A
GCaMP6s	0 <sup>e</sup>	498	515	4.5	ND	ND	9.77	30×	2.4	144 <sup>f</sup>	1.08
	5	498	512	73.4	61		6.00				
GCaMP3 <sup>g</sup>	0 <sup>e</sup>	496	513	ND	ND	ND	8.40	13×	2.1	405	ND
	1	496	513	37.0	65		6.97				

Abbreviations: Ex, fluorescence excitation maximum; Em, fluorescence emission maximum; EC, extinction coefficient; QY, quantum yield; t<sub>1/2</sub>, half-time; pK<sub>a</sub>, pH corresponding to 50% of the maximal fluorescence brightness measured at optimal pH; K<sub>d</sub>, K<sub>d</sub> for Ca<sup>2+</sup>; k<sub>off</sub>, Ca<sup>2+</sup>-dissociation kinetics measured by stopped-flow spectrometer; N/A, not applicable. ND, not determined.

<sup>a</sup>Measured in cultured neurons under continuous 631/28 nm wide-field illumination at 38 mW/mm<sup>2</sup>.

<sup>b</sup>F (zero free Ca<sup>2+</sup>)/F (~39 μM free Ca<sup>2+</sup>) for NIR-GECO1 and F (~39 μM free Ca<sup>2+</sup>)/F (zero free Ca<sup>2+</sup>) for GCaMP6s. NIR-GECO1 is not completely saturated in 39 μM free Ca<sup>2+</sup>. The value of F (zero free Ca<sup>2+</sup>)/F (5 mM Ca<sup>2+</sup>) is 10.6.

<sup>c</sup>In presence of 10 mM EGTA (zero free Ca<sup>2+</sup>).

<sup>d</sup>Data from Ref. 1.

<sup>e</sup>Extrapolated using the data shown in **Fig. 1h**.

<sup>f</sup>Data from Ref. 2,3.

<sup>g</sup>Data from Ref. 4.

### **Supplementary Note 1: Rationale for a non-permuted indicator topology.**

The primary challenge of designing a single FP-based GEI is to engineer an allosteric connection between a  $\text{Ca}^{2+}$ -dependent conformational change (e.g., by calmodulin (CaM)<sup>5</sup>, interaction of CaM and a  $\text{Ca}^{2+}$ -CaM-binding peptide (CBP)<sup>2,6</sup>, or troponin C (TnC)<sup>7</sup>), into a change in the FP fluorescence. Achieving this goal requires that the  $\text{Ca}^{2+}$ -binding domain be in close proximity to the FP chromophore, whether it is the autogenically synthesized chromophore of a  $\beta$ -FP, or the bound BV of a BV-FP. In the case of  $\beta$ -FPs, this has been achieved by either fusing CaM and the CBP to the termini of the protein that has been circularly permuted such that the termini are in close proximity to the chromophore<sup>2,6</sup>, or by directly inserting the  $\text{Ca}^{2+}$ -binding domain into  $\beta$ -FP at a position close to the chromophore<sup>5,7</sup>. Single FP-based  $\text{Ca}^{2+}$  indicators with both circularly permuted (i.e.,  $\text{Ca}^{2+}$ -sensing domains fused to the termini of a circularly permuted FP) and non-circularly permuted (i.e., a  $\text{Ca}^{2+}$ -sensing domain inserted into an FP) topologies have been reported. Examples of circularly permuted indicators include GCaMP<sup>2,3</sup>, Pericam<sup>6</sup>, R-GECO1 (Ref. 8), RCaMP1 (Ref. 9), and K-GECO1 (Ref. 10) and derivatives thereof<sup>11-15</sup>. There are fewer examples to date of non-circularly permuted indicators, with camgaroo<sup>5</sup> and NTnC<sup>7</sup> serving as prototypical examples.

While the apparent success of the circularly permuted design suggests that it would be a good basis for designing a BV-FP GEI, we chose to pursue a non-circularly permuted design based on  $\text{Ca}^{2+}$ -binding domain insertion. There were two reasons for choosing this design. The first reason is that we have found that some circularly permuted indicators can be converted to non-permuted topologies, with minimal impact on their function. For example, non-circularly permuted iGluSnFR ( $\text{G}^{\text{np}}$ -iGluSnFR) retains a fluorescence response and glutamate affinity that is very similar to iGluSnFR<sup>16</sup>. The second reason is that the N- and C-termini of BV-FPs are  $\sim 33$  Å from each other (vs.  $\sim 24$  Å for GFP) suggesting that a particularly long linker would be required to join the termini in a circularly permuted variant.

We suspect that the non-circularly permuted topology, in which the critical, and biologically promiscuous, CaM domain is genetically linked at both termini, may have two key advantages relative to a circularly permuted (i.e., GCaMP-type) topology. In a circularly permuted topology, the CaM is fused at one terminus and thus may be more accessible for interaction with endogenous protein binding partners leading to perturbations of normal cell biology. The first advantage is that the non-circularly permuted topology leaves the original N- and C-termini of

the FP available for genetic fusion to other proteins of interest or targeting motifs. In contrast to the circularly permuted topology, where the N- and C-termini are associated with RS20 and CaM, respectively, fusion to the normal FP termini is less likely to adversely affect the performance of the indicator itself.

### **Supplementary Note 2: Methods for two-photon spectral measurements.**

Two-photon spectra and cross sections were measured using femtosecond excitation of fluorescence relative to known standards. The optical setup consists of a tunable femtosecond laser (DeepSee, InSight) coupled with a PC1 ISS fluorometer operating in photon-counting mode. The sample solution was continuously stirred in a 1 cm cuvette (Starna), and the laser beam was focused onto the sample with an achromatic lens ( $f = 60$  mm, Qioptiq) close to the edge of the cuvette ( $\sim 1$  mm) to minimize the effects of solvent absorption. LDS798 (Exciton) in slightly alkaline  $\text{CDCl}_3$  was used to correct for the two-photon spectral shape<sup>17</sup>. LDS798 in  $\text{CHCl}_3$  served as the standard for two-photon cross section measurements<sup>17</sup>. Fluorescence of both the sample and the standard was excited at 1000 nm and recorded with the PC1 ISS monochromator at 720 nm. To eliminate possible errors resulting from independent measurements of the ECs and optical densities of dilute solutions, the Strickler-Berg approach was used to calculate the cross sections, using Equation 9 in the Supplementary Information of Ref. 18. This approach relies on the fluorescence lifetime ( $\tau$ ) of the sample and the QY and EC of the two-photon standard (LDS798 in  $\text{CHCl}_3$ ,  $\text{EC} = 41,000 \text{ M}^{-1}\text{cm}^{-1}$ )<sup>17</sup>. Rose Bengal (Sigma Aldrich) in MeOH served as a lifetime standard ( $\tau = 0.519$  ns)<sup>19</sup>. The fluorescence lifetimes of the samples were measured with the digital frequency domain technique (ChronosDFD, ISS) implemented with the PC1 ISS fluorometer (NIR-GECO1  $\text{Ca}^{2+}$ -saturated  $\tau = 0.48$  ns,  $\text{Ca}^{2+}$ -free  $\tau = 0.42$  ns). Fluorescence was excited at 450 nm with a diode laser and recorded through a 700/13 bandpass filter. The fluorescence QY of LDS798 in  $\text{CHCl}_3$  was measured with an integrating sphere (Quantaaurus-QY Absolute PL quantum yield spectrometer, Hamamatsu) (QY = 0.16; 640 nm Ex).

As shown in **Fig. 3a**, two-photon absorbance spectrum of NIR-GECO1 is similar to that of other iRFPs<sup>20</sup>. That is, the cross-sectional value for the Soret band at  $<950$  nm (50-75 GM) is substantially larger than for the Q band at  $\sim 1255$  nm ( $<27$  GM)

### **Supplementary Note 3: Methods for *in vivo* two-photon microscopy.**

*AAV injection protocol.* For two-photon *in vivo* imaging for **Supplementary Fig. 12f** we expressed NIR-GECO1 in the mouse cortex via AAV and installed a chronic head plate with optical window above the corresponding brain area. Anesthesia was induced using isoflurane (induction, 3%; maintenance, 1-2%). We administered meloxicam (2 mg/kg i.p.) and slow-release buprenorphine (1 mg/kg) as analgesics. After animals were placed in a stereotaxic frame (Kopf Instruments), sterile eye lubricant (Puralube, Fisher Scientific) was administered to prevent corneal drying, and a heating pad was used to maintain body temperature. The scalp was opened using a midline incision, and the region to be imaged (primary visual cortex) was identified using stereotaxic coordinates (2.5 mm anterior to bregma, 2.55 mm lateral from the midline). A small craniotomy was opened in the skull using a 0.5-mm burr (Fine Science Tools) and a high-speed hand dental drill. The AAV (AAV2/9-hSyn1-NIR-GECO1, 500 nL) was injected 200  $\mu$ m beneath the surface of the brain at a rate of 150 nL/min using a Nanofil syringe (World Precision Instruments) with a 33 G beveled needle (World Precision Instruments) and pump (World Precision Instruments). After the injection, the needle was kept in place for two minutes to allow time for diffusion of the virus prior to removing the needle from the brain. The scalp was closed using Vetbond.

*Cranial window surgery.* We allowed animals to recover from AAV injection surgeries before placing cranial windows. Anesthesia was induced using isoflurane (induction, 3%; maintenance, 1-2%). We administered meloxicam (2 mg/kg i.p.) and slow-release buprenorphine (1 mg/kg) as analgesics. After animals were placed in a stereotaxic frame (Kopf Instruments), sterile eye lubricant (Puralube, Fisher Scientific) was administered to prevent corneal drying, and a heating pad was used to maintain body temperature. Scalp fur was trimmed and a small circular section of skin (~1 cm in diameter) was excised using surgical scissors (Fine Science Tools). The periosteum was removed using fine forceps (Fine Science Tools). A custom-made circular head plate was attached to the skull using dental cement (C&B Metabond, Parkell Inc.) and centered around the region to be imaged. The head plate was then screwed into a custom-built fork fixed to a solid metal base.

Under a continuous gentle flow of phosphate-buffered saline (137 mM NaCl, 27 mM KCl, 10 mM phosphate buffer), a ~4-mm circular section of the skull, slightly larger than the window and centered over the injection site, was removed using a 0.5-mm burr (Fine Science Tools) and a high-speed hand dental drill, taking great care not to compress brain tissue or damage the

underlying vasculature. Sterile sugi swabs (John Weiss & Son, Ltd) were used to absorb trace bleeding. A 3-mm glass coverslip (Warner Instruments) was gently placed over the brain. Veterinary adhesive (Vetbond, Fisher Scientific) was used to form a seal between the coverslip and the skull. A layer of Metabond was then applied for added durability. Meloxicam (2 mg/kg i.p.) was administered as an analgesic 24 hours after surgery, and as needed thereafter. After allowing two weeks for expression, we imaged NIR-GECO1 in anesthetized, head-fixed mice using the two-photon microscope described in **Online Methods**.

#### **Supplementary Note 4: Methods for *in vivo* mesoscale imaging.**

*AAV injection protocol.* Four-week-old athymic female nude mice (Envigo, New Jersey, USA; stock number *Foxn1*<sup>tm069</sup>) were injected with one of the following: 3  $\mu$ L of AAV2/9-hSYN1-NIR-GECO1 virus at a concentration of  $10^{13}$  genome copies/mL (Neurophotonics Centre, Université Laval, Canada); 3  $\mu$ L of AAV2-hSyn1-miRFP virus at a concentration of  $10^{12}$  genome copies/mL (UNC Vector core facility); or 3  $\mu$ L of Dulbecco's Phosphate Buffered Saline solution (PBS) (D8357, Sigma-Aldrich, Taufkirchen, Germany). For analgesia, mice were administered a single oral drop of a 125 mg/mL Metamizole solution (Novalgine®, Sanofi-Aventis Deutschland GmbH, Frankfurt am Main, Germany) directly before and 4 hours after the injection. Anesthesia was induced via isoflurane (Isothesia®, Henry Schein®, NY, USA) at 3% v/v in 100% O<sub>2</sub>. The mouse was placed into a custom head holder (SGM-4, Narishige International Limited, London, United Kingdom) connected to an anesthesia unit (Sigma Delta Vaporize, Penlon, UK). This head holder employs three points of fixation to hold the head in place: the incisors are placed into an opening in the metal holder, an anesthesia mask then covers the nose and an ear bar is placed into respective ears. Fixation in this way allows for easy access to the top of the head whilst allowing adjustment of head height, tilt and rotation. All of this is achieved without the need for implantation of external components on the skull of the mouse<sup>21</sup>. Once correctly positioned, a small incision was made down the middle of the scalp using a scalpel. Both sides of the scalp were pulled aside to allow access to the skull. Hemostatic sponges (Gelfoam®, Pfizer Pharmaceutical, NY, USA) were used to contain any bleeding during the procedure. A hole approximately 1 mm in diameter was carefully drilled into the skull, above the primary somatosensory cortex hind limb region (S1HL), using a micro-drill (110-4103, CircuitMedic, MA, USA). This hole was used to inject virus into the brain. Injections were carried out via a

glass capillary connected to a wireless nanoinjector (Neurostar, Tuebingen, Germany). To consistently inject into S1HL<sup>22</sup>, the capillary was placed above bregma, defining this point as 0 for all axes. Then the capillary was moved using a joystick to the aforementioned drilled hole and lowered to the entry of the hole. The injection site was located at 0.02 mm anterior to bregma and 2 mm from the midline. From here the capillary was lowered 1.4 mm into the brain at a rate of 0.2 mm/s. Once at the required depth, the capillary was retracted 100  $\mu$ m to an injection depth of 1.3 mm. Injection of the virus was carried out at this location (S1HL region) at a rate of 2.5 nL/s. Five minutes after the injection was completed the capillary was retracted from the brain. The hole in the brain was sealed using adhesive luting cement (S380, Parkell Inc., NY, USA). The scalp was closed via suturing and tissue glue (Histoacryl<sup>®</sup>, Braun, Germany). For all experiments, the physiologic status of the mice including heart rate, body temperature and blood oxygenation were constantly monitored using the PhysioSuite<sup>®</sup> physiological monitor (Kent Scientific, Torrington, CT, USA). A rectal thermometer and a feedback-controlled heating pad were used to ensure the body temperature of the mice were constant and at a physiological condition (PhysioSuite<sup>®</sup>, Kent Scientific, Torrington, CT, USA). During surgical procedures anesthesia was maintained using isoflurane at a concentration of 1.0% to 1.5% v/v in 100% O<sub>2</sub> with a flow rate of approximately 0.7 L/min. After the surgery mice were closely monitored for signs of pain and when needed were treated with another drop of Metamizole. All mice removed stitches themselves once the tissue glue had dissolved after 3 days.

*Electrical Hindpaw Stimulation.* Stainless steel needle electrodes were connected to the mouse paw by carefully inserting them under the skin of the foot pad. The electrodes were connected to a World Precision Instruments Stimulus Isolator (A365, World Precision Instruments, FL, USA). In all cases the applied voltage was set to 0.5 mA. The entire experiment was started via an external trigger that ensured the synchronization of the image acquisition and the paw stimulus. The outputs of the paw stimulus generator were connected to the electrodes in the paw of the mouse via a BNC cable. For single paw stimuli, a 50 ms electrical pulse was applied once every 25 s, at t = 5 s. For stimulation trains 10 pulses with a 20 ms on and 50 ms off duration were applied every 25 s, at t = 5 s. For both paradigms this allowed the first 5 s of the cycle to be used for baseline activity determination. In both cases the stimulation paradigm was repeated every 25 seconds (1 cycle) for a total of 20 cycles. The fluorescence recording was synchronized with the paw stimulation via the initial trigger. Anesthesia levels were kept at 1-1.2% isoflurane v/v in

occurs. For all stimulation paradigms of the 20 stimulation cycles the first was removed and the remaining 19 were averaged into a single cycle. Background subtraction was then carried out across the cycle from a 50×50 pixel region of interest (ROI) outside the fluorescent area. The images were smoothed using the `imfilter` function in Matlab with a kernel size of 25. Due to the photobleaching of the protein the entire cycle was detrended using linear detrending on a pixel by pixel basis. Next,  $\Delta F/F_0$  values were determined by dividing the entire cycle by the baseline activity which was defined from a 50×50 pixel region of interest (ROI) from the first 5 seconds of the cycle. The cycle was multiplied by 100 to get the change values in %. The response of the protein across the averaged cycle was calculated from an averaged 50×50 pixel ROI within the fluorescent area. A low pass filter was applied to all traces. For *in vivo* mesoscale activation figures and videos, manual segmentation was applied to highlight the injected brain hemisphere.

**Supplementary Note 5: Number of times experiments were repeated independently with similar results.**

**Fig. 1c:** Representative of  $n > 3$  independent experiments.

**Fig. 1d:** Representative of  $n > 3$  independent experiments.

**Fig. 2a:** Representative of  $n = 4$  slices from 2 mice.

**Fig. 2c:** Representative of  $n = 129$  neurons from 1 slice from 1 mouse.

**Fig. 2f:** Mean response data from a single mouse as shown in **Fig. 2e**. Representative of  $n = 3$  mice (independent repeats).

**Fig. 2g:** Mean response data from a single mouse as shown in **Fig. 2e**. Representative of  $n = 3$  mice (independent repeats).

**Fig. 3a:** Representative of  $n > 3$  independent experiments for 1-photon spectra (identical to **Fig. 1c**).  $n = 2$  independent experiments for 2-photon spectra.

**Fig. 3b:** Representative of  $n = 2$  cultures.

**Fig. 3c:** Representative of  $n = 32$  neurons from 2 cultures.

**Fig. 3d:** Representative of  $n > 3$  independent experiments (identical to **Fig. 1c**).

**Fig. 3e:** Representative of  $n = 9$  slices from 2 mice.

**Fig. 3f:** Representative of  $n = 9$  slices from 2 mice.

**Fig. 3g:** Data is representative of 11 cells from 8 independent experiments with similar results. Four additional examples are provided in **Supplementary Fig. 14**.

**Fig. 3h:** Data is representative of  $n = 2$  independent cultures.

**Fig. 3i:** Representative of  $n = 271, 178, 331$  neurons for GCaMP6f, RCaMP1.07, NIR-GECO1, respectively, from 2 cultures.

**Supplementary Fig. 5d:** Repeated independently more than 3 times with similar results.

**Supplementary Fig. 6b:** Data is the mean value of  $n = 5$  replicates from one experiment.

**Supplementary Fig. 7a:** Representative of  $n = 39$  neurons for NIR-GECO1+BV and  $n = 51$  neurons for NIR-GECO1.

**Supplementary Fig. 7c:** Representative of  $n = 15$  neurons for both NIR-GECO1 and NIR-GECO1-T2A-HO1.

**Supplementary Fig. 8a:** Repeated independently 55 times with similar results (see **Fig. 1i-l**).

**Supplementary Fig. 8b:** Representative of  $n = 4$  slices from 2 mice.

**Supplementary Fig. 8c:** Data is Representative of  $n = 6$  neurons from 4 mice.

**Supplementary Fig. 9e:** Representative of  $n = 5$  neurons from 2 cultures.

**Supplementary Fig. 9f:** Representative of  $n = 5$  neurons from 2 cultures.

**Supplementary Fig. 10a:** Single image representative of  $n = 3$  PBS injected mice (2 injected on the RHS and 1 injected on the LHS) or  $n = 3$  mice expressing NIR-GECO1 (1 injected on the RHS and 2 injected on the LHS).

**Supplementary Fig. 10c:** Mean response data from a single mouse as shown in **Fig. 10b**. Representative of  $n = 3$  mice (independent repeats).

**Supplementary Fig. 10d:** Mean response data from a single mouse as shown in **Fig. 10b**. Representative of  $n = 3$  mice (independent repeats).

**Supplementary Fig. 11a:** Single images representative of  $n = 3$  PBS injected mice,  $n = 3$  mice expressing NIR-GECO1,  $n = 3$  mice expressing GCaMP6s,  $n = 3$  mice expressing mRFP and  $n = 8$  FoxN1 nude mice under LED illumination (same mice as used for viral or PBS injections).

**Supplementary Fig. 11b:** Mean response data from  $n = 3$  NIR-GECO1 expressing mice (shown in **Fig. 2e**) and  $n = 3$  GCaMP6s mice (independent repeats).

**Supplementary Fig. 11c:** Mean response data from  $n = 3$  NIR-GECO1 expressing mice (shown in **Supplementary Fig. 10b**) and  $n = 3$  GCaMP6s mice (independent repeats).

**Supplementary Fig. 12b:** Representative of  $n = 184, 106,$  and  $77$  cells, respectively, from one culture.

**Supplementary Fig. 12c:** Representative of  $n = 4$  neurons from 2 cultures.

**Supplementary Fig. 12d:**  $n = 184, 106,$  and  $77$  cells, respectively, from one culture.

**Supplementary Fig. 12e:** Representative of  $n = 2$  slices from one mouse.

**Supplementary Fig. 12f:** Representative of  $n = 3$  field of view from 1 mouse.

**Supplementary Fig. 13a:** Representative of  $n = 45$  and  $93$  neurons for NIR-GECO1 and NIR-GECO1 + CoChR-EGFP, respectively, from two cultures.

**Supplementary Fig. 13b:** Representative of  $n = 45$  and  $93$  neurons for NIR-GECO1 and NIR-GECO1 + CoChR-EGFP, respectively, from two cultures.

**Supplementary Fig. 13d-e:** Repeated more than 10 times with similar results.

**Supplementary Fig. 14a-d:** Data is representative of 11 cells from 8 independent experiments with similar results. One additional example is provided in **Fig. 3g**.

**Supplementary Videos 1:** Mean response data from a single mouse as shown in **Fig. 2e**. Representative of  $n = 3$  mice (independent repeats).

**Supplementary Video 2:** Mean response data from a single mouse as shown in **Supplementary Fig. 10b**. Representative of  $n = 3$  mice (independent repeats).

**Supplementary Video 3:** Data is representative of 11 cells from 8 independent experiments with similar results.

**Supplementary Video 4:** Data is representative of  $n = 271, 178, 331$  neurons for GCaMP6f, RCaMP1.07, NIR-GECO1, respectively from 2 cultures.

### Supplementary References

1. Piatkevich, K.D. et al. *Nat. Chem. Biol.* **14**, 352-360 (2018).
2. Nakai, J., Ohkura, M. & Imoto, K. *Nat. Biotechnol.* **19**, 137-141 (2001).
3. Chen, T.-W.W. et al. *Nature* **499**, 295-300 (2013).
4. Akerboom, J. et al. *J. Neurosci.* **32**, 13819-13840 (2012).
5. Baird, G.S., Zacharias, D.A. & Tsien, R.Y. *Proc. Natl. Acad. Sci. U. S. A.* **96**, 11241-11246 (1999).
6. Nagai, T., Sawano, A., Park, E.S. & Miyawaki, A. *Proc. Natl. Acad. Sci. U. S. A.* **98**, 3197-3202 (2001).
7. Barykina, N.V. et al. *Sci. Rep.* **6**, 34447 (2016).
8. Zhao, Y. et al. *Science* **333**, 1888-1891 (2011).
9. Akerboom, J. et al. *Front. Mol. Neurosci.* **6**, 2 (2013).
10. Shen, Y. et al. *BMC Biol.* **16**, 9 (2018).
11. Ohkura, M., Sasaki, T., Kobayashi, C., Ikegaya, Y. & Nakai, J. *PLoS One* **7**, e39933 (2012).
12. Wu, J. et al. *ACS Chem. Neurosci.* **4**, 963-972 (2013).
13. Inoue, M. et al. *Nat. Methods* **12**, 64-70 (2014).
14. Wu, J. et al. *Nat. Commun.* **5**, 5262 (2014).
15. Dana, H. et al. *Elife* **5**, e12727 (2016).
16. Wu, J. et al. *ACS Chem. Biol.* **13**, 1832-1837 (2018).
17. Makarov, N.S., Campo, J., Hales, J.M. & Perry, J.W. *Opt. Mater. Express, OME* **1**, 551-563 (2011).
18. Drobizhev, M., Makarov, N.S., Tillo, S.E., Hughes, T.E. & Rebane, A. *Nat. Methods* **8**, 393-399 (2011).
19. Lakowicz, J. R. *Principles of Fluorescence Spectroscopy* 3<sup>rd</sup> edn (Springer, Berlin, 2006).
20. Piatkevich, K.D. et al. *Biophys. J.* **113**, 2299-2309 (2017).
21. Gottschalk, S., Fehm, T.F., Deán-Ben, X.L. & Razansky, D. *J. Cereb. Blood Flow Metab.* **35**, 531-535 (2015).
22. Franklin, K.B. & Paxinos, G. *The mouse brain in stereotaxic coordinates, compact. The coronal plates and diagrams* 3<sup>rd</sup> edition (Amsterdam: Elsevier Academic Press: 2008).

## 5 Conclusion and Outlook

The goal of this dissertation was to volumetrically image large scale electrophysiology in scattering tissues with 5D OAT. Due to the optically scattering nature of the brain, it was determined that imaging neuronal communication within the mouse brain in real time would serve as an ideal model for this problem which, if successful would have large implications for brain imaging as a whole. 5D OAT when imaging the brain, is referred to as FONT, and currently serves the most applicable method for brain imaging in murine research. FONTs strengths allow it to bridge the gaps between high resolution small FOV microscopy and large FOV low resolution MRI.[1] The inherent advantages of optical contrast with the resolution and depth penetration of US provided by OAT were employed to advance neuroimaging with FONT. Initially, the ability of the FONT system to image an entire mouse brain *ex vivo* was investigated.

In Chapter 2, a rapidly prototyped 3D printed chamber was designed and adapted to optimize the placement of fibers for a uniform illumination profile across the FOV of the system.[2] This showed that given the correct setup, FONT can readily image an entire murine brain and heart with a single laser pulse providing a wealth of anatomical information. The resolution of the system was proven to be isotropic at 150  $\mu\text{m}$  across the entire FOV. Whilst used for *ex vivo* brain imaging, this system will likely have other robust imaging applications where uniform illumination is required e.g., Langendorff imaging or histology imaging.[3, 4] This system laid a strong foundation for scattering tissues imaging with sufficient resolution and FOV for whole-brain imaging. However, this was only suitable for anatomical imaging and the system's ability to image functional responses needed to be investigated. Due to the limited access to the brains of mice, it may be worthwhile to develop a FONT system with integrated multiple fiber ports along the cup or a mouse head holder with integrated illumination points, in line with the suggestions made in Chapter 2.

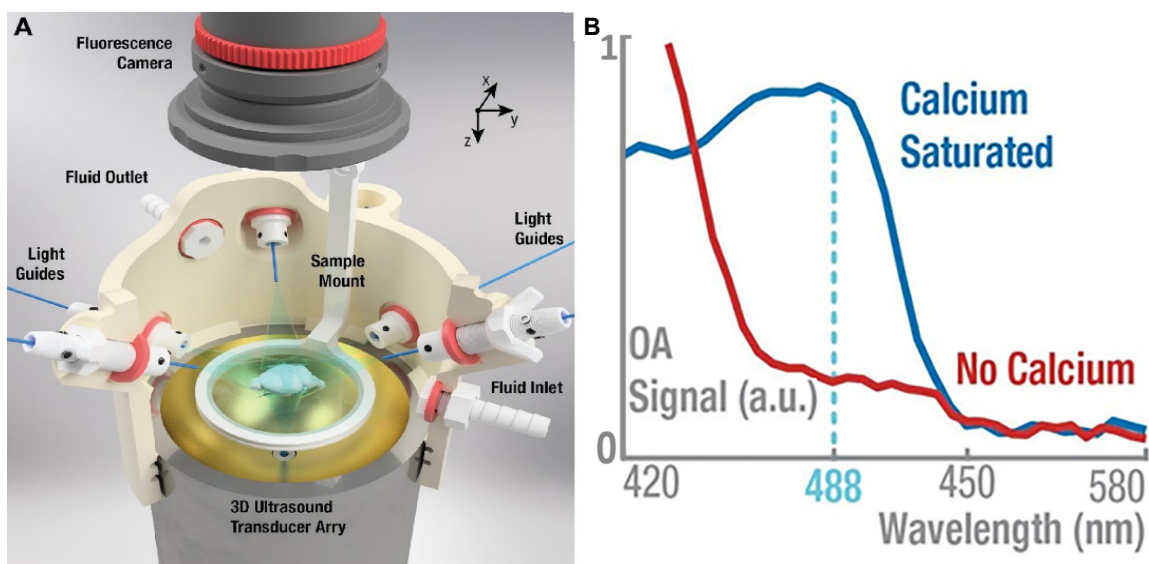


**Figure 5.1 Schematic of the experimental setup and process.** A) Adaptation of the system outlined in chapter 2 for the successful perfusion of the brain along with simultaneous recording of fluorescence and OAT data. B) The GCaMP6f OAT spectrum of the calcium free and calcium bound forms of the protein. Image adapted from [5], © Springer Nature, 2019.

A similar FONT system to that used in this work had shown promise in imaging GCaMP5g in zebrafish.[6] Considering the development of GCaMP6 since then, it was decided to use the transgenic GCaMP6f line for testing.[6] GCaMP6f enables the direct monitoring of electrophysiological activity via calcium activity, one of the main components of neuronal signaling.[7] To ensure the sensitivity of FONT, isolated GCaMP6f protein both calcium bound and calcium free was imaged with a clear difference in the detected FONT response between both states, as shown in Figure 5.1. The system developed in Chapter 2 was further modified with pumps to provide ACSF to sustain an extracted mouse brain. The brain remained functional for a period of time long enough to stimulate activity via PTZ. Brains from transgenic mice expressing GCaMP6f were extracted and shown to be viable over enough time to carry out the experiment. This is in many ways like a Langendorff setup but instead relies on passive superfusion. Elicited responses are shown in Figure 5.2, from a co-authored paper. Other work has extracted and sustained brains *ex vivo* for extended periods of time however, such methods used larger organisms than mice easing the required microsurgery on vessels.[8]

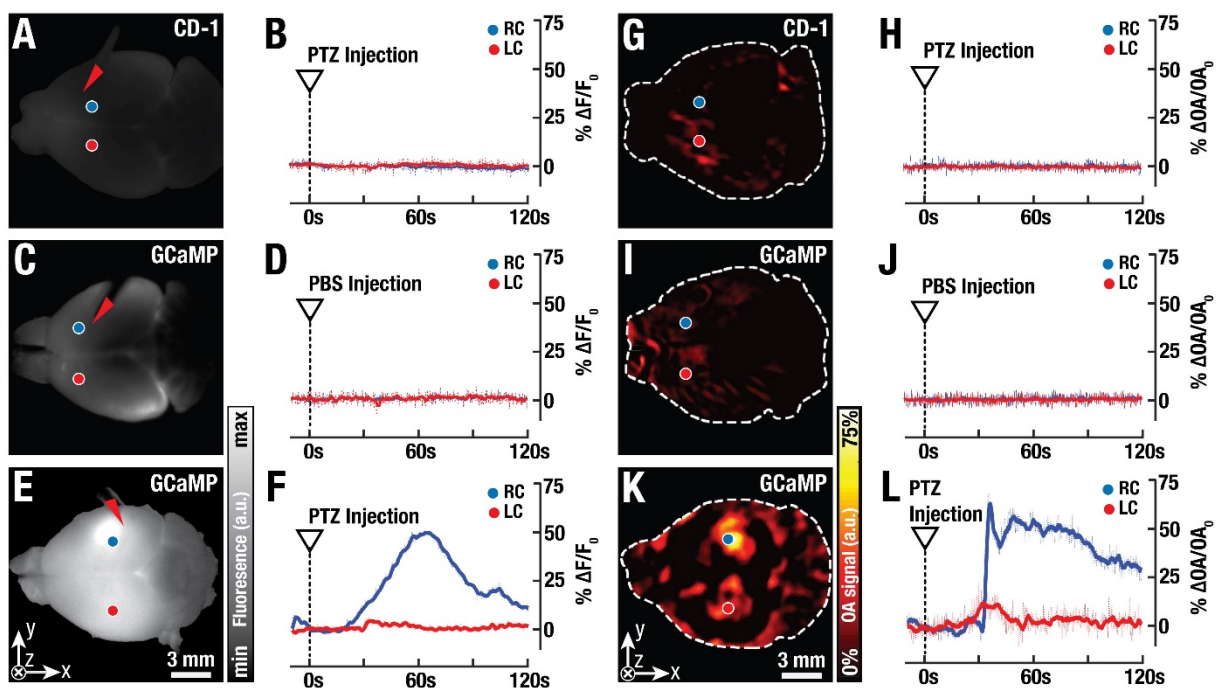


**Figure 5.2 Comparative responses in both fluorescence and FONT for all brains in response to PTZ injection.** A) Wide field fluorescence of an isolated CD-1 mouse brain. B) Corresponding time traces of activity in the brain showing no fluorescence changes. C) GCaMP6f brain showing higher background fluorescence levels. D) Corresponding fluorescence traces showing no increase in activity following PBS injection. E) Fluorescent image of a GCaMP6f brain at 40s post injection of PTZ. F) Resulting time trace following PTZ injection with changes of up to 50%. G) Slice of the CD1 brain from 1 mm deep. H) The OAT time trace with no change following the injection. I) 1 mm slice from a GCaMP6f brain that was injected with PBS. J) Corresponding time trace from the PBS injected GCaMP6f brain with no activity following the injection. K) Increases in GCaMP6f activity can readily be seen at a slice 1 mm deep within the brain (40s post injection of PTZ). L) Traces showing the direct increase of GCaMP6f activity in the FONT signals with responses up to 70%. Image adapted from [9], © Frontiers Media S.A, 2019.

The chamber providing uniform illumination was slightly adapted and arranged for simultaneous fluorescence and FONT imaging. An epileptic inducing drug (PTZ) was used to induce GCaMP6f transients in isolated brains with the evoked GCaMP6f response being readily detected by FONT.[9] Injections of PBS in GCaMP6f brains or in PTZ in WT brains

showed no response. The detected responses were simultaneously validated using fluorescence confirming that FONT could detect GCaMP6f activity in an isolated hemoglobin free brain. Activity could be detected at up to 1 mm deep in 3D and across the entire brain- far surpassing current fluorescent techniques. Whilst robust, this stimulation technique is difficult to optimize with PTZ having an all or nothing response.[10] What would be of interest in the future would be to combine this technique with other more controllable methods for neuronal stimulation. This could include electrical stimulation via electrode replacement but the electrode would likely lead to imaging artefacts.[11] However, optogenetic stimulation could provide a more localized, controlled and improved method of stimulation especially as the laser used for FONT could simply be tuned to excite the actuator.[12, 13]

Isolated (*ex vivo*) brain imaging provided a suitable platform with reduced variables to conclusively detect GCaMP6f with FONT, enabling large scale electrophysiology in scattering tissues with FONT. Based on this, it was determined that electrophysiology imaging would be more achievable *in vivo* in brains as opposed to hearts due to the inherent lack of motion. Before testing the system in an *in vivo* setting, the capability of FONT was investigated to image stimulus evoked hemodynamic activity, an indirect measure of electrophysiology. This was done to understand the influence hemodynamic activity could have on any GCaMP6 detected responses and possibly, how to eliminate or suppress them.[14] In comparison to MRI or fUS, FONT is capable of detecting all three hemodynamic components (HbR, HbO and HbT) and at a scale and depth surpassing optical imaging like DOT. Careful selection of the illumination wavelengths based on the molar extinction coefficient of hemoglobin ensured the multispectral (5D) unmixing of all components, which could then be individually monitored across the somatosensory cortex.[15, 16] A paw stimulation paradigm commonly used in fMRI along with suitable anesthesia settings readily evoked the hemodynamic response in four mice. The response was correlated to the hind-paw region of the somatosensory cortex.[16, 17] This was shown to be strongest on the contralateral side of the brain with the presence of an initial-dip in the hind-paw region. The initial-dip has and continues to be a contentious issue in neuroimaging, likely due to the fact that no other modality can image it in the same way FONT can.[18] As expected, the response (but no initial-dip) was also present in all other regions of the cortex but at a reduced or minimal level. Numerous components from the traces were analyzed with the peak percentage change showing the most significant difference over all other regions. HbR (the only component seen by fMRI) showed minimum specificity, highlighting the capabilities of FONT over comparable imaging methods.

Having shown the strength of FONT over current imaging methods for hemodynamic imaging, the ability of FONT to image GCaMP6f responses *in vivo* was investigated. For this, the same transgenic line that had shown success in the isolated brain experiments was used.[19] The experimental settings (especially the paw stimulation paradigm) to elicit the hemodynamic response in FONT imaging were determined. The evoked responses are shown in Figure 5.3. Based on the knowledge from the hemodynamic experiments a paw stimulation paradigm was developed to ensure that a minimal hemodynamic response was evoked whilst preserving the GCaMP6f response. Due to the physical constraints of the FONT system when used for *in vivo* imaging, FONT and fluorescence imaging were carried out sequentially. The evoked GCaMP6f responses were mapped in 3D *in vivo* using the current FONT system, successfully overcoming the high background hemoglobin absorption and the scattering of light problems faced by fluorescence.[5] Activity was detected at up to 1.5 mm deep, completely non-invasively surpassing current possibilities with fluorescence imaging and achieving direct electrophysiological imaging in a highly scattering tissue *in vivo*. The kinetics

of the protein were in line with fluorescent responses and in some cases, FONT detected a stronger response than those seen with fluorescence.[5, 9] This can be attributed to the fact that fluorescence imaging only detects a spatially averaged (across the Z axis) response but FONT can locate the responses in 3D. Additionally, FONT can differentiate between both forms of GCaMP6 (s and f) highlighting its sensitivity and spatiotemporal resolution.

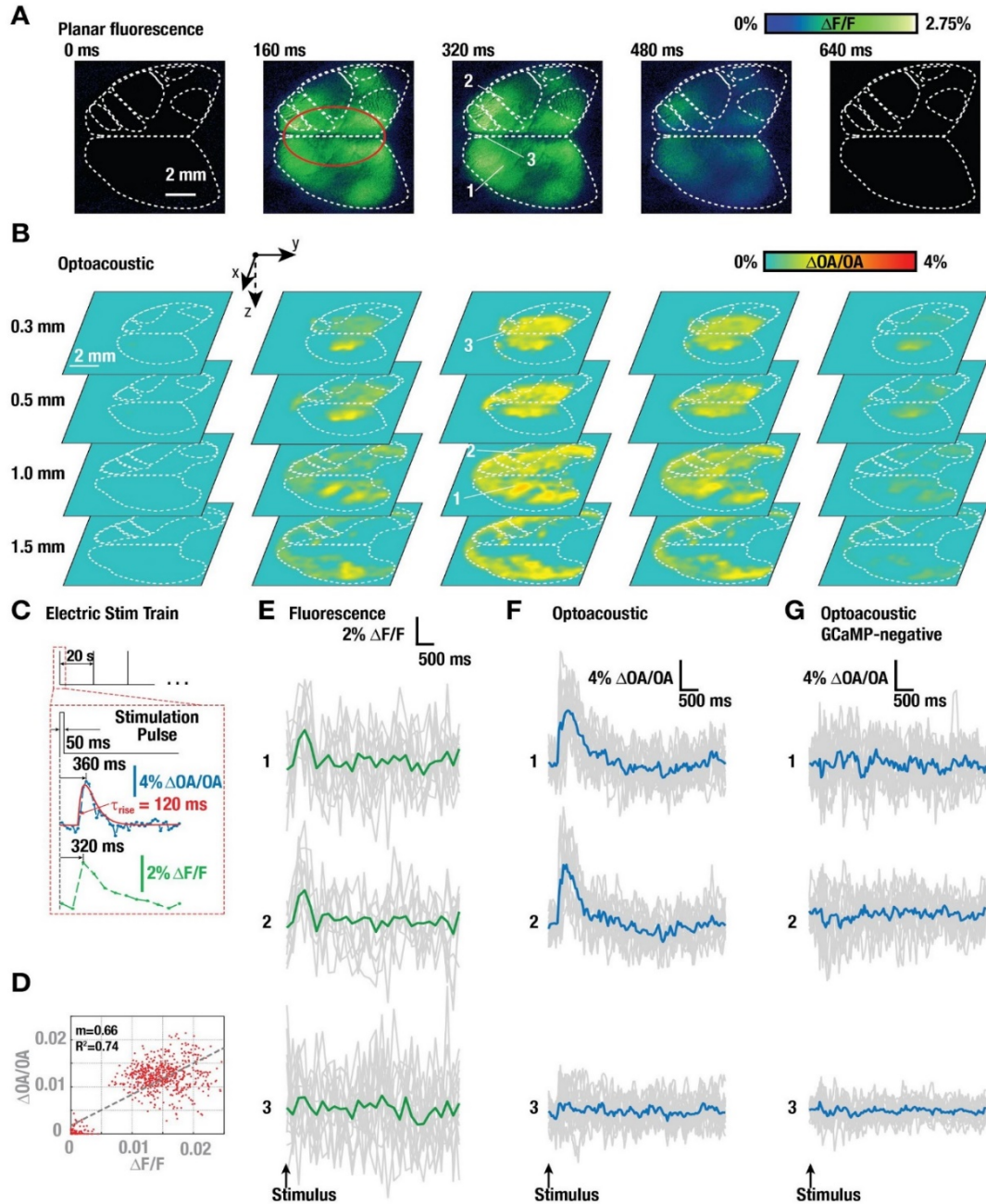


**Figure 5.3 Non-invasive *in vivo* imaging of electrical paw stimulus (somatosensory) evoked transients in the GCaMP6f-brain** A) Temporal *in vivo* maps of GCaMP6f fluorescence signals ( $\Delta F/F$ ) in response to the electrical stimulus at  $t=0$  (right hindpaw). Functional regions of the cortex are highlighted (dashed white lines). B) Temporal 4D FONT *in vivo* maps ( $\Delta OA/OA$ ) of elicited responses to the same stimulus at  $t=0$ . Transverse slices of the entire brain activity at depths of up to 1.5 mm (from the brain surface) are shown. Functional regions of the cortex are highlighted (dashed white lines). C) Illustration outlining the electrical paw stimulation paradigm to elicit *in vivo* responses. At 20 s intervals a single 50 ms stimulus of 0.5 mA was applied (top panel). Below, comparative single-voxel FONT (blue, 25 Hz) and single-pixel fluorescence (green, 6.25 Hz) GCaMP6f traces are shown.  $\tau_{rise}$  is defined as the

time between the 20<sup>th</sup> and 80<sup>th</sup> percentile of the maximum FONT signal. D) FONT voxel signals increase versus fluorescence pixel signals increases for set points within the red region in A) at 160, 320 and 640 ms. FONT signal increases were calculated from the MIP of all slices. The best fit (dashed line) was calculated using a least square method with  $m$  representing its slope and  $R^2$  representing the coefficient of determination. E) Fluorescence signal traces ( $\Delta F/F$ ) from three separate pixels post paw stimulation. Pixels were located within the contra- and ipsilateral primary somatosensory cortex (1 and 2) and the SSS (3). F) FONT signal traces ( $\Delta OA/OA$ ) from three separate voxels post paw stimulation within the contra- and ipsilateral primary somatosensory cortex and outside major vessels (1 and 2, ~1 mm deep) and the SSS (3). G) FONT signal traces ( $\Delta OA/OA$ ) post paw stimulation in GCaMP6f negative (wild type) mice for single voxels located similarly to those in in F). All traces underwent background subtraction and normalization and represent  $n = 4$  independent experiments in  $n = 3$  biologically independent animals for all panels. Image reproduced from [5], © Springer Nature.

The success of imaging globally expressed GCaMP6s/f with the FONT setup raised the question of the *in vivo* sensitivity of FONT. Therefore, to further test the sensitivity of FONT, sparsely labelled GCaMP6 mice were imaged using a slightly different FONT system (7 MHz as opposed to 5 MHz) at Prof. Shy Shoham's lab at NYU. Having helped to set up the system, it was tested and as expected it was found to have similar sensitivity and resolution (150  $\mu\text{m}$ ) to the 5 MHz FONT system in Munich. The original GCaMP6 detection was achieved with the Thy-1 promoter transgenic line, which generically express GCaMP across all excitatory neurons across the somatosensory cortex.[19] Sparsely labelled transgenic mice that only expressed GCaMP6 in either parvalbumin or somatostatin expressing interneurons were imaged with this system, representing an approximate 90% reduction in spatial expression. The system could detect sparsely labelled neuronal calcium activity from both GCaMP6s/f as shown in Figure 5.4. The delta was increased to levels like that seen in the isolated brain responses. This was attributed to the age at which these mice were imaged, the removal of the scalp and the increased expression levels driven by this genetic line (like that of viral expression). Responsive voxels and their kinetics were detected at up to 1.5 mm in depth also in line with the Thy-1 mice. The developed automated analysis with thresholding applied to every voxel accelerates the analysis process. Masking ensures that only responsive voxels remain. This also serves to remove the non-responsive vasculature from the images. The automated analysis used here will be useful for future FONT applications, where the analysis can be tweaked for proteins of differing kinetics. It is also greatly beneficial when analyzing sparsely labelled samples, where manual searching through the data would take significantly longer and is more prone to human error.

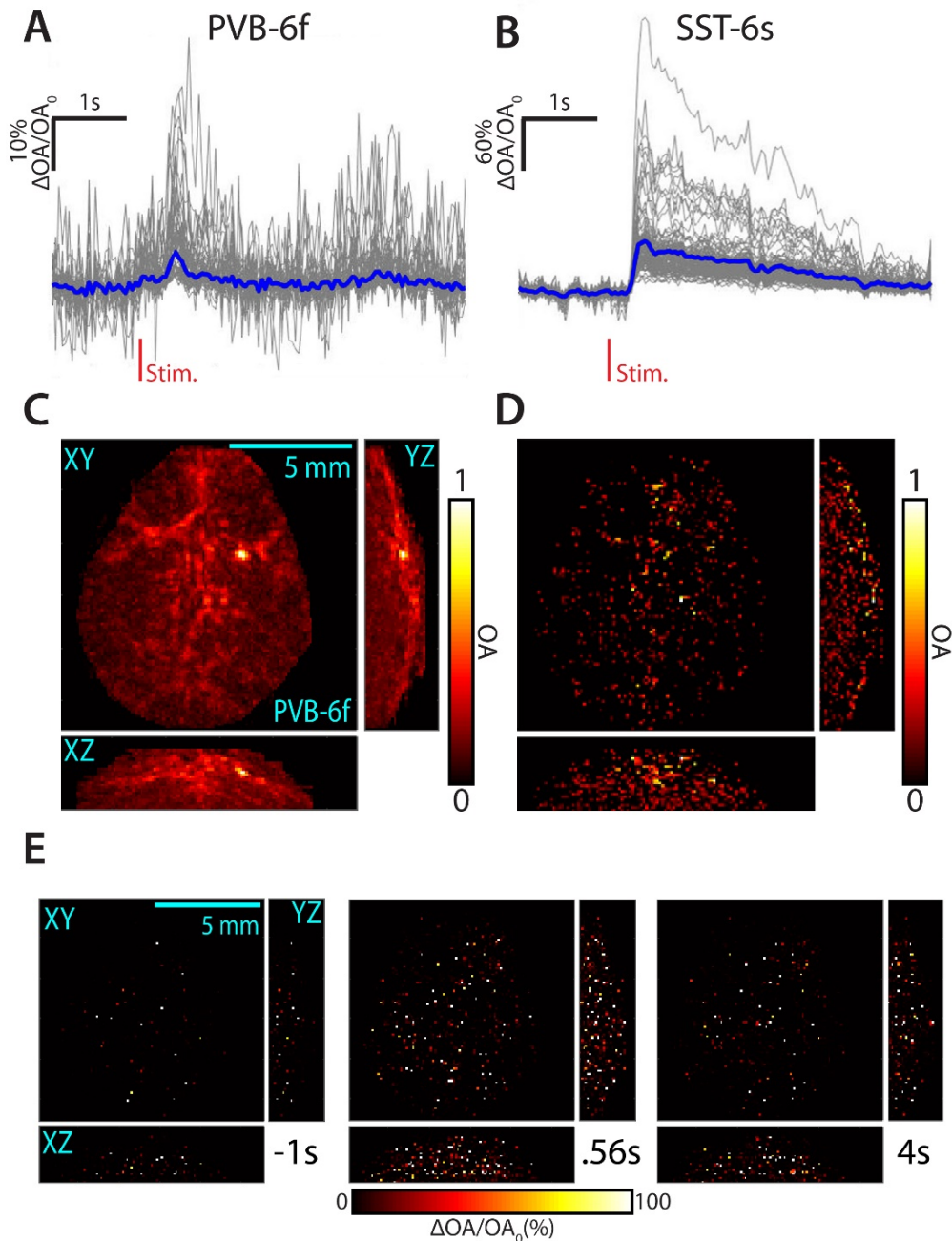


**Figure 5.4 Representative images of evoked responses in sparsely labelled GCaMP6f/s mice.** A) Evoked response in PVB-GCaMP6f mice ( $n = 1$  mouse, 977 responsive voxels). An upward spike of  $\sim 10\%$  in activity is seen 0.61s after paw stimulation. B) Evoked response in an SST-GCaMP6s expressing mouse with a significant spike of almost  $\sim 50\%$  after paw stimulation ( $n = 1$  mouse, 1037 responsive voxels). In both cases grey lines represent single voxel responses from all 19 respective trials and the blue line represents the mean trace of all responsive voxels. C) MIPs of PVB-6f mouse post manual segmentation in 3D. The segmentation was guided by the layer of glue (ring) on the surface of the brain. D) MIPs and location of all responsive voxels in C) post automated masking. All 19 cycles have been averaged into a single cycle. E) Delta activation map of responsive voxels in D). Left, 1s before stimulation. Middle, 0.56s post stimulation (peak). Right, 4s post activation.

The main limitation for FONT imaging is not a lack of sensitivity but rather a lack of an optimized sensor. There is a need for a GEVI that is suitable for FONT imaging and a GECI absorbing in the NIR spectrum. Two proteins of interest were tested to assess their potential for FONT imaging. The first was the GEVI Butterfly 1.2, a highly sensitive FRET based voltage

sensitive protein.[20] A high speed fluorescence camera was developed and used to test the approximate responses of the protein *in vivo* when imaged in a non-invasive manner. The fluorescence system could readily detect both mCitrine and mKate2 dynamics with ratiometric readings between both showing a response of 0.8% with a rise time of 40 ms, much faster than the responses seen from GECIs. The low delta changes of neither mCitrine nor mKate2 (0.4 to 0.5 %) are not suitable for FONT and were not pursued. This is especially relevant since the absorption profile of Butterfly 1.2 is similar to GCaMP6, where hemoglobin absorption is a highly contributing factor.[20, 21] Although not published, the result from imaging the protein completely non-invasively are shown in Figure 5.5. These images were acquired with the high-speed fluorescent system I helped establish in the lab.

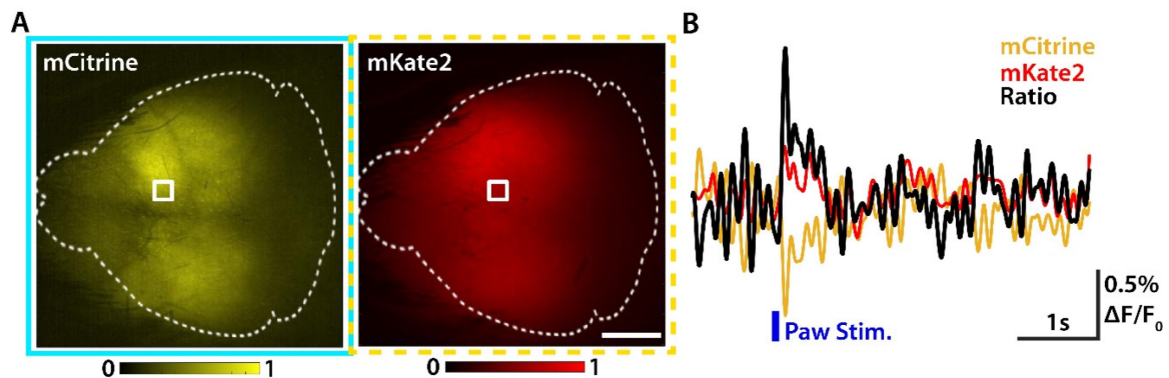


**Figure 5.5 Expression and responses of Butterfly 1.2 in the transgenic mouse line.** A) Sample images of the fluorescence seen from both mCitrine (absorbing at 473 nm) and mKate2 (absorbing fluorescence from mCitrine) as detected by the high-speed camera setup (single frame from 100 Hz). Scale bar: 2 mm. B) Responses detected from the mCitrine and mKate2 proteins including the ratiometric response from the region indicated by the white box in A). Both mCitrine and mKate2 traces are an average of 31 cycles each. mCitrine shows a drop of 0.5% with mKate2 undergoing an increase of 0.4%. The ratiometric increase is ~0.8%. The rise time of the protein is 40 ms with a recovery to baseline after ~500 ms.

To overcome visible absorption, the first NIR GECI, NIR-GECO1 was virally expressed in mice and imaged using fluorescence. The protein showed initial promise as it absorbed at 671 nm, a wavelength that could enable whole-brain non-invasive FONT. The OA spectrum of the  $\text{Ca}^{2+}$  bound and  $\text{Ca}^{2+}$  free form of the purified protein showed a similar trend to GCaMP6, as shown in Figure 5.6. As this was the first GECI of its kind and as it has been developed from a completely different organism (bacteria vs aquamarine animals), the kinetics; expression and sensitivity of the protein are not yet fully optimized. The protein requires biliverdin co-factors (unlike GFP based sensors) to fluoresce and it is much more susceptible to bleaching than GFP based sensors. Additionally, it undergoes a drop in absorption during activation which further increases bleaching effects.[22] Nevertheless, the responses could be detected by fluorescence but only with deltas of 0.3% whilst OAT could successfully unmix the protein *in vivo* as shown in Figure 5.6. The inherent shot noise in FONT from the laser does not allow for such low SNR deltas to be detected right now, but this is only a matter of instrumentation optimization and improvements upon the NIR-GECO1 protein.

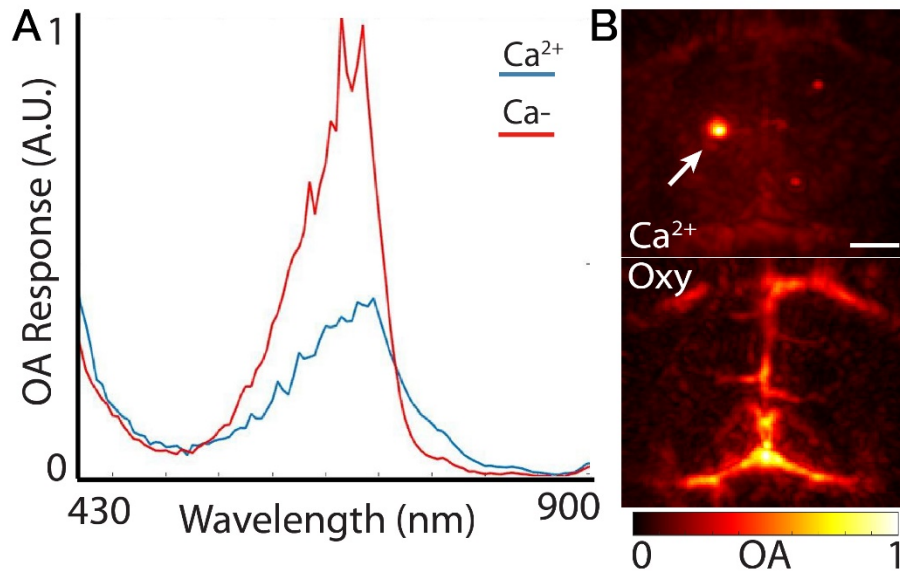


**Figure 5.6 Spectral OA profile of NIR-GECO1** A) Spectrally unmixed OA profile (arbitrary units) of NIR-GECO1 for calcium bound ( $\text{Ca}^{2+}$ ) and calcium free forms of the protein. B) Top; spectrally unmixed profile of calcium bound NIR-GECO1 acquired with the FONT system. The white arrow highlights the injection site. Bottom; spectrally unmixed HbO for anatomical reference. Scale bar = 2 mm.

This research has set out to achieve five-dimensional FONT imaging for large scale electrophysiology in scattering tissues. As shown in the previous chapters, this was achieved using current technology, adapting already existing ones when suitable and the correct selection of model organisms across the entire mouse cortex, which is one of the most highly scattering tissues. The capabilities of FONT surpass those seen with classical two-photon imaging in terms of FOV and spatiotemporal resolution. However, there is still room for improvement, and this should be carried out on two fronts. The inherent noise and limited repetition rates of the OPO lasers is one current limiting factor for FONT. Developing a method of reducing this noise was attempted, using an absorbing microsphere for beam fluctuation reference along with the internal power meter from the laser itself to correct this noise. Nevertheless, the noise is an issue with low frequency oscillations being present in the system - from the cooling system water pump (0.1 Hz) which were also accounted for. This OPO noise is the reason why using this laser for fluorescence resulted in no detection of activity from either Butterfly 1.2 or NIR-GECO1 and required highly stable CW lasers to be used for imaging.

The second key area to tackle is the development of a protein designed with and for FONT as opposed to repurposing proteins, even though this has proven successful. High throughput screening of *in vivo* expressed proteins should be carried out with a combination of fluorescence and FONT.[23] As has been the case in fluorescent imaging, this approach will develop suitable candidates for FONT.[23] However, whilst useful *in vitro* expression is limited in complexity in comparison to *in vivo* expression (e.g. no hemoglobin). Therefore, the *in vivo* expression of candidate electrophysiology proteins is a true test of their suitability to FONT. As shown for non-invasive GCaMP6 imaging, the increased organism complexity dramatically reduces the delta SNR when comparing single cell to whole brain responses. Whilst a protein may be highly successful in cell cultures and slices, this does not directly translate to non-invasive FONT or mesoscale fluorescence imaging. Protein engineering with Butterfly 1.2 or NIR-GECO1 should be carried out with a focus on FONT imaging. As shown by this work, for mouse brain imaging FONT is often a superior method to current neuroimaging methods.

Establishing a pipeline for such protein development would accelerate FONT to completely surpass fluorescence for whole brain imaging and it could have dramatic implications on neuroscience research as a whole.[23] Suitable proteins should be expressed using viral vectors, as the process is less time consuming and easier than generating transgenic lines. Essentially this allows rapid prototyping of electrophysiological proteins with similar expression levels.[24] Currently, no system could provide the same resolution, sensitivity and FOV as FONT does. A suitable GECI or GEVI indicator (once determined) absorbing in the NIR spectrum, transgenically expressed in a mouse line would allow complete non-invasive brain imaging in 3D with FONT. Here, direct monitoring of neuronal communication could be tracked from its origin to destination, which is a long term goal of neuroimaging in general.[24] Current solutions require implantation of optical fibers, skull clearing and skull thinning or craniotomy for example.[25-27] In this work steps have already been made towards awake animal imaging with FONT and given the FOV and spatiotemporal resolution, this could deliver new insights to brain function as a whole as opposed to small sections or surface imaging.[28, 29] The work presented here shows that given the right experimental design and setup, FONT could and will eliminate many of the issues with current neuroimaging modalities.

The methods established here have focused on reliable and established methods of stimulating activity in the mouse brain i.e., electrical paw stimulation. Future work could take advantage of the open access to the mouse body (aside from the scalp) to stimulate other regions of the body and map both hemodynamic and calcium response e.g. multiple paw stimulation and whisker stimulation.[30, 31] The inherent multispectral capabilities of FONT could readily be applied to optogenetic stimulation and monitoring of elicited responses, especially over the whole brain with correct actuators and reporters.[13, 22] Aside from awake mouse imaging, it would also be of interest to investigate the application of FONT to larger more complex organisms such as simians where larger FOV and deeper imaging of electrophysiology and hemodynamics would be of significant value.[32-34] In addition, other sensors could be investigated for their application to FONT such as glutamate and dopamine sensitive fluorescent proteins.[35, 36] Whilst the adaptation of FONT to these investigations will undoubtedly come with many challenges, the work carried out in this thesis should provide a stable base upon which a more physiological environment to image brain function with FONT can be established.

## References

1. Dean-Ben, X.L., et al., *Advanced optoacoustic methods for multiscale imaging of in vivo dynamics*. Chemical Society Reviews, 2017. **46**(8): p. 2158-2198.
2. Mc Larney, B., et al., *Uniform light delivery in volumetric optoacoustic tomography*. Journal of Biophotonics, 2019. **12**(6): p. e201800387.
3. Lang, D., et al., *Optical Mapping of Action Potentials and Calcium Transients in the Mouse Heart*. Jove-Journal of Visualized Experiments, 2011(55).
4. Lin, H.-C.A., et al., *Ultrafast Volumetric Optoacoustic Imaging of Whole Isolated Beating Mouse Heart*. Scientific reports, 2018. **8**(1): p. 1-7.
5. Gottschalk, S., et al., *Rapid volumetric optoacoustic imaging of neural dynamics across the mouse brain*. Nature Biomedical Engineering, 2019. **3**(5): p. 392-401.
6. Deán-Ben, X.L., et al., *Functional optoacoustic neuro-tomography of calcium fluxes in adult zebrafish brain in vivo*. Optics letters, 2017. **42**(5): p. 959-962.
7. Chen, T.-W., et al., *Ultrasensitive fluorescent proteins for imaging neuronal activity*. Nature, 2013. **499**(7458): p. 295.
8. Mühlethaler, M., et al., *The isolated and perfused brain of the guinea-pig in vitro*. European Journal of Neuroscience, 1993. **5**(7): p. 915-926.
9. Gottschalk, S., et al., *Isolated Murine Brain Model for Large-Scale Optoacoustic Calcium Imaging*. Frontiers in neuroscience, 2019. **13**: p. 290.
10. Dhir, A., *Pentylentetrazol (PTZ) kindling model of epilepsy*. Current protocols in neuroscience, 2012. **58**(1): p. 9.37. 1-9.37. 12.
11. Jeffrey, M., et al., *A reliable method for intracranial electrode implantation and chronic electrical stimulation in the mouse brain*. BMC neuroscience, 2013. **14**(1): p. 82.
12. Kim, C.K., A. Adhikari, and K. Deisseroth, *Integration of optogenetics with complementary methodologies in systems neuroscience*. Nature Reviews Neuroscience, 2017. **18**(4): p. 222.
13. Ovsepian, S.V., et al., *Visualizing Cortical Response to Optogenetic Stimulation and Sensory Inputs Using Multispectral Handheld Optoacoustic Imaging*. Photoacoustics, 2019: p. 100153.
14. Liao, L.-D., et al., *Neurovascular coupling: in vivo optical techniques for functional brain imaging*. Biomedical engineering online, 2013. **12**(1): p. 38.
15. Jacques, S.L., *Optical properties of biological tissues: a review*. Physics in Medicine & Biology, 2013. **58**(11): p. R37.
16. Mc Larney, B., et al., *Monitoring of stimulus evoked murine somatosensory cortex hemodynamic activity with volumetric multi-spectral optoacoustic tomography*. Frontiers in neuroscience, 2020. **14**: p. 536.
17. Schroeter, A., et al., *Specificity of stimulus-evoked fMRI responses in the mouse: the influence of systemic physiological changes associated with innocuous stimulation under four different anesthetics*. Neuroimage, 2014. **94**: p. 372-384.
18. Hu, X. and E. Yacoub, *The story of the initial dip in fMRI*. Neuroimage, 2012. **62**(2): p. 1103-1108.
19. Dana, H., et al., *Thy1-GCaMP6 transgenic mice for neuronal population imaging in vivo*. PloS one, 2014. **9**(9): p. e108697.
20. Mishina, Y., et al., *Exploration of genetically encoded voltage indicators based on a chimeric voltage sensing domain*. Frontiers in molecular neuroscience, 2014. **7**: p. 78.
21. Akemann, W., et al., *Two-photon voltage imaging using a genetically encoded voltage indicator*. Scientific reports, 2013. **3**: p. 2231.
22. Qian, Y., et al., *A genetically encoded near-infrared fluorescent calcium ion indicator*. Nature Methods, 2019.
23. Hofmann, U.A., et al., *High-Throughput Platform for Optoacoustic Probing of Genetically Encoded Calcium Ion Indicators*. iScience, 2019. **22**: p. 400-408.
24. Barson, D., et al., *Simultaneous mesoscopic and two-photon imaging of neuronal activity in cortical circuits*. Nature methods, 2019: p. 1-7.

25. Ohayon, S., et al., *Minimally invasive multimode optical fiber microendoscope for deep brain fluorescence imaging*. Biomedical optics express, 2018. **9**(4): p. 1492-1509.
26. Zhao, Y.-J., et al., *Skull optical clearing window for in vivo imaging of the mouse cortex at synaptic resolution*. Light: Science & Applications, 2018. **7**(2): p. 17153.
27. Nimmerjahn, A., *Optical window preparation for two-photon imaging of microglia in mice*. Cold Spring Harbor Protocols, 2012. **2012**(5): p. pdb. prot069286.
28. Desjardins, M., et al., *Awake Mouse Imaging: From Two-Photon Microscopy to Blood Oxygen Level-Dependent Functional Magnetic Resonance Imaging*. Biological Psychiatry: Cognitive Neuroscience and Neuroimaging, 2019. **4**(6): p. 533-542.
29. Thurley, K. and A. Ayaz, *Virtual reality systems for rodents*. Current zoology, 2017. **63**(1): p. 109-119.
30. Bock, C., et al., *Brainmapping of  $\alpha$ -chloralose anesthetized rats with T2\*-weighted imaging: distinction between the representation of the forepaw and hindpaw in the somatosensory cortex*. NMR in Biomedicine: An International Journal Devoted to the Development and Application of Magnetic Resonance In Vivo, 1998. **11**(3): p. 115-119.
31. Olefir, I., et al., *Spatial and spectral mapping and decomposition of neural dynamics and organization of the mouse brain with multispectral optoacoustic tomography*. Cell reports, 2019. **26**(10): p. 2833-2846. e3.
32. Li, C.-X. and X. Zhang, *Evaluation of prolonged administration of isoflurane on cerebral blood flow and default mode network in macaque monkeys anesthetized with different maintenance doses*. Neuroscience letters, 2018. **662**: p. 402-408.
33. Li, M., et al., *Long-term two-photon imaging in awake macaque monkey*. Neuron, 2017. **93**(5): p. 1049-1057. e3.
34. Nie, L., Z. Guo, and L.V. Wang, *Photoacoustic tomography of monkey brain using virtual point ultrasonic transducers*. Journal of biomedical optics, 2011. **16**(7): p. 076005.
35. Helassa, N., et al., *Ultrafast glutamate sensors resolve high-frequency release at Schaffer collateral synapses*. Proceedings of the National Academy of Sciences, 2018. **115**(21): p. 5594-5599.
36. Sun, F., et al., *A genetically encoded fluorescent sensor enables rapid and specific detection of dopamine in flies, fish, and mice*. Cell, 2018. **174**(2): p. 481-496. e19.

# Permission letters from publishers

## Permission for “Uniform light delivery in volumetric optoacoustic tomography”:

### License Details

This Agreement between Mr. Benedict Mc Larney (“You”) and John Wiley and Sons (“John Wiley and Sons”) consists of your license details and the terms and conditions provided by John Wiley and Sons and Copyright Clearance Center.

Print Copy

License Number	4780380972391
License date	Mar 01, 2020
Licensed Content Publisher	John Wiley and Sons
Licensed Content Publication	Journal of Biophotonics
Licensed Content Title	Uniform light delivery in volumetric optoacoustic tomography
Licensed Content Author	Benedict Mc Larney, Johannes Rebling, Zhenyue Chen, et al
Licensed Content Date	Feb 20, 2019
Licensed Content Volume	12
Licensed Content Issue	6
Licensed Content Pages	9
Type of Use	Dissertation/Thesis
Requestor type	Author of this Wiley article
Format	Print and electronic
Portion	Full article
Will you be translating?	No
Title of your thesis / dissertation	Five Dimensional Optoacoustic Tomography for Large Scale Electrophysiology in Scattering Tissues
Expected completion date	Jan 2020
Expected size (number of pages)	100
Requestor Location	Mr. Benedict Mc Larney Lüneburger Str. 7  München, 80809 Germany Attn: Mr. Benedict Mc Larney
Publisher Tax ID	EU826007151
Total	<b>0.00 EUR</b>

## Permission for “Monitoring of Stimulus Evoked Murine Somatosensory Cortex Hemodynamic Activity With Volumetric Multi-Spectral Optoacoustic Tomography”

**Keywords:** optoacoustics, hemodynamics, somatosensory, cortex, initial-dip

**Citation:** Mc Larney B, Hutter MA, Degtyaruk O, Deán-Ben XL and Razansky D (2020) Monitoring of Stimulus Evoked Murine Somatosensory Cortex Hemodynamic Activity With Volumetric Multi-Spectral Optoacoustic Tomography. *Front. Neurosci.* 14:536. doi: 10.3389/fnins.2020.00536

**Received:** 03 January 2020; **Accepted:** 01 May 2020;

**Published:** 03 June 2020.

Edited by:

**Itamar Ronen**, Leiden University Medical Center, Netherlands

Reviewed by:

**Itamar Kahn**, Technion Israel Institute of Technology, Israel

**Adrian Rodriguez-Contreras**, City College of New York (CUNY), United States

**Saak V. Ovsepián**, National Institute of Mental Health, Czechia

**Stratis Tzoumas**, Carl Zeiss, Germany

**Copyright** © 2020 Mc Larney, Hutter, Degtyaruk, Deán-Ben and Razansky. This is an open-access article distributed under the terms of the **Creative Commons Attribution License (CC BY)**. The use, distribution or reproduction in other forums is permitted, provided the original author(s) and the copyright owner(s) are credited and that the original publication in this journal is cited, in accordance with accepted academic practice. No use, distribution or reproduction is permitted which does not comply with these terms.

**\*Correspondence:** Daniel Razansky, [daniel.razansky@uzh.ch](mailto:daniel.razansky@uzh.ch)

**†Present address:** Benedict Mc Larney, Molecular Pharmacology Program, Department of Radiology, Memorial Sloan Kettering Cancer Center, New York, NY, United States

**‡**These authors have contributed equally to this work

## **Permission for “A genetically encoded near-infrared fluorescent calcium ion indicator”**

**SPRINGER NATURE**

A genetically encoded near-infrared fluorescent calcium ion indicator

Author: Yong Qian et al

Publication: Nature Methods

Publisher: Springer Nature

Date: Jan 21, 2019

Copyright © 2019, Springer Nature

### **Author Request**

If you are the author of this content (or his/her designated agent) please read the following. If you are not the author of this content, please click the Back button and select no to the question "Are you the Author of this Springer Nature content?".

Ownership of copyright in original research articles remains with the Author, and provided that, when reproducing the contribution or extracts from it or from the Supplementary Information, the Author acknowledges first and reference publication in the Journal, the Author retains the following non-exclusive rights:

To reproduce the contribution in whole or in part in any printed volume (book or thesis) of which they are the author(s).

The author and any academic institution, where they work, at the time may reproduce the contribution for the purpose of course teaching.

To reuse figures or tables created by the Author and contained in the Contribution in oral presentations and other works created by them.

To post a copy of the contribution as accepted for publication after peer review (in locked Word processing file, of a PDF version thereof) on the Author's own web site, or the Author's institutional repository, or the Author's funding body's archive, six months after publication of the printed or online edition of the Journal, provided that they also link to the contribution on the publisher's website.

Authors wishing to use the published version of their article for promotional use or on a web site must request in the normal way.

If you require further assistance please read Springer Nature's online author reuse guidelines.

For full paper portion: Authors of original research papers published by Springer Nature are encouraged to submit the author's version of the accepted, peer-reviewed manuscript to their relevant funding body's archive, for release six months after publication. In addition, authors are encouraged to archive their version of the manuscript in their institution's repositories (as well as their personal Web sites), also six months after original publication.